ABSTRACT

Title of Dissertation: CREATION AND DESTRUCTION OF LITHOSPHERIC MANTLE BENEATH THE NORTH CHINA CRATON

Jingao Liu, Ph.D., 2011

Dissertation directed by: Professor Roberta L. Rudnick, Geology
Professor Richard J. Walker, Geology

Mantle peridotites carried in volcanic rocks provide a window into the composition, age and origin of deep lithospheric mantle. Previous studies of mantle peridotites have shown that the central-eastern North China Craton experienced lithospheric reactivation in the past, which makes the craton an important location to investigate reactivation processes and mechanisms. In order to better understand the formation and evolution of the North China Craton, the petrology, major and trace element geochemistry of both whole rocks and minerals, whole rock Re-Os isotope systematics, and highly siderophile element (HSE) abundances, were carried out on peridotites entrained in Cretaceous to Tertiary lavas from the craton. Strontium-Nd-Hf-Pb isotopic compositions of clinopyroxenes separated from some of these rocks were also examined.

Studies of these peridotites show that: 1) Peridotites from the western-central North China Craton record a north-south composition and age dichotomy. The northern portion of the central region of the craton experienced lithospheric mantle replacement via a ~1.8 Ga collision associated with amalgamation of the craton. The

comparative Late Archean age between crust and lithospheric mantle in the southern portion of the central region suggests that the cratonization in this region occurred at ~2.5 Ga; 2) Lithospheric thinning and replacement beneath the northern edge of the eastern North China Craton occurred prior to ~100 Ma. Phanerozoic lithospheric thinning and replacement in the eastern North China Craton may have evolved from east to west, or from the margins to the interior of the continent with time in the Mesozoic; 3) Highly fractionated HSE patterns found in a majority of peridotite suites and characterized by Os, Pd and Re depletions relative to Ir were caused by recent sulfide breakdown via interaction with a S-undersaturated oxidizing melt/fluid; and, 4) The trace element characteristics and isotopic tracers (Sr-Nd-Hf-Pb) present in clinopyroxenes, combined with their whole-rock Re-Os data, record a multi-stage history of primary melt depletion and secondary overprinting processes. Lu-Hf isotopic compositions of pyroxenes may record the cooling age when peridotites cooled down below the closure temperature of the system.

CREATION AND DESTRUCTION OF LITHOSPHERIC MANTLE BENEATH THE NORTH CHINA CRATON

By

Jingao Liu

Dissertation submitted to the Faculty of the Graduate School of the
University of Maryland, College Park in partial fulfillment of
the requirements for the degree of
Doctor of Philosophy
2011

Advisory Committee:

Professor Roberta L. Rudnick, Chair
Professor Richard J. Walker, Co-Chair
Professor Richard W. Carlson
Professor Igor S. Puchtel
Professor Laurent G.J. Montesi
Professor Douglas Hamilton

Preface

The work condensed in this dissertation was performed between August 2006 and August 2011 when I was a full-time graduate student in the Department of Geology, University of Maryland-College Park. All xenolithic samples were either collected by me and my coauthors during field trips to China in 2007 and 2010, or provided by my coauthors. Most analyses, including petrology, mineralogy, whole-rock Re-Os isotope systematics and highly siderophile element abundances, as well as Sr-Nd-Hf-Pb isotopic compositions in clinopyroxenes, were conducted by me, while whole rock major and trace element compositions, including Se and S analyses, were conducted at commercial labs at other institutions with powders prepared by me. Most of the chapters in this dissertation are either published or soon to be submitted for publication. My role, relative to that of my coauthors is specified for each chapter. Overall, I wrote first-drafts of all the materials in publications and manuscripts in preparation that were revised with assistance of my coauthors, particularly my supervisors Roberta Rudnick and Rich Walker.

Dedication

This dissertation is dedicated to my grandma, Xiaomi Luo.

Acknowledgements

Special big thanks go to my supervisors, Dr. Roberta Rudnick and Dr. Rich Walker who both supported and mentored me throughout this project. By looking back at what happened on me in the past five years, I knew I was so lucky to have such outstanding supervisors. Roberta kept me well, as a whole, on the right track of the project. Rich taught me a lot on the analytical measurements, from point to point. Their mentoring inspired me with a better understanding of how to raise and approach scientific questions. Their attitude to science and knowledge in addressing problems led to a positive direction towards my future research. They taught me how the work should be appropriately presented to audience. They provided me, as an international student, enormous help in speaking and particularly writing English with patience. I could not use any words (both English and Chinese) to fully express how I appreciate what they gave me. Everything I learned from them will benefit me continuously through my research career. Finally, I want to say, "Roberta and Rich, YOU TWO ARE SUPER SUPERVISORS I EVER GOT TO KNOW AND WORK WITH".

Dr. Shan Gao and Dr. Fu-yuan Wu, as well as their students and colleagues, are thanked for providing great effort during China field trips. Without their help and warm host, it would not be possible for us to collect hundreds of xenoliths from the North China Craton. Both Shan and Fu-yuan also provided constructive comments in revising the manuscripts I wrote.

Dr. Rick Carlson, Dr. Igor Puchtel, and Dr. Laurent Montesi are thanked for serving on my dissertation committee and providing constructive comments in revising this dissertation. Moreover, Rick provided invaluable assistance in the analyses of Sr-Nd-Hf-Pb isotopic compositions at the Department of Terrestrial

Magnetism, Carnegie Institution of Washington. Dr. Douglas Hamilton is thanked for serving as an active Dean's representative on my committee.

Dr. Phil Piccoli is thanked for providing assistance during the enormous electron probe work in the past few years. Dr. Igor Puchtel and Lynnette Pitcher are thanked for providing help in the chemistry lab. Dr. Richard Ash is thanked for being helpful in the ICP-MS lab, both Element 2 and Nu Plasma. Dr. James Day is thanked for assisting me in doing NiS fusion work and providing helpful comments in some manuscripts I wrote. Dr. Mary Horan and Dr. Tim Mock are thanked for assisting me in determining Sr-Nd-Hf-Pb isotopic compositions of clinopyroxenes.

Dr. Wen-liang Xu, Dr. Yi-gang Xu and Dr. Hong-fu Zhang are thanked for providing powders of some peridotites studied in this project. I am also grateful to a number of fellow students and friends, Jeremy Bellucci, Tom Ireland, Sheng-Ao Liu, Sara Peek, Miriam Galenas, Nanping Wu, and Wei Yang, who read and improved earlier versions of the manuscripts I wrote.

I would like to deliver my thanks to the staff of the department, including Jeanne Martin, Sandy Romeo, Dorothy Brown, Todd Karwoski, Michelle Montero, Suzanne Martin and Bernadette Gatewood, for being very helpful. I would also like to thank all other faculty members in the department for your support and encouragement. I would like to thank all the graduate students in the Department of Geology, for improving my speaking English and making the time in Maryland enjoyable and fast.

Last but not least, I would like to thank my parents, my brother Fugao and his family, and my wife Liping for your endless love and support.

Table of Contents

List of Tables

Chapter 3

Chapter 3

Chapter 5

Chapter 6

List of Figures

Chapter 2

Chapter 3

Chapter 4

Chapter 5

Chapter 6

Chapter 7

Chapter 1: Introduction[1]

[1] The text in this chapter was created/written by J.G. Liu.

Archean cratons are ancient continental regions that have remained stable for billions of years on Earth. A craton is generally comprised of a thick crust and a deep lithospheric root that extends into the mantle to depths of up to 300 km (Pollack and Chapman, 1977; Ritsema et al., 1998; Rudnick et al., 1998). Cratonic peridotites typically are more refractory due to higher degrees of mantle melt extraction in the Archean (probably because of a hotter mantle during that time; Boyd, 1989), when compared to their off-craton counterparts. Extensive melt extraction, particularly the removal of FeO and Al_2O_3, makes cratonic peridotitic residues less dense (and, hence, more buoyant) than off-craton peridotites (O'Hara, 1975; Jordan, 1988). Thermobarometric studies of mineral phase pairs in mantle peridotites document that cratonic peridotites typically plot along cooler geotherms than off-craton peridotites (e.g., Finnerty and Boyd, 1987; Rudnick et al., 1998), suggesting that cratonic mantle is relatively cool to the base of lithosphere. Collectively, such distinctive features keep ancient cratonic lithosphere buoyant, intact and insulated from reworking and recycling back into the convecting mantle.

Previous studies have shown that the eastern North China Craton experienced lithospheric reactivation subsequent to the Paleozoic (e.g., Menzies et al., 1993; Griffin et al., 1998). Studies of mantle xenoliths and diamond inclusions hosted in Paleozoic kimberlites from the eastern portion of the craton document a typical refractory, thick lithospheric root with Archean Os model ages (Gao et al., 2002; Wu et al., 2006; Zhang et al., 2008), suggesting the existence of a typical intact Archean

craton beneath this region prior to the eruption time. By contrast, mantle peridotites carried in Cenozoic basalts from this area are mostly spinel lherzolites that are relatively fertile in composition. Osmium isotopic analyses have shown that these peridotites are isotopically similar to abyssal peridotites that sample modern convecting upper mantle (Gao et al., 2002; Wu et al., 2003; 2006; Chu et al., 2009). Seismic studies have suggested that the lithosphere beneath this area is < 100 km thick (e.g., Tian et al., 2009; Chen et al., 2010), consistent with relatively high surface heat flow (Hu et al., 2000) and generally positive Bouguer gravity anomalies (Yuan, 1996). The change in lithospheric composition, temperature and age from the Paleozoic to Cenozoic indicates that the eastern portion of the North China Craton lost its ancient lithospheric keel during the Mesozoic (Menzies et al., 1993; Griffin et al., 1998; Wu et al., 2005a). Yet, the exact timing and mechanism(s) responsible for the lithospheric thinning and replacement are debated.

In contrast to the eastern portion of the North China Craton, a different sequence of events may have occurred in the central portion of the North China Craton, as implied by previously reported composition and age complexity of mantle peridotites carried in Cenozoic basalts from this area. A Re-Os isochron for Hannuoba peridotites in the northernmost part of the central portion of the North China Craton indicates an age of ~1.9 Ga for lithospheric mantle, which is younger than the overlying Archean crust (Gao et al., 2002). This result has been taken as evidence for lithospheric replacement in the Paleoproterozic, when the central region of the craton formed in a continent-continent collision (Gao et al., 2002). However, Y.G. Xu et al. (2008) reported Late Archean Os model ages for the Yangyuan peridotites that are located approximately 100 km south of Hannuoba. The finding of Late Archean Os model

ages in the Yangyuan peridotites would be not consistent with lithospheric replacement in the Paleoproterozoic. Moreover, Os data for the Fansi peridotites (~100 km south of Yangyuan) show Early Paleoproterozoic Os model ages (Rudnick et al., 2006). Peridotites from the southern portion of the central region are more refractory in composition than those from the northern portion, and have been considered to be fragments of relict Archean lithospheric mantle (Zheng et al., 2001; Xu et al., 2010), which is supported by Archean model ages in two sulfides from Hebi peridotites (Zheng et al., 2007). Determining the composition and age of lithospheric mantle beneath this region is critical to understanding the relationship between the lithospheric mantle and overlying crust, as well as the history of tectonic amalgamation of the craton.

In this study, the xenoliths mentioned above, and new samples collected from several other mantle xenolith localities (i.e., Fuxin, Datong and Jining) were studied. All the xenoliths studied here were entrained in Cretaceous to Tertiary lavas.

The Re-Os isotope system has been extensively used to date primary melt depletion events in mantle peridotites (e.g., Walker et al., 1989; Pearson et al., 1995a; Reisberg and Lorand, 1995; Handler et al., 1997). The Re-Os isotope compositions were determined for the peridotites in this study, and highly siderophile element (HSE) abundances were also measured for the same powder aliquots to evaluate the influence of secondary processes on the Re-Os isotope system. The Lu-Hf isotope system has been shown by several studies to be relatively immune to overprinting events and may be useful to date the timing of melt depletion in peridotites (Schmidberger et al., 2002; Pearson and Nowell, 2003; Wittig et al., 2006; Bizimis et al., 2007; Choi et al., 2008, 2010), in complement to the whole-rock Re-Os isotopic

system. Consequently, the Lu-Hf isotopic systematics of clinopyroxenes separated from a suite of well-characterized peridotites were determined in order to evaluate the utility of Lu-Hf in dating melt depletion in peridotites.

In this project, I analyzed over a hundred peridotites from eight localities in the North China Craton. This work included the petrology, major and trace element geochemistry of the bulk rocks and minerals, whole-rock Re-Os isotopic compositions, and highly siderophile element abundances, as well as Sr-Nd-Hf-Pb isotopic compositions of clinopyroxene separates from a subset of the well-characterized peridotites. The aims of this project were 1) to determine the history of mantle processes recorded in the peridotites, 2) to examine the composition and age structure of the lithospheric mantle beneath the North China Craton, and 3) to use the observed lithospheric structure to constrain the origin and evolution of the North China Craton.

The work of this dissertation is presented in the following five chapters. Chapter Two summarizes the geological setting of the North China Craton, and highlights the existing controversies regarding the tectonic framework of the craton. Chapter Three reports HSE abundances and Os isotopic compositions for peridotites from two adjacent localities in the North China Craton (published as Liu et al., 2010, EPSL) in order to examine effects of primary and secondary events on HSE abundances and Os isotopic compositions. Highly fractionated HSE patterns characterized by Os, Pd and Re depletions relative to Ir are interpreted to be caused by recent sulfide breakdown via interaction with a S-undersaturated oxidizing melt/fluid. The observed positive correlation between melt depletion indicators (e.g., Al_2O_3) and $^{187}Os/^{188}Os$ suggests

that the recent sulfide breakdown did not significantly modify Os isotopic compositions of peridotites.

Chapter Four reports the petrology, mineral compositions, whole rock major/trace element concentrations, including HSE abundances, and Re-Os isotope systematics of peridotite xenoliths from the central-western portions of the North China Craton in order to systematically constrain the structure and evolution of the deep lithosphere (published as Liu et al., 2011a, GCA). These peridotites record a north-south coupled composition and age dichotomy in the central region. The northern portion of the central region of the craton experienced lithospheric mantle replacement via ~1.8 Ga collision associated with amalgamation of the craton. Phanerozoic lithospheric thinning and replacement in the eastern portion of the North China Craton may have evolved from east to west, or from the margins to its interior with time in the Mesozoic.

Chapter Five reports Sr-Nd-Hf-Pb isotopic systematics of clinopyroxene separates from a well-characterized suite of peridotites. These data record a multi-stage history of melt depletion and overprinting processes in peridotites. The Nd-Hf decoupling in peridotites resulted from ancient Lu/Hf and Sm/Nd decoupling soon after mantle partial melting. Despite overprinting events, these clinopyroxenes exhibit a large range of Hf isotopic compositions (ε_{Hf} = +13.5 to +167) and yield a Lu-Hf 'errorchron' of 1.66 ± 0.10 Ga. The Lu-Hf errorchron age is within uncertainty of the whole-rock Os model ages (1.8 ± 0.2 Ga; Liu et al., 2010, 2011a), supporting the Paleoproterozoic primary melt depletion event in these samples.

Chapter Six reports the Re-Os isotopic compositions and HSE abundances of xenolithic peridotites from Fuxin, which were entrained in Late Cretaceous (~100 Ma) alkali basalts from the northern edge of the eastern portion of the North China Craton. The Fuxin peridotites fall into two groups: refractory, Archean-Paleoproterozoic peridotites and fertile, young peridotites. The coexistence of ancient and young peridotites at Fuxin suggests that here, lithospheric thinning occurred no later than ~100 Ma.

Chapter Seven presents a synthesis of this dissertation and describes possible future directions that could be undertaken in order to place better constraints on the formation and evolution of lithospheric mantle beneath the North China Craton.

Chapter 2: Geological Setting of the North China Craton[1]

[1] The text and figure in this chapter were created/written by J.G. Liu.

The North China Craton is a relatively small, ancient craton that is bounded to the west by the early Paleozoic Central China Orogen and to the north by the late Paleozoic Xing-Meng Orogenic Belt, and is bordered by the Triassic Qinling-Dabie-Sulu ultrahigh-pressure metamorphic belts to the south and east (Fig. 2-1). The North China Craton is predominantly composed of Archean to Paleoproterozoic basement that formed during four events, namely *Qianxi* (>3.0 Ga), *Fuping* (3.0-2.5 Ga), *Wutai* (2.4-2.4 Ga) and *Lüliang* (2.4-1.8 Ga) (Huang, 1977; Ma and Wu, 1981; Zhao, 1993; Shen and Qian, 1995).

Based on integrated studies of lithology, structure, geochronology, and metamorphic pressure-temperature-time (P-T-t) paths, the North China Craton has been divided into three blocks (Fig. 2-1): the Western Block, the Eastern Block, and the intervening central region, which has been called the Trans-North China Orogen (Fig. 2-1a; Zhao et al., 2000, 2001, 2005), or the Central Orogenic Belt (Fig. 2-1b; e.g., Kusky and Li, 2003). The Western Block is characterized by rather thick (~45 km; Li et al., 2006) Archean crust (Zhao et al., 2001), relatively low surface heat flow (50-60 mW/m^2; Hu et al., 2000; Tao and Shen, 2008) and thick lithosphere (>150 km constrained from seismology; Tian et al., 2009; Chen, 2010). This block has experienced only minor Phanerozoic volcanism and rare seismicity. Within the northern portion of the Western Block is a nearly east-west trending belt consisting largely of khondalites (i.e., high-grade metapelitic gneisses composed of quartz-feldspar-sillimanite, with graphite, garnet and biotite, ± cordierite) and is, thus,

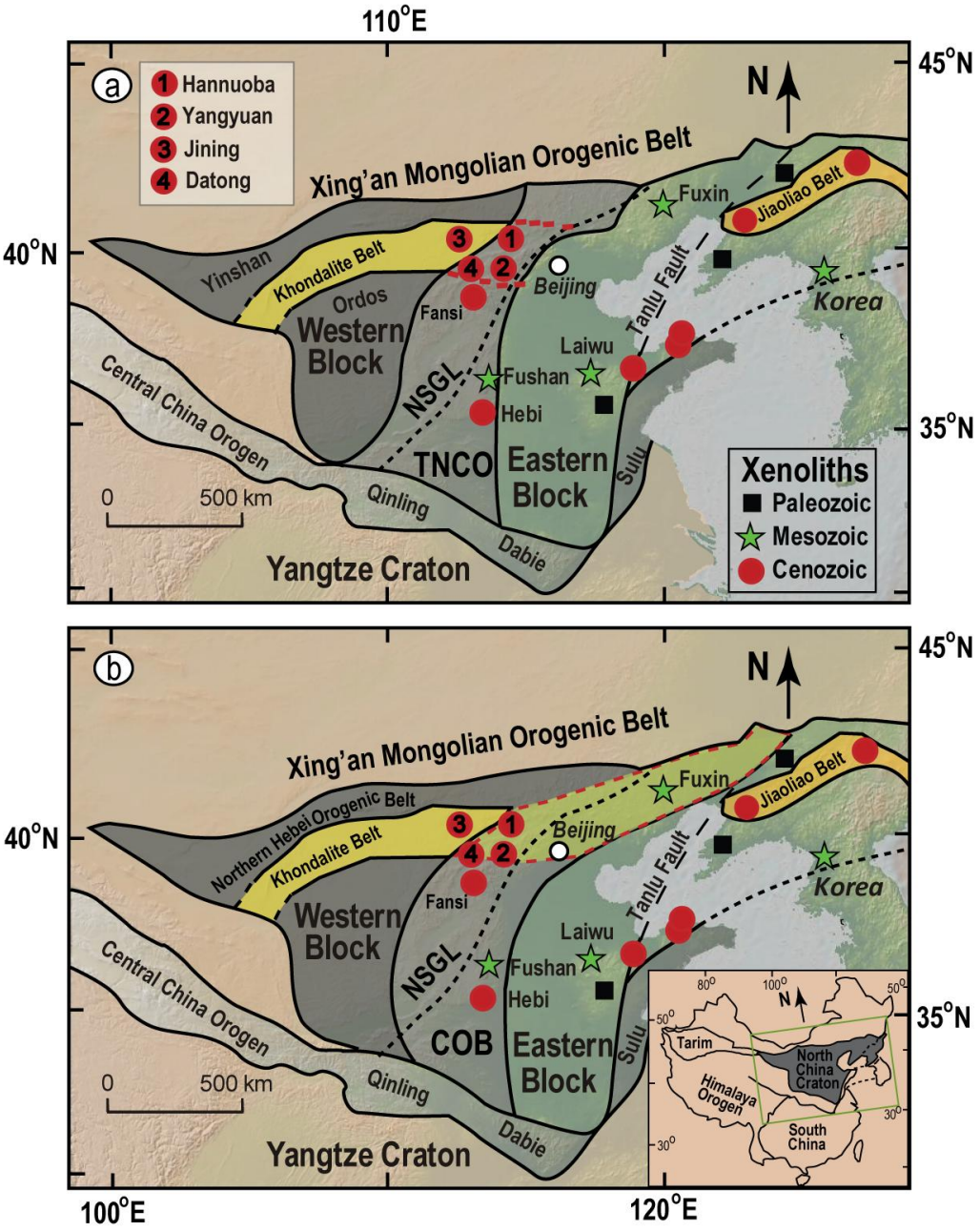

Fig. 2-1. Tectonic sketch map of the North China Craton composed of the Eastern Block, Western Block, and the central region. In panel a, the central region is called "Trans-North China Orogen (TNCO)" formed between the Eastern and Western blocks at ~1.85 Ga (modified from Zhao et al., 2005). In panel b, the central region is called "Central Orogenic Belt (COB)" formed between the Eastern and Western blocks at ~2.5 Ga (modified from Kusky and Li, 2003). Mantle xenolith localities shown as squares (Paleozoic eruption age), stars (Mesozoic), and circles (Cenozoic). The NSGL is the North-South Gravity Lineament (Griffin et al., 1998).

referred to as the Khondalite Belt (Lu et al., 1996) (Fig. 2-1). P-T-t paths of metamorphic rocks in the belt show isothermal decompression, suggesting that it formed during a continent-continent collision at ca. 1.9 Ga (Kusky and Li, 2003; Zhao et al., 2005; 2010; Wan et al., 2006; Santosh et al., 2006, 2007; Dong et al., 2007; Yin et al., 2009).

In contrast to the Western Block, the Eastern Block mainly consists of relatively thin (30-40 km; Li et al., 2006) Archean crust and thin lithosphere (<100 km; Tian et al., 2009; Chen, 2010), and has relatively high surface heat flow (>64 mW/m^2; Hu et al., 2000; Tao and Shen, 2008) and is seismically active. Studies of xenolithic peridotites in this block have suggested that during the Mesozoic, the original cold, thick, and refractory Archean lithospheric mantle was removed and replaced by fertile, thin, Phanerozoic lithospheric mantle, which currently underlies this block (Menzies, 1993; Griffin et al., 1998; Gao et al., 2002; Wu et al., 2003, 2006; Rudnick et al., 2004; Chu et al., 2009). The westernmost limit of Mesozoic thinning is commonly assumed to coincide with the North-South Gravity Lineament (Griffin et al., 1998; Zheng et al., 2001; Menzies et al., 2007; Zhao et al., 2007), which separates a comparatively higher Bouguer gravity anomaly (ranging from negative to positive) in the east than the west and runs through the central portion of the North China Craton (Fig. 2-1).

The roughly north-south trending belt in the central North China Craton (Fig. 2-1) consists mainly of a series of Neoarchean to Paleoproterozoic greenschist- to granulite-facies metamorphic terranes (Zhao et al., 2005, and references therein). The tectonic history of this central region is in debate. Kusky et al. (2001) suggested that it formed at ~2.5 Ga, based on their interpretation that a Late Archean ophiolite

complex exists on the western margin of the Eastern Block (Kusky and Li, 2010). This region then experienced granulite facies metamorphism along the northern boundary in the Paleoproterozoic (ca. 1.85 Ga; Kusky and Li, 2003; Kusky et al., 2007a), which extends into the Khondalite Belt in the Western Block (Fig. 2-1b). Kusky and co-workers refer to this central region as the Central Orogenic Belt. By contrast, "clockwise" P-T paths for the granulites from the northern section of the belt, which formed in the Paleoproterozoic, have been interpreted to suggest that the collision between the Eastern and Western Blocks occurred at ca. 1.85 Ga, forming the so called Trans-North China Orogen (Fig. 2-1a; e.g., Zhao et al., 2000, 2001; Wilde et al., 2002; Kröner et al, 2005, 2006).

Xenolithic peridotites from Early Cretaceous-Tertiary volcanic centers occur over a wide area of the central North China Craton (Fig. 2-1) and show a large range in compositions, from refractory (typical of cratonic peridotites) to fertile (similar to primitive mantle (PM) - a hypothetical undifferentiated mantle; McDonough and Sun, 1995) (e.g., Zheng et al., 2001; Tang et al., 2008; Y.G. Xu et al., 2008; Liu et al., 2010; Xu et al., 2010). The previously available age information for these peridotites (Gao et al., 2002; Zheng et al., 2007; Y.G. Xu et al., 2008; X.S. Xu et al., 2008; Zhang et al., 2009; Liu et al., 2010) suggest that they are considerably older than the Phanerozoic age of lithospheric mantle sampled by Tertiary lavas from the eastern North China Craton (Fig. 2-1) (Gao et al., 2002; Wu et al., 2003; 2006; Chu et al., 2009), though debate exists about whether the Proterozoic ages reflect mantle formed in the Proterozoic (Gao et al., 2002; Liu et al., 2010) or refertilized Archean mantle (Tang et al., 2008; Zhang et al., 2009), and the degree to which original Archean

lithospheric mantle was preserved (Zheng et al., 2001, 2007; Gao et al., 2002; Tang et al., 2008; Y.G. Xu et al., 2008; Zhang et al., 2009; Xu et al., 2010).

Chapter 3: Processes controlling highly siderophile element fractionations in xenolithic peridotites and their influence on Os isotopes[1, 2, 3]

[1] The original version of this chapter was created/written by J.G. Liu. J.G. Liu, R.L. Rudnick, and R.J. Walker contributed to the interpretation of the data.

[2] The sample selection and preparation for measurement were carried out by J.G. Liu. Electronic Micro-Probe Analyses of the samples reported in this chapter were performed mainly by J.G. Liu with assistance of P.M. Piccoli. Whole-rock major element compositions of the Yangyuan samples were measured by S.A. Mertzman at the Franklin and Marshall College, United States. The S and Se contents of the Yangyuan samples and the Se contents of the Hannuoba samples were measured by L.P. Bedard at the Université du Québec à Chicoutimi. Osmium isotopic compositions and HSE abundances reported in this chapter were determined by J.G. Liu.

[3] This chapter has been published as:
Liu, J. G., Rudnick, R. L., Walker, R. J., Gao, S., Wu, F. Y., and Piccoli, P. M., 2010. Processes controlling highly siderophile element fractionations in xenolithic peridotites and their influence on Os isotopes. Earth and Planetary Science Letters, v. 297, p. 287-297. DOI: 10.1016/j.epsl.2010.06.030

Abstract

Xenolithic peridotites having a similar range of major element compositions from two nearby localities in the Trans-North China Orogen, North China Craton, provide a rare opportunity to explore effects resulting from both primary partial melting and secondary processes on Os isotopes and highly siderophile element (HSE) abundances. HSE patterns of peridotites from Hannuoba are similar to those of orogenic peridotite massifs worldwide, but are rare for xenolithic peridotites. These patterns can be explained by relatively low degrees of melt depletion, coupled with long-term preservation of sulfides. By contrast, peridotites from Yangyuan have major element compositions similar to or slightly more depleted than Hannuoba xenoliths, but are characterized by distinct, highly fractionated HSE patterns with lower total HSE

abundances and Os, Pd and Re depletions relative to Ir. Some of the latter HSE characteristics must reflect secondary processes. The low S and Se contents of Yangyuan peridotites, coupled with scarcity of observable sulfides, suggest that they experienced sulfide breakdown, possibly as a result of interaction with a S-undersaturated melt/fluid. This may have occurred under oxidizing conditions, as suggested by the somewhat higher fO_2 recorded in the Yangyuan peridotites compared to the Hannuoba peridotites, as well as the metal-deficient composition of rare, mono-sulfide-solid solution (mss) sulfides within the Yangyuan peridotites. It is speculated that under such conditions, Os, Pd, and possibly Re, more strongly partition into a sulfide liquid, or the oxidizing medium (melt or fluid), than Ir and Pt and, thus, become depleted. These effects would have been imposed on original patterns that were similar to those in the Hannuoba suite. The good correlation between $^{187}Os/^{188}Os$ and major-element indices of melt depletion in the Yangyuan rocks, coupled with the poor correlation between $^{187}Os/^{188}Os$ and $^{187}Re/^{188}Os$, suggests that the S, Os, Pd and Re removal was recent. Hence, the long-term Re-Os isotopic systematics of these rocks would not have been affected, and Re depletion model ages, based on Os isotopes, remain viable to constrain the timing of melt deletion in these peridotites. The similarity of model age distributions between Yangyuan and Hannuoba peridotites (T_{RD} = 0 to 1.7 and 0 to 1.5 Ga, respectively) is consistent with this, and further indicates that these peridotites formed in the Paleoproterozoic.

3.1 Introduction

Highly siderophile element (HSE, including Os, Ir, Ru, Pt, Pd and Re) abundances of mantle rocks are important in tracing the Earth's core-mantle segregation, late

accretion, and mantle differentiation (e.g., Morgan et al., 2001). Further, the ^{187}Re-^{187}Os isotopic system provides a potential means to date formation of lithospheric mantle (e.g., Walker et al., 1989). Unlike lithophile elements in mantle peridotites, HSE dominantly reside in trace phases, such as sulfides and alloys, rather than major phases (e.g., Hart and Ravizza, 1996; Alard et al., 2000; Bockrath et al., 2004; Lorand et al., 2008a, 2010). During partial melting of the mantle, base metal sulfides that concentrate Re, Pt and Pd may preferentially enter the melt phase relative to more refractory sulfides, such as monosulfide solid solution (mss), and alloys that sequester Os, Ir and Ru (e.g., Alard et al., 2000; Luguet et al., 2003; 2007). This division of HSE into sulfides with distinct melting characteristics, along with possible molten sulfide entrained into melts (Bockrath et al., 2004; Balhaus et al., 2006), can lead to depletions of Re and platinum-like platinum group elements (PPGE: Pd and Pt), relative to iridium-like platinum group elements (IPGE: Os, Ir and Ru), as long as mss remains in the residue (e.g., Pearson et al., 2004). In addition to partial melting, mantle peridotites might also undergo secondary processes (i.e., all processes postdating partial melting), such as refertilization (addition of melt) (e.g., Elthon, 1992; Saal et al., 2001; Le Roux et al., 2007), mantle metasomatism via melt-rock reaction (Büchl et al., 2002; Ackerman et al., 2009), and sulfide breakdown, a general term used to describe several possible processes associated with sulfur loss (e.g., Handler et al., 1999; Handler and Bennett, 1999; Lorand et al., 2003a). Secondary processes may strongly modify HSE abundances of peridotites, e.g., Os loss relative to Ir (Handler et al., 1999), and also potentially affect their Re-Os isotopic systematics (e.g., Büchl et al., 2002).

This chapter reports on two suites of xenolithic peridotites from nearby areas in China that have largely similar major element compositions but distinct HSE patterns. These suites provide an unusual opportunity to explore primary and secondary processes that may act on HSE contained within mantle peridotites and assess the impacts of these processes on Os isotope and HSE systematics.

3.2 Samples

The xenoliths studied here are anhydrous spinel peridotites entrained in Tertiary basaltic lavas from the Hannuoba (N40^{0}58.160', E 114^{0}32.980') and Yangyuan (N40^{0}08.292', E114^{0}08.806') areas in the northern part of the Trans-North China Orogen, North China Craton (see Fig. 2-1). These two localities lie approximately 100 km apart. The Hannuoba basalts erupted between 14 and 24 Ma ago (Liu et al., 1992) and consist of interlayered alkali and tholeiitic basalt (Zhi et al, 1990); the Damaping lavas, which host the xenoliths studied here, are alkali basalts. The Yangyuan basalts erupted 30-35 Ma ago (Liu et al., 1992) and mainly consist of alkali basalts (Ma and Xu, 2004).

Petrologic and geochemical characteristics of peridotite xenoliths from these localities were previously documented in Song and Frey (1989) and Rudnick et al. (2004) for Hannuoba, and Y.G. Xu et al. (2008) for Yangyuan. Both peridotite suites are dominated by protogranular to equigranular spinel lherzolites, but also contain a small proportion of harzburgites (Rudnick et al., 2004; Y.G. Xu et al., 2008). While both suites are generally fresh, the Hannuoba peridotites typically contain grain-boundary serpentine, while the Yangyuan peridotites do not.

The Hannuoba samples considered here were previously analyzed for major elements, sulfur and Re-Os isotope systematics by Gao et al. (2002), for mineral chemistry, lithophile trace elements and Sr-Nd isotopic compositions by Rudnick et al. (2004), and for HSE and reanalysis of Re-Os isotopic compositions by Becker et al. (2006). In addition, I have analyzed the HSE and re-analyzed Re-Os isotopic compositions in an additional Hannuoba sample from the Gao et al. (2002) study, as well as a subset of Hannuoba peridotites recently investigated by Zhang et al. (2009).

The Yangyuan samples investigated here are from a new collection that has not been previously studied. In addition, I have analyzed the HSE and re-analyzed Re-Os isotopic compositions in a subset of Yangyuan peridotites recently investigated by Y.G. Xu et al. (2008), who also reported whole rock major and lithophile trace elements, as well as Sr-Nd-Os isotopic compositions for Yangyuan samples.

3.3 Analytical Methods

3.3.1 Sample selection and mineral compositions

Olivines from 80 Yangyuan peridotites were analyzed in mineral mounts using a JEOL 8900 Electron Probe Micro-analyzer (EPMA) at the University of Maryland (UMd) in order to obtain an overview of the compositional variation present within the suite. The EPMA analyses were performed using wavelength dispersive spectroscopy (WDS) with a 15 kV accelerating voltage, a 20 nA cup current, and a 10 μm diameter beam. A variety of natural materials were used as primary and secondary standards. Raw x-ray intensities were corrected using a ZAF algorithm. Eighteen samples spanning the entire range of Fo (molar $Mg/(Mg+Fe^{2+})\times100$ of olivine) found in the suite, i.e., 90.2 to 92.0, were then selected on the basis of sample size and

freshness for further study. These samples were pulverized following the procedures described in Rudnick et al. (2004) using the sequent combination of a jaw crusher, a shatter box and a disk mill, and polished thin sections were analyzed by EPMA for mineral compositions (Table S3-1) using the conditions cited above. Additional analyses of spinels from the Hannuoba peridotites were carried out at UMd in order to compare with the earlier data of Rudnick et al. (2004) that were partially determined at Harvard University. The results are the same, within uncertainty.

3.3.2 Whole-rock major element compositions

Whole-rock major element compositions were determined by X-ray fluorescence (XRF) on fused glass disks made from powders (see Boyd and Mertzman (1987) for detailed protocols) at the Franklin and Marshall College, United States. Analytical precision and accuracy was typically better than 1% for major elements of concentrations greater than 0.5% and better than 5% for the remaining major elements, as determined from data for international reference materials analyzed by these laboratories (e.g., Boyd and Mertzman, 1987; Rudnick et al., 2004).

3.3.3 Sulfide petrology and geochemistry

Sulfides were examined on polished thin sections using reflected light microscopy. Sulfides in several representative samples from Yangyuan and Hannuoba were selected for analysis by EPMA employing WDS techniques with the following operating conditions: an accelerating voltage of 15 kV, a cup current of 50 nA, and a fully focused 1μm diameter beam. During the course of analyses, Si was monitored to assess beam overlap with silicate phases, and any analyses with detectable SiO_2 were discarded. X-ray counts were corrected using the ZAF method. A series of natural and

pure element standards (e.g., pyrrhotite, chalcopyrite, olivine, Ni, Cu) were used as both primary and secondary standards.

Bulk sulfur contents of the Yangyuan peridotites were determined using high temperature combustion combined with infrared spectrometry at the Université du Québec à Chicoutimi, the protocol of which was described in Bédard et al. (2008). The S quantification limit for this method is ~22 ppm (Bédard et al., 2008). Selenium concentrations were also determined at the Université du Québec à Chicoutimi by instrumental neutron activation analysis (INAA) employing preconcentration of Se with thiol cotton fiber (TCF). The Se quantification limit is ~10 ppb for 1-3 g of material (Savard et al., 2006), the amounts used here. Details of the Se/TCF-INAA technique are outlined in Savard et al. (2006).

3.3.4 Osmium isotopes and HSE abundances

Mixed ^{185}Re-^{190}Os and HSE (^{99}Ru, ^{105}Pd, ^{191}Ir, ^{194}Pt) spikes were added to each sample powder (1-1.5 g), sealed along with 3ml concentrated Teflon distilled HCl and 6ml concentrated Teflon distilled HNO_3 into a chilled, thick-walled borosilicate Carius tube, and heated to 270 ºC for four days. Osmium was extracted from the acid solution using CCl_4 (Cohen and Waters, 1996), then back-extracted into HBr, and finally purified via microdistillation (Birck et al., 1997). Iridium, Ru, Pt, Pd and Re were separated and purified using anion exchange column chromatography, following the steps described in Ireland et al. (2009).

Osmium isotopic measurements were performed by negative thermal ionization mass spectrometry (N-TIMS) at UMd. All samples were measured using a single electron multiplier on VG Sector 54 or NBS mass spectrometers. Mass fractionation

was corrected using $^{192}Os/^{188}Os$ = 3.083, and the internal precision on $^{187}Os/^{188}Os$ ratios was typically better than 0.2 % (2σ). The reported $^{187}Os/^{188}Os$ of samples was corrected for instrumental bias by comparison of the analyzed $^{187}Os/^{188}Os$ of the Johnson–Matthey Os standard in each analytical session with the recommended value of 0.11380. This correction for $^{187}Os/^{188}Os$ was less than 0.2 %.

Because some studies have advocated higher pressure/temperature dissolutions than are commonly performed using Carius tubes in order to assure complete digestion of HSE-bearing phases, I also digested a subset of Hannuoba samples using an *Anton Paar* High Pressure Asher (HPA) for ~3h at 280^{0}C and 130 bars. Two Hannuoba samples measured by Becker et al. (2006) (DMP series) and re-analyzed here by HPA, yield Os isotopic compositions and HSE abundances within uncertainties of those previously reported. Five additional Hannuoba samples (DA20 series) from the study of Zhang et al. (2009) were measured by Carius tube digestion and three of these were also measured using HPA. Both methods produced results within uncertainties for a given sample. However, Os concentrations and isotopic compositions determined at UMd are substantially different from those reported in Zhang et al. (2009), which were analyzed by Os sparging-MC-ICP-MS after NiS fusion digestion. Likewise, four Yangyuan samples analyzed by sparging from the study of Y.G. Xu et al. (2008) studied here give significantly higher Os isotopic ratios than previously reported (Table 3-2). Additional detailed discussion of these results is provided in the Supplement Material (e.g., Table S3-2, Figs. S3-3 and S3-4). In addition, in order to evaluate further the discrepancies between the Xu/Zhang studies and my data, in particular, whether the generally more radiogenic $^{187}Os/^{188}Os$ values I find result from failure to access non-radiogenic Os that may reside within

acid-resistant phase, I analyzed two aliquots of relatively refractory Yangyuan sample (YY-22, Fo = 91.2) by the NiS fusion/N-TIMS method. The results are reported in Supplemental Material (Table S3-3) and yield $^{187}Os/^{188}Os$ within uncertainty of the previously published results obtained for this sample from both high and low temperature Carius tube digestion/N-TIMS. These results demonstrate that the source of the discrepancies is unlikely to reside in the dissolution method. The reason for the discrepancy remains unclear. In this and following chapters, I consider our results robust, and here do not include the Re-Os isotope data reported by Y.G. Xu et al. (2008) and Zhang et al. (2009) in the discussions of this dissertation.

All other HSE were analyzed using a Nu Plasma MC-ICP-MS at UMd. Isotopic mass fractionation was corrected by periodic measurements of standards (usually one per three sample analyses) using the standard bracketing method. The accuracy of this analytical method was evaluated by measuring reference materials such as UB-N and GP-13 in our laboratory (e.g., Puchtel et al., 2008; Table S3-2 of this chapter), the results of which are comparable, within uncertainties, to those of other labs (e.g., Meisel et al., 2003; Pearson et al., 2004). Averaged blanks for these measurements are as follows: Os (0.38±0.22 pg), Ir (0.40±0.31 pg), Ru (2.9±2.9 pg), Pt (6.8±2.2 pg), Pd (9.5±3.5 pg) and Re (1.6±0.6 pg) (uncertainties are 1σ, calculated from 11 blank measurements). Blank corrections for Os, Ir, Ru, Pt, and Pd are negligible (less than 0.2 %) for the samples, while the Re blank constitutes 0.3 to 20 % of the total Re in all samples.

3.4 Results

Major and minor element compositions for Yangyuan peridotites are given in Table 3-1, along with Fo contents of olivines. Mineral compositions of the Yangyuan peridotites are provided in Supplemental Material (Table S3-1). Forsterite contents of Hannuoba peridotites range from 89.5 to 91.6 (Rudnick et al., 2004), whereas Yangyuan peridotites range to slightly more refractory compositions (e.g., Fo = 90.2 to 92.0). These two suites of peridotites display many other compositional similarities including concentrations of MgO (36.7-43.9 % vs. 38.2-46.1 % for Hannuoba vs. Yangyuan, respectively), Al_2O_3 (1.2-3.9 % vs. 0.9-4.0 %), and CaO (1.0-3.5 % vs. 0.4-3.68 %) (Fig. 3-1). Thus, Hannuoba and Yangyuan peridotites are chemically similar with respect to major and minor element compositions. Based on the empirical olivine-spinel oxygen barometer of Ballhaus et al. (1990), oxygen fugacities (fO_2) of the peridotites were calculated from the olivine and spinel compositions, assuming that spinels are perfectly stoichiometric ($MO:M_2O_3$ = 1:1). For this calculation, temperature was calculated from the orthopyroxene-clinopyroxene thermometer of Brey and Kölher (1990), assuming a pressure of 1.5 GPa. The resulting calculated fO_2 estimates are provided in Table 3-2. Yangyuan peridotites are generally characterized by a higher fO_2 (ΔFMQ: -0.7 to 0.2, with an average of -0.2) compared to Hannuoba peridotites (ΔFMQ: -3.6 to -0.4 with an average of -1.5) (Fig. 3-2). Sulfide abundances are highly variable in Hannuoba peridotites, ranging from no observed sulfides (e.g., samples DMP-25 and DMP-67c) to hundreds of sulfides per thin section (e.g., DMP-60, Table 3-2). The abundances of sulfides are generally positively correlated with the sulfur contents of the whole rocks (Fig. S3-1). Both enclosed (Type-e) and interstitial (Type-i) base metal sulfides are present in Hannuoba

Table 3-1. Whole rock analyses for spinel peridotites determined using XRF

Samples	SiO_2	TiO_2	Al_2O_3	Fe_2O_{3T}[a]	MnO	MgO	CaO	Na_2O	LOI[b]	Total
Hannuoba										
DMP-04	44.4	0.06	2.29	8.14	0.13	42.1	1.94	0.28		98.8
DMP-05	44.2	0.13	2.83	8.37	0.13	41.6	2.18	0.26		99.5
DMP-19	44.8	0.03	1.91	7.85	0.12	40.7	1.80	0.19		97.4
DMP-23a	44.2	0.10	2.32	8.63	0.13	41.3	1.64	0.24		98.5
DMP-25	44.4	0.08	1.61	7.90	0.12	43.9	1.00	0.3		99.3
DMP-41	44.8	0.06	2.76	8.60	0.13	40.2	2.12	0.27		98.7
DMP-51	44.8	0.05	1.96	8.23	0.12	42.0	1.89	0.24		99.1
DMP-56	44.8	0.13	3.49	8.85	0.14	38.2	3.21	0.36		98.9
DMP-57	44.3	0.06	1.96	8.23	0.12	42.5	1.56	0.16		98.8
DMP-58	44.9	0.08	3.16	8.80	0.13	38.8	2.76	0.34		98.7
DMP-59	44.0	0.06	2.58	8.88	0.13	40.4	2.43	0.27		98.5
DMP-60	46.3	0.11	3.67	8.31	0.13	36.7	3.47	0.38		98.9
DMP-67c	44.0	0.20	3.78	9.32	0.14	37.8	2.88	0.30		98.5
DA20-02	44.8	0.10	3.12	8.69	0.11	40.0	2.70	0.08	0.39	100.0
DA20-05	45.3	0.05	2.71	7.86	0.10	40.8	2.48	0.07	0.55	99.8
DA20-16	43.1	0.08	1.20	9.94	0.10	43.6	1.55	0.04	0.65	100.2
DA20-17	44.7	0.05	2.40	8.07	0.18	39.1	2.38	0.12	2.79	99.7
DA20-19	44.9	0.14	3.74	8.69	0.11	38.2	3.07	0.19	0.91	99.9
Yangyuan										
YY-04	43.9	0.04	1.63	8.00	0.13	44.4	1.03	0.02	0.22	99.1
YY-08	44.4	0.08	2.97	8.79	0.14	39.9	2.89	0.11	0.22	99.3
YY-09	44.4	0.09	3.04	8.39	0.14	40.8	2.12	0.13	0.06	99.1
YY-11	42.5	0.05	1.77	9.22	0.14	44.8	1.08	0.03	0.72	99.6
YY-13	43.8	0.11	2.44	8.70	0.13	41.9	1.90	0.11	-0.06	99.1
YY-22	44.0	0.05	2.45	8.25	0.13	42.3	1.81	0.08	0.06	99.0
YY-23	43.5	0.11	3.06	8.33	0.13	39.7	3.68	0.23	0.57	99.3
YY-26	43.4	0.08	3.08	8.76	0.14	41.7	2.15	0.10	0.26	99.4
YY-27	42.8	0.12	2.87	9.49	0.15	41.2	2.48	0.13	-0.07	99.2
YY-36	44.0	0.06	2.30	8.43	0.13	41.7	2.46	0.17	0.13	99.4
YY-40B	44.6	0.06	2.80	8.09	0.13	40.0	2.93	0.16	-0.05	98.7
YY-42	43.3	0.04	2.35	8.66	0.13	42.4	2.40	0.10	-0.02	99.3
YY-45	43.5	0.10	2.44	8.55	0.13	41.1	2.84	0.19	0.34	99.2
YY-50	44.5	0.15	4.02	8.29	0.13	38.2	3.63	0.26	0.23	99.4
YY-51	41.3	0.03	1.12	8.54	0.13	46.0	1.40	0.02	0.66	98.6
YY-52	43.7	0.08	2.70	8.52	0.14	41.5	2.26	0.12	0.18	99.0
YY-58	43.8	0.07	2.40	8.07	0.13	42.4	2.00	0.12	0.15	98.9
YY-60	42.5	0.05	1.26	8.86	0.13	44.9	1.23	0.03	0.65	99.0
YYB-2	46.1	0.02	1.45	9.03	0.12	42.8	0.90	0.07	− 0.49	99.9
YYB-4	46.7	0.06	2.15	8.85	0.12	40.6	1.85	0.17	− 0.48	100.0
YYB-7	44.9	0.01	0.89	9.75	0.12	44.7	0.44	0.04	− 0.88	100.0
YG-18	42.7	0.02	1.20	9.43	0.13	46.1	0.73	0.11	0.13	100.6

Note: Major elements are reported as oxides with units of wt. %. Fe_2O_{3T}: total Fe. LOI: loss on ignition

Data sources: Hannuoba (Rudnick et al., 2004; Zhang et al., 2009)

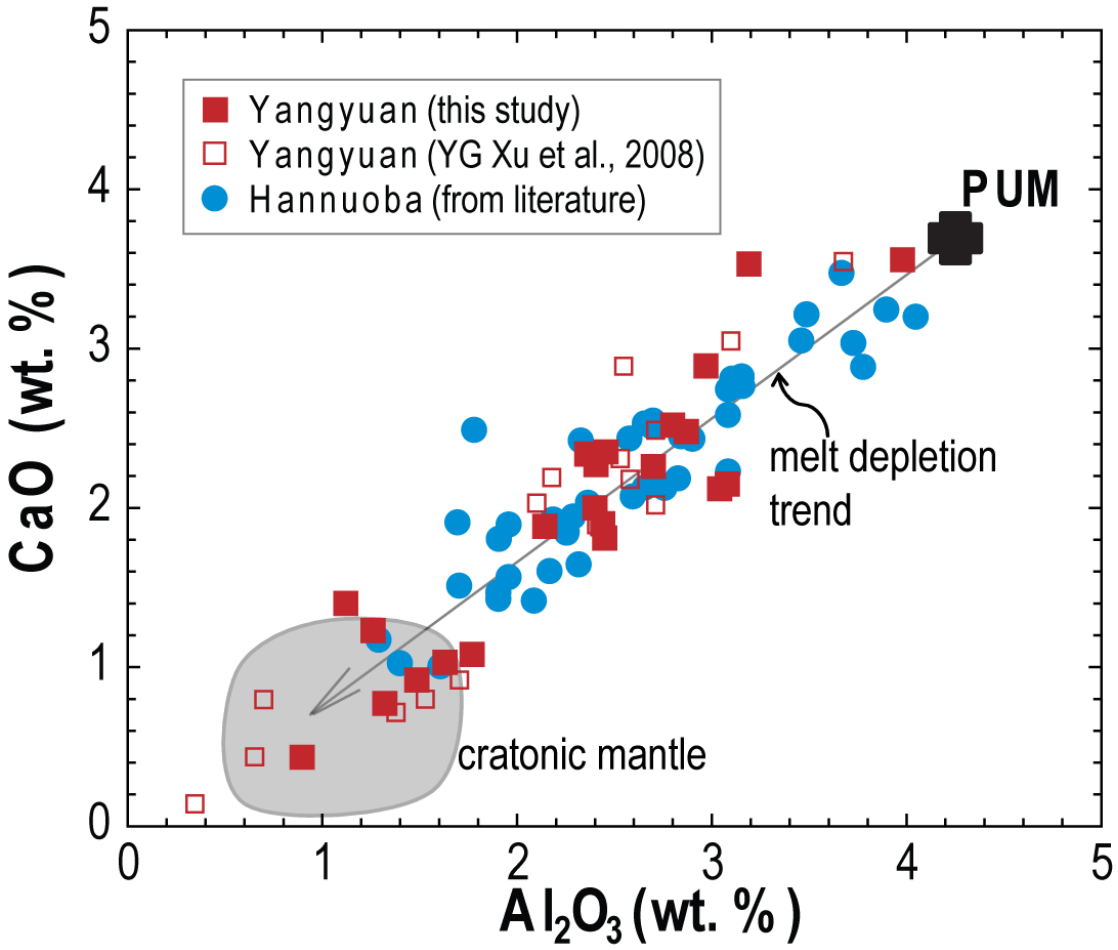

Fig. 3-1. Whole rock CaO versus Al_2O_3 (in wt. %) of Yangyuan and Hannuoba peridotites. Open squares of Yangyuan peridotites are from Y.G. Xu et al. (2008). Hannuoba data are from Song and Frey (1989), Chen et al. (2001), Rudnick et al. (2004), Choi et al. (2008), and Zhang et al. (2009). PM: primitive mantle (McDonough and Sun, 1995). Cratonic mantle data are from Boyd and Mertzman (1987), Boyd et al. (1993) and Pearson et al. (2004).

(Fig. 3-3). Type-i sulfides are more abundant than Type-e sulfides (Fig. 3-4). The Hannuoba sulfides (<1 μm to 250 μm in diameter) range in shape from spherical, sub-spherical to polyhedral blebs (Fig. 3-3). Pentlandite is dominant relative to chalcopyrite (Fig. 3-4 and Table S3-4), and both may occur within the same sulfide (Fig. 3-3a and c). Considering their similar compositions, both Type-e and Type-i sulfides likely formed as immiscible melts trapped during partial melting (Szabó and Bodnar, 1995). At least some of these sulfides subsequently experienced exsolution and recrystallization, either in the mantle, or during entrainment in the host basalts (Szabó and Bodnar, 1995), resulting in formation of secondary sulfides, e.g., sulfide chains along healed fractures in silicates (Type-f) or veins along grain boundaries (Type-iv) (Fig. 3-3 d and e, respectively). Type-f and Type-iv secondary sulfides are indistinguishable mineralogically and chemically from the Type-e and Type-i sulfides (Fig. 3-4, Table S3-4). In addition to primary and high temperature secondary sulfides, Ni-rich sulfides (e.g., millerite, godlevskite, and heazlewoodite), are spatially associated with grain boundary serpentine, and may have formed as a result of serpentinization at low temperatures (Klein and Bach, 2009).

In comparison, despite similar or slightly lower fertility compared to Hannuoba peridotites, Yangyuan peridotites are sulfide-poor. Thin sections typically contain less than two sulfide grains, and most have none (Table 3-2). The sulfides are mostly rounded inclusions of mss, or multiphase assemblages of mss, pentlandite and/or chalcopyrite. Mss grains typically are metal deficient, as evidenced by their low atomic (Fe+Ni+Cu)/S ratios (0.87±0.04, 2σ), while both pentlandites and chalcopyrites from Yangyuan, as well as all Hannuoba sulfides are metal-saturated, given their near perfect stoichiometric metal-to-S ratios (Table S3-4).

Table 3-2. Highly siderophile elements, S and Se abundances, Os isotopic compositions, and fO_2 of Yangyuan and Hannuoba peridotites

Sample	Os	Ir	Ru	Pt	Pd	Re	ΣHSE[e]	$^{187}Re/^{188}Os$	$^{187}Os/^{188}Os$	$(Pd/Ir)_N$[f]	Al_2O_3[g]	Fo	S[h]	Se	fO_2[i]	T_{RD}[j]	T_{MA}[j]	n[k]
	ppb	ppb	ppb	ppb	ppb	ppb	ppb				%		ppm	ppb	(ΔFMQ)	Ga	Ga	
Hannuoba locality																		
DMP 04[b]	3.76	3.56	7.41	6.62	4.96	0.211	26.5	0.271	0.1229	1.13	2.29	91.1	73	40	-0.7	0.63	1.9	64
DMP 19[b]	4.13	4.34	8.54	8.53	6.66	0.181	32.4	0.211	0.1200	1.24	1.91	91.3	91	28	-1.0	1.1	2.2	50
DMP 19R	3.76	4.26	8.33	7.79	6.66	0.169	30.9	0.216	0.1200	1,27						1.0	2.2	
DMP 25	3.23	2.49	5.71	3.55	2.13	0.030	17.1	0.045	0.1166	0.69	1.61	91.6	20	11	-0.4	1.5	1.7	n.f.
DMP25R[b]	2.70	2.27	5.14	3.46	-	0.032	13.6	0.056	0.1168							1.5	1.7	
DMP 41[b]	2.91	3.00	5.82	5.50	4.25	0.172	21.7	0.285	0.1233	1.15	2.76	90.4	110	-	-3.6	0.57	1.9	
DMP 51	3.01	3.06	6.37	5.21	4.18	0.130	21.9	0.208	0.1231	1.10	1.96	91.1	130	31	-1.3	0.59	1.2	135
DMP 56[b]	3.55	3.21	6.34	6.60	5.69	0.257	25.7	0.35	0.1275	1.43	3.49	89.9	260	46	-1.3	-0.1	-0.6	
DMP 58[b]	3.78	3.59	7.33	6.96	5.86	0.190	27.7	0.242	0.1254	1.32	3.16	90.2	230	-	-1.3	0.25	0.6	180
DMP 60[b]	4.00	3.59	7.24	7.31	6.21	0.303	28.7	0.365	0.1263	1.40	3.67	90.1	320	230	-2.8	0.13	1.2	208
DMP 67c	1.66	1.27	1.58	3.00	1.74	0.036	9.29	0.10	0.1224	1.11	3.78	89.5	23	-	-0.1	0.69	0.91	n.f.
DA20-02	3.63	3.41	7.06	7.18	6.24	0.333	27.9	0.443	0.1254	1.48	3.12	90.1	-	-	-	0.25	-2.5	
DA20-02R[c]	3.64	3.54	7.05	7.10	5.90	0.349	27.6	0.461	0.1255	1.35						0.24	-	
DA20-02R[d]	6.18					0.295		0.229	0.1187							1.2	-	
DA20-05	3.45	3.59	7.42	7.44	5.55	0.24	27.7	0.336	0.1233	1.25	2.71	91.1	-	-	-	0.55	3.3	
DA20-05R[c]	3.23	3.67	7.47	7.25	5.35	0.231	27.2	0.344	0.1236	1.18						0.51	3.4	
DA20-05R[d]	5.76					0.241		0.201	0.1151							1.8	-	
DA20-16	3.60	2.62	6.41	5.52	4.91	0.054	23.1	0.073	0.1238	1.52	1.20	89.6	-	-	-	0.48	0.59	
DA20-16R[d]	3.79					0.077		0.098	0.1227							0.64	-	
DA20-17	3.17	3.83	7.76	6.90	5.74	0.094	27.5	0.14	0.1232	1.21	2.40	90.5	-	-	-	0.57	0.88	
DA20-17R[d]	4.95					0.082		0.079	0.1190							1.2		
DA20-19	2.44	2.79	6.04	5.37	4.71	0.137	21.5	0.271	0.1270	1.37	3.74	89.6	-	-	-	0	-	
DA20-19R[c]	2.39	2.94	6.02	6.32	4.43	0.139	22.2	0.279	0.1272	1.22						0	-	
DA20-19R[d]	5.08					0.012		0.011	0.1138							1.9		
Yangyuan locality																		
YY-04	1.27	2.50	4.79	2.76	0.89	-	12.2	-	0.1150	0.29	1.63	92.0	<22	-	-0.7	1.8	-	n.f.
YY-04R	1.18	2.54	4.40	2.78	0.84	0.019	11.8	0.076	0.1152	0.27						1.8	2.1	
YY-08	0.847	2.39	4.59	3.20	1.62	0.023	12.7	0.13	0.1261	0.55	2.97	90.5	<22	43	0	0.15	0.21	2
YY-09	0.495	1.86	3.79	2.64	0.98	0.015	9.78	0.15	0.1216	0.43	3.04	90.9	<22	-	-0.1	0.81	1.3	n.f.
YY-11	0.213	0.74	1.64	0.63	0.19	0.005	3.42	0.1	0.1212	0.21	1.77	90.8	<22	-	-0.4	0.88	1.2	n.f.
YY-13	0.387	1.02	2.08	1.42	-	0.014	4.92	0.17	0.1210		2.44	90.9	<22	<10	0.1	0.9	1.5	n.f.
YY-13R	0.351	0.98	2.03	1.38	0.51	0.010	5.26	0.14	0.1212	0.42						0.88	1.3	
YY-22	0.925	2.98	4.81	5.07	1.83	0.045	15.7	0.23	0.1207	0.50	2.45	91.2	<22	-	-0.5	0.99	2.3	n.f.
YY-22R	1.15	2.98	5.03	5.27	1.87	0.047	16.4	0.2	0.1206	0.51						0.98	1.88	
YY-23	0.92	2.38	4.02	3.86	0.82	0.028	12.0	0.15	0.1240	0.29	3.06					0.5	0.7	

Table 3-2 continued…

Sample	Os	Ir	Ru	Pt	Pd	Re	ΣHSE[e]	$^{187}Re/^{188}Os$	$^{187}Os/^{188}Os$	$(Pd/Ir)_N$[f]	Al_2O_3[g]	Fo	S[h]	Se	fO_2[i]	T_{RD}[j]	T_{MA}[j]	n[k]
	ppb	ppb	ppb	ppb	ppb	ppb	ppb				%							
YY-26	1.07	2.64	4.41	2.94	0.60	0.103	11.8	0.462	0.1189	0.18	3.08	90.7	24	<10	-0.5	1.2	-8.6	1
YY-26R	0.766	2.46	4.17	2.83	0.55	0.103	10.9	0.647	0.1197	0.18						1.1	-1.8	
YY-27	-	1.92	4.21	2.93	0.93	0.018	10.0	-	-	0.39	2.87	90.2	<22	-	-0.1	-	-	n.f.
YY-27R	1.14	2.10	4.57	3.64	0.97	0.015	12.4	0.065	0.1195	0.37						1.1	1.3	
YY-36	0.60	2.31	4.43	5.04	1.34	0.060	13.8	0.48	0.1219	0.48	2.30					0.8	-3.8	
YY-40B	0.47	0.83	1.69	5.27	1.37	0.031	9.66	0.31	0.1241	1.37	2.80					0.4	2.0	
YY-42	0.4	1.14	2.48	2.10	0.48	0.027	6.63	0.33	0.1256	0.35	2.35					0.2	1.1	
YY-45	1.12	1.57	2.62	3.16	0.37	0.022	8.86	0.1	0.1220	0.19	2.44					0.7	1.0	
YY-50	1.00	1.81	2.93	3.06	0.87	0.057	9.73	0.31	0.1261	0.40	4.02					0.1	0.6	
YY-51	2.34	2.93	6.18	2.47	0.39	0.009	14.3	0.02	0.1160	0.11	1.12	91.6	<22	-	0.2	1.6	1.7	n.f.
YY-51R	2.21	2.79	5.88	2.99	0.41	0.007	14.3	0.01	0.1164	0.12						1.6	1.6	
YY-52	0.52	1.32	2.89	2.24	0.76	0.022	7.75	0.2	0.1235	0.47	2.70	90.8	<22		0.2	0.54	1.1	n.f.
YY-58	0.511	1.82	3.32	2.96	1.09	0.024	9.73	0.23	0.1212	0.48	2.40	91.7	27	<10	-0.1	0.87	2.0	2
YY-60	0.399	1.67	3.26	3.13	0.45	0.020	8.93	0.24	0.1208	0.22	1.26	91.3	<22	-	0.0	0.94	2.3	n.f.
YYB-2	1.28	1.85	3.56	3.33	0.75	0.020	10.8	0.076	0.1186	0.33	1.45	91.8	<22	-	-	1.3	1.5	
YYB-2R[a]	1.40								0.1124							2.1	-	
YYB-4	0.738	2.67	5.25	4.67	1.82	0.061	15.2	0.39	0.1202	0.55	2.15	91.9	-	-	-	1.0	40	
YYB-4R[a]	0.797								0.1146							1.8	-	
YYB-7	0.785	1.32	3.41	1.24	0.71	0.024	7.49	0.15	0.1153	0.43	0.89	91.8	-	-	-	1.7	2.7	
YYB-7R[a]	1.37								0.1110							2.3	-	
YG-18	1.78	2.83	5.01	2.68	0.72	0.017	13.0	0.046	0.1163	0.20	1.20	90.6	-	-	-	1.6	1.8	
YG-18R[a]	2.67								0.1106							2.4	-	

Note: R represents an analytical replicate of the sample.

a. Osmium data are from Xu et al. (2008) by Os-sparging ICP-MS

b. HSE data of Hannuoba peridotites are from Becker et al. (2006).

c. Dissolution by HPA; all other samples in this study were dissolved by Carius tube digestion.

d. Re-Os data are from Zhang et al. (2009) by Os-sparging ICP-MS.

e. ΣHSE = Os + Ir + Ru + Pt + Pd + Re

f. Chondrite(Orgueil from Horan et al., 2006)-normalized Pd/Ir ratios

g. Al_2O_3 contents of DMP series of Hannuoba samples are from Gao et al. (2002). Those of DA20 series are from Zhang et al. (2009).

h. S contents of Hannuoba peridotites are from Gao et al. (2002) with blanks of ~0.3ppm.

i. Oxygen fugacity (fO_2) is denoted by divergence from the fayalite-magnetite-quartz) buffer (ΔFMQ)

j. The parameters used in model age calculation are: $\lambda_{Re} = 1.666 \times 10^{-11}$/year $(^{187}Re/^{188}Os)_{CI} = 0.40186$, $(^{187}Os/^{188}Os)_{CI,0} = 0.1270$ (Shirey and Walker, 1998).

k. The number of sulfide grains per thin section. n.f. means 'not found'.

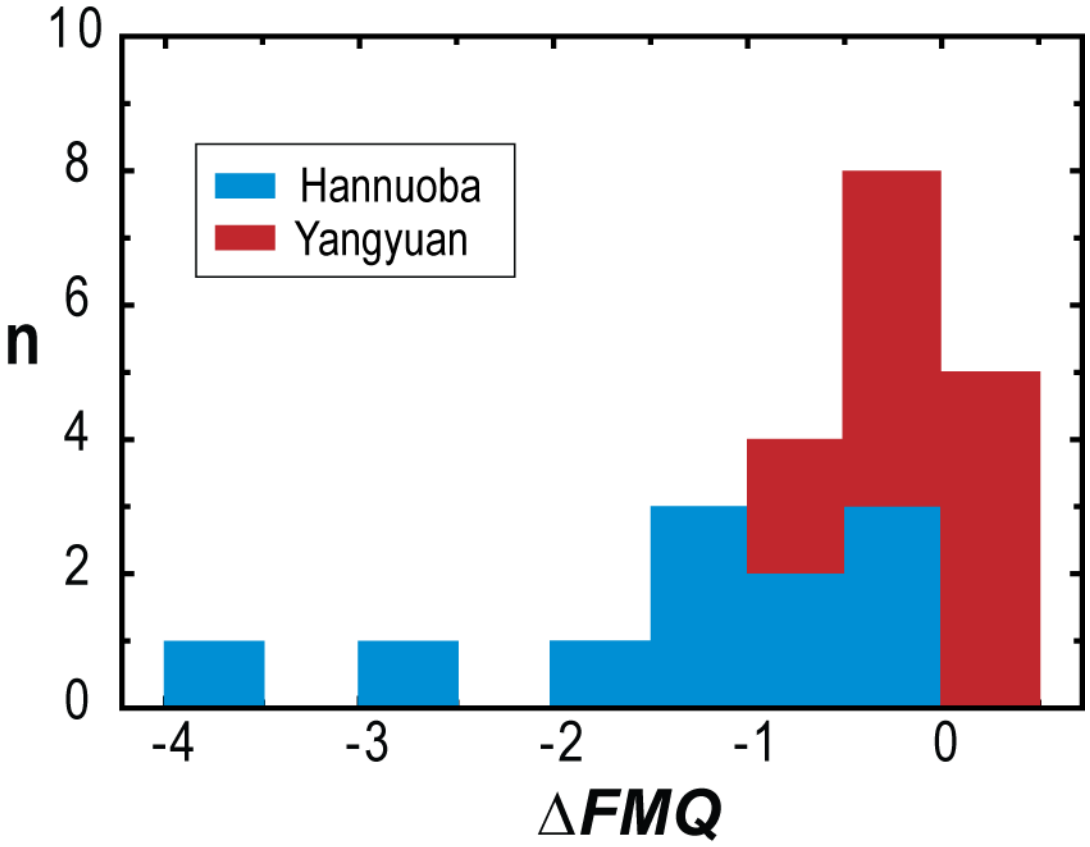

Fig. 3-2. Oxygen fugacities (fO_2) of Yangyuan and Hannuoba peridotites calculated based on the empirical olivine-spinel barometer (assuming P = 1.5 GPa) of Ballhaus et al. (1990). Mineral compositions of Hannuoba peridotites are from Rudnick et al. (2004). Spinel analyses from this previous study, which were partially determined at a different laboratory, were verified to be consistent with data from this study.

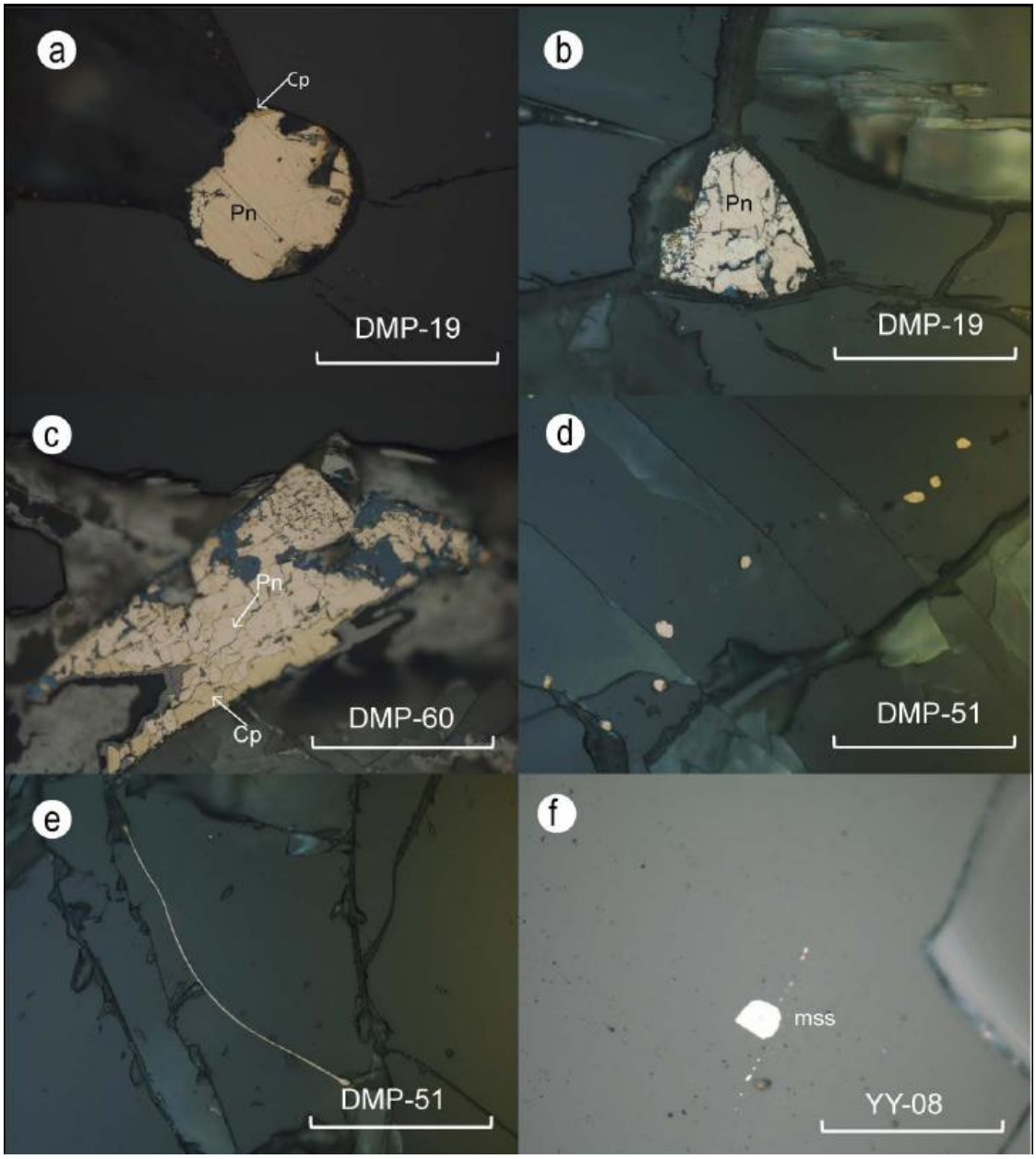

Fig. 3-3. Photomicrographs of sulfides in the Hannuoba and Yangyuan peridotites under reflected light microscopy (scale bar equals 100 μm). Hannuoba: a. Type-e sulfide occurs as an inclusion in olivine; b. Type-i sulfide occurs at the triple junction of silicates; c. Type-i sulfides with a polyhedral texture; d. Type-f sulfides along healed fractures; and e. Type-iv sulfides along grain boundary. Yangyuan: f. Type-e mss as inclusion in olivine. Pn: pentlandite; Cp: chalcopyrite; and mss: monosulfide solid solution.

Highly siderophile elements, Os isotopic compositions, S, and Se data are provided in Table 3-2. In general, Hannuoba peridotites show a large range of S (20-320 ppm) (Gao et al., 2002) and Se (11-230 ppb) concentrations, broadly correlating with major-element depletion indices, such as MgO and Al_2O_3 (e.g., Gao et al., 2002, and Fig. S3-1 in Supplemental Material). The only exception to this is sample DMP 67c, which has a very low S content and sulfide abundances that are incongruous with its apparent fertility. Consistent with previous studies, Hannuoba peridotites display HSE patterns (normalized to CI chondrites) that are globally similar to those of primitive upper mantle (PUM; Becker et al., 2006), except for two samples – the refractory sample DMP 25, and the previously mentioned low-sulfur (and sulfide) sample DMP-67c (Fig. 3-5a). No obvious Os-Ir fractionation appears in the Hannuoba suite. Nevertheless, despite the generally PUM-like patterns, chondrite-normalized $(Pd/Ir)_N$ are well correlated with melt depletion indices, such as Al_2O_3 (Fig. 3-6), and overlap with ratios commonly observed in massif peridotites (e.g., Pearson et al., 2004; Becker et al., 2006; Luguet et al., 2007). Re/Os ratios are also similarly correlated with degree of melt extraction.

By contrast, despite spanning a range of melt depletion similar to that of the Hannuoba peridotites, the Yangyuan peridotites are characterized by much lower S (at or below the quantification limit of ~22 ppm) and Se contents (at or below the quantification limit of ~10 ppb, except for one sample having 43 ppb). Yangyuan peridotites also have significantly lower total HSE concentrations (ΣHSE = Os + Ir + Ru + Pt + Pd + Re) of 3 to 16 ppb, compared to Hannuoba peridotites, which have 17 to 32 ppb. Moreover, the HSE patterns of Yangyuan samples are characterized by striking Os, Pd and Re depletions, relative to Ir (Fig. 3-5b). Such fractionated patterns

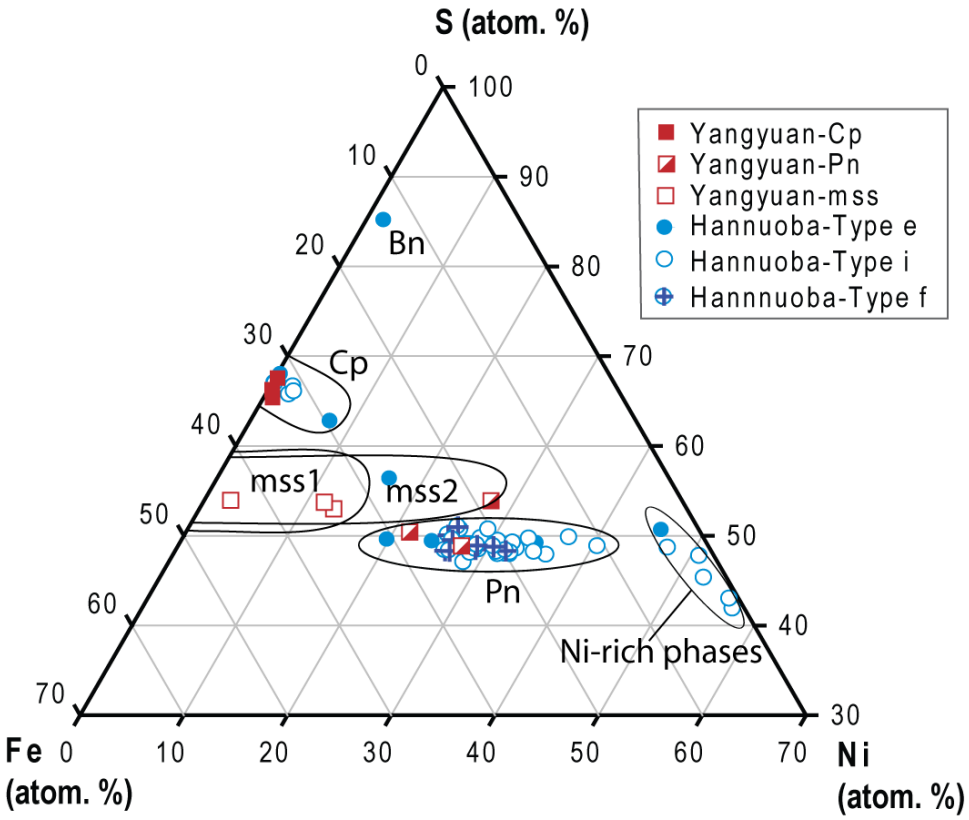

Fig. 3-4. Sulfide compositions plotted in the Fe-Ni-S system (Cu is subtracted and Fe, Ni and S are normalized to 100% atomic). All observed sulfides in Yangyuan peridotites are enclosed sulfides having mss, pentlandite (Pn) and/or chalcopyrite (Cp) compositions. Hannuoba sulfides are dominated by Pn with minor Cp and mss as well as Ni-rich phases (e.g., millerite (Ml), godlevskite (Gv), and heazlewoodite (Hw)). Bn: bornite. Phase fields mss1 and 2: 1100^{0}C and 1000^{0}C, respectively, according to Kullerud et al. (1969). Type-e: enclosed sulfides; Type-i: interstitial sulfides including sulfide veins along grain boundaries; and type-f: sulfide chains along healed fractures.

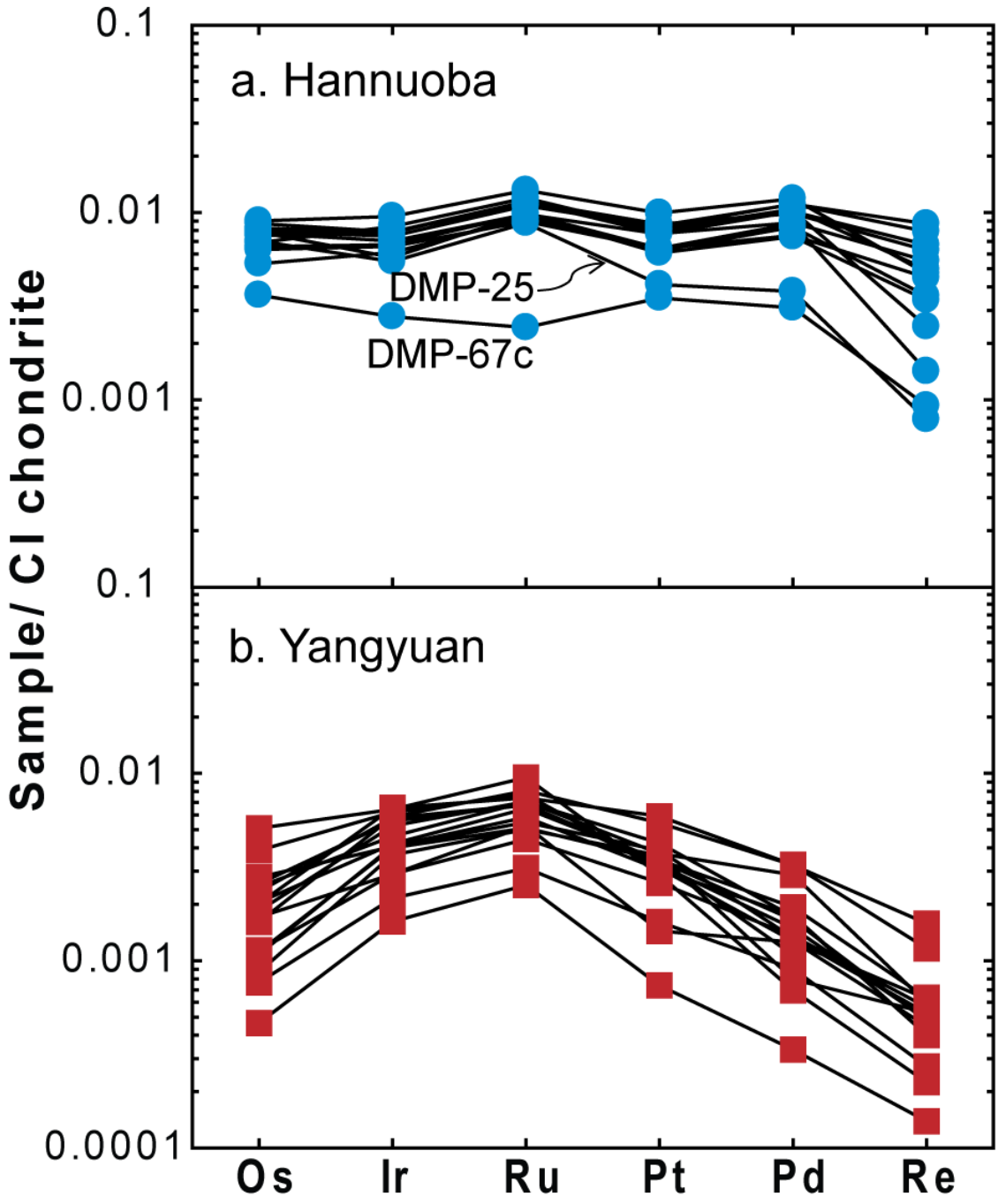

Fig. 3-5. HSE patterns of whole rock peridotites normalized to the CI chondrite, Orgueil (Horan et al., 2003): a. Hannuoba. b. Yangyuan. Some of the Hannuoba data are from Becker et al. (2006).

do not appear in the Hannuoba suite. Similar depletions in Os, Pd and Re, relative to Ir, have been observed in several other xenolithic peridotite suites worldwide, including Oak Creek, Sierra Nevada, USA (Lee, 2002), Cima, Basin and Range, USA (Lee, 2002), Vitim, Siberia (Pearson et al., 2004), North Queensland, Australia (Handler et al., 1999; Handler and Bennett, 1999), and Penglai, North China Craton (Chu et al., 2009) (Fig. S3-2 in Supplemental Material).

3.5 Discussion

Xenolithic peridotites entrained by basalts or kimberlites are fragments of the lithospheric mantle that formed as residues produced by partial melting of asthenospheric mantle. In addition to melt depletion, lithospheric peridotites may also record the effects of secondary processes. Here, I consider the effects of both partial melting and secondary processes on the relative and absolute abundances of the HSE in lithospheric peridotites underlying the North China Craton, and what effects these processes have had on model ages based on Os isotopes.

3.5.1 Partial melting

Partial melting of mantle peridotite is an important process leading to the formation of lithospheric mantle. Given the typical established relative order of the compatibility of HSE (Os~Ir~Ru>Pt>Pd>Re) (Pearson et al., 2004), melt extraction progressively results in depletions of PPGE and Re relative to the more refractory IPGE (Bockrath et al., 2004; Pearson et al., 2004; Ballhaus et al., 2006). Thus, $(Pd/Ir)_N$, combined with an indicator of melt depletion, such as whole rock Al_2O_3, can potentially be used to assess whether HSE fractionations were caused by primary melting or secondary processes.

The $(Pd/Ir)_N$ of Hannuoba peridotites, except for samples DMP-67c and DA20-16, are positively correlated with Al_2O_3, and overlap with the range defined by orogenic massif peridotites (model lower curve in Fig. 3-6). Hannuoba samples also display a rough negative correlation between MgO and S (Gao et al., 2002; except for S-poor sample DMP-67c) or Se (see Fig. S3-1 in Supplemental Material; except for sample DMP-60 with an extremely high Se content of 230 ppb), which is consistent with these samples having formed as residues of varying extents of partial melting, with subsequent preservation of sulfides. Moreover, the sulfides in the Hannuoba peridotites are indistinguishable mineralogically and chemically, irrespective of their position (grain boundary, inclusion, healed fracture) or morphology, and are dominated by pentlandite; chalcopyrite is rare and generally forms as exsolution rims on pentlandite (Figs. 3-3 and 3-4). This observation suggests little addition of secondary, Cu-rich sulfides (cf. Alard et al., 2000; X.S. Xu et al., 2008). In addition, Hannuoba peridotites exhibit a whole-rock Re-Os errorchron and a positive correlation between $^{187}Os/^{188}Os$ and Al_2O_3 (excluding samples DMP-67c and DA20-16) (Fig. 3-7), which also likely reflects the dominant effects of partial melting (Gao et al., 2002). Alternatively, Zhang et al. (2009) proposed that Hannuoba peridotites are Archean residues that experienced late melt refertilization based on the finding of a series of Archean to Phanerozoic Os model ages, the data of which are likely incorrect (Supplemental Material). However, addition of basaltic or picritic melts, which have high Al_2O_3 and low Os contents relative to ancient residual peridotite, would have little impact on Os isotopic compositions, but a much greater impact on the Al_2O_3 contents of the peridotites (Fig. 3-7). Such refertilization will

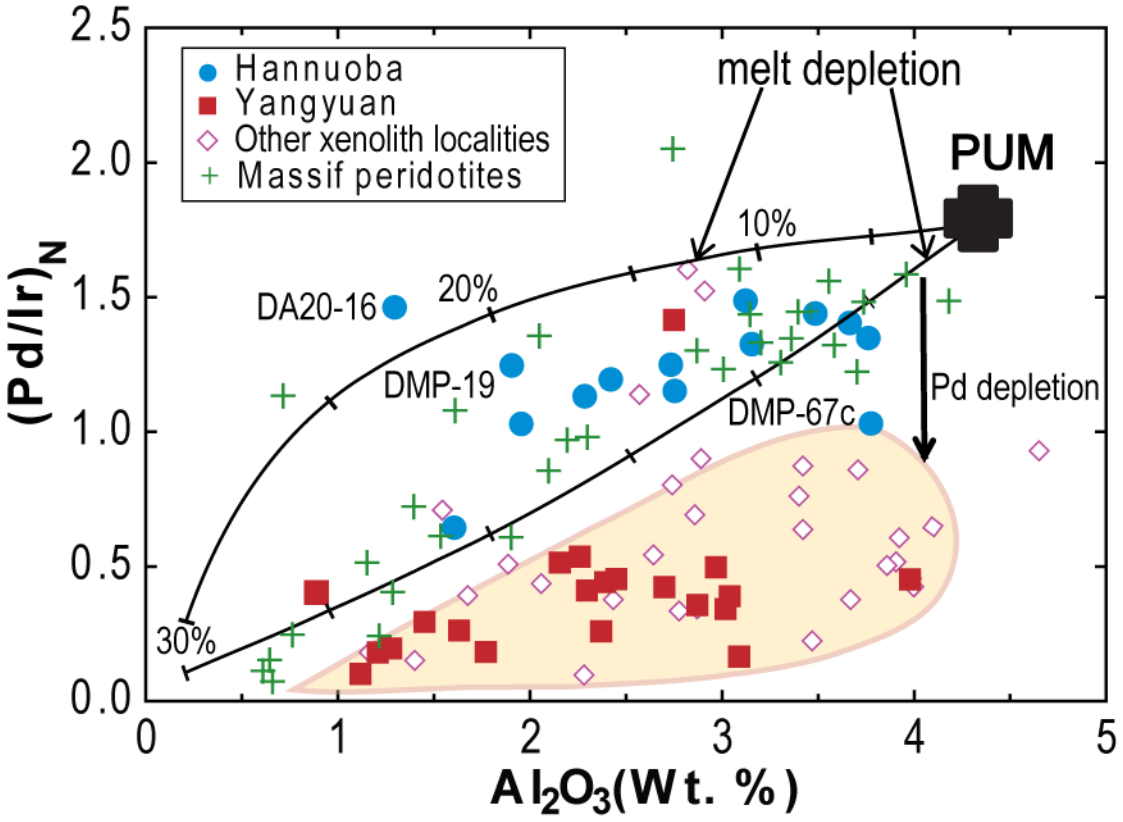

Fig. 3-6. Al_2O_3 versus $(Pd/Ir)_N$ for xenolithic peridotites from the North China Craton compared to other xenolithic and massif peridotites. Open diamond symbols depict xenoliths that show Os depletion relative to Ir from Vitim, Siberia (Pearson et al., 2004), North Queensland, Australia (Handler et al., 1999; Handler and Bennett, 1999), and Penglai, North China Craton (Chu et al., 2009). Melting model curves were calculated for non-modal, fractional melting using a primitive upper mantle (PUM) source containing 300 ppm S, while the extracted melts have a S capacity of 1000 ppm. The partition coefficients between sulfide and melt, $D_{HSE(sulfide/melt)}$, used in the models are: $D_{Pd(sulfide/melt)}$ of 10^4 and 10^3 for model upper curve and lower curve, respectively, according to Fleet et al (1999); $D_{Ir(sulfide/melt)}$ was set at 10^5. Tick marks show 5% melting increments. Data sources: PUM is from Becker et al. (2006) and McDonough and Sun (1995). Massif data are from a variety of literature sources for the following locations: Pyrenees (France) (Becker et al., 2006; Luguet et al., 2007; Lorand et al., 2008b), Italian Alps (Becker et al., 2006), Beni Bousera (Morocco) (Pearson et al., 2004), Ronda (Spain) (Becker et al., 2006), Lower Austria (Becker et al., 2006), and Ashaway (America) (Becker et al., 2006).

result in strongly curved mixing arrays on Al_2O_3 vs. $^{187}Os/^{188}Os$ plots (Reisberg and Lorand, 1995), which are not observed in the Hannuoba data (Fig. 3-7). I conclude that most Hannuoba samples are unlikely to have experienced melt refertilization long after melt depletion. Thus, the compositional and petrographic features highlighted above, as well as the similarities to massif peridotites, indicate that partial melting was the dominant process affecting HSE and Os isotopic compositions in Hannuoba samples.

In contrast to the Hannuoba samples, $(Pd/Ir)_N$ of Yangyuan peridotites show no clear correlation when plotted against Al_2O_3, and most samples plot below the trend defined by the Hannuoba and massif peridotite data (Fig. 3-6). The inter-element HSE fractionations of Yangyuan peridotites cannot simply be the result of a single stage of partial melting, because partial melting alone would not fractionate Os from Ir and Ru, given similar geochemical compatibilities of IPGE. Further, the peridotite's Pd/Ir and Re/Ir ratios are much lower than would be consistent with their fertility (e.g., Fig. 3-6). Thus, the distinct HSE characteristics of Yangyuan samples must reflect secondary processes, rather than primary melt depletion. Similar HSE characteristics have been observed in other alkali-basalt-hosted peridotite xenoliths worldwide (e.g., Handler et al., 1999; Lee, 2002; Pearson et al., 2004; Chu et al., 2009), suggesting that certain recurring secondary processes affect HSE abundances of xenolithic peridotites in a systematic manner.

3.5.2 Secondary Processes

Secondary processes that may affect whole rock HSE abundances include serpentinization, refertilization via melt addition (Saal et al., 2001), mantle

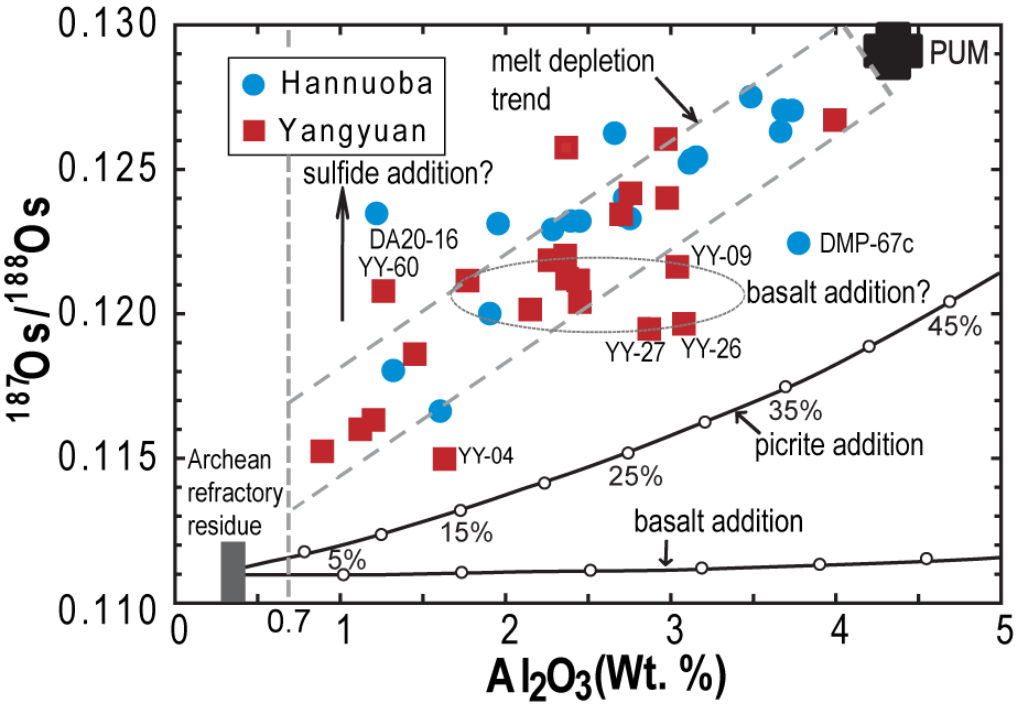

Fig. 3-7. Whole rock Al_2O_3 versus $^{187}Os/^{188}Os$ of Hannuoba and Yangyuan peridotites. A melt depletion trend is outlined by the dashed bar. PUM: Meisel et al., 2001 (for $^{187}Os/^{188}Os$) and McDonough and Sun, 1995 (for Al_2O_3). Hannuoba data sources: Meisel et al., 2001; Gao et al., 2002; Becker et al., 2006; and this study. Gray bar (labeled "Archean refractory residue") represents a refractory peridotite formed by high degrees of melt extraction at 2.2 to 2.5 Ga with $^{187}Os/^{188}Os$ ranging from 0.110 to 0.112, where all Re was lost during melting. Present-day refertilization of this residue by addition of picritic or basaltic melt is illustrated. Mixing parameters used: picritic melt has 1 ppb Os, 10 wt. % Al_2O_3 and an $^{187}Os/^{188}Os$ of 0.16; basaltic melt has 0.05 ppb Os, 15 wt. % Al_2O_3 and an $^{187}Os/^{188}Os$ of 0.16; the refractory peridotitic residue has 3.5 ppb Os, 0.3 wt. % Al_2O_3 and an $^{187}Os/^{188}Os$ of 0.111±0.001. Open circles along curves represent increments of 5 % melt addition. The vertical dashed line represents peridotites with Al_2O_3 of 0.7%, where peridotites lose all Re (Handler et al., 1997).

metasomatism via melt-rock reaction (Büchl et al., 2002), and sulfide breakdown prior to, during, or subsequent to entrainment and eruption of the host basalt (Handler et al., 1999; Handler and Bennett, 1999; Lorand et al., 2003a; Reisberg et al., 2005). The latter may occur via several processes, which are discussed below.

3.5.2.1 Serpentinization

The Yangyuan samples are devoid of serpentine, so serpentinization cannot explain their fractionated HSE patterns. Furthermore, although I observe minor serpentinization along grain boundaries of some Hannuoba peridotites (e.g., DMP-19), there is no correlation between the degree of serpentinization and HSE patterns, which are all rather uniform (Fig. 3-5). These observations are consistent with published data that suggests that the HSE remain stable during serpentinization, which occurs at relatively low temperatures in a reducing environment (Snow and Schmidt, 1998; Liu et al., 2009), in which sulfides are preserved (Klein and Bach, 2009).

3.5.2.2 Refertilization

Addition of melt to refractory peridotites (refertilization) will lead to enrichment of incompatible major and trace elements. For example, refertilization via basalt infiltration long after melt depletion will lead to Al_2O_3 enrichment, without significantly changing $^{187}Os/^{188}Os$, due to the very low abundances of Os in typical basalts (e.g., Reisberg and Lorand, 1995). Because mantle-derived melts are commonly enriched in Re and PPGE, relative to IPGE (e.g., Puchtel et al., 2000), refertilization is normally expected to increase Pt, Pd and Re relative to Ir (e.g., Rehkämper et al., 1999; Lorand et al., 2009). This is the opposite of what is observed in the Yangyuan suite, and I conclude that refertilization is not responsible for the

distinctive HSE patterns of these samples. Nevertheless, several Yangyuan samples (i.e., YY-04, YY-09, YY-26, and YY-27) plot to the right of the trend defined by $^{187}Os/^{188}Os$ and Al_2O_3 (Fig. 3-7). These samples exhibit higher Al_2O_3 than others that have similar $^{187}Os/^{188}Os$, which can be explained by small degrees (<3%) of basalt addition long after melt depletion (Fig. 3-7). Given the similarity of the HSE patterns in all of these rocks, either this small amount of basalt addition did not influence the HSE patterns, or the process(es) responsible for the distinctive HSE patterns in the Yangyuan samples obliterated any fractionation associated with basalt addition.

3.5.2.3 Metasomatism via Melt-rock Reaction

The effects of melt/fluid-rock reactions are frequently observed in mantle peridotites. For example, the enrichment of light rare earth elements (LREE) in refractory peridotites is commonly interpreted to result from mantle metasomatism (e.g., Frey and Green, 1974). This category of process is distinct from refertilization in that refertilization can add major phases to the affected lithology, while metasomatism may not affect the major mineralogy. In peridotites, metasomatism can potentially result in sulfide precipitation (e.g., Alard et al., 2000; Luguet et al., 2003), or sulfide dissolution or breakdown (Büchl et al., 2002; Reisberg et al., 2005; Ackerman et al., 2009).

Trace element data, including LREE enrichment in some samples, suggest that melt/fluid-rock reaction occurred in some Yangyuan peridotites (Y.G. Xu et al., 2008). For example, sample YY-60 has an Os isotopic composition (0.1208) that is more radiogenic than would be consistent with its refractory composition (e.g., Al_2O_3: 1.26%, CaO: 1.23%, and Fo: 91.3). This Os isotopic composition may reflect addition

of radiogenic sulfide prior to sulfide breakdown. Nevertheless, there is no evidence for substantial sulfide addition via metasomatism for the Yangyuan peridotites, which instead show a notable deficit of sulfides, and have very low S and Se abundances that are consistent with the rarity of sulfides in the rocks. Furthermore, the addition of sulfides normally rich in PPGE and Re would tend to elevate PPGE/IPGE ratios (Rehkämper et al., 1999; Alard et al., 2000; Lorand et al., 2009), which is not observed. However, sulfide-breakdown via melt-rock reaction under oxidizing conditions (e.g., Reisberg et al., 2005) may be responsible for the HSE patterns of the Yangyuan peridotites, as discussed in the next section.

3.5.2.4 Sulfide Loss

Compared to Hannuoba and massif peridotites, the low whole-rock S contents and the rarity of sulfides in the Yangyuan peridotites allow us to propose that sulfide dissolution, removal and/or breakdown was likely a prime factor leading to their distinctive HSE patterns. Sulfur and sulfides could have been removed from these rocks by at least three processes.

One form of sulfur loss is through surficial weathering that may take place following eruption. This occurs when sulfides become oxidized and are then replaced by hydroxides and oxides, leading to S loss (Lorand, 1990). The ratio of S to a less mobile element that is enriched in sulfides, such as Cu (Handler et al., 1999) or Se (Lorand et al., 2003a), can be used to estimate the amount of oxidative sulfide breakdown that a peridotite xenolith has experienced. Selenium contents were determined for four relatively fertile Yangyuan peridotites, which would be expected to contain the greatest amount of original sulfides. Only one of these samples has Se

above the quantification limit of ~ 10 ppb. Thus, the coupled low S and Se contents of most Yangyuan samples suggest that sulfide weathering was likely not the primary process that removed sulfides (e.g., Lorand et al., 2003a), and hence, was likely not the dominant process affecting their HSE. This conclusion is also consistent with the lack of secondary oxides or hydroxides in these samples, as well as the general immobility of HSE in peridotites that experience low temperature alteration (Rehkamper et al., 1999; Liu et al., 2009).

Lorand et al. (2003a, b) suggested an alternative means by which sulfides may be removed from peridotites. Sulfides, which are molten at mantle temperatures and have much higher densities than silicates, may drain downward in peridotite with high porosities (Lorand et al., 2003a, b). Such migration could result in low S and HSE contents (Lorand et al., 2003a, b). However, sulfide draining cannot account for at least some of the observed HSE fractionations in the Yangyuan peridotites, for example, Os depletion relative to Ir. Thus, this process is unlikely to have strongly impacted the Yangyuan HSE patterns.

Sulfide dissolution or breakdown during melt/fluid percolation or transit to the surface (e.g., Handler et al., 1999; Büchl et al., 2002; Lorand et al., 2003a; Reisberg et al., 2005) was most likely the process leading to the HSE characteristics of Yangyuan samples. Sulfide breakdown can strongly affect whole rock HSE concentrations. There are several processes that must be considered.

First, it has been suggested that melt-rock reaction at the high melt/rock ratios that produce replacive dunites, may destroy the majority of sulfides, stripping the peridotite of most HSE (Büchl et al., 2002). In this case, subsequent precipitation of

sulfides from later melts will dominate the shape of HSE patterns as well as Os isotope composition in the replacive dunites, which may lead to low Os/Ir ratios, high Pd/Ir ratios, and melt-dominant radiogenic Os isotopic compositions (Büchl et al., 2002; 2004). However, there is no evidence for extensive melt-rock reaction in the Yangyuan suite; for example, there are no replacive dunites or evidence of secondary sulfide precipitation. Further, Yangyuan peridotites show very low Pd/Ir ratios and subchondritic $^{187}Os/^{188}Os$, rather than the suprachondritic Pd/Ir ratios and radiogenic $^{187}Os/^{188}Os$ seen in replacive dunites (Büchl et al., 2002). Thus, melt-rock reaction at a high melt/rock ratio is inconsistent with the observed HSE characteristics of Yangyuan peridotites.

Second, as Yangyuan peridotites exhibit somewhat higher fO_2 than those of Hannuoba peridotites, I consider the possibility of oxidative sulfide breakdown. During this process, S can be oxidized into more mobile sulfates and then lost from the rocks. When sulfide breaks down, the sulfide-borne HSE are released. They may either remain in the rocks as alloy phases, or be lost as volatiles, depending on their volatilities. Experimental data and thermodynamic calculations suggest that Pd metal and certain oxides of Os and Ru are volatile under highly oxidized conditions at high temperatures (greater than 1100^0C) (Wood, 1987). If the Yangyuan peridotites were highly oxidized, it might be expected that not only Pd and Os depletions would be present relative to Ir, but that Ru/Ir ratios would also be low. However, both Yangyuan and Hannuoba peridotites have essentially PUM-like $(Ru/Ir)_N$ ratios (1.40 ± 0.33 for Yangyuan and 1.46 ± 0.20 for Hannuoba, cf. 1.49±0.18 for PUM, Becker et al., 2006). Furthermore, the calculated fO_2's of Yangyuan peridotites (Table 3-2) are much lower than those required to oxidize sulfides, i.e., fO_2=FMQ +2 or greater

(Mungall et al., 2006). Finally, heating experiments have shown that Os volatilization loss is unlikely under mantle conditions (Wulf et al., 1995). Therefore, I conclude that oxidative sulfide breakdown was probably not responsible for producing the distinctive HSE patterns in the Yangyuan peridotites.

Lithophile trace element data document interaction between an invasive melt or fluid phase and the Yangyuan peridotites (Y.G. Xu et al., 2008). I propose that, in the presence of variable fO_2 and fS_2 conditions during melt-rock interaction, partition coefficients for HSE might change (Brenan et al., 2008; Fonseca et al 2008). When melts/fluids are S-undersaturated, i.e., with a low fS_2, desulfurization, a process of S loss, may occur in the peridotites. In this process, sulfides may incongruently break down to form refractory mss, Pd-rich sulfide liquid, and Ir-Pt alloys (Peregoedova et al., 2004; 2006). Moreover, interaction with oxidized melts would impart a metal deficiency to any surviving mss (Eggler and Lorand, 1993), consistent with the mss compositions in the Yangyuan peridotites. Although metal-deficient mss is expected to have high partition coefficients for Os and Pd (Barnes et al., 2001), the lack of Os and Pd enrichments in the whole rocks, indeed, the observed depletion of these elements, means that the residual mss has had little leverage on the whole rock HSE content. Incongruent sulfide breakdown lowers total HSE abundances (Lorand et al., 2003a) and causes further fractionations of HSE (Handler et al., 1999), such as Pd depletions relative to Ir. Although the behavior of Os during incongruent sulfide breakdown has not yet been experimentally constrained (e.g., Peregoedova et al., 2004; 2006; Mungall et al., 2006), I propose that, in an oxidizing environment, it is possible to fractionate Os from Ir-Ru-Pt via this process. In such an environment, Os contained in HSE-hosting phases may be partially dissolved into the melt/fluid

phase, leaving Ir-Ru-Pt to be taken up into refractory sulfides or alloys (Li et al., 1996; Barnes et al., 2001), creating the observed low Os/Ir ratios. In addition, Re becomes less chalcophile at higher fO_2 (Fonseca et al 2008), which could explain the incompatible behavior of Re as well as low Re/Ir ratios in the Yangyuan peridotites.

3.5.3 Comparison of Secondary Processes in Yangyuan and Hannuoba Peridotites

Compared to the Yangyuan peridotites, the S and Se concentrations and HSE patterns of Hannuoba peridotites do not show evidence for sulfide removal, except for sample DMP-67c, which is depleted in S and falls off the Re-Os correlation (Gao et al., 2002). This sample has low total HSE (Table 3-2, Fig. 3-5) and Pd/Ir ratio, but does not exhibit the low Os/Ir that is characteristic of the sulfide-depleted Yangyuan samples. These features suggest that the mechanism of sulfide depletion in this sample was different than that experienced by the Yangyuan samples.

Like the Yangyuan samples, Hannuoba peridotites also show evidence for melt/fluid metasomatism, based on lithophile trace element patterns (Song and Frey, 1989; Rudnick et al., 2004; Choi et al., 2008). However, there are no robust correlations between HSE and lithophile trace element patterns such as Pd/Ir vs. La/Yb, suggesting that HSE were less mobile than lithophile trace elements during this metasomatism. The lower fO_2 of the Hannuoba peridotites (Fig. 3-2) suggests that the metasomatic agent had a lower fO_2 and relatively high fS_2 compared to that at Yangyuan. Consequently, sulfides survived during melt/fluid-rock reaction, consistent with the presence of metal-saturated sulfides in this suite. Further, some sulfide precipitation may have occurred (X.S. Xu et al., 2008), as suggested by the extraordinarily high S and Se content of at least one Hannuoba peridotite (DMP-60,

having 320 ppm S and 230 ppb Se), which has a higher proportion of Cu-rich sulfides than the other Hannuoba samples (Table S3-4). As this sample has the same general HSE pattern as the other Hannuoba peridotites (Fig. 3-5a), apparently sulfide addition did not heavily modify the HSE patterns, probably due to the relatively low HSE concentrations of these additional sulfides (Alard et al., 2000).

One Hannuoba sample, DA20-16, plots significantly to the left of the Al_2O_3 vs. $(Pd/Ir)_N$ and Al_2O_3 vs. $^{187}Os/^{188}Os$ trends (Figs. 3-6 and 3-7). This sample has a peculiar major element composition, with low whole rock Mg# (89.6) coupled with low Al_2O_3 and CaO (Zhang et al., 2009), suggesting that it experienced Fe enrichment without affecting the other major elements. Given the position of this sample on the HSE plots, it appears that the Fe enrichment likely accompanied sulfide addition, which could explain the elevated its Pd/Ir and $^{187}Os/^{188}Os$ ratios (Figs. 3-6 and 3-7).

3.5.4 Impact on Os isotopic compositions

The effects of sulfide breakdown on Os isotopic compositions appear to be minimal. If the suite of Yangyuan peridotites shared the same initial $^{187}Os/^{188}Os$, then the present-day $^{187}Os/^{188}Os$ of each sample should positively correlate with its $^{187}Re/^{188}Os$, assuming a closed system (i.e., the isochron principle). Over time, $^{187}Os/^{188}Os$ will reflect melt depletion, similar to Al_2O_3, given the moderate incompatibility of Re and the strong compatibility of Os during partial melting. As such, the present-day $^{187}Os/^{188}Os$ is related to fertility, i.e., the lower the $^{187}Os/^{188}Os$, the more refractory the rock is.

Although the Yangyuan peridotites appear to have lost sulfides, as documented above, the suite nevertheless shows a positive correlation between $^{187}Os/^{188}Os$ and

robust immobile element indicators of melt depletion, such as olivine forsterite content, whole rock Yb, and Al_2O_3 (Fig. 3-7). Similar correlations are seen in samples from other suites that are characterized by fractionated Os/Ir (e.g., Pearson et al., 2004). Thus, incongruent sulfide breakdown does not appear to have affected Os isotopic compositions and, hence, Re depletion model ages (T_{RD}-minimum estimated age of melt depletion assuming no Re in the residue since formation, Walker et al., 1989). This suggests that the sulfide breakdown (and Re/Os fractionation) occurred relatively recently (i.e., since the Mesozoic). In contrast, Os model ages calculated using observed Re/Os relative to a chondritic reservoir (T_{MA}; Walker et al., 1989; Shirey and Walker, 1998) might dramatically change due to Re/Os fractionation.

Similar ranges of $^{187}Os/^{188}Os$ for Hannuoba and Yangyuan peridotites (0.116-0.127 vs. 0.115-0.126, respectively, Table 3-2) and their resulting similar T_{RD} model ages (Table 3-2), suggest that the Os model ages from our new data are robust. Omitting the outliers associated with refertilization and sulfide addition discussed above, the positive and overlapping $^{187}Os/^{188}Os$ vs. Al_2O_3 correlations for both Hannuoba and Yangyuan suites intersect 0.7 wt.% Al_2O_3 (the value considered best representative of maximum melt-depletion in off-craton peridotites by Handler et al.(1997)) at $^{187}Os/^{188}Os$ of ~0.113 to 0.117, corresponding to model ages of ~1.6 to 2.0 Ga (Fig. 3-7). By contrast, an Archean peridotite that has been refertilized by basaltic or picritic melts (e.g., Y.G. Xu et al., 2008; Zhang et al., 2009) would plot along the mixing lines depicted in Fig. 3-7 – far from where any of the data plot. Thus, it is highly unlikely that the lithospheric mantle in this portion of the Trans North-China Orogen formed in the Archean.

3.6 Conclusions

Variable but relatively low degrees of partial melting of the mantle can produce the HSE patterns observed in the Hannuoba peridotites, given long-term preservation of sulfides. By contrast, the distinct HSE patterns of Yangyuan peridotites, characterized by low total HSE and Os, Pd and Re depletions relative to Ir, cannot be produced by partial melting alone. These characteristics reflect secondary processes. Given the low S and Se of these samples and the metal-deficient composition of their mss, I suggest that incongruent sulfide breakdown occurred during interaction with a S-undersaturated melt/fluid under a high fO_2 and low fS_2. This resulted in S, Se, Os, Pd and Re loss relative to Ir and, thus, was likely an important process leading to the observed HSE characteristics in Yangyuan peridotites. The similarity of the Yangyuan HSE patterns to those of xenolithic peridotites from a number of other localities, worldwide, suggests that this process is common within some regions of the upper mantle.

Preservation of the correlation between $^{187}Os/^{188}Os$ and immobile melt depletion indices (e.g., Yb and Al_2O_3) indicates that incongruent sulfide breakdown was a recent event. The similarity of T_{RD} model ages of Yangyuan and Hannuoba peridotites is also consistent with this; both peridotite suites appear to have formed in the Paleoproterozoic (ca. 1.6~2.0 Ga).

Supplemental Material for Chapter 3

Table S3-1a. Average EPMA analyses of olivines from spinel peridotites

Sample	n	SiO_2	FeO	MnO	NiO	MgO	Total	Fo
Hannuoba								
DMP04	5	41.3	8.66	0.12	0.36	49.5	99.9	91.1
DMP19	6	41.1	8.38	0.11	0.37	49.5	99.4	91.3
DMP23a	6	40.9	8.53	0.12	0.36	49.0	98.9	91.1
DMP25	5	41.2	8.15	0.10	0.38	49.8	99.7	91.6
DMP41	5	40.4	9.34	0.14	0.39	49.5	99.7	90.4
DMP51	4	40.5	8.62	0.12	0.39	49.2	98.8	91.1
DMP56	5	40.2	9.82	0.15	0.37	48.8	99.4	89.9
DMP58	5	40.5	9.42	0.13	0.37	48.7	99.1	90.2
DMP59	5	40.6	9.25	0.14	0.38	49.0	99.4	90.4
DMP60	5	40.2	9.60	0.14	0.36	48.8	99.0	90.1
DMP67c	6	40.9	10.10	0.14	0.35	48.2	99.6	89.5
Yangyuan								
YY-04	8	41.1	8.04	0.10	0.38	50.7	100.4	91.8
YY-08	6	41.1	9.72	0.13	0.39	50.3	101.6	90.2
YY-09	6	41.1	9.16	0.14	0.37	50.3	101.1	90.7
YY-11	5	41.2	9.34	0.12	0.39	50.6	101.7	90.6
YY-13	5	40.9	9.16	0.11	0.40	49.9	100.5	90.7
YY-22	5	40.7	8.80	0.13	0.39	49.7	99.8	91.0
YY-23	5	40.8	9.07	0.13	0.39	50.1	100.5	90.8
YY-26	4	40.8	9.29	0.11	0.39	50.0	100.6	90.6
YY-27	6	40.8	9.95	0.15	0.37	49.7	101.0	89.9
YY-36	5	40.8	8.91	0.13	0.40	50.3	100.5	91.0
YY-40B	5	40.8	8.78	0.11	0.41	50.2	100.4	91.1
YY-42	5	40.9	8.90	0.12	0.39	50.4	100.7	91.0
YY-45	5	40.7	9.00	0.12	0.39	49.7	99.9	90.8
YY-50	5	40.7	9.41	0.13	0.40	49.6	100.2	90.4
YY-51	5	40.8	8.14	0.14	0.39	50.4	99.9	91.7
YY-52	5	41.0	9.17	0.15	0.38	50.4	101.1	90.7
YY-58	5	41.3	8.59	0.10	0.39	51.2	101.5	91.4
YY-60	5	41.0	8.68	0.13	0.39	50.7	100.9	91.2

Table S3-1b. Average EPMA analyses of orthopyroxenes from spinel peridotites

Sample	n	SiO_2	TiO_2	Al_2O_3	Cr_2O_3	FeO	MnO	MgO	CaO	Na_2O	Total
Hannuoba											
DMP-04	6	55.6	0.06	4.21	0.46	5.49	0.12	33.1	0.64	0.08	99.9
DMP-19	6	55.6	0.03	3.69	0.55	5.15	0.11	33.4	0.59	0.07	99.2
DMP-23a	9	55.6	0.05	3.84	0.50	5.31	0.12	32.4	0.62	0.14	98.6
DMP-25	6	56.5	0.04	2.85	0.52	5.02	0.11	33.9	0.61	0.03	99.7
DMP-41	8	55.5	0.07	3.77	0.35	5.90	0.14	33.9	0.51	0.08	100.1
DMP-51	7	55.5	0.08	3.67	0.46	5.39	0.13	33.7	0.69	0.09	99.6
DMP-56	7	55.0	0.13	4.61	0.31	6.18	0.12	32.7	0.70	0.11	99.8
DMP-58	5	55.3	0.09	4.44	0.33	5.94	0.14	33.1	0.68	0.12	100.1
DMP-59	9	55.3	0.09	3.95	0.41	5.79	0.13	33.1	0.59	0.08	99.5
DMP-60	9	54.7	0.09	4.25	0.31	6.01	0.13	33.4	0.56	0.09	99.5
DMP-67c	6	54.9	0.13	5.17	0.35	6.26	0.14	32.0	0.69	0.14	99.9
Yangyuan											
YY-04	5	55.4	0.03	4.12	0.50	5.39	0.12	33.3	0.75	0.05	99.6
YY-08	5	54.6	0.07	5.19	0.34	6.47	0.15	32.6	0.64	0.03	100.1
YY-09	5	54.3	0.09	5.85	0.42	5.95	0.13	32.3	0.97	0.10	100.1
YY-11	5	54.6	0.10	5.69	0.42	6.09	0.13	32.6	0.87	0.09	100.6
YY-13	5	54.4	0.14	5.58	0.49	5.92	0.12	32.2	0.99	0.09	99.9
YY-22	5	54.3	0.04	5.05	0.46	5.69	0.13	32.6	0.82	0.06	99.2
YY-23	5	54.1	0.11	6.58	0.49	5.94	0.11	32.0	1.16	0.14	100.7
YY-26	5	54.5	0.08	4.82	0.35	6.16	0.13	32.7	0.61	0.05	99.4
YY-27	5	54.5	0.11	5.40	0.33	6.59	0.14	32.4	0.76	0.05	100.3
YY-36	5	55.2	0.05	4.59	0.44	5.89	0.13	33.1	0.61	0.04	100.1
YY-40B	5	54.7	0.04	5.51	0.43	5.79	0.12	32.6	0.67	0.05	99.9
YY-42	5	54.9	0.05	5.12	0.41	5.92	0.11	32.8	0.72	0.05	100.1
YY-45	5	54.0	0.11	6.45	0.54	5.85	0.11	31.4	1.13	0.13	99.7
YY-50	5	54.5	0.12	6.31	0.31	6.12	0.13	32.1	0.82	0.11	100.5
YY-51	5	55.2	0.02	3.05	0.60	5.32	0.13	33.0	1.09	0.05	98.4
YY-52	5	54.0	0.09	6.32	0.51	5.92	0.12	31.8	1.26	0.11	100.2
YY-58	5	54.6	0.08	5.89	0.58	5.56	0.12	32.5	1.21	0.14	100.6
YY-60	5	55.4	0.10	3.62	0.53	5.63	0.12	33.4	0.85	0.05	99.7

Table S3-1c. Average EPMA analyses of clinopyroxenes from spinel peridotites

Sample	n	SiO_2	TiO_2	Al_2O_3	Cr_2O_3	FeO	MnO	MgO	CaO	Na_2O	Total
Hannuoba											
DMP-04	7	53.0	0.26	5.66	0.92	2.35	0.08	15.7	20.3	1.35	99.6
DMP-19	6	52.9	0.14	5.02	1.28	1.96	0.08	15.7	20.5	1.31	98.8
DMP-23a	5	52.7	0.13	3.25	1.24	2.45	0.09	16.7	21.3	0.51	98.4
DMP-25	7	53.4	0.13	3.49	1.09	2.03	0.08	16.8	21.3	0.79	99.0
DMP-41	9	52.6	0.35	6.13	0.99	2.26	0.08	15.3	20.6	1.77	100.0
DMP-51	5	52.8	0.27	4.96	0.96	2.33	0.07	16.1	20.4	1.35	99.2
DMP-56	8	52.2	0.60	6.62	0.66	2.79	0.08	15.2	19.6	1.73	99.5
DMP-58	9	52.5	0.38	6.32	0.73	2.66	0.09	15.5	19.8	1.72	99.7
DMP-59	10	52.5	0.39	5.65	0.91	2.33	0.08	15.4	20.6	1.57	99.5
DMP-60	10	52.1	0.45	6.49	0.75	2.33	0.09	15.2	20.1	1.71	99.2
DMP-67c	7	51.3	0.92	4.56	0.85	3.43	0.11	16.2	21.1	0.46	98.9
Yangyuan											
YY-04	5	52.8	0.17	4.38	1.32	2.04	0.07	16.2	22.0	1.16	100.2
YY-08	5	51.8	0.28	5.17	0.79	2.68	0.06	15.6	22.3	1.04	99.7
YY-09	5	51.6	0.36	6.36	1.05	2.69	0.08	15.7	20.0	1.57	99.4
YY-11	5	52.2	0.40	6.39	0.95	2.56	0.08	15.7	20.4	1.69	100.3
YY-13	3	51.4	0.55	6.12	1.02	2.68	0.09	15.8	20.2	1.41	99.3
YY-22	5	51.9	0.23	5.37	1.08	2.29	0.08	15.9	21.2	1.26	99.3
YY-23	5	53.1	0.42	6.49	0.99	2.88	0.08	16.2	18.8	1.53	100.5
YY-26	5	51.6	0.40	5.85	0.89	2.52	0.08	15.2	21.2	1.43	99.1
YY-27	5	51.5	0.58	6.50	0.81	2.91	0.08	14.9	21.1	1.53	99.9
YY-36	6	53.7	0.25	5.00	1.10	2.22	0.08	15.8	21.2	1.29	100.5
YY-40B	5	53.5	0.20	5.66	0.95	2.16	0.08	15.6	20.9	1.39	100.5
YY-42	5	53.4	0.14	4.98	0.91	2.25	0.07	16.2	21.1	1.03	100.1
YY-45	5	53.1	0.41	6.38	0.95	2.82	0.07	16.3	18.9	1.54	100.5
YY-50	5	52.8	0.57	6.99	0.77	2.53	0.07	15.3	19.6	1.65	100.3
YY-51	5	52.5	0.07	2.87	1.24	2.29	0.09	17.3	21.2	0.76	98.4
YY-52	5	51.5	0.30	6.17	0.92	3.03	0.09	16.4	19.6	1.29	99.3
YY-58	5	52.1	0.30	6.34	1.21	2.73	0.10	16.4	19.5	1.54	100.2
YY-60	5	52.5	0.28	3.75	1.29	2.29	0.08	16.9	21.6	0.98	99.8

Table S3-1d. Average EPMA analyses of spinels from spinel peridotites

Sample	n	SiO_2	TiO_2	Al_2O_3	Cr_2O_3	FeO	MnO	NiO	MgO	Total	Cr#
Hannuoba											
DMP-04	6			52.9	15.9	10.34	0.10		21.2	100.4	16.8
DMP-19	5			46.4	22.4	10.21	0.09		20.1	99.2	24.5
DMP-23a	5			43.9	24.3	11.94	0.11		19.4	99.7	27.1
DMP-25	5			37.4	31.3	11.72	0.13		18.9	99.4	36.0
DMP-41	5		0.09	57.1	12.5	10.12	0.09	0.34	20.5	100.7	12.8
DMP-51	6		0.14	49.3	18.7	10.65	0.10	0.30	19.7	98.8	20.2
DMP-56	5		0.16	58.7	8.8	10.23	0.09	0.40	21.1	99.4	9.1
DMP-58	5		0.11	57.4	10.4	10.19	0.09	0.34	20.9	99.4	10.8
DMP-59	5		0.11	54.9	13.3	10.15	0.10	0.33	20.4	99.2	14.0
DMP-60	5		0.10	59.1	9.0	9.60	0.09	0.40	20.8	99.1	9.3
DMP-67c	6			57.3	9.4	12.84	0.09		20.6	100.3	9.9
Yangyuan											
YY-04	5	0.03	0.10	45.7	24.2	10.73	0.13	0.26	20.0	101.1	26.2
YY-08	5	0.03	0.06	55.3	12.3	11.72	0.11	0.37	20.9	100.9	13.0
YY-09	5	0.05	0.14	54.9	13.3	10.71	0.11	0.36	21.6	101.1	14.0
YY-11	5	0.04	0.12	54.1	12.5	9.76	0.11	0.32	21.1	98.1	13.4
YY-13	4	0.06	0.24	50.8	16.4	11.66	0.13	0.34	20.8	100.4	17.8
YY-22	4	0.04	0.07	52.1	16.1	10.34	0.12	0.32	20.9	100.0	17.2
YY-23	5	0.05	0.21	52.7	15.0	11.18	0.12	0.37	21.4	101.0	16.1
YY-26	5	0.02	0.06	55.6	12.8	10.58	0.12	0.35	21.0	100.5	13.3
YY-27	5	0.03	0.09	56.5	10.8	11.56	0.11	0.38	21.0	100.5	11.4
YY-36	5	0.01	0.04	49.5	18.8	11.00	0.13	0.30	20.2	99.9	20.3
YY-40B	5	0.01	0.06	54.2	14.0	10.43	0.10	0.37	20.8	99.9	14.8
YY-42	5	0.02	0.06	52.7	15.5	10.76	0.13	0.33	21.0	100.5	16.5
YY-45	5	0.06	0.21	51.6	15.1	11.10	0.11	0.35	21.2	99.7	16.4
YY-50	5	0.04	0.11	57.7	9.4	10.30	0.11	0.43	21.9	100.0	9.8
YY-51	5	0.04	0.15	28.0	39.7	14.04	0.21	0.18	16.9	99.2	48.8
YY-52	5	0.07	0.15	51.9	14.8	11.54	0.11	0.35	21.2	100.1	16.1
YY-58	5	0.08	0.15	50.7	18.2	10.53	0.12	0.34	21.5	101.6	19.4
YY-60	5	0.03	0.35	35.9	32.5	13.25	0.19	0.21	18.3	100.7	37.7

Table S3-2. Os concentrations and isotope compositions of peridotite reference materials

Sample	Method	n	Os conc. (ppb)	$^{187}Os/^{188}Os$
UB-N	CT-N-TIMS (UMCP)[a]	1	3.95	0.12693
	CT-N-TIMS (UMCP)[b]	4	3.85 ± 0.32	0.12722 ± 38
	CT-N-TIMS (UMCP)[c]	4	3.51 ± 0.12	0.12737 ± 25
	CT-ICP-MS (Chicago)[d]	6	3.72 ± 0.35	-
	HPA-N-TIMS (Leoben)[e]	14	3.85 ± 0.13	0.12780 ± 20
GP-13	CT-N-TIMS (UMCP)[b]	5	3.74 ± 0.11	0.12645 ± 12
	CT-ICP-MS (Chicago)[d]	3	3.70 ± 0.02	-
	CT-N-TIMS (Durham)[f]	8	3.87 ± 0.17	0.1262
	CT-N-TIMS (Durham)[g]	5	3.61 ± 0.12	0.12632±9
	HPA-N-TIMS (Leoben)[e]	7	4.06 ± 0.07	
	HPA-N-TIMS (UMCP)[h]	3	3.3 ± 0.1	0.12644 ± 22

n represents the number of analyses. Uncertainties quoted as $2\sigma_{mean}$ if n>1.

a. This study

b. Puchtel et al., 2008.

c. Becker et al., 2006.

d. Puchtel and Humayun, 2005.

e. Meisel et al., 2003 & Meisel and Moser, 2004.

f. Pearson et al., 2004.

g. Day et al., 2008.

h. James Day, unpublished data.

Table S3-3. Comparison between Carius tube digestion and NiS fusion results for Os isotopic compositions using N-TIMS

Sample	Method	$^{187}Os/^{188}Os$	Os conc. (ppb)
YY-22	Low T (270^{o}C)-Carius tube digestion/N-TIMS	0.12072	0.927
YY-22	High T (340^{o}C)-Carius tube digestion/N-TIMS	0.12063	1.156
YY-22	Os spiked before NiS fusion/N-TIMS	0.12070	0.962
YY-22	Os spiked after NiS fusion/N-TIMS	0.12044	0.574

Note: the method-CT/N-TIMS is stated in the text. Two aliquots (~5 g of powder each) of Yangyuan sample YY-22 were digested using NiS fusion: one spiked before fusion and the other spiked after fusion. Both residual NiS aliquots were re-dissolved by concentrated HCl-HNO3 (1:2) solutions. Osmium was extracted from the acid solution using CCl_4 (Cohen and Waters, 1996), then back-extracted into HBr, and finally purified via microdistillation (Birck et al., 1997). Osmium was measured using multiplier on a negative thermal ionization mass spectrometer (N-TIMS).

Table S3-4a. Major element compositions of sulfides from Yangyuan peridotites

Sample	n	Fe	Cu	S	Si	Ni	Total	atom. (Fe+Cu+Ni)/S	2σ	Sulfide type
Grain1										
YY-08-s1	8	31.31	31.70	34.82	<0.03	0.82	98.66	0.99	0.02	Cp
YY-08-s1(2)	3	32.61	6.29	33.66	<0.03	26.39	98.97	1.08	0.02	Pn
Grain2										
YY-08-s2	5	42.17	0.15	37.68	<0.03	16.88	96.90	0.89	0.10	mss
YY-08-s2(2)	5	29.46	33.16	35.49	<0.03	0.23	98.37	0.95	0.02	Cp
Grain 3										
YY-26-s1	6	55.76	<0.06	39.68	0.03	3.44	98.93	0.85	0.02	mss
Grain4										
YY-26n-s1	6	44.06	<0.06	39.32	<0.03	15.66	99.06	0.86	0.05	mss
Grain 5										
YY-58-s1	6	31.19	33.30	35.57	<0.03	0.36	100.43	0.98	0.02	Cp
YY-58-s1(2)	2	21.61	0.98	36.24	0.04	34.09	92.96	0.87	0.01	Pn
Grain6										
YY-58-s2	2	27.35	<0.06	33.69	0.06	35.23	96.34	1.04	0.01	Pn
QL		0.10	0.06	0.02	0.03	0.03				

Note: Six type-e grains of sulfides from three samples of Yangyuan were analyzed. n represents the number of the analyses in the grain. In each individual grain, if more than one phase appears, I report the average of each of these phases separately. 2σ represents the standard deviation of atomic ratio (Fe+Ni+Cu)/S. Cp: chalcopyrite; Pn: pentlandite; and mss: monosulfide solid solution. QL: quantification limit

Table S3-4b. Major element compositions of sulfides from Hannuoba peridotites

Sample	n	Fe	Cu	S	Si	Ni	Total	atom. (Fe+Cu+Ni)/S	2σ	Sulfide type
DMP-19										
Type-e										
DMP-19-s6	3	28.46	<0.06	33.59	<0.03	36.42	98.52	1.08	0.02	Pn
DMP-19-s6-4		30.22	32.52	34.91	0.03	0.49	98.16	0.97		Cp
DMP-19-s12	3	28.80	2.02	33.73	<0.03	34.79	99.34	1.08	0.04	Pn
DMP-19-s12-4		26.48	35.41	32.57	0.52	0.35	95.33	1.02		Cp
sulfides enclosed in serpentine										
DMP-19-s9-2		1.70	0.48	32.34	0.46	63.27	98.24	1.11		Gv
DMP-19-s9(2)-1		12.85	0.19	33.56	<0.03	51.10	97.70	1.05		Pn
DMP-19-s9(2)-2		21.14	<0.06	34.03	<0.03	44.97	100.15	1.08		Pn
Type-i										
DMP-19-s11	3	24.61	0.25	33.67	<0.03	41.18	99.71	1.09	0.01	Pn
DMP-19-s11(2)	2	1.33	1.91	27.74	<0.03	69.35	100.35	1.43	0.05	Hw
DMP-19-s1-2		4.82	0.23	33.43	<0.03	59.73	98.21	1.06		Ml
DMP-19-s1-3		1.06	0.62	28.39	0.70	68.08	98.85	1.34		Hw
DMP-19-s2-1		19.37	<0.06	32.92	<0.03	45.50	97.81	1.09		Pn
DMP-19-s10real-1		27.89	0.25	32.92	0.51	33.90	95.47	1.05		Pn
Type-f										
DMP-19-s13i-1		23.51	<0.06	32.89	0.07	39.74	96.22	1.07		Pn
DMP-51										
Type-e										
DMP-51-s20e	2	31.12	2.56	33.37	<0.03	30.15	97.22	1.07	0.02	Pn
DMP-51-s20e-3		6.69	66.89	24.82	0.03	0.95	99.36	1.54		Bn
Type-i										
DMP-51-s5i	2	22.64	0.10	33.81	<0.03	41.95	98.51	1.06	0.01	Pn
DMP-51-s12i-2		26.58	<0.06	33.36	0.05	36.04	96.04	1.05		Pn
DMP-51-s13i-1		2.51	0.75	29.64	0.07	63.05	96.02	1.22		Gv-Hw
DMP-51-s13i-2		24.55	<0.06	33.43	0.04	36.96	94.98	1.03		Pn
DMP-51-s14i-1		23.33	<0.06	33.04	0.07	37.58	94.06	1.03		Pn
DMP-51-s21	4	28.23	0.44	32.93	0.21	34.12	95.92	1.06	0.02	Pn
DMP-51-s21-2		29.09	31.60	34.42	0.14	1.85	97.10	0.98		Cp
Type-i-veins										
DMP-51-s12iv-1		24.66	<0.06	32.63	0.06	39.14	96.49	1.09		Pn
DMP-51-s16iv	2	28.22	31.12	34.60	0.32	2.19	96.44	0.96	0.03	Cp
Type-f										
DMP-51-s1f-1		28.66	2.15	33.63	0.07	31.36	95.87	1.03		Pn
DMP-51-s2f-1		24.98	<0.06	33.68	0.06	38.54	97.28	1.05		Pn
DMP-51-s2f-2		26.49	4.42	33.58	0.07	31.30	95.86	1.03		Pn
DMP-51-s3f-1		30.01	0.46	32.44	<0.03	31.96	94.89	1.08		Pn

DMP-51-s11f-1		26.92	0.16	33.05	0.15	36.04	96.32	1.07		Pn
DMP-58										
Type-e										
DMP-58-s8e	2	36.12	2.43	33.51	<0.03	24.66	96.74	1.06	0.02	mss
Type-i										
DMP-58-s1iv-1		28.00	<0.06	30.77	0.34	34.21	93.32	1.13		Pn
DMP-58-s3i-1		26.72	2.81	33.77	0.14	32.18	95.63	1.02		Pn
DMP-58-s5i-1		25.66	0.27	33.98	0.08	36.13	96.11	1.02		Pn
DMP-58-s9i-1		24.20	1.30	34.63	0.10	36.42	96.65	0.99		Pn
DMP-58-s9i-2		26.52	<0.06	32.94	<0.03	36.35	95.85	1.06		Pn
Type-f										
DMP-58-s2f-1		26.72	<0.06	33.65	<0.03	36.30	96.69	1.05		Pn
DMP-58-s4f-1		28.76	1.59	33.59	<0.03	32.49	96.46	1.04		Pn
DMP-58-s4f-2		29.43	0.11	32.31	0.37	32.45	94.67	1.07		Pn
DMP-60										
Type-e										
DMP-60-s10e	4	23.56	0.09	32.95	<0.03	41.19	97.80	1.09	0.02	Pn
DMP-60-s10e(2)	2	28.96	33.22	34.35	<0.03	0.77	97.30	0.98	0.03	Cp
DMP-60-s10e(3)	2	28.11	18.07	33.64	<0.03	18.32	98.18	1.05	0.01	mss
DMP-60-s9e	3	22.22	0.07	33.07	0.26	40.07	95.68	1.05	0.01	Pn
DMP-60-s9e(2)		27.94	26.60	34.05	<0.03	7.74	96.35	0.99		Cp
DMP-60-s11e	2	4.49	0.13	35.66	<0.03	59.17	99.45	0.98	0.01	Ml
DMP-60-s14-1		18.73	0.35	32.09	0.27	41.24	92.67	1.04		Pn
DMP-60-s14-2		28.90	32.80	33.89	<0.03	0.15	95.82	0.98		Cp
Type-i										
DMP-60-s1iv(2)-4		15.51	0.20	34.16	0.05	46.90	96.82	1.01		Pn
DMP-60-s2i-1		22.29	<0.06	33.71	0.06	40.39	96.44	1.03		Pn
DMP-60-s3-1		27.89	0.31	34.16	<0.03	36.38	98.77	1.06		Pn
DMP-60-s8i	3	27.08	<0.06	33.68	0.12	37.30	98.20	1.07	0.02	Pn
DMP-60-s8i(2)		29.24	30.78	34.42	0.37	2.25	97.06	0.97		Cp
DMP-60-s11i-3		20.54	<0.06	34.63	<0.03	42.84	98.02	1.02		Pn
DMP-60-s13i-2		27.45	0.17	32.38	0.27	35.34	95.61	1.09		Pn
DMP-60-s14i	2	23.58	0.06	33.38	<0.03	41.32	98.34	1.08	0.01	Pn
DMP-60-s11i-1		28.65	30.87	34.61	0.11	2.56	96.79	0.97		Cp
DMP-60-s12i	2	25.39	0.08	33.77	0.05	39.97	99.26	1.08	0.01	Pn
DMP-60-s12i(2)	2	30.14	33.20	35.36	<0.02	0.37	99.06	0.97	0.03	Cp

Note: Four representative Hannuoba samples were selected. n represents the number of analyses in each phase of a grain, while the blank represents only one analysis. Some grains show multiple phases. Cp: chalcopyrite; Pn: pentlandite; Hw:heazlewoodite; Gv:godlevskite; Ml:millerite; Bn:bornite; and mss: monosulfide solid solution. Type-e: sulfides enclosed in silicates; Type-i: interstitial sulfides; Type-f: sulfides along healed fractures. Some sulfides appear in serpentine for serpentinized samples, e.g., DMP-19. 2σ represents the standard deviation of atomic ratio (Fe+Ni+Cu)/S.

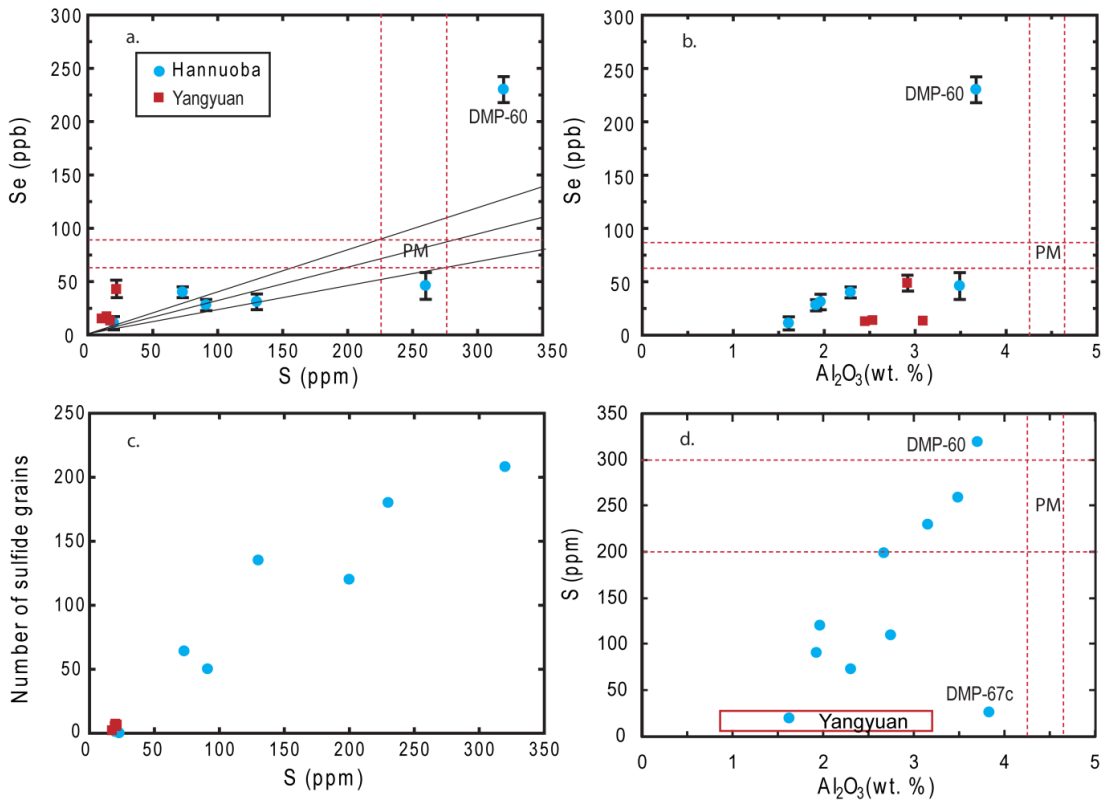

Fig. S3-1a-d. Plots of (a) S vs. Se concentrations, (b) Al_2O_3 vs. Se concentrations (c) sulfur vs. the number of sulfide grains per thin section and (d) S vs. Al_2O_3 concentrations for Hannuoba and Yangyuan peridotites. PM: primitive mantle (McDonough and Sun, 1995); the solid lines in panel (a) represent the average S/Se ratios (±2σ) of the reference mantle "UM" suite (Morgan et al., 1986); S and Al_2O_3 data of Hannuoba peridotites are from Gao et al. (2002).

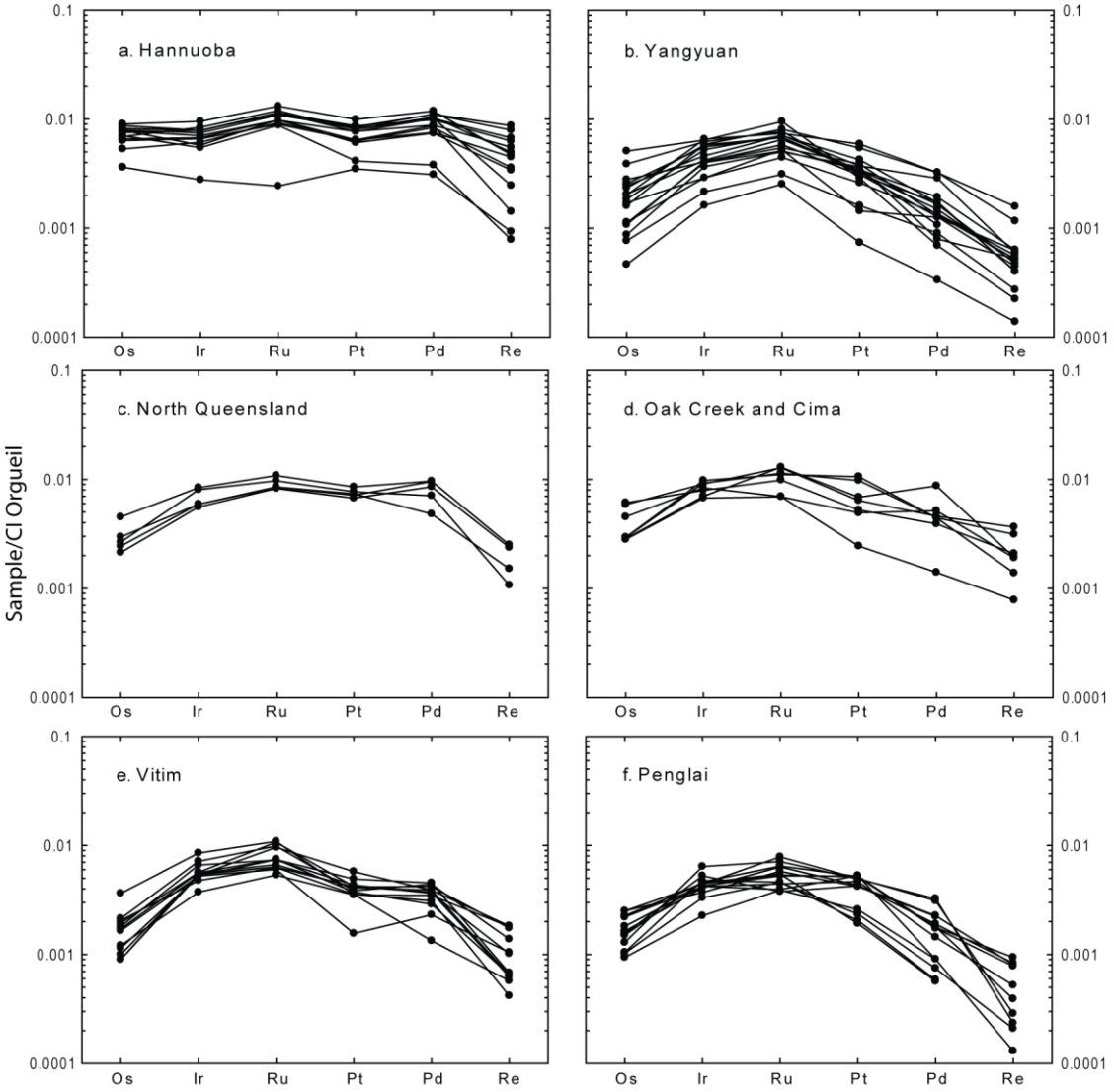

Fig. S3-2 a-f. CI chondrite (Orgueil)-normalized patterns for HSE from xenolithic peridotites. a. Hannuoba, North China (Becker et al., 2006; this study); b. Yangyuan, North China (this study); c. North Queensland, Australia (Handler et al., 1999; Handler and Bennett, 1999); d. Oak Creek, Sierra Nevada and Cima, Basin and Range (Lee, 2002); e. Vitim, Siberia (Pearson et al., 2004); f. Penglai, North China Craton (Chu et al., 2009).

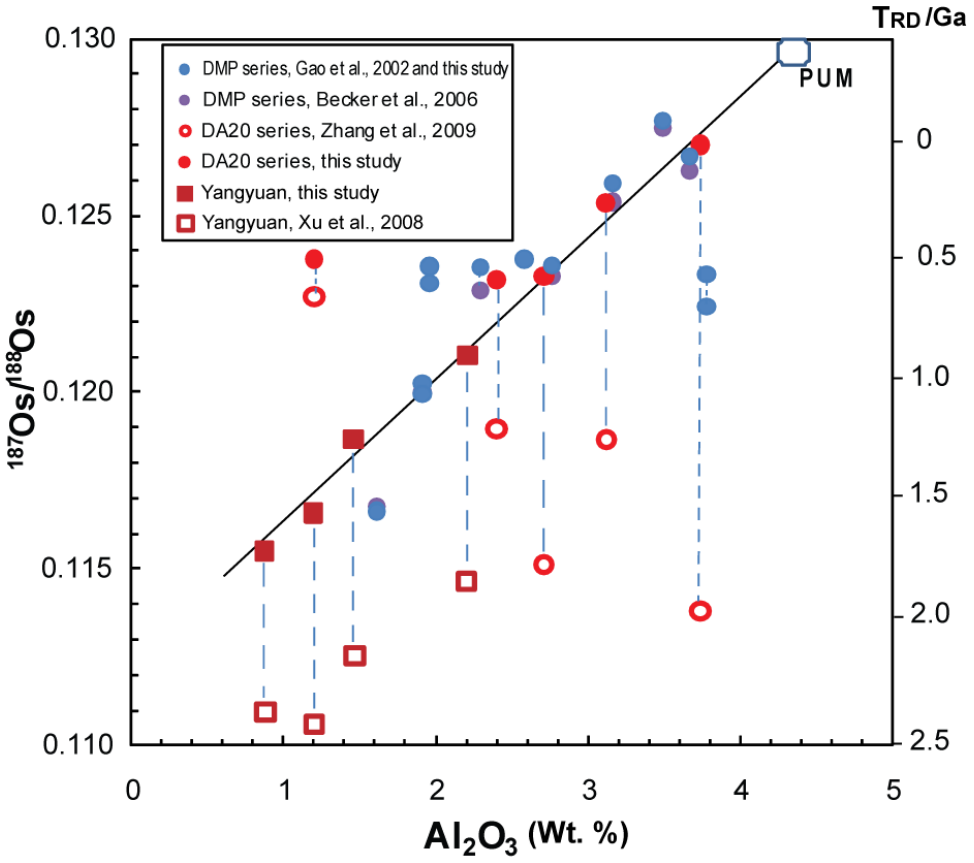

Fig. S3-3. Plot of Al_2O_3 vs. $^{187}Os/^{188}Os$ for Hannuoba and Yangyuan peridotites. Data points for the same samples in which $^{187}Os/^{188}Os$ was measured by different methods are connected by a dashed line. The DMP sample series were analyzed by CT-N-TIMS (i.e., Carius tube digestion combined with a negative Thermal Ionization Mass Spectrometry) (Gao et al., 2002; Becker et al., 2006; this study). The DA20 sample series was analyzed by NiS fusion-Os sparging-ICP-MS in the study of Zhang et al. (2009) or and CT-N-TIMS (this study). In addition, three were also measured by HPA (high pressure asher digestion)-N-TIMS. For these three samples, the CT-N-TIMS and HPA-N-TIMS results are indistinguishable. Four Yangyuan samples that were previously measured by NiS-Os sparging-ICP-MS by Y.G. Xu et al. (2008), were re-analyzed here by CT-NTIMS. PUM: primitive upper mantle (Meisel et al., 2001). The solid line represents the trend defined by the correlation between $^{187}Os/^{188}Os$ and Al_2O_3 for the majority of the samples from both localities.

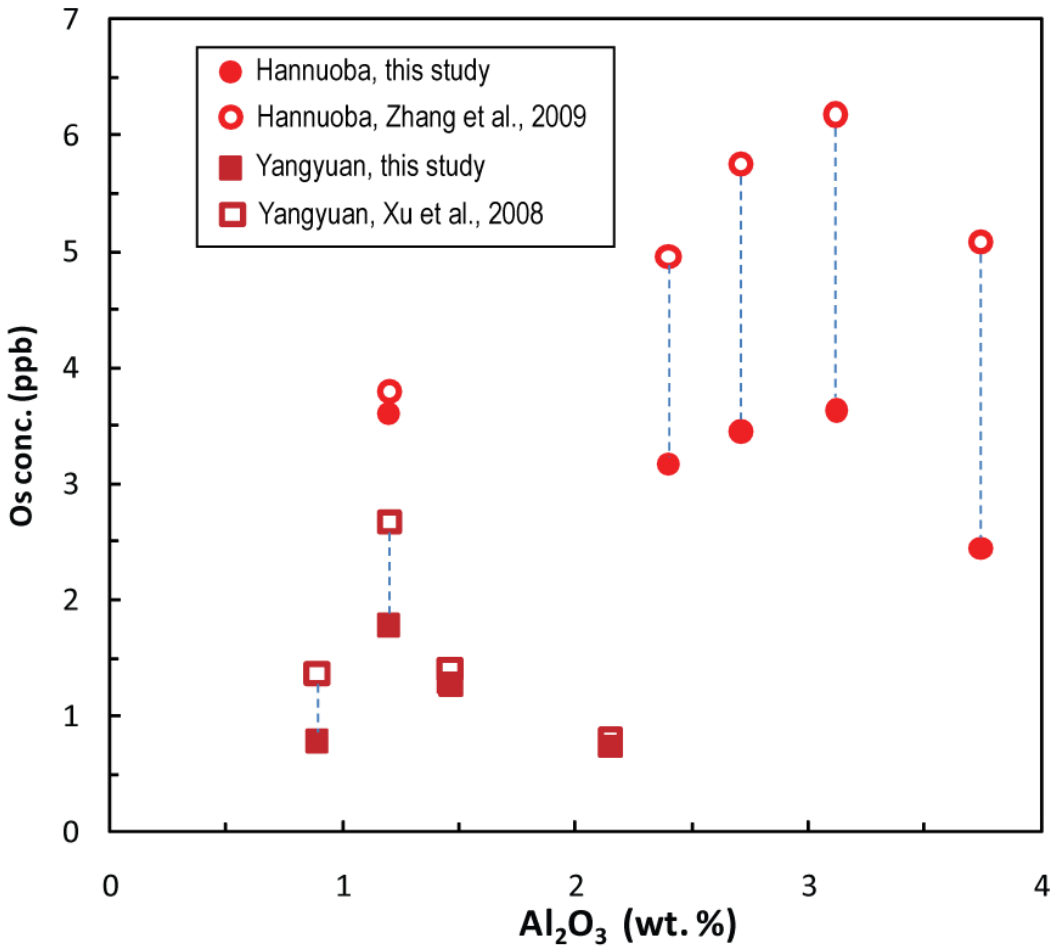

Fig. S3-4. Plot of Al_2O_3 vs. Os concentrations of Yangyuan and Hannuoba peridotites that were analyzed by both CT-N-TIMS (this study) and NiS-Os sparging-ICP-MS (Y.G. Xu et al., 2008; Zhang et al., 2009).

Comparison of Os data from N-TIMS vs. sparging results

As shown in Table 3-2 and Figs. 3-3S and 3-4S, there are large discrepancies in Os abundances and isotope compositions measured on the same peridotite powders by sparging (Xu et al., 2008; Zhang et al., 2009) versus N-TIMS (this study) for both Yangyuan and Hannuoba samples. The large differences between results affect the model ages for these peridotites and, hence, geodynamic interpretations. Here, I summarize the methods I have taken to assess the accuracy of the data in this study.

In this study, I used the techniques of ID-CT/HPA-N-TIMS: isotope dilution (ID) combined with Carius tube (CT) or high pressure asher (HPA) digestion and measurement by negative thermal ionization mass spectrometry (N-TIMS), the detailed procedures of which are provided in the *Analytical methods* section of this chapter (and references therein). By contrast, Y.G. Xu et al. (2008) and Zhang et al. (2009) employed the NiS fusion-Os sparging-ICP-MS method, the protocol of which is outlined in these two papers and references therein.

In order to compare techniques, I measured four Yangyuan samples from the study of Y.G. Xu et al. (2008) and five Hannuoba samples from the study of Zhang et al. (2009) by CT-N-TIMS. Three of these five Hannuoba samples were also analyzed by HPA-N-TIMS. In addition, to evaluate the accuracy of the methods utilized in this study, I also measured the peridotite reference material UB-N, which is widely used by the Os isotope, and highly siderophile element (HSE) community. UB-N yielded an Os concentration of 3.95 ppb and $^{187}Os/^{188}Os$ of 0.12693±12 (2σ) using the method of CT-N-TIMS. Both Os concentration and isotope composition of UB-N are well within the range of previously published data (e.g., Meisel et al., 2003; Meisel and Moser, 2004; Puchtel and Humayun, 2005; Becker et al., 2006; Puchtel et al., 2008) (Table S3-2). Further, the analyses of the peridotite reference material GP-13 produced identical results for Os abundances and isotopic compositions using CT-N-TIMS versus HPA-N-TIMS techniques in our laboratory (Puchtel et al., 2008; James Day, unpublished data), which are also consistent with results from other labs using similar methods (Meisel and Moser, 2004; Pearson et al., 2004; Day et al., 2008) (Table S3-2). Likewise, Os isotope compositions and concentrations determined for three Hannuoba peridotites using both CT-NTIMS and HPA-NTIMS methods gave identical results within analytical uncertainties (Table 3-2).

There are substantial discrepancies between my results and those obtained using NiS-Os sparging-ICP-MS (Y.G. Xu et al., 2008 and Zhang et al., 2009) (Table 3-2). For Yangyuan peridotites, the Os sparging method by Y.G. Xu et al. (2008) generated $^{187}Os/^{188}Os$ ratios that are 3.8% to 5.5% (average 4.8%) lower (Fig. S3-3), and Os concentrations that are 8% to 75% (average 35%) higher (Fig. S3-4) than the N-TIMS results. Similarly, for Hannuoba peridotites, these numbers are 0.9% to 11.6% (average 5.7%) lower in $^{187}Os/^{188}Os$ (Fig. S3-3), and 5% to 113% (average 64%) higher in Os

concentrations (Fig. S3-4) when the sparging results of Zhang et al. (2009) are compared to my N-TIMS results. The different mass fractionation corrections (i.e., $^{189}Os/^{188}Os$=1.2212 in Zhang et al. (2009) vs. $^{192}Os/^{188}Os$=3.083 in this study) would only result in very small differences in $^{187}Os/^{188}Os$ (<0.03%) between the labs. These differences in $^{187}Os/^{188}Os$ correspond to 100 to 1500 Ma differences in Os model ages (Fig. S3-3). Neither of the previous papers (Y.G. Xu et al., 2008; Zhang et al., 2009) report sparging data for peridotite reference materials (e.g., UB-N or GP-13) to evaluate the accuracy of the measurements. Zhang et al. (2008) report sparging $^{187}Os/^{188}Os$ results for a highly refractory and serpentinized peridotite from the Mengyin kimberlite (sample F50-9270) that are the same within uncertainty to those reported by Gao et al. (2002) via N-TIMS and Carius tube digestion. However, Os concentrations exhibited a three-fold difference (3.45 ppb (sparging) vs. 1.20 ppb (N-TIMS), respectively).

In contrast to the data reported by Y.G. Xu et al. (2008) and Zhang et al. (2009), these new data generally plot along the trend of $^{187}Os/^{188}Os$ and melt depletion indices such as Al_2O_3, defined by previously studied Hannuoba peridotites (DMP series: Gao et al., 2002; Becker et al., 2006; this study) (Fig. S3-3). Most importantly for this study, Yangyuan and Hannuoba peridotites have similar distributions of Os model ages (T_{RD}), consistent with their geographic proximity. In addition, in order to evaluate further the discrepancies between the Xu/Zhang studies and my data, in particular, whether the generally more radiogenic $^{187}Os/^{188}Os$ values I find result from failure to access non-radiogenic Os that may reside within acid-resistant phase, I analyzed two aliquots of relatively refractory Yangyuan sample (YY-22, Fo = 91.2) by the NiS fusion/N-TIMS method. The results yield $^{187}Os/^{188}Os$ within uncertainty of the previously published results obtained for this sample from both high and low temperature Carius tube digestion/N-TIMS (Table S3-3). These results demonstrate that the source of the discrepancies is unlikely to reside in the dissolution method. The reason for the discrepancy remains unclear. Although I cannot determine why the sparging method generates such different results, I see no evidence for an Archean or near-Archean component in either locality in this study.

Chapter 4: Mapping lithospheric boundaries using Os isotopes of mantle xenoliths: an example from the North China Craton[1, 2, 3]

[1] The original version of this chapter was created/written by J.G. Liu. J.G. Liu, R.L. Rudnick, and R.J. Walker contributed to the interpretation of the data.

[2] The sample selection and preparation for measurement were conducted by J.G. Liu. Electronic Micro-Probe Analyses of the samples reported in this chapter were performed by J.G. Liu with assistance of P.M. Piccoli. Whole-rock major element compositions of the samples reported in this chapter were measured by S.A. Mertzman at the Franklin and Marshall College, United States, or by S. Gao at the Northwest University, Xi'an, China. Whole rock trace element compositions of the samples reported in this chapter were determined by S. Gao at the Northwest University. The Re-Os isotope and HSE analyses of all samples were carried out by J.G. Liu, except for the following: most of the Hannuoba samples were previously reported by Gao et al. (2002) and Becker et al. (2006). Re-Os data for two Datong and three Fansi samples were determined by Honglin Yuan at the University of Maryland.

[3] This chapter has been published as:
Liu, J. G., Rudnick, R. L., Walker, R. J., Gao, S., Wu, F. Y., Piccoli, P. M., Yuan, H. L., Xu, W. L., and Xu, Y. G., 2011. Mapping lithospheric boundaries using Os isotopes of mantle xenoliths: an example from the North China Craton. Geochimica et Cosmochimica Acta, v. 75, p. 3881-3902. DOI: 10.1016/j.gca.2011.04.018.

Abstract

The petrology, mineral compositions, whole rock major/trace element concentrations, including highly siderophile elements, and Re-Os isotopic compositions of 99 peridotite xenoliths from the central North China Craton were determined in order to constrain the structure and evolution of the deep lithosphere. Samples from seven Early Cretaceous-Tertiary volcanic centers display distinct geochemical characteristics from north to south. Peridotites from the northern section are generally more fertile (e.g., Al_2O_3 = 0.9-4.0 %) than those from the south (e.g., Al_2O_3 = 0.2-2.2 %), and have maximum whole-rock Re-depletion Os model ages (T_{RD}) of ~1.8 Ga suggesting their coeval formation in the latest Paleoproterozoic. By contrast, peridotites from the south have maximum T_{RD} model ages that span the

Archean-Proterozoic boundary (2.1 to 2.5 Ga). Peridotites with model ages from both groups are found at Fansi, the southernmost locality in the northern group, which likely marks a lithospheric boundary. The Neoarchean age of the lithospheric mantle in the southern section matches that of the overlying crust and likely reflects the time of amalgamation of the North China Craton via collision between the Eastern and Western blocks. The Late Paleoproterozoic (~1.8 Ga) lithospheric mantle beneath the northern section is significantly younger than the overlying Archean crust, indicating that the original lithospheric mantle was replaced in this region, either during a major north-south continent-continent collision that occurred during assembly of the Columbia supercontinent at ~1.8-1.9 Ga, or from extrusion of ~1.9 Ga lithosphere from the Khondalite Belt beneath the northern Trans-North China Orogen, during the ~1.85 Ga continental collision between Eastern and Western blocks. Post-Cretaceous heating of the southern section is indicated by high temperatures (>1000ºC) recorded in peridotites from the 4 Ma Hebi suite, which are significantly higher than the temperatures recorded in peridotites from the nearby Early Cretaceous Fushan suite (<720ºC), and likely reflects significant lithospheric thinning after the Early Cretaceous. Combining previous Os isotope results on mantle xenoliths from the eastern North China Craton with the new data, it appears that lithospheric thinning and replacement may have evolved from east to west with time, commencing before the Triassic on the eastern edge of the craton, occurring during the Jurassic-Cretaceous within the interior, and post-dating 125 Ma on the westernmost boundary.

4.1 Introduction

Xenolithic peridotites transported to the surface by lavas provide information about the deep lithospheric mantle at the time of eruption. Rhenium-Os isotopic systematics

can potentially date melt depletion events in the peridotites via Os model ages (e.g., Walker et al., 1989; Rudnick and Walker, 2009). Assuming that lithosphere formation is coincident with melt depletion, Os model ages may be used to determine the age of the lithospheric mantle. In this way, the age of lithospheric mantle can be mapped (e.g., Pearson et al., 1995a) and may provide insights into the tectonic assembly and structure of the continents.

The Late Archean to Paleoproterozoic interval (between 2.5 and 1.8 Ga) marks the assembly of the Paleoproterozoic (2.1-1.8 Ga) Columbia supercontinent (e.g., Rogers and Santosh, 2003) and is recorded in the tectonic evolution of the North China Craton (e.g., Kusky and Li, 2003; Zhao et al., 2005; Kusky et al., 2007a; Kusky and Santosh, 2009). Understanding this portion of the geologic history of the North China Craton provides insights into the configuration of the Paleoproterozic Columbia supercontinent.

However, the history for the Archean-Paleoproterozoic amalgamation of the North China Craton remains controversial (e.g., Kusky and Li, 2003; Zhao et al., 2005; Kusky, 2011, and references therein). One model suggests that the Eastern and Western blocks collided at 1.85 Ga to form the Trans-North China Orogen, which runs north to south in the central portion of the craton (Fig. 4-1a), and marks the final amalgamation of the North China Craton (e.g., Zhao et al., 2005). A second model proposes that the Eastern and Western blocks collided at 2.5 Ga and that this event was followed by a major 1.8-1.9 Ga continent-continent collision

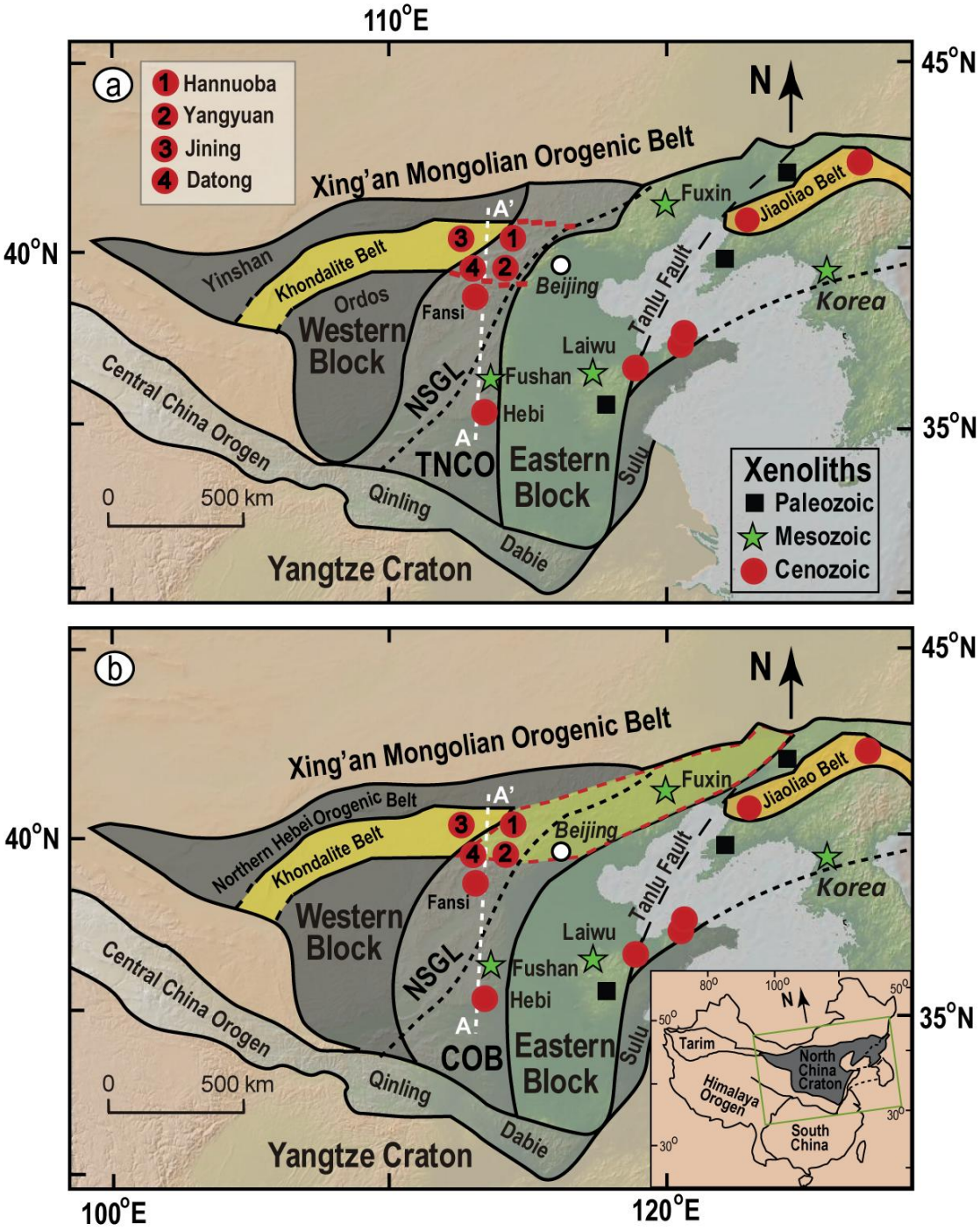

Fig. 4-1

Fig. 4-1. Tectonic sketch map of the North China Craton composed of the Eastern Block, Western Block, and the central region (modified from Fig. 2-1). In panel a, the central region is called "Trans-North China Orogen (TNCO)" formed between the Eastern and Western blocks at ~1.85 Ga (modified from Zhao et al., 2005). In panel b, the central region is called "Central Orogenic Belt (COB)" formed between the Eastern and Western blocks at ~2.5 Ga (modified from Kusky and Li, 2003). The

Khondalite Belt is a Paleoproterozoic, nearly east-west trending metamorphic belt in the Western Block that formed earlier than the TNCO (e.g., Zhao et al., 2005; panel a), while Kusky and Li (2003) suggest that this belt, which formed after the COB, extends eastwards (panel b), representing the final amalgamation of the craton. Mantle xenolith localities shown as squares (Paleozoic eruption age), stars (Mesozoic eruption age), and circles (Cenozoic eruption age). The NSGL is the North-South Gravity Lineament (Griffin et al., 1998). The profile A-A' is marked for the construction of the age structure of crust and underlying lithospheric mantle in Fig. 4-9.

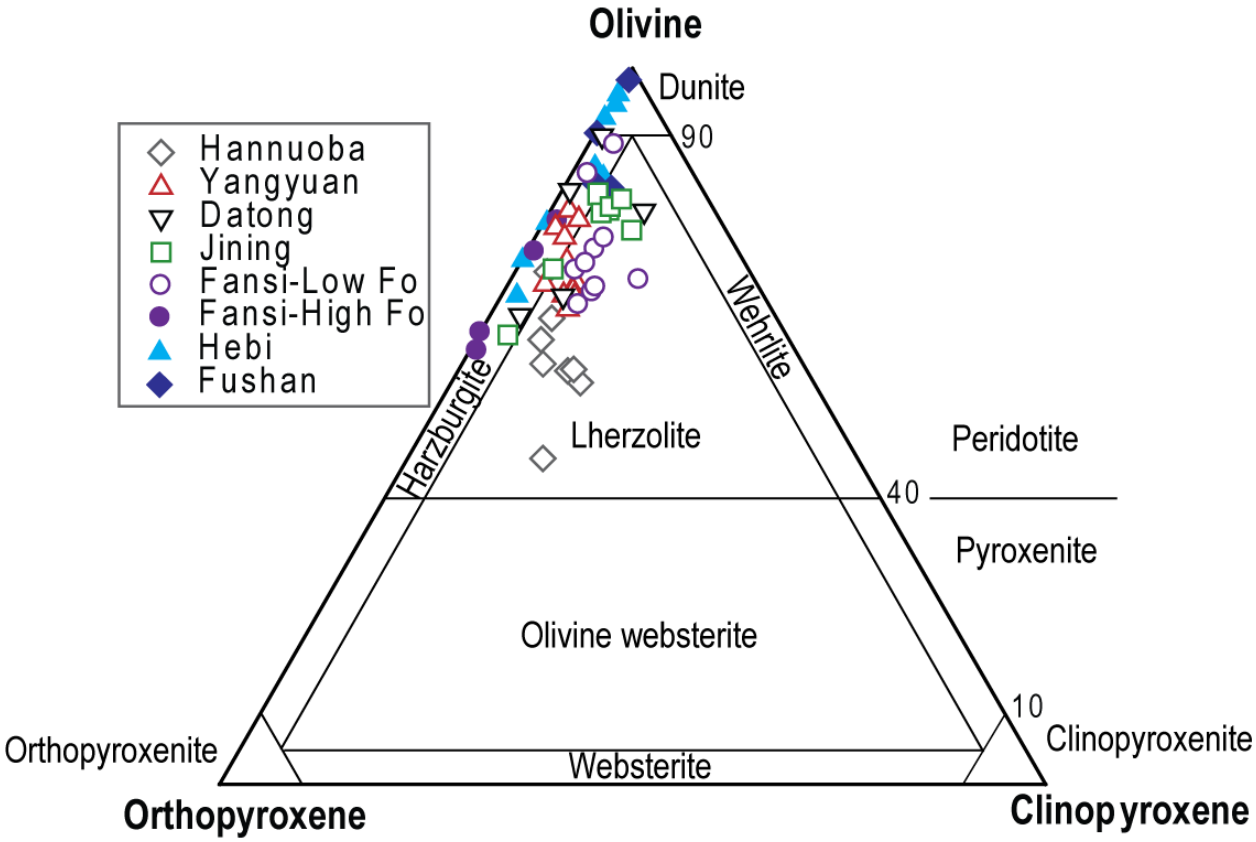

Fig. 4-2. Petrographic classification of the peridotites, based on proportions of olivine and pyroxene. Data sources in addition to this study: Hannuoba (Rudnick et al., 2004), and Fushan (Xu et al., 2010).

along the northern margin during formation of the Columbia supercontinent (Fig. 4-1b; Kusky and Li, 2003; Kusky et al., 2007a). The critical distinction between these two models lies in the interpretation of a 1.8-1.9 Ga granulite facies metamorphic event in the central North China Craton and a Late Archean ophiolitic complex in the eastern North China Craton.

Here, I report Re-Os model ages, as well as comprehensive petrography, major and trace element geochemistry for 99 xenolithic peridotites (including 67 new data supplemented by 32 analyses from previous studies; Gao et al., 2002; Becker et al., 2006; Liu et al., 2010) from seven localities (i.e., Hannuoba, Yangyuan, Datong, Jining, Fansi, Hebi, and Fushan) covering a broad area in the central North China Craton (Fig. 4-1). I show that Os isotopes of peridotites have the ability to map deep lithospheric boundaries. The data obtained in this study provide unique constraints on the Late Archean-Paleoproterozoic tectonic framework of the North China Craton, as well as the timing of Mesozoic-Tertiary lithospheric thinning in this region.

4.2 Samples

The xenoliths studied here come from a wide area in the central North China Craton (Fig. 4-1). Samples from the northern section (Hannuoba, Yangyuan, and Datong (N40^{0}06.387', E 113^{0}37.784')), as well as the more southerly Fansi (N 39^{0}14.655', E113^{0}11.781'; also spelled "Fanshi" by some authors, e.g., Tang et al., 2008), are all carried in Tertiary alkali basalts that erupted to the west of the North-South Gravity Lineament (Fig. 4-1). Samples from the southern region (Hebi (N35^{0}50.350', E114^{0}07.284') and Fushan (N36^{0}43.417', E113^{0}45.550')), lie to the east of this lineament. Fushan hornblende-diorites erupted in the Early Cretaceous (~125 Ma; Xu et al., 2010), whereas olivine nephelinites at nearby Hebi erupted much

later, at 4 Ma (Liu et al., 1990). Jining is located in the Khondalite Belt of the Western Block, where xenolith-bearing alkali basalts erupted in the Tertiary period (Zhang and Han, 2006).

The xenoliths investigated here are predominately protogranular to equigranular, coarse- to medium-grained, garnet-free spinel lherzolites and harzburgites, as well as rare dunites. The modal mineralogy of these samples (Supplemental Material Table S4-1) is illustrated in Fig. 4-2. Petrography and whole-rock compositions of many of these xenolith suites have been previously described (Hannuoba: Song and Frey, 1989; Chen et al., 2001; Rudnick et al., 2004; Tang et al., 2007; Choi et al., 2008; Zhang et al., 2009; Yangyuan: Y.G. Xu et al., 2008; Liu et al., 2010; Fansi: Tang et al., 2008; Hebi: Zheng et al., 2001; and Fushan: Xu et al., 2010). A brief description of each suite is summarized in Table 4-1 and petrographic descriptions of the samples investigated here are provided in Supplemental Material (Table S4-1).

I briefly review the petrology of each suite in order from north to south (Table 4-1). Peridotites from Hannuoba are mostly fresh and large (10-60 cm in diameter), with good preservation of sulfides, both as inclusions in silicates, and interstitial phases at grain boundaries (e.g., Rudnick et al., 2004; X.S. Xu et al., 2008; Liu et al., 2010). Petrology and whole-rock compositions of all Hannuoba samples, including the Re-Os and HSE data, from the studies of Gao et al. (2002), Rudnick et al. (2004), Becker et al (2006) and Liu et al. (2010).

Table 4-1. Petrology of the peridotite suites examined in this study

Locality	n	Lithology		Size	Freshness	Sulfide preservation	Whole rock Al_2O_3	Average Fo of olivine
Hannuoba	16	lherzolite with rare harzburgite		10-60 cm	fresh	good	1.2-3.8 %	90.5 ± 0.8
Yangyuan	22	lherzolite and harzburgite		4-35 cm	fresh	poor	0.9-4.0 %	90.9 ± 0.6
Datong	7	lherzolite and harzburgite		<3 cm	fresh	poor	1.6-3.7 %	91.0 ± 0.6
Jining	13	lherzolite and harzburgite		4-9 cm but thin	highly weathered	poor	0.9-6.5 %	90.4 ± 0.8
Fansi	20	low Fo	lherzolite with rare harzburgite	3-8 cm	fresh to moderately weathered	poor	1.1-3.9 %	90.1 ± 0.7
		high Fo	harzburgite				0.8-2.0 %	92.0 ± 0.3
Hebi	12	lherzolite and harzburgite with rare dunite		<4 cm	fresh	good but rare	0.9-2.2 %	92.0 ± 0.9
Fushan	9	lherzolite and harzburgite with rare dunite		3-7 cm	moderately weathered	N/A	0.2-1.5 %	92.0 ±0.7

Note: n, the number of samples; lithology terms as in Fig. 4-2; size indicates the maximum length of the specimen; and average Fo of olivine ±1 σ. Data sources provided in text.

Like Hannuoba, peridotites from Yangyuan are generally fresh and large, with maximum diameters typically greater than 50 cm (Y.G. Xu et al., 2008; Liu et al., 2010). However, Yangyuan peridotites are characterized by poor preservation of sulfides, to the point where most thin sections contain no sulfides (Liu et al., 2010). All Yangyuan samples described here were previously described in Y.G. Xu et al. (2008) or Liu et al. (2010).

Peridotites from Datong are generally fresh, with poor preservation of sulfides. Xenoliths are small, ranging from less than a centimeter to several centimeters across. Only five relatively large samples were prepared for whole-rock major element and HSE analyses. Data for two additional samples, analyzed only for Re-Os isotopic systematics, are reported here.

Like Datong samples, peridotites from Jining are relatively small (<10 cm). In addition, Jining samples are moderately to heavily altered along grain boundaries, with poor preservation of sulfides. The small size of the samples prevented us from making sufficient powder for whole-rock trace element analysis.

Peridotites from Fansi are generally moderately altered and relatively small (<15 cm in diameter), with poor preservation of sulfides. Several of the samples studied here were accessed from their lava host using a rock drill. Most samples have protogranular to porphyroclastic textures, but a few lherzolites show a corona texture, where spinel breaks down into tiny grains at grain boundaries. Three additional samples, analyzed only for Re-Os isotopic systematics, are reported here.

Peridotites from Hebi are small (only a few centimeters across; many of them were sampled by a rock drill from the lavas), fresh, and generally coarse-grained,

harzburgites with a few dunites. In contrast to the study of Zheng et al. (2001), who described five spinel lherzolites with olivines of low forsterite contents (i.e., Fo = molar $Mg/(Mg+Fe^{2+})$ x 100 = 88.6-91.4) and fertile calculated whole-rock compositions, none of the Hebi peridotites collected here were fertile lherzolites. Only a few sulfides are present as inclusions in silicates (Zheng et al., 2007; this study).

Xenoliths from Fushan are dominated by refractory harzburgites and cpx-poor lherzolites with a few chromite-bearing dunites. Hydrous minerals (e.g., phlogopite and amphibole), may occur in harzburgite and cpx-poor lherzolites, and were interpreted as secondary phases after original mantle partial melting (Xu et al., 2010). Spinel grains that are in contact with phlogopite or amphibole commonly break down into small grains of spinel or chromite (Xu et al., 2010). All Fushan sample powders are from the study of Xu et al. (2010).

In addition to the 11 Re-Os and HSE analyses previously reported for the Hannuoba peridotites (Gao et al., 2002; Becker et al., 2006), I have analyzed new elemental and isotopic data for 91 peridotitic samples (Table 4-1), including an additional eight from Hannuoba, 22 from Yangyuan, seven from Datong, 13 from Jining, 20 from Fansi, 12 from Hebi, and nine from Fushan.

4.3 Analytical methods

4.3.1 Sample selection and preparation

Mineral mounts of olivine from each of the xenoliths collected at each locality were analyzed in order to assess the range in degree of melt depletion exhibited by the peridotite suites. Olivine compositions were measured using a JEOL 8900 EPMA at UMd. The work parameters and calculation method are provided in the section 3.3.1

of Chapter Three. About one to two spots per olivine grain, and two to three grains of olivines were analyzed per sample. Based on the forsterite contents (Fo) of olivines, a representative suite of peridotites, chosen to span the range in Fo contents, was selected from each locality for further elemental and isotopic analyses. Portions of the samples were powdered for whole rock analyses using the sequent combination of a jar crusher, a shatter box, and a disk mill.

4.3.2 Mineral compositions

Major element compositions of olivine, orthopyroxene, clinopyroxene (which may be absent in some harzburgites and dunites) and spinel were determined on polished thin sections by EPMA at UMd, using the parameters and methods described in the section 3.3.1 of Chapter Three. About two spots per grain, including cores and rims, from three to five grains of each phase were measured for each sample.

4.3.3 Whole rock major and trace elements

Whole rock major element compositions were determined by X-ray fluorescence (XRF) on fused glass disks made from powders (see Boyd and Mertzman (1987) for detailed protocols) at Franklin and Marshall College, United States, or Northwest University, China. Analytical precision and accuracy was typically better than 1% for major elements of concentrations greater than 0.5% and better than 5% for the remaining major elements, as determined from data for international reference rocks analyzed by these laboratories (e.g., Boyd and Mertzman, 1987; Rudnick et al., 2004).

Whole rock trace element compositions were determined using an inductively coupled plasma mass spectrometry (ICP-MS; Agilent 7500a) after acid digestion of powders in Teflon bombs at Northwest University, China. Four reference samples

(AGV-2, BHOV-2, BCR-2 and RGM-1) were analyzed during the course of these analyses. The precision and accuracy was generally better than 10%, with a majority of elements better than 5% relative to the reference values (Rudnick et al., 2004). Exceptions are for a few elements such as Cr and Sn in BCR-2 (up to 26% difference) and Ni and Mo in RGM-1 (up to 31% difference).

4.3.4 Osmium isotopes and HSE abundances

The analytical procedures are detailed in the section 3.3.4 of Chapter Three. Blank corrections for Os, Ir, Ru, Pt, and Pd are negligible (less than 0.2 %) for most samples, except for those with very low HSE concentrations (five Hebi samples (HB-02, HB-09, HB-12, HB-21-2, and HB-22), and three Fushan samples (FS6-19, FS6-29, and FS6-56), e.g., having Os generally less than 0.2 ppb), while the Re blank constitutes 0.3 to 20 % of the total Re in all samples.

4.4 Results

4.4.1 Mineral chemistry and equilibration temperatures

The average forsterite contents of olivines analyzed in grain mounts for xenoliths from all localities (381 xenoliths in total, Supplemental Material Table S4-2) are plotted as histograms in Fig. 4-3. The olivine compositions in the peridotites from the northern region (Hannuoba, Yangyuan, and Datong), as well as Jining, are characterized by similar ranges in Fo (i.e., 87.4-92.2 with an average of 90.5±0.5 (1σ)), reflecting relatively fertile compositions. By comparison, olivines in the peridotites from the southern region (Hebi and Fushan) generally have higher Fo (88.3-92.9 with an average of 91.9±0.9; Zheng et al., 2001; Xu et al., 2010; this study)

that is similar to, or slightly lower than those of olivines in cratonic peridotites from the eastern North China Craton (Fig. 4-3), reflecting the more refractory

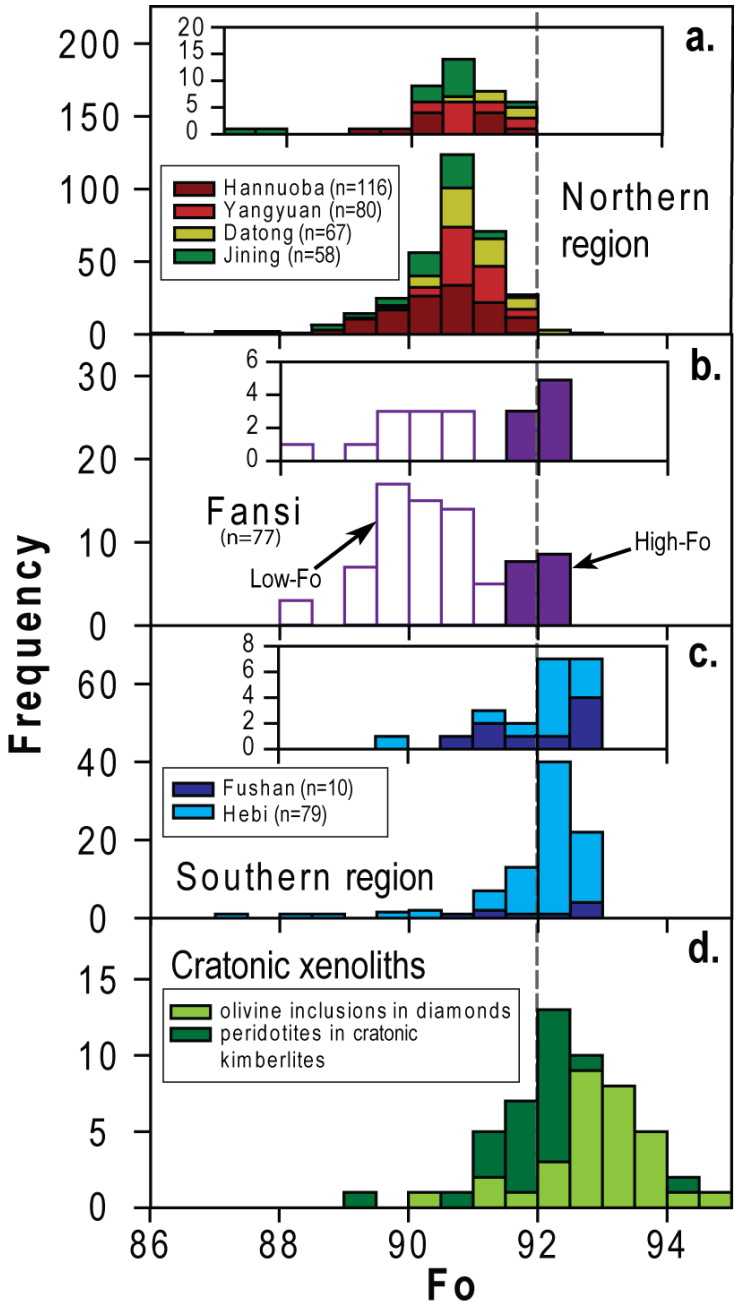

Fig. 4-3. Histograms of average forsterite contents (Fo of olivine = mol $Mg/(Mg+Fe^{2+})$) of olivines from individual peridotite xenoliths and diamond inclusions. a. peridotites from Hannuoba (Song and Frey, 1989; Chen et al., 2001; Rudnick et al., 2004; Tang et al., 2007; this study), Yangyuan (this study), and Datong, which are carried in Tertiary basalts in the northern region of the central North China Craton, as well as Jining, which lies in the Khondalite Belt of the Western Block; inset panel (as well as in b and c) represents the Fo distribution of the samples selected for further elemental and isotopic analyses; b. peridotites from Fansi showing two populations divided into low- and high-Fo groups; c. peridotites from Fushan (Xu et al., 2010) and Hebi (data for Hebi from this study and Zheng et al., 2001) from the southern region; and d. xenolithic peridotites and olivine inclusions in diamonds from Ordovician kimberlites in the eastern North China Craton (data from Zheng, 1999). The vertical dashed line marks a Fo value of 92.

subcontinental mantle that underlies this region. Fansi peridotites show a bimodal distribution of Fo contents (Fig. 4-3) (as in Tang et al., 2008). The low-Fo group (88.0-91.6 with an average of 90.1±0.7, 1σ) reflects relatively fertile mantle, similar to that present in the other northern localities. By contrast, the high-Fo group (91.6-92.5 with an average of 92.0±0.3, 1σ) represents refractory mantle, similar in composition to peridotites from Hebi and Fushan in the south. I selected a sub-suite of peridotites from each locality (7-20 samples) that span the observed range of Fo (see inset panels of Fig. 4-3), taking into account size and freshness, for further elemental and isotopic analyses.

Major element compositions of minerals of the selected samples measured in polished thin sections are given in Supplemental Material Table S4-3. Olivine compositions analyzed in polished thin sections are within uncertainties of those measured on mineral mounts. The Cr# (i.e., molar Cr/(Cr+Al) x 100) of spinels from these peridotites correlate with the Fo contents of olivines; the high-Fo samples generally have higher Cr# (Fig. 4-4), reflecting melt depletion (Arai et al., 1994, and references therein). A few samples fall off the main trend, suggesting disequilibria between olivine and spinel. This includes two samples from Fansi and one from Jining from this study, four Hebi samples from the published data of Zheng et al. (2001), including the only three samples from their “low Mg#” group for which both spinel and olivine compositions are published, and one Fushan sample from the published data of Xu et al. (2010).

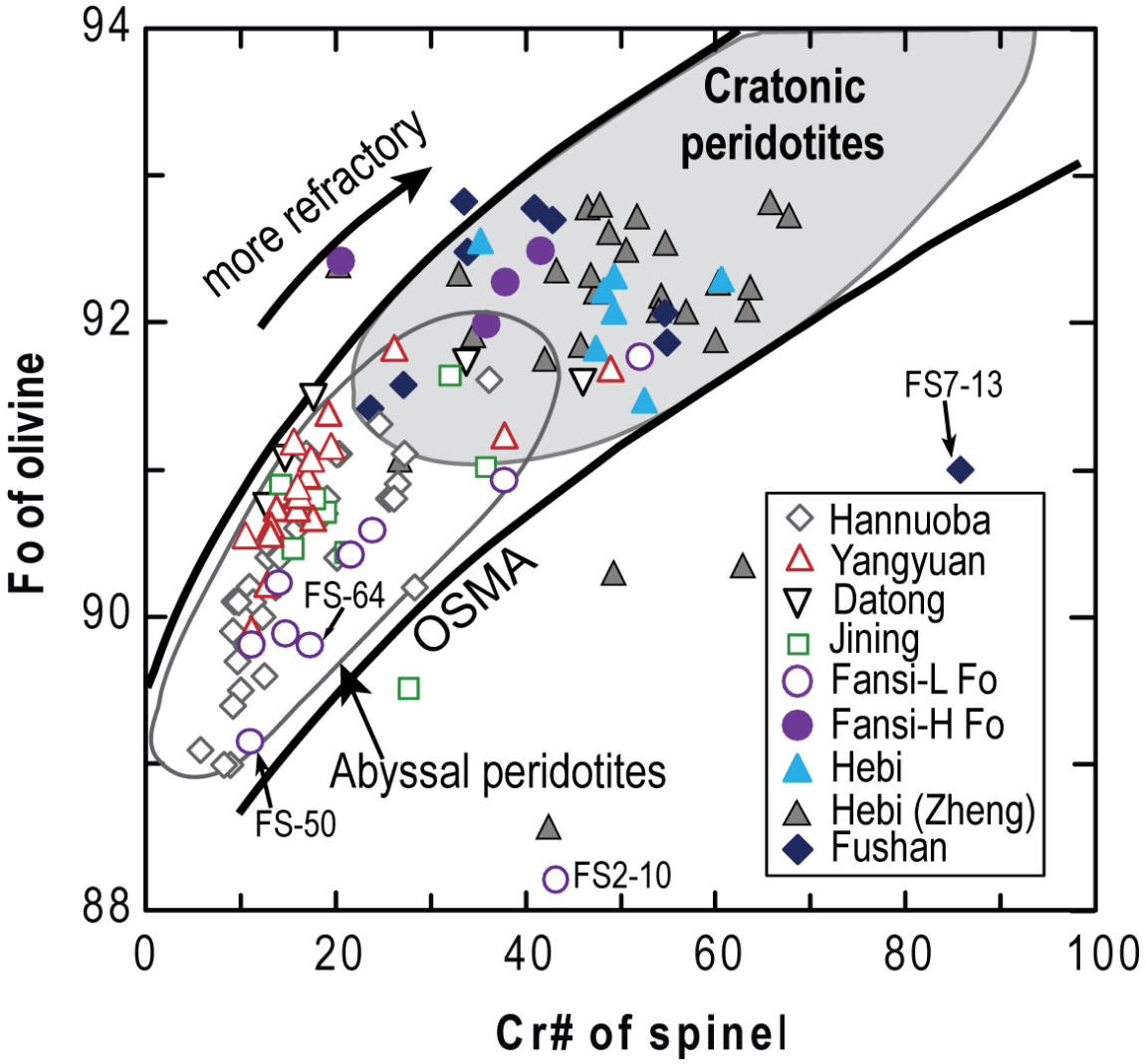

Fig. 4-4. Cr# (mol Cr/(Cr+Al)x100) of spinels versus Fo of coexisting olivines in peridotite xenoliths from Hannuoba (data from Chen et al., 2001; Rudnick et al., 2004), Yangyuan (data from Liu et al., 2010), Datong, Jining, Fansi (including Fansi L(low)-Fo and Fansi H(high)-Fo), Fushan (data from Xu et al., 2010), and Hebi (data from Zheng et al., 2001 are shown as gray triangles). Gray field encompasses data for typical cratonic spinel peridotites (Pearson and Wittig, 2008, and references therein). Abyssal peridotites: Arai et al., 1994, and references therein. OSMA: olivine-spinel mantle array (after Arai et al., 1994, and references therein).

Equilibrium temperatures of the peridotites were calculated using the two-pyroxene thermometer of Brey and Köhler (1990) and assuming a pressure of 1.5 GPa (close to the minimum depth (~50 km) of lithospheric mantle, since pressure cannot be determined in the absence of garnet) (Supplemental Material Table S4-4). The estimated equilibrium temperatures of peridotites from Hannuoba, Yangyuan, Datong and Jining are similar at 980-1060ºC, 840-1100ºC, 1060-1100ºC, and 850-990ºC, respectively, although those from Yangyuan and Jining range to lower temperatures than peridotites from the other localities. The equilibrium temperatures of the low-Fo Fansi peridotites (880-1100 ºC) overlap with those of the Yangyuan peridotites, while the high-Fo Fansi peridotites exhibit a relatively narrow range of equilibrium temperatures (960-1040 ºC), overlapping that seen in their low-Fo counterparts. Consistent with previous studies (Zheng et al., 2001), the Hebi peridotites show a narrow range in equilibrium temperatures (1020-1090ºC) that are significantly higher than those of the Fushan peridotites (620-720 ºC) (Xu et al., 2010). The Fushan peridotites exhibit the lowest temperatures of all samples. There is no correlation between equilibrium temperature and major element composition in any of the suites.

4.4.2 Whole rock major and trace elements

Major and/or trace element analyses of xenoliths considered in this study are provided in Supplemental Material Table S4-4 and S4-5); trace element data are absent for Datong and Jining peridotites due to the limited sample powder available.

Peridotites from the northern region show overlapping and large ranges in major element compositions and show good correlations on plots of MgO vs. Al_2O_3 or CaO,

with a few plotting in the field of typical cratonic peridotites (Fig. 4-5). Such correlations between MgO and Al_2O_3 or CaO are commonly interpreted to reflect melt depletion (Pearson et al., 2003, and references therein), but can also be produced via refertilization (e.g., Le Roux et al., 2007). The majority of the northern peridotites are relatively fertile compared to cratonic peridotites, consistent with the low Fo of olivine and Cr# of spinel. Jining peridotites have a similar range of MgO (39.6-45.7 %) and CaO (0.4-2.4 %) compared to the other northern suites; however their Al_2O_3 contents range from 0.9 % to higher than the PM (~4.4 %; McDonough and Sun, 1995). The abnormally high Al_2O_3 contents are inconsistent with calculated whole-rock compositions based on mineral modal abundances (Supplemental Material Table S4-4), and suggest that such high Al_2O_3 contents are an analytical artifact produced during processing of these rather small and weathered peridotites.

By contrast, peridotites from the southern region are generally depleted in Al_2O_3 (0.9-2.2 % and 0.2-1.5 % for Hebi and Fushan, respectively) and CaO (0.4-2.2 % and 0.3-1.1 %), and are rich in MgO (44-47 % and 44-48 %) (Xu et al., 2010; this study). Most of them plot in the field of cratonic peridotites (Fig. 4-5).

Xenoliths from Fansi, the southernmost locality in the northern region, show a mixed population. The low-Fo group of Fansi peridotites are compositionally similar (MgO: 37-45 %, Al_2O_3: 1.1-3.9 %, and CaO: 0.8-3.4 %) to those from the other northern suites, and distinct from the high-Fo group of Fansi peridotites (MgO: 44-47 %, Al_2O_3: 0.9-2.0 %, and CaO: 0.4-1.4 %) that are refractory, like the Hebi and Fushan peridotites.

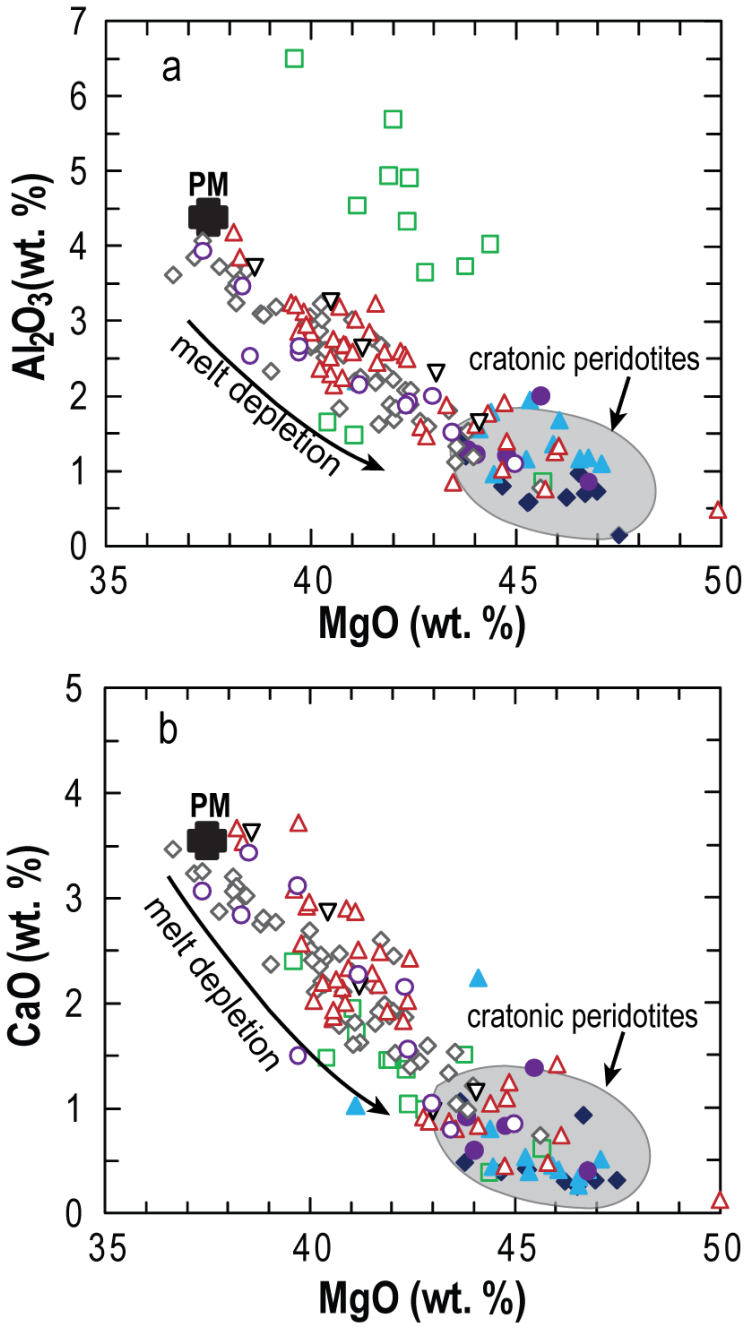

Fig. 4-5. Whole rock MgO versus Al_2O_3 (a) and CaO (b) (in wt. %) of peridotites from Jining (the majority of samples from this suite show abnormally high Al_2O_3), Datong, Hannuoba (Song and Frey, 1989; Chen et al., 2001; Rudnick et al., 2004; Choi et al., 2008; Zhang et al., 2009), Yangyuan (Y.G. Xu et al., 2008; Liu et al., 2010), Fansi, Fushan (Xu et al., 2010), and Hebi. Symbols as in Fig. 4-4. Melt depletion typically results in low Al_2O_3 and CaO and high MgO, which is delineated by the melt depletion trends in the plot. PM: primitive mantle (McDonough and Sun, 1995). Gray field shows typical cratonic mantle (Pearson and Wittig, 2008, and references therein).

The data described above reflect a spatial compositional dichotomy in the lithospheric mantle underlying the central North China Craton. Peridotites from the northern region, including Jining, are relatively fertile, while those from the southern region are more refractory in composition, similar to cratonic peridotites. Peridotites from Fansi, located in the southernmost position within the northern region, include both fertile and refractory compositions.

Whole rock trace element concentrations are plotted in Supplemental Material (Figs. S4-1 and S4-2). The peridotites in this study show significant variations in both absolute concentrations of trace elements and chondrite-normalized rare earth element (REE) patterns. The Hannuoba peridotites are characterized by total REE concentrations of 1.7-17.5 ppm, with an average of 5.1 ppm (Rudnick et al., 2004). Their REE patterns range from light REE (LREE) enriched to LREE depleted, with relatively flat heavy REE (HREE) (Figs. S4-1a and S4-2a). The Yangyuan peridotites display lower total REE (0.3-4.7 ppm, with an average of 1.9 ppm), but show similar variation in REE patterns as the Hannuoba peridotites (Fig. S4-1b). Both Hannuoba and Yangyuan peridotites generally show somewhat chaotic patterns in the primitive mantle-normalized trace element diagrams (Fig. S4-2a and b), which likely reflects the comparable influence of partial melting and metasomatism on these rocks in lithophile elements.

By comparison, the Fansi peridotites exhibit somewhat higher total REE abundances (3.0-61.3 ppm, with an average of 11.0 ppm) than Hannuoba and Yangyuan peridotites. The low- and high-Fo Fansi samples show similar REE

patterns, with uniformly enriched LREE and flat HREE (Fig. S4-1c). One sample (FS-36), however, has high HREE, low MREE and strong enrichment in La and Ce; in this respect, it is similar to some of the Hannuoba peridotites (e.g., DMP-60; Fig. S4-1a). The low-Fo Fansi peridotites display negative anomalies of high field strength elements (HFSE), such as Zr, Hf, Nb and Ta, a typical feature of mantle partial melting (Norman, 1998), while the high-Fo Fansi samples do not. This contrasting feature may reflect that the lithophile elements in refractory peridotites are more easily affected by metasomatic processes than fertile samples. Both Hebi and Fushan peridotites are characterized by low total REE abundances (1.1-11.9 ppm, an average of 3.8 ppm for Hebi, and 0.6-5.2 ppm, an average of 2.3 ppm for Fushan), strong LREE enrichment and a characteristic concave upwards HREE pattern (Fig. S4-1 d and e). Similar to the high-Fo Fansi peridotites, the Hebi peridotites generally do not show negative anomalies of HFSE, while the Fushan peridotites have patterns that vary from negative to positive HFSE anomalies.

In the Hebi suite, dunite HB-24 has low Fo (89.3), high Fe_2O_3 (10.6 %) and low Al_2O_3 (0.96 %) and CaO (0.44%), which are likely indicative of Fe enrichment, and has the lowest $^{187}Os/^{188}Os$ in the suite (0.1125). This sample has the most abundant REE among the Hebi suite, which were likely enriched in the same process as Fe. Accordingly, the negative Ce anomaly (Fig. S4-1 d) might reflect the presence of Ce^{4+} (Ionov et al., 1995), recording an oxidized environment during Fe enrichment. Importantly, the Fe enrichment event apparently did not significantly change the Os isotopic composition of the whole rock. In addition, the only three Hebi samples in the "low Fo" group of Zheng et al. (2001) plot off the correlation defined by the Fo and Cr# of spinel for the rest of the samples (Fig. S4-5); the calculated whole-rock Al

contents of these samples are in the range of the high-Fo group, although the calculated CaO appears to be higher. These observations suggest that the Fo of olivines of these low-Fo samples are simply due to recent disequilibrium exchange. Thus, the few low-Fo Hebi samples reported in Zheng et al. (2001) may not necessarily represent Phanerozoic mantle, but rather Fe-enriched Archean mantle.

4.4.3 Osmium isotopes and HSE abundances

Whole rock Os isotopic compositions and HSE abundances are reported in Table 4-2. For comparison, previously published data from our group for Hannuoba (Gao et al., 2002; Becker et al., 2006; Liu et al., 2010) and Yangyuan (Liu et al., 2010), are included.

4.4.3.1 Hannuoba peridotites

Hannuoba peridotites display high total HSE abundances (ΣHSE = Os + Ir + Ru + Pt + Pd + Re) ranging from 17 to 32 ppb, with Ir ranging from 2.5 to 4.3 ppb; Becker et al., 2006; Liu et al., 2010) and patterns that are similar to that of model Primitive Upper Mantle (PUM) (Fig. 4-6a). No obvious Os-Ir fractionation appears in the Hannuoba suite. The Pd/Ir ratios ($(Pd/Ir)_N$ = 0.7 to 1.5), $^{187}Re/^{188}Os$ (0.045-0.44) and $^{187}Os/^{188}Os$ (0.116-0.128) are all well correlated with melt depletion indices, such as Al_2O_3 (Gao et al., 2002; Liu et al., 2010).

4.4.3.2 Yangyuan peridotites

Yangyuan peridotites have significantly lower HSE concentrations (ΣHSE: 3 to 16 ppb, and Ir: 0.7 to 3.0 ppb) (Liu et al., 2010; this study) compared to Hannuoba peridotites. They are characterized by significant Os, Pd and Re depletions, relative to Ir (Fig. 4-6b; $(Pd/Ir)_N$ = 0.11 to 0.55; Liu et al., 2010), which are not likely to be

the result of partial melting, given their similarity in major element compositions to the Hannuoba peridotites. Their $^{187}Os/^{188}Os$ (0.115-0.126) is fairly well correlated with fertility indices such as Al_2O_3 (Liu et al., 2010).

4.4.3.3 Datong peridotites

Like Yangyuan peridotites, the Datong peridotites are characterized by relatively low HSE abundances (ΣHSE: 8 to 26 ppb, and Ir: 1.3 to 2.3 ppb). Despite the fact that only five samples were analyzed, these peridotites show a diverse range of HSE patterns (Fig. 4-6c). Sample DAT-15 has a HSE pattern similar to that of PUM. The HSE patterns of DAT-09 and DAT-30 are characterized by Re and platinum-like platinum group elements (PPGE: Pt and Pd) depletions relative to iridium-like platinum group elements (IPGE: Os, Ir and Ru). The remaining samples (DAT-05 and DAT-31) have variably positive Pt anomalies. These samples, together with the two additional samples analyzed only for Re-Os isotope systematics, are characterized by $^{187}Os/^{188}Os$ ranging from 0.115 to 0.126, identical to the range exhibited by Yangyuan peridotites (Table 4-2).

4.4.3.4 Jining peridotites

These are characterized by relatively low and variable HSE abundances (ΣHSE: 1 to 16 ppb, and Ir: 0.2 to 3.4 ppb). Large differences are seen in HSE abundances between some replicates, which are likely due to a nugget effect in these small samples; however, the HSE pattern shapes for replicates are similar (Table 4-2). Two types of HSE patterns are identified (Fig. 4-6d): one with nearly chondritic Os/Ir ratios, and the other with clearly subchondritic Os/Ir ratios. A typical member of the

Table 4-2. Highly siderophile element abundances, Os isotope compositions, Fo and Cr# of peridotites from the North China Craton

Sample	t	Os	Ir	Ru	Pt	Pd	Re	ΣHSE	$^{187}Re/^{188}Os$	$^{187}Os/^{188}Os$	$^{187}Os/^{188}Os_i$	Al_2O_3	Fo[c]	Cr#[d]	T_{RD}[e]	T_{MA}[e]
	Ma	ppb	ppb	ppb	ppb	ppb	ppb	ppb				%			Ga	Ga
Hannuoba[a]																
DMP 04	22	3.76	3.56	7.41	6.62	4.96	0.211	26.5	0.271	0.1229	0.1228	2.29	91.1	16.8	0.6	1.9
DMP 19	22	4.13	4.34	8.54	8.53	6.66	0.181	32.4	0.211	0.1200	0.1199	1.91	91.3	24.5	1.1	2.2
DMP 19R	22	3.76	4.26	8.33	7.79	6.66	0.169	31.0	0.216	0.1200	0.1199				1.0	2.2
DMP 25	22	3.23	2.49	5.71	3.55	2.13	0.030	17.1	0.045	0.1166	0.1166	1.61	91.6	36.0	1.5	1.7
DMP25R	22	2.70	2.27	5.14	3.46	n.d.	0.032	13.6	0.056	0.1168	0.1168				1.5	1.7
DMP 41	22	2.91	3.00	5.82	5.50	4.25	0.172	21.7	0.285	0.1233	0.1232	2.76	90.4	12.8	0.6	1.9
DMP 51	22	3.01	3.06	6.37	5.21	4.18	0.130	22.0	0.208	0.1231	0.1230	1.96	91.1	20.2	0.6	1.2
DMP 56	22	3.55	3.21	6.34	6.60	5.69	0.257	25.6	0.35	0.1275	0.1274	3.49	89.9	9.1	-0.1	-0.6
DMP 58	22	3.78	3.59	7.33	6.96	5.86	0.190	27.7	0.242	0.1254	0.1253	3.16	90.2	10.8	0.3	0.6
DMP 60	22	4.00	3.59	7.24	7.31	6.21	0.303	28.7	0.365	0.1263	0.1261	3.67	90.1	9.3	0.1	1.2
DMP 67c	22	1.66	1.27	1.58	3.00	1.74	0.036	9.3	0.10	0.1224	0.1224	3.78	89.5	9.9	0.7	0.9
DA20-02	22	3.63	3.41	7.06	7.18	6.24	0.333	27.9	0.443	0.1254	0.1252	3.12	90.1	n.d.	0.3	-2.5
DA20-02R	22	3.64	3.54	7.05	7.10	5.90	0.349	27.6	0.461	0.1255	0.1253				0.2	-
DA20-05	22	3.45	3.59	7.42	7.44	5.55	0.240	27.7	0.336	0.1233	0.1232	2.71	91.1	n.d.	0.6	3.3
DA20-05R	22	3.23	3.67	7.47	7.25	5.35	0.231	27.2	0.344	0.1236	0.1235				0.5	3.4
DA20-16	22	3.60	2.62	6.41	5.52	4.91	0.054	23.1	0.073	0.1238	0.1237	1.20	89.6	n.d.	0.5	0.6
DA20-17	22	3.17	3.83	7.76	6.9	5.74	0.094	27.5	0.14	0.1232	0.1231	2.40	90.5	n.d.	0.6	0.9
DA20-19	22	2.44	2.79	6.04	5.37	4.71	0.137	21.5	0.271	0.1270	0.1269	3.74	89.6	n.d.	0	-
DA20-19R	22	2.39	2.94	6.02	6.32	4.43	0.139	22.2	0.279	0.1272	0.1270				0	-
Yangyuan[b]																
YY-04	30	1.27	2.50	4.79	2.76	0.89	n.d.	12.2		0.1150		1.63	92	26.2	1.8	-
YY-04R	30	1.18	2.54	4.40	2.78	0.84	0.019	11.8	0.076	0.1152	0.1151				1.8	2.1
YY-08	30	0.85	2.39	4.59	3.20	1.62	0.023	12.7	0.13	0.1261	0.1260	2.97	90.5	13.0	0.2	0.2
YY-09	30	0.50	1.86	3.79	2.64	0.98	0.015	9.8	0.15	0.1216	0.1216	3.04	90.9	14.0	0.8	1.3
YY-11	30	0.21	0.74	1.64	0.63	0.19	0.005	3.4	0.1	0.1212	0.1211	1.77	90.8	13.4	0.9	1.2

Table 4-2 *continued*

Sample	t	Os	Ir	Ru	Pt	Pd	Re	ΣHSE	$^{187}Re/^{188}Os$	$^{187}Os/^{188}Os$	$^{187}Os/^{188}Os_i$	Al_2O_3	Fo[c]	Cr#[d]	T_{RD}[e]	T_{MA}[e]
	Ma	ppb	ppb	ppb	ppb	ppb	ppb	ppb				%			Ga	Ga
YY-13	30	0.39	1.02	2.08	1.42	-	0.014	4.9	0.17	0.121	0.1209	2.44	90.9	17.8	0.9	1.5
YY-13R	30	0.35	0.98	2.03	1.38	0.51	0.010	5.3	0.14	0.1212	0.1211				0.9	1.3
YY-22	30	0.93	2.98	4.81	5.07	1.83	0.045	15.7	0.23	0.1207	0.1206	2.45	91.2	17.2	1	2.3
YY-22R	30	1.15	2.98	5.03	5.27	1.87	0.047	16.3	0.2	0.1206	0.1205				1	1.9
YY-23	*30*	*0.92*	*2.38*	*4.02*	*3.86*	*0.82*	*0.028*	*12.0*	*0.15*	*0.1240*	*0.1240*	*3.06*	*90.8*	*16.1*	*0.5*	*0.7*
YY-26	30	1.07	2.64	4.41	2.94	0.6	0.103	11.8	0.462	0.1189	0.1187	3.08	90.7	13.3	1.2	-8.6
YY-26R	30	0.77	2.46	4.17	2.83	0.55	0.103	10.9	0.647	0.1197	0.1193				1.1	-1.8
YY-27	30	n.d.	1.92	4.21	2.93	0.93	0.018	10.0		n.d		2.87	90.2	11.4	-	-
YY-27R	30	1.14	2.10	4.57	3.64	0.97	0.015	12.4	0.065	0.1195	0.1194				1.1	1.3
YY-36	30	0.6	2.31	4.43	5.04	1.34	0.060	13.8	0.48	0.1219	0.1219	2.30	91.1	20.3	0.8	-3.8
YY-40B	30	0.47	0.83	1.69	5.27	1.37	0.031	9.7	0.31	0.1241	0.1241	2.80	91.2	14.8	0.4	2
YY-42	30	0.40	1.14	2.48	2.10	0.48	0.027	6.6	0.33	0.1256	0.1256	2.35	91	16.5	0.2	1.1
YY-45	30	1.12	1.57	2.62	3.16	0.37	0.022	8.9	0.1	0.1220	0.1220	2.44	90.8	16.4	0.7	1
YY-50	30	1.00	1.81	2.93	3.06	0.87	0.057	9.7	0.31	0.1261	0.1261	4.02	90.6	9.8	0.1	0.6
YY-51	30	2.34	2.93	6.18	2.47	0.39	0.009	14.3	0.02	0.1160	0.1160	1.12	91.6	48.8	1.6	1.7
YY-51R	30	2.21	2.79	5.88	2.99	0.41	0.007	14.3	0.01	0.1164	0.1164				1.6	1.6
YY-52	30	0.52	1.32	2.89	2.24	0.76	0.022	7.8	0.20	0.1235	0.1234	2.70	90.8	16.1	0.5	1.1
YY-58	30	0.51	1.82	3.32	2.96	1.09	0.024	9.7	0.23	0.1212	0.1211	2.40	91.7	19.4	0.9	2
YY-60	30	0.40	1.67	3.26	3.13	0.45	0.020	8.9	0.24	0.1208	0.1207	1.26	91.3	37.7	0.9	2.3
YYB-2	30	1.28	1.85	3.56	3.33	0.75	0.02	10.8	0.076	0.1186	0.1186	1.45	91.8	n.d.	1.3	1.5
YYB-4	30	0.74	2.67	5.25	4.67	1.82	0.061	15.2	0.39	0.1202	0.1200	2.15	91.9	n.d.	1.0	40
YYB-7	30	0.79	1.32	3.41	1.24	0.71	0.024	7.5	0.15	0.1153	0.1152	0.89	91.8	n.d.	1.7	2.7
YG-18	30	1.78	2.83	5.01	2.68	0.72	0.017	13	0.046	0.1163	0.1163	1.20	90.6	n.d.	1.6	1.8
Datong																
DAT-05	1	0.98	1.25	2.53	17.6	3.29	0.035	25.7	0.17	0.1218	0.1218	3.21	91.5	17.7	0.8	1.3
DAT-09	1	1.63	1.54	2.84	1.75	0.3	0.019	8.1	0.057	0.1165	0.1165	1.62	91.6	45.4	1.5	1.8
DAT-15	1	1.46	2.18	4.17	3.67	2.54	0.111	14.1	0.367	0.1262	0.1262	3.66	90.8	12.9	0.1	1.4
DAT-30	1	2.63	2.24	5.75	5.57	2.80	0.014	19.0	0.026	0.1178	0.1178	2.27	91.7	33.5	1.4	1.5

Table 4-2 *continued*

Sample	t	Os	Ir	Ru	Pt	Pd	Re	ΣHSE	$^{187}Re/^{188}Os$	$^{187}Os/^{188}Os$	$^{187}Os/^{188}Os_i$	Al_2O_3	Fo[c]	Cr#[d]	T_{RD}[e]	T_{MA}[e]
	Ma	ppb	ppb	ppb	ppb	ppb	ppb	ppb				%			Ga	Ga
DAT-31	1	1.27	1.65	2.98	7.64	2.16	0.05	15.8	0.19	0.1219	0.1219	2.60	91.1	14.8	0.8	1.4
D7	1	0.65	n.d.	n.d.	n.d.	n.d.	0.036	0.7	0.27	0.1213	0.1213	n.d.	91.1	n.d.	0.8	2.5
D18	1	1.09	n.d.	n.d.	n.d.	n.d.	0.014	1.1	0.063	0.1156	0.1156	n.d.	91.6	n.d.	1.7	2.0
Jining																
JN-01	32	1.31	1.26	1.90	1.3	0.58	0.016	6.4	0.06	0.1173	0.1173	4.91	90.7	14.6	1.4	1.7
JN-01R	32	0.94	0.98	1.67	1.21	0.30	0.027	5.1	0.14	0.1173	0.1172				1.4	2.2
JN-02	32	1.57	1.57	2.10	1.43	0.43	0.015	7.1	0.046	0.1177	0.1177	4.33	90.9	15.4	1.4	1.5
JN-06	32	1.63	1.71	3.14	4.96	0.81	0.130	12.4	0.385	0.1214	0.1212	3.65	90.7	27.5	0.9	17
JN-06R	32	1.20	1.19	2.19	3.46	1.63	0.018	9.7	0.072	0.1201	0.1201				1.0	1.2
JN-16	32	0.91	0.8	2.12	1.17	0.68	0.029	5.7	0.16	0.1237	0.1236	0.86	90.5	20.8	0.5	0.8
JN-17	32	0.66	1.07	2.36	1.45	1.12	0.014	6.7	0.10	0.1272	0.1271	1.65	87.9	16.4	0	0
JN-19	32	1.64	1.35	2.60	2.49	6.72	0.006	14.8	0.02	0.1204	0.1204	4.03	90.1	35.6	1.0	1.0
JN-19R	32	0.88	0.74	1.05	1.71	0.36	0.003	4.7	0.02	0.1200	0.1200				1.0	1.1
JN-26	32	1.48	1.70	3.83	1.40	0.75	0.007	9.2	0.02	0.1183	0.1183	4.94	91.6	31.8	1.3	1.4
JN-27	32	0.15	0.23	0.59	0.13	0.25	0.002	1.4	0.08	0.1265	0.1265		90.5	n.d.	0.1	0.1
JN-29	32	0.88	1.22	2.06	1.45	0.78	0.016	6.4	0.088	0.1234	0.1234	5.69	90.6	18.8	0.5	0.7
JN-29R	32	0.75	1.06	1.95	1.02	0.55	0.017	5.3	0.11	0.1231	0.1230				0.6	0.8
JN-31	32	0.98	1.85	3.64	2.94	2.24	0.024	11.7	0.12	0.1280	0.1279	1.48	87.5	18.8	-0.1	-0.2
JN-35	32	1.13	3.44	6.00	3.57	1.53	0.026	15.7	0.11	0.1250	0.1249	6.50	90.8	14.2	0.3	0.4
JN-41	32	0.49	1.50	3.18	1.85	0.81	0.059	7.9	0.58	0.1256	0.1253	3.73	90.7	n.d.	0.3	-0.5
JN-41R	32	0.58	1.46	2.95	1.70	0.61	0.01	7.3	0.086	0.1254	0.1254				0.2	0.3
JN-52	32	1.04	1.83	3.33	1.88	0.99	0.024	9.1	0.11	0.1252	0.1251	4.54	90.7	17.7	0.3	0.4
Fansi																
FS-01	25	1.21	1.65	2.79	1.78	0.47	0.057	8	0.23	0.1211	0.1210	1.94	90.3	14.1	0.9	2.0
FS-04	25	3.77	2.76	5.82	4.30	0.71	0.020	17.4	0.026	0.1189	0.1189	n.d.	n.d.	n.d.	1.2	1.3
FS-36	25	2.79	2.57	5.32	5.11	4.85	0.249	20.9	0.431	0.1249	0.1247	3.46	89.8	11.2	0.3	-4.4
FS-44	25	1.20	1.99	4.68	3.84	2.70	0.037	14.4	0.15	0.1247	0.1246	2.16	90.4	21.6	0.4	0.5

Table 4-2 *continued*

Sample	t	Os	Ir	Ru	Pt	Pd	Re	ΣHSE	$^{187}Re/^{188}Os$	$^{187}Os/^{188}Os$	$^{187}Os/^{188}Os_i$	Al_2O_3	Fo[c]	Cr#[d]	T_{RD}[e]	T_{MA}[e]
	Ma	ppb	ppb	ppb	ppb	ppb	ppb	ppb				%			Ga	Ga
FS-45	25	0.84	1.51	2.91	3.45	1.17	0.007	9.9	0.04	0.1244	0.1244	2.54	90.2	n.d.	0.4	0.4
FS-50	25	0.93	1.76	3.21	9.33	1.61	0.019	16.9	0.1	0.1223	0.1223	2.59	89.2	11.1	0.7	0.9
FS-64	25	2.89	2.12	5.21	4.81	0.85	0.012	15.9	0.02	0.1191	0.1191	2.01	89.8	17.4	1.2	1.2
FS-68	25	2.30	2.25	2.83	12.7	4.43	0.034	24.5	0.07	0.1191	0.1191	1.12	91.7	51.9	1.2	1.4
FS2-04	25	1.31	2.67	4.53	2.61	0.67	0.057	11.8	0.21	0.1170	0.1169	1.53	90.9	37.7	1.5	3
FS2-05	25	0.65	1.79	2.88	3.38	0.87	0.072	9.6	0.53	0.1262	0.1260	1.89	90.6	23.9	0.1	-0.4
FS2-09	25	1.15	2.30	4.59	4.93	1.51	0.064	14.5	0.27	0.1237	0.1236	3.93	89.9	14.8	0.5	1.5
FS2-10	25	1.81	2.33	4.54	3.20	1.10	0.034	13	0.1	0.1182	0.1182	2.67	88.2	43.7	1.3	1.7
FS-04(2)	25	1.41	1.77	3.59	1.94	0.39	0.01	9.1	0.036	0.1099	0.1099	0.88	92.5	n.d.	2.5	2.7
FS-18	25	1.92	2.02	5.20	1.23	0.17	0.009	10.5	0.02	0.1129	0.1129	2.00	92.4	20.5	2.1	2.2
FS-42	25	0.97	2.00	3.32	1.33	0.17	0.021	7.8	0.10	0.1101	0.1101	1.31	92.2	37.8	2.5	3.3
FS-43	25	1.13	1.77	3.28	1.51	0.17	0.009	7.9	0.04	0.1133	0.1133	1.23	91.9	35.8	2.0	2.2
FS-62	25	1.04	1.86	3.31	1.61	0.33	0.018	8.2	0.084	0.1125	0.1125	1.26	92.4	41.5	2.1	2.7
F2	25	1.50	n.d.	n.d.	n.d.	n.d.	0.038	1.5	0.12	0.1116	0.1116	n.d.	92.4	n.d.	2.3	3.4
F17	25	0.87	n.d.	n.d.	n.d.	n.d.	0.018	0.9	0.099	0.1265	0.1265	n.d.	91.9	n.d.	0.1	0.6
F44	25	1.79	n.d.	n.d.	n.d.	n.d.	0.006	1.8	0.016	0.1134	0.1134	n.d.	92.3	n.d.	2.0	2.3
Hebi																
HB-01	4	0.66	0.72	3.60	0.55	0.41	0.009	5.9	0.06	0.1136	0.1136	1.18	92.6	n.d.	2.0	2.3
HB-02	4	0.042	0.19	2.24	0.032	0.021	0.004	2.5	0.4	0.1191	0.1191	1.79	92.2	n.d.	1.2	-
HB-07	4	6.09	3.30	8.87	2.93	0.60	0.017	21.8	0.013	0.1151	0.1151	1.36	92.3	n.d.	1.7	1.8
HB-09	4	0.092	0.11	2.15	0.035	0.086	0.009	2.5	0.48	0.1142	0.1142	1.95	92.5	35.2	1.9	-
HB-10	4	3.75	5.15	7.24	5.45	1.43	0.025	23	0.032	0.1135	0.1135	1.16	91.5	52.4	2.0	2.2
HB-12	4	0.27	0.22	3.91	0.20	0.093	0.004	4.7	0.08	0.1150	0.1150	1.68	92.2	49.3	1.8	2.2
HB-13	4	1.55	1.56	5.84	1.03	0.56	0.014	10.6	0.044	0.1146	0.1146	1.10	92.2	48.2	1.8	2.1
HB-15	4	1.28	1.19	2.10	1.88	0.19	0.019	6.7	0.07	0.1154	0.1154	2.21	91.7	47.4	1.7	2.1

Table 4-2 *continued*

Sample	t	Os	Ir	Ru	Pt	Pd	Re	ΣHSE	$^{187}Re/^{188}Os$	$^{187}Os/^{188}Os$	$^{187}Os/^{188}Os_i$	Al_2O_3	Fo[c]	Cr#[d]	T_{RD}[e]	T_{MA}[e]
	Ma	ppb	ppb	ppb	ppb	ppb	ppb	ppb				%			Ga	Ga
HB-15	4	1.28	1.19	2.10	1.88	0.19	0.019	6.7	0.070	0.1154	0.1154	2.21	91.7	47.4	1.7	2.1
HB-19	4	2.58	2.55	19.0	1.76	1.23	0.008	27.1	0.02	0.1147	0.1147	1.56	92.2	n.d.	1.8	1.9
HB-21-2	4	0.081	0.21	0.50	n.d.	0.019	0.004	0.8	0.26	n.d.		1.16				
HB-21-2R	4	0.80	0.33	0.57	0.027	0.023	0.11	1.9	0.67	0.1135	0.1135		92.6	60.6	2.0	-3.1
HB-22	4	0.24	0.26	4.26	0.34	0.48	0.027	5.6	0.54	0.1167	0.1167	1.17	92.1	49.3	1.5	-4.6
HB-24	4	10.3	7.93	31.6	15.3	1.94	0.024	67.1	0.011	0.1125	0.1125	0.96	89.6	47.0	2.1	2.2
Fushan																
FS7-13	125	0.64	0.96	1.82	0.36	0.65	0.008	4.4	0.06	0.2612	0.2611	0.15	90.9	82.2	-24	-30
FS6-19	125	0.037	0.057	0.56	0.18	0.057	0.008	0.9	1.1	0.1240	0.1217	0.70	91.7	56.0	0.8	-0.3
FS7-10	125	3.91	3.56	7.89	0.82	0.026	0.010	16.2	0.012	0.1124	0.1124	0.65	92.7	42.8	2.1	2.2
FS7-10R	125	3.78	3.65	6.20	0.59	0.038	0.004	14.3	0.004	0.1123	0.1123				2.2	2.2
FS6-56	125	0.024	0.12	1.79	n.d.	0.074	0.006	2.0		0.1179	0.1179	0.97	92.8	40.9	1.4	
FS6-18	125	2.15	2.46	5.56	3.52	0.69	0.008	14.4	0.02	0.1134	0.1134	0.59	91.9	54.9	2.0	2.1
FS6-29	125	0.023	0.15	1.23	0.073	0.019	0.002	1.5	0.44	0.1189	0.1180	1.20	92.8	33.5	1.3	-14
FS6-55	125	3.82	3.63	6.48	3.98	3.23	0.036	21.2	0.045	0.1142	0.1141	1.47	91.5	24.4	1.9	2.1
FS7-1	125	3.13	2.85	7.87	1.88	0.71	0.011	16.5	0.017	0.1097	0.1097	0.73	91.4	23.6	2.5	2.6
FS7-9	125	4.49	4.54	5.72	4.33	2.00	0.059	21.1	0.063	0.1148	0.1147	0.80	92.5	33.9	1.8	2.1
PUM		3.9	3.5	7.0	7.6	7.1	0.35	29.5	0.433	0.1296	0.1296	4.4				

Note: R represents a replicate analysis of a second aliquot of the same powder. t: eruption time. 'n.d.' means 'not determined'. PUM: primitive upper mantle.

a. Data from Becker et al. (2006), and Liu et al. (2010).

b. Data from Liu et al. (2010)

c. Fo: forsterite content (molar Mg/(Mg+Fe)x100).

d. Cr# of spinel: molar Cr/(Cr+Al)x100.

e. The parameters used in model age calculation are: $\lambda_{Re} = 1.666 \times 10^{-11}$/year $(^{187}Re/^{188}Os)_{CI} = 0.402$, $(^{187}Os/^{188}Os)_{CI,0} = 0.1270$ (Shirey and Walker, 1998). $(^{187}Os/^{188}Os)_i$ represents the initial value when xenolith was erupted.

f. PUM: primitive upper mantle. Concentration data from Becker et al. (2006), and Re-Os data from Meisel et al. (2001).

nearly chondritic Os/Ir group is characterized by minimal fractionation of the IPGE compared to PUM, but exhibits a depletion of Re and PPGE (Pt and Pd). The second group is characterized by concave-downward HSE patterns that are similar to those of Yangyuan peridotites (Liu et al., 2010). Jining peridotites exhibit a large range in $^{187}Os/^{188}Os$ (0.117 to 0.128), similar to Hannuoba and Yangyuan peridotite suites.

4.4.3.5 Fansi peridotites

The HSE abundances of Fansi peridotites are generally lower than those of PUM (ΣHSE: 8 to 25 ppb, and Ir: 1.5 to 2.8 ppb). The HSE patterns of these samples are shown in Fig. 4-6e and f for the high-Fo and low-Fo groups, respectively. Like Yangyuan, the majority of the Fansi peridotites are characterized by Re and PPGE depletions relative to IPGE, with a minimal to moderate Os depletion relative to Ir. Like Datong peridotites DAT-05 and DAT-31, two low-Fo Fansi peridotites (FS-50 and FS-68) show Pt enrichments (Fig. 4-6f). Sample FS-36 shows a PUM-like HSE pattern, similar to DAT-15. In this suite, the high-Fo group has low $^{187}Os/^{188}Os$ (0.110-0.114), whereas the low-Fo group is characterized by substantially higher $^{187}Os/^{188}Os$ (0.117-0.127). In spite of a poor correlation between $^{187}Re/^{188}Os$ and $^{187}Os/^{188}Os$, a rough positive correlation between $^{187}Os/^{188}Os$ and indicators of fertility (Al_2O_3 or Yb) is present for the majority of the low-Fo samples, but not for the high-Fo samples, mainly due to a limited range of compositions (e.g., Al_2O_3 = 0.9-1.3 wt. %, with one at 2.0 wt. %).

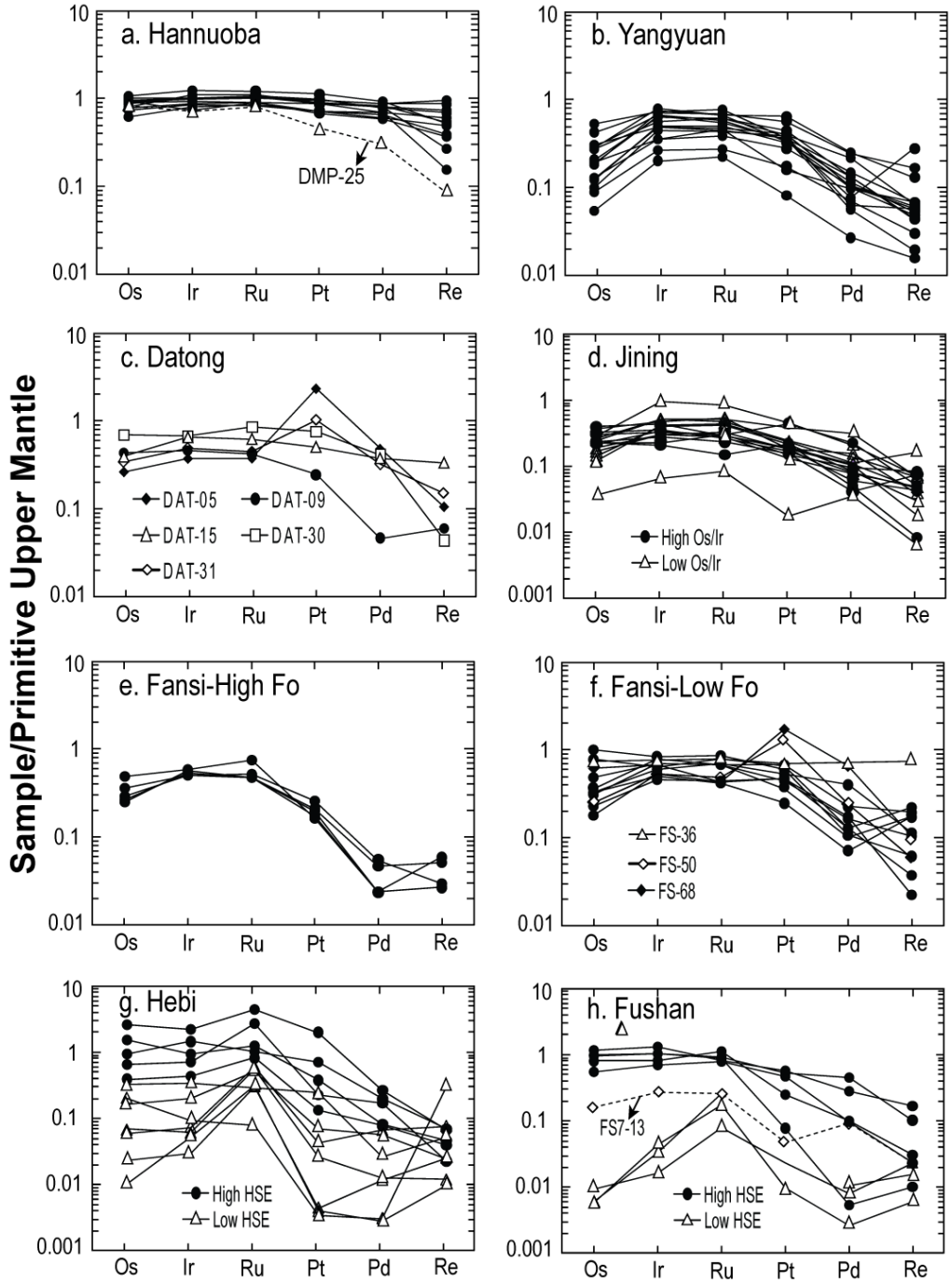

Fig. 4-6. Primitive-upper-mantle (PUM)-normalized HSE patterns of whole rock peridotites: Hannuoba (a; data from Becker et al., 2006; Liu et al., 2010), Yangyuan (b; data from Liu et al., 2010), Datong (c), Jining (d), Fansi (e. high Fo group; f. low Fo group with some samples of Pt and/or Pd anomalies), Hebi (g), and Fushan (h). PUM recommended values (Table 4-2) from Becker et al., 2006.

4.4.3.6 Hebi peridotites

The Hebi peridotites fall into two groups in terms of HSE abundances: a low-HSE group (ΣHSE: 2 to 7 ppb, and Ir: 0.1 to 1.2 ppb), and a high-HSE group (ΣHSE: 11 to 67 ppb, and Ir: 1.6 to 7.9 ppb). The patterns of the high-HSE group are generally characterized by chondritic or near chondritic IPGE, and Re and PPGE depletions relative to the IPGE (Fig. 4-6g). The low-HSE group is generally characterized by positive Ru anomalies (Fig. 4-6g). Both groups have overlapping, low $^{187}Os/^{188}Os$ (0.112-0.119). Osmium model ages (both rhenium depletion model age, T_{RD}, Walker et al., 1989, and T_{MA} model age, Allégre and Luck, 1980) show similar ranges within the high HSE group (T_{RD} = 1.7 to 2.1 Ga; T_{MA} = 1.8 to 2.2 Ga; Table 4-2). The low HSE group shows similar T_{RD} ages (T_{RD} = 1.5 to 2.0 Ga), but much more variable T_{MA} (T_{MA} = -11 to 2.3 Ga) (Table 4-2), reflecting the more variable Re/Os ratio in the low HSE group.

4.4.3.7 Fushan peridotites

Like Hebi, the Fushan peridotites have highly variable HSE abundances, and can be divided into two groups: low-HSE (ΣHSE: 1 to 2 ppb, and Ir: 0.06 to 0.15 ppb) and high-HSE (ΣHSE: 14 to 21 ppb, and Ir: 2.5 to 4.5 ppb). The high-HSE group is characterized by unfractionated IPGE and strong depletions of Re and PPGE relative to the IPGE (Fig. 4-6h); it is also characterized by high Os concentrations of 2.2-4.5 ppb and low $^{187}Os/^{188}Os$ of 0.110-0.115, which yield consistent and overlapping model ages (T_{RD} = 1.8 to 2.5 Ga, T_{MA} = 2.1 to 2.6 Ga) that are similar to those of the Hebi high-HSE peridotites. The patterns of the low-HSE group are characterized by positive Ru anomalies (Fig. 4-6h), like the Hebi low-HSE peridotites, but, unlike Hebi, the low-HSE group (Os = 0.023 to 0.037 ppb) has more radiogenic Os isotopic

compositions ($^{187}Os/^{188}Os$ = 0.118-0.124). An exceptional sample, dunite FS7-13, has moderate HSE abundances (ΣHSE = 4.4 ppb, and Ir = 0.96 ppb) and is somewhat enriched in Pd relative to Pt. The $^{187}Os/^{188}Os$ of FS7-13 is the only strongly suprachondritic sample ($^{187}Os/^{188}Os$ = 0.261) analyzed from any of the suites examined here.

4.5 Discussion

In order to use Os isotopes to establish the age structure of lithospheric mantle beneath the central North China Craton, I need to: 1) determine whether the Re-Os isotopic systematics in peridotites have been disturbed by secondary processes, and if so, evaluate their effects on Os model ages; and 2) distinguish Proterozoic-aged peridotites from modern convecting upper mantle, a small fraction of which also yields Proterozoic model ages (e.g., Harvey et al., 2006; Liu et al., 2008; Fig. 4-7).

4.5.1 Effects of secondary processes on HSE abundances and Os isotopic compositions

Secondary processes have clearly affected most of the rocks considered here. For example, LREE enrichment is observed in xenoliths from all suites (e.g., Zheng et al., 2001; Rudnick et al., 2004; Tang et al., 2008; Y.G. Xu et al, 2008; Fig. S4-1). The LREE enrichment reflects overprinting and interaction with LREE-enriched melts or fluids during one or more events following initial partial melting of the mantle (Frey and Green, 1974).

Unlike lithophile trace elements, HSE, being both siderophile and chalcophile, mainly reside in base metal sulfides and/or HSE-bearing alloys in mantle rocks (e.g., Hart and Ravizza, 1996; Alard et al., 2000; Bockrath et al., 2004; Bauhaus et al., 2006;

Lorand et al., 2008, 2010). The degree to which secondary processes have influenced the Re-Os isotopic systematics, and thus, affected the accuracy of the Re-Os chronometer in peridotites can potentially be assessed by examining HSE systematics (e.g., Lorand and Alard, 2001; Büchl et al., 2002; Lorand et al., 2004; Reisberg et al., 2005; Ackerman et al., 2009; Liu et al., 2010). For example, secondary sulfides are typically enriched in PPGE relative to IPGE (e.g., Alard et al., 2000), and their addition to residual peridotite should be reflected in enhanced PPGE and sulfur concentrations in bulk samples (Rudnick and Walker, 2009, and references therein). Below, I discuss the HSE characteristics of xenoliths from each locality and explore whether the HSE were significantly impacted by secondary processes; I then evaluate possible impacts on Os isotopic compositions and model ages.

4.5.1.1 Hannuoba and Yangyuan

Previous studies have demonstrated that the Os isotopic compositions of both Hannuoba and Yangyuan peridotites were little affected by secondary processes, based mainly on the following lines of evidence:

1) in the Hannuoba suite, the observed multiple linear correlations between S, Pd/Ir, Re/Os, $^{187}Os/^{188}Os$, and immobile melt depletion indicators such as Al_2O_3 (Fig. 4-8), together with relatively high HSE abundances, primarily reflect the effects of ancient partial melting, with subsequent good preservation of primary sulfides and only minor addition of secondary sulfides (Gao et al, 2002; Liu et al., 2010). It is worth emphasizing here that refertilization that significantly post-dates melt depletion would lead to near horizontal trends on a plot of Al_2O_3 vs. $^{187}Os/^{188}Os$, as originally noted by

Reisberg and Lorand (1995) and further emphasized by Rudnick and Walker (2009). The fact that both the Hannuoba and Yangyuan suites show linear correlations having a significant positive slope between PUM and a low $^{187}Os/^{188}Os$, low Al_2O_3 end member on this plot (Figs. S4-3 a and b) indicate that these peridotites experienced minimal late refertilization (cf. X.S. Xu et al., 2008; Zhang et al., 2009).

2) HSE characteristics in the Yangyuan suite, such as low HSE concentrations, Os, Pd and Re depletions relative to Ir, and low S and Se contents, were interpreted to be a result of sulfide breakdown in an oxidized environment following infiltration of a S-undersaturated melt/fluid (Liu et al., 2010). Because $^{187}Os/^{188}Os$ correlates positively with fertility indices such as Al_2O_3 (Fig. 4-8, and Fig. S4-3b)), sulfide breakdown was interpreted to be a recent phenomenon that has had little impact on Os isotopic compositions of these peridotites (Liu et al., 2010). Thus, the Re-Os isotopic systematics of Hannuoba and Yangyuan peridotites may be used to constrain their melt depletion ages (Gao et al., 2002; Liu et al., 2010).

4.5.1.2Datong

The depletions of Re and PPGE relative to the IPGE in samples DAT-09 and DAT-30 may reflect high degrees of partial melting (Pearson et al., 2004), consistent with the refractory compositions of the samples (e.g., Al_2O_3 = 1.6-2.3 %, $Fo_{91.6-91.7}$). If this interpretation is correct, the non-radiogenic Os isotopic compositions of these samples indicate an ancient depletion event. The PUM-like pattern of sample DAT-15 reflects a low degree of partial melting, consistent with its fertility (e.g., Al_2O_3 =

3.2 %, $Fo_{90.8}$). Positive Pt anomalies observed in the remaining two samples (DAT-05 and DAT-31) likely reflect the mobility of Pt via melt percolation involving loss/gain of base metal sulfides (Ackerman et al., 2009).

Collectively, the Datong peridotites show a good positive correlation between $^{187}Os/^{188}Os$ and $^{187}Re/^{188}Os$ ($r^2 = 0.85$, with an errorchron age of 1.80 ± 0.56 Ga; Fig. S4-4), and melt depletion indicators such as Al_2O_3, although the aforementioned Pt-enriched samples DAT-05 and DAT-31 plot slightly to the right of the $^{187}Os/^{188}Os$ vs. Al_2O_3 trend defined by the other samples (Fig. 4-8). Given the HSE fractionation in these two samples, and their relatively low Os concentrations, I suggest that their position to the right of the other Datong samples in Fig. 4-8 reflects minor basaltic addition, possibly associated with melt percolation prior to eruption. Alternatively, the slightly elevated Al_2O_3 contents of these two samples may have resulted from biased sampling of these very small, rather coarse-grained peridotites. These observations indicate that the growth of ^{187}Os in the Datong peridotites is the result of long-term decay of radioactive ^{187}Re in a relatively closed residual system, after varying extents of ancient partial melting. Evidently melt percolation that may have enriched Al_2O_3 did not significantly modify the Re-Os isotopic systematics, consistent with melt-rock mixing trends (Reisberg and Lorand, 1995).

4.5.1.3 Jining

Those samples with nearly chondritic Os/Ir ratios (seven out of 13 samples) are characterized by depletions in Re and PPGE relative to the IPGE (Fig. 4-6d), which is a typical signature of a high degree of partial melting (Pearson et al., 2004), consistent with their low $^{187}Os/^{188}Os$. By contrast, the concave-downward HSE patterns of samples with low Os/Ir (Fig. 4-6d) are similar to those seen in the Yangyuan

peridotites, which were previously interpreted to be the result of recent sulfide breakdown after infiltration of an oxidative, S-undersaturated melt/fluid (Liu et al., 2010). Although Os was lost relative to Ir, the Os isotopic signatures of peridotites were likely little affected by the putative recent, oxidative sulfide breakdown, as observed in Yangyuan peridotites (Liu et al., 2010).

4.5.1.4 Fansi

This suite is characterized by HSE patterns showing Re and PPGE depletions relative to the IPGE, with a minimal to moderate Os depletion relative to Ir (Fig. 4-6e and f). These patterns are similar to those of the Yangyuan peridotites interpreted to have experienced recent oxidative sulfide breakdown through melt percolation (Liu et al., 2010). However, the significant depletions of Re and PPGE relative to the IPGE of the high-Fo samples (Fig. 4-6e) may have resulted from high degrees of melting rather than oxidative sulfide breakdown. Their non-radiogenic Os isotopic compositions must reflect the antiquity of partial melting. The PUM-like pattern of low-Fo sample FS-36, like DAT-15, reflects a limited degree of melting and little sulfide breakdown, consistent with its fertility (e.g., Fo = 89.8 and Al_2O_3 = 3.5 %) and its relatively radiogenic $^{187}Os/^{188}Os$ (0.1249). Like some Datong peridotites, Pt enrichments are present in two low-Fo Fansi samples (FS-50 and FS-68; Fig. 4-6f), presumably resulting from Pt mobility during melt percolation (Ackerman et al., 2009).

The scattered, poor correlations between $^{187}Os/^{188}Os$ and melt depletion indicators (e.g., Al_2O_3, Fo, Cr#, and $^{187}Re/^{188}Os$) for the low-Fo samples of this suite, and for one of the high-Fo samples (F17), presumably point to significant impacts on either $^{187}Os/^{188}Os$, or melt depletion indicators resulting from secondary processes other

than oxidative sulfide breakdown. For example, samples FS-50, FS-64 and FS2-10 show evidence of recent Fe enrichment, either on the basis of olivine that is too Fe-rich relative to coexisting spinel Cr# (e.g., FS2-10, Fig. 4-4), or displacement of the samples to the left (low Fo) side of the Fo vs. $^{187}Os/^{188}Os$ trend defined by the other samples (e.g., all three samples in Fig. S4-5 in Supplemental Material). Moreover, samples FS2-05 and F17 may have experienced addition of radiogenic Os during melt-rock reaction, given relatively low Al_2O_3 (Fig. 4-8) or high Fo (Fig. S4-5; Table 4-2) for their $^{187}Os/^{188}Os$ values, respectively; their relatively low Os concentrations (0.65 and 0.87 ppb, respectively) would make these samples more susceptible to overprinting. Finally, the slightly elevated Al_2O_3 contents of FS2-09 and FS2-10 may be due to addition of minor amounts of basaltic melt (Liu et al., 2010), which would have had minimal impact on Os isotopic compositions, because basaltic melt normally has one to three orders of magnitude lower Os concentrations than peridotites (e.g., Walker et al., 1999; Puchtel and Humayun, 2000). In spite of the scatter that is likely generated by secondary processes, the low-Fo Fansi samples display a rough positive correlation between $^{187}Os/^{188}Os$ and Al_2O_3 (excluding the outliers discussed above; Fig. 4-8), which presumably reflects the vestige of ancient partial melting of these samples.

4.5.1.5 Hebi

The large range of HSE abundances and patterns in the Hebi peridotites may partially reflect the small sample sizes, coupled with inhomogeneous distribution of the HSE-bearing phases, and/or HSE mobility within the upper mantle. Minimal fractionation of IPGE, and Re and PPGE depletions relative to the IPGE (Fig. 4-6g) in the high-HSE samples, reflect a high degree of melt extraction (Pearson et al., 2004;

Luguet et al., 2007). This is consistent with their high Fo values and low Al_2O_3 contents. By contrast, the low-HSE samples (ΣHSE: 2 to 7 ppb) may have been influenced by melt percolation (Büchl et al., 2002). However, because melts normally have radiogenic Os isotopic compositions evolving from high Re/Os ratios and/or radiogenic sources, peridotites stripped of Os due to melt percolation typically show an enrichment of radiogenic Os isotopic compositions, which is not observed here ($^{187}Os/^{188}Os$ = 0.114-0.119). In theory, total consumption of HSE-bearing sulfides without formation of HSE-bearing alloys at high degrees of melt depletion can lead to such low HSE abundances (e.g., Rehkämper et al., 1999), and may account for the low-HSE Hebi peridotites. Such HSE characteristics are also observed in orthopyroxene separates from refractory harzburgites that are devoid of visible sulfides and alloys (Luguet et al., 2007). However, it is unclear why some of the Hebi peridotites apparently preserved their HSE contents (in refractory sulfides and/or alloys) at the same degree of melt depletion while others did not. Moreover, the positive Ru anomaly observed in the low HSE Hebi samples requires at least one unique stable phase to host Ru, apart from other HSE in the residues.

The low-HSE Hebi samples generally show chondritic to suprachondritic Re/Os ratios ($^{187}Re/^{188}Os$ between 0.4 and 0.5; Table 4-2), which, over time, would lead to chondritic to suprachondritic Os isotopic compositions, instead of the observed non-radiogenic Os isotopic compositions. Due to the very low Re concentrations in these samples (0.003 to 0.010 ppb), a small amount of recent Re addition (e.g., from host basalts) could easily elevate Re/Os ratios to the observed high values, but would not significantly change Os isotopic compositions. Overall, the non-radiogenic Os

isotopic compositions of both high- and low-HSE Hebi peridotites must reflect ancient melt depletion experienced by these rocks.

4.5.1.6 Fushan

The HSE patterns of the high-HSE Fushan samples are characteristic of residues of high degrees of partial melting, whereas the low-HSE samples, like the low-HSE Hebi samples, have experienced depletions of both IPGE and PPGE, with minor Re addition. Further, the two dunites (FS6-19 and FS7-13), which have lower Fo contents (90-91) than those of lherzolites and harzburgites (~92), were interpreted to have formed through melt-peridotite reaction (Xu et al., 2010). The suprachondritic $^{187}Os/^{188}Os$ (0.261) of FS7-13, together with Pd (relative to Pt) enrichment, further supports dunite formation by melt-peridotite reaction. In the process of melt-peridotite reaction, S-saturated melts may precipitate sulfides that control the shape of the HSE patterns and Os isotopic compositions of the whole rock (Büchl et al., 2002). Compared to FS7-13, sample FS6-19 has significantly lower $^{187}Os/^{188}Os$ (0.1240), but the ratio is still much higher than those of the other two low-HSE samples FS6-29 and FS6-56 (Table 4-2). The negative correlation between $^{187}Os/^{188}Os$ and 1/Os ($r^2 = 0.88$) among these low-HSE samples (see Fig. S4-6 in Supplemental Material) suggests addition of secondary sulfides, but to a lesser extent for dunite FS6-19, compared to dunite FS7-13. Thus, excluding the dunites that formed by melt rock reaction, the non-radiogenic Os isotopic compositions of the remaining Fushan peridotites document their long-term evolution under low Re/Os ratios, reflecting the antiquity of partial melting.

4.5.2 Age of the lithospheric mantle

The above discussion suggests that most (but not all) of the peridotites studied here have retained their original Os isotope signature with little modification due to secondary processes. The next important consideration before robust model ages can be determined is to what degree non-radiogenic Os reflects ancient melting events that led to the formation of the continental lithosphere, versus remnants of ancient melting events that are known to be present as a minor component in the convecting upper mantle (see discussion in Rudnick and Walker, 2009).

When plotted on a histogram (Fig. 4-7), the $^{187}Os/^{188}Os$ values of peridotites from all suites show a distribution that is distinct from that of modern abyssal peridotites. Samples from the southern region range to lower $^{187}Os/^{188}Os$ than any abyssal peridotite, and their overall distribution, with a peak in $^{187}Os/^{188}Os$ at ~0.114 is clearly resolved from modern convecting mantle. These samples must, therefore, represent ancient lithospheric mantle. By contrast, the range in $^{187}Os/^{188}Os$ of peridotites from the northern region completely overlaps that seen in abyssal peridotites. Nevertheless, the distribution of $^{187}Os/^{188}Os$ in these suites is distinct from that seen in abyssal peridotites, or, for that matter Mesozoic upper mantle, as sampled by the Josephine Ophiolite (Meibom et al., 2002), with the greatest number of samples falling below $^{187}Os/^{188}Os = 0.125$ (the dotted line). By contrast, though the $^{187}Os/^{188}Os$ of abyssal peridotites show the same overall range, the peak in $^{187}Os/^{188}Os$ occurs at more radiogenic values (Fig. 4-7), consistent with their distinct cumulative probability distributions (Fig. 4-7, inset). In addition, the statistic test shows that the $^{187}Os/^{188}Os$ population of peridotites from the northern region is characterized by significantly

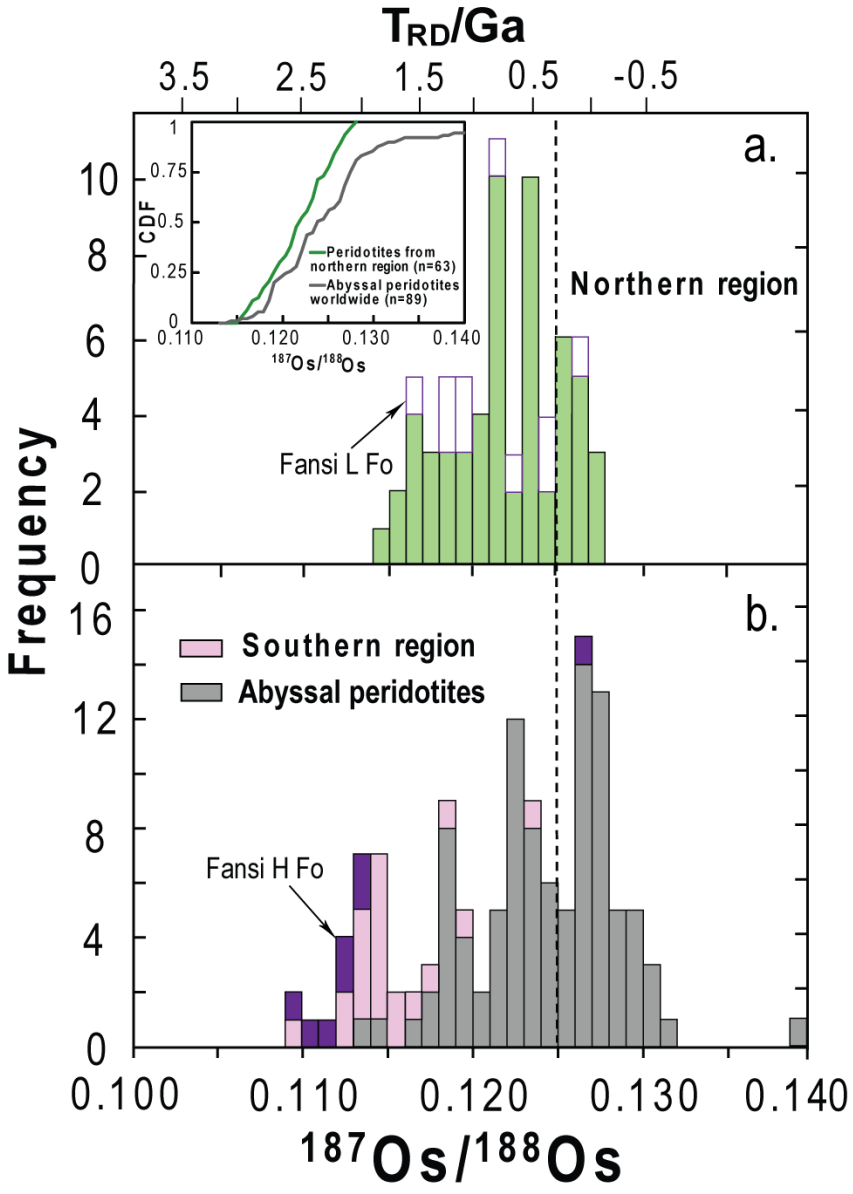

Fig. 4-7. Histograms of $^{187}Os/^{188}Os$ of whole rock peridotites from the northern region (a, with low Fo Fansi samples plotted), and the southern region (b, with high Fo Fansi samples as well as abyssal peridotites plotted). The cumulative distribution functions (CDF) of $^{187}Os/^{188}Os$ for peridotites from the northern region of the North China Craton and abyssal peridotites worldwide are shown as an inset of the upper panel. The CDF for peridotites from the northern region plots to the left (i.e., lower values of $^{187}Os/^{188}Os$) of that of abyssal peridotites. Abyssal peridotite data are from Parkinson et al., 1998; Brandon et al., 2000; Standish et al., 2002; Harvey et al., 2006; and Liu et al., 2008. The vertical dashed line is at a value of $^{187}Os/^{188}Os = 0.1250$.

lower $^{187}Os/^{188}Os$ than that of abyssal peridotites at the confidence level of 95% (see Supplemental Material). Thus, it is highly unlikely that these peridotites were derived from convecting upper mantle during the Mesozoic or later. Below I examine the age constraints provided by the Os isotopic data.

4.5.2.1 Northern region: Datong, Yangyuan, Hannuoba, and Jining

Correlations between $^{187}Os/^{188}Os$ and melt depletion indices (e.g., Al_2O_3, CaO, or Yb; Handler et al., 1997; Reisberg et al., 2005) allow the initial $^{187}Os/^{188}Os$ of a suite of peridotites to be estimated. Comparison of this ratio with a model for Os isotopic evolution in the mantle, allows derivation of a model age for the suite of peridotites. The $^{187}Os/^{188}Os$ values of peridotites from the northern region for which I have reliable Al_2O_3 concentrations (i.e., Hannuoba, Datong and Yangyuan) generally show positive correlations with Al_2O_3 (Fig. 4-8). Using linear regression of the data and extrapolating to 0.7 % Al_2O_3 (suggested to be the Al_2O_3 value at or below which all Re is removed in peridotites during progressive melt depletion (Handler et al., 1997)), I estimate the initial $^{187}Os/^{188}Os$ of the three northern peridotite suites to be ~0.115. This isotopic composition corresponds to an Os model age of ca. 1.8 Ga (Fig. 4-8), which is similar to the maximum T_{RD} ages of peridotites from each locality (Table 4-2). This is generally consistent with the oldest Paleoproterozoic T_{RD} (~1.5 Ga) and T_{MA} (1.8-2.0 Ga) ages of sulfides ($^{187}Re/^{188}Os < 0.1$) from Hannuoba peridotites (X.S. Xu et al., 2008), and a Lu-Hf errorchron age (1.7 ± 0.1 Ga; 2σ) of clinopyroxenes separated from Yangyuan peridotites (Liu et al., 2011b; Chapter 5). Although the Jining peridotites show no good correlation between $^{187}Os/^{188}Os$ and Al_2O_3, mainly due to their abnormal Al_2O_3 contents, their $^{187}Os/^{188}Os$ ratios do correlate negatively with olivine Fo content and the Cr# of spinels (see Fig. S4-5 in Supplemental

Material), as would be expected if they formed as residues of earlier partial melting. As their $^{187}Os/^{188}Os$ ratios (0.117 to 0.128) overlap with peridotites from the northern region (0.115-0.128), the Jining peridotites probably experienced melt extraction at the same time, e.g., about 1.8 Ga ago. I conclude that the lithosphere beneath the northern region formed by melt depletion at ca. 1.8 Ga. This is significantly younger than the age of crust formation in this region, which is 2.4-2.8 Ga (Wu et al., 2005b).

4.5.2.2 Southern region: Hebi and Fushan

In comparison with peridotites in the northern region, peridotites from the southern region (Hebi and Fushan) do not exhibit good correlations between $^{187}Os/^{188}Os$ and Al_2O_3, largely due to the lack of a spread in Al_2O_3 resulting from their generally refractory compositions. For refractory peridotites, with low Re/Os ratios, the T_{RD} model age should approximate the timing of melt depletion. In addition, if Re/Os has not been affected by secondary processes, the T_{MA} Os model age may more accurately represent the melt depletion age than T_{RD} age. Low Re/Os ratio samples will show little difference between T_{RD} and T_{MA}.

As shown above, the low-HSE samples in both Hebi and Fushan are more susceptible to overprinting. I therefore focus the attention here on the high-HSE samples in order to constrain the timing of melt depletion and, hence, lithospheric formation. These high-HSE peridotites are characterized by low $^{187}Os/^{188}Os$ of 0.112 to 0.115 (corresponding to T_{RD} = 1.7 to 2.1 Ga and T_{MA} = 1.8 to 2.3 Ga) for Hebi and 0.110 to 0.115 (T_{RD} = 1.8 to 2.5 Ga and T_{MA} = 2.1 to 2.6 Ga) for Fushan, respectively. The small differences (<0.3 Ga) between T_{RD} and T_{MA} ages are consistent with their low Re/Os ratios, which are characteristic of peridotites that experienced high degrees

of partial melting. The ancient T_{RD} and T_{MA} ages suggest that peridotites from both Hebi and Fushan experienced melt depletion event(s) in the Neoarchean to Paleoproterozoic (2.1-2.5 Ga). These ages are equal to or slightly younger than the ages derived from in situ Re-Os analyses reported for two sulfide grains from two Hebi peridotites (Zheng et al., 2007); the range to older ages in the sulfides (with T_{MA} of 2.5 Ga and 3.0 Ga, respectively) may reflect isotopic heterogeneity of the mantle that melted at ~2.5 Ga, or minor overprinting of the whole rocks due to sulfide metasomatism, though no secondary sulfides have been observed here or described in previous studies (Zheng et al., 2007). I conclude that peridotites from the southern region formed by melt depletion at ~2.5 Ga, which is earlier than those from the northern region (ca. 1.8 Ga), but similar to the age of the crust in this region (Wu et al., 2005b; Liu et al., 2009).

4.5.2.3 Fansi

The high-Fo samples have non-radiogenic $^{187}Os/^{188}Os$ of 0.110 to 0.114, corresponding to Neoarchean to Paleoproterozoic model ages (T_{RD} = 2.0 to 2.5 Ga and T_{MA} = 2.2 to 2.7 Ga), similar to those of the Hebi and Fushan peridotites. By contrast, the low-Fo samples display a range of higher $^{187}Os/^{188}Os$ (0.117 to 0.126) that largely overlaps with the range seen in other peridotites from the northern region (0.115 to 0.128) (Figs. 4-7 and 4-8). Excluding the few samples that show overprinting of either $^{187}Os/^{188}Os$ or Al_2O_3 from secondary processes, there appears to be a crude positive correlation between $^{187}Os/^{188}Os$ and Al_2O_3. Using a linear regression of these data, I derive a formation model age of ~1.8 Ga at 0.7 % Al_2O_3, identical to that of peridotites from the northern region (Fig. 4-8). The low-Fo and high-Fo samples have overlapping Al_2O_3 contents (1.1-3.9 % vs. 0.9-2.0 %,

respectively), but there is a large difference in $^{187}Os/^{188}Os$ values (0.117-0.126 vs. 0.110-0.114) at a given Al_2O_3. This observation demonstrates that the low-Fo samples were not derived from the high-Fo samples by melt addition or melt-peridotite reaction (cf. Tang et al., 2008), which would have led to Al_2O_3 enrichment, while having little impact on $^{187}Os/^{188}Os$ (e.g., Reisberg and Lorand, 1995; Rudnick and Walker, 2009, and references therein; Liu et al., 2010). Therefore, I conclude that there are two ages of lithospheric mantle beneath Fansi: refractory mantle that underwent melt depletion in the Neoarchean-Paleoproterozoic (~2.2 to 2.5 Ga), like peridotites from the southern region, and more fertile mantle that underwent melt depletion in the late Paleoproterozoic (~1.8 Ga). No clear correlation is observed between calculated equilibrium temperatures and ages, suggesting that ancient, refractory, and younger, fertile mantle may not be stacked upon one another, but are probably interleaved.

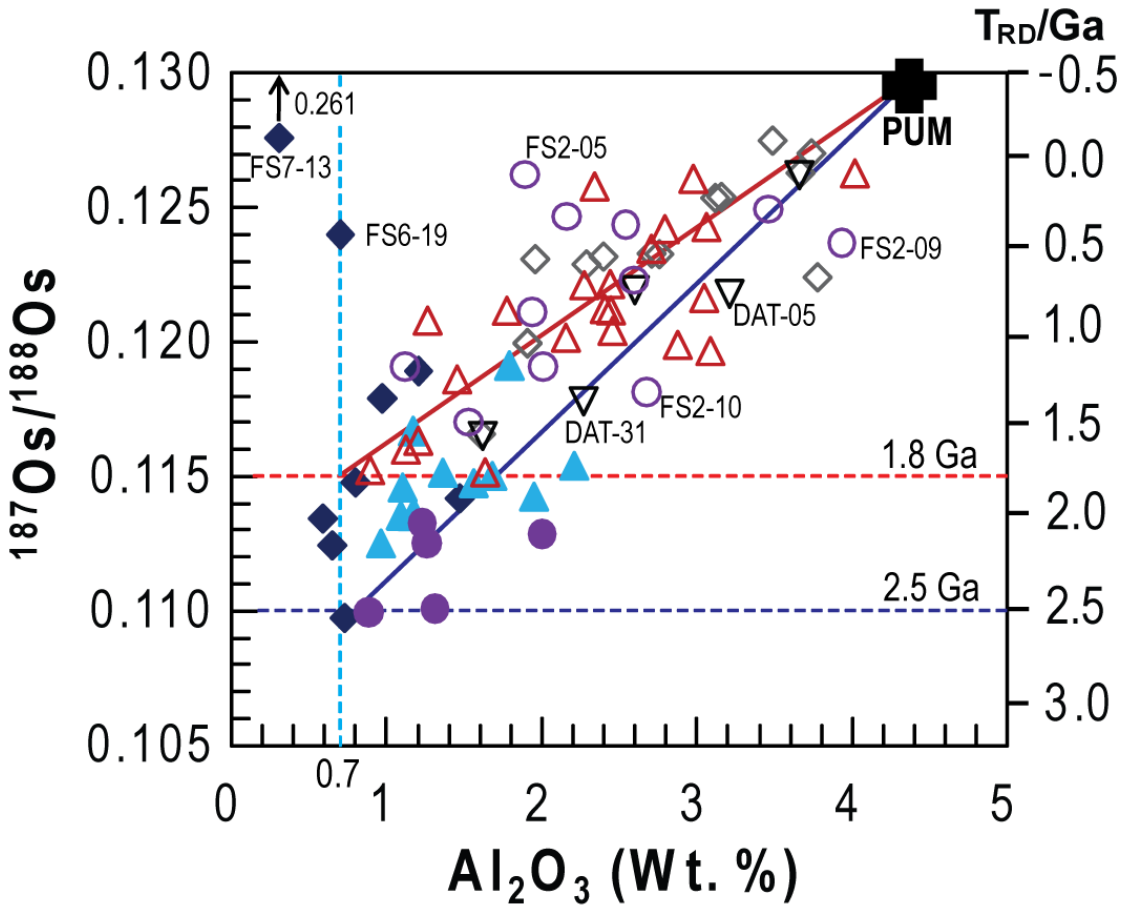

Fig. 4-8. Whole rock Al_2O_3 versus $^{187}Os/^{188}Os$ of peridotites. The majority of samples from Datong, Hannuoba (Meisel et al., 2001; Gao et al., 2002; Becker et al., 2006; Liu et al., 2010), Yangyuan (Liu et al., 2010), and Fansi low-Fo group follow the upper curve of melt depletions trends, while some outliers are detailed in the text. Samples from Fushan, Hebi and Fansi high-Fo group tend to evolve from more ancient mantle sources as outlined by the lower curve of melt depletion trends. Samples from Jining are not plotted in this diagram due to abnormal Al_2O_3 contents. PUM: Meisel et al., 2001 (for $^{187}Os/^{188}Os$) and McDonough and Sun, 1995 (for Al_2O_3). Symbols as in Fig. 4-4. The vertical dashed line is Al_2O_3 of 0.7%, below which it has been proposed that peridotites lose all Re (Handler et al., 1997). Upper and lower dashed lines indicate the initial $^{187}Os/^{188}Os$ of upper and lower curves of melt depletion trends, respectively. Model T_{RD} ages are calculated based on a chondritic mantle of $^{187}Os/^{188}Os$=0.127 and $^{187}Re/^{188}Os$=0.402 (Shirey and Walker, 1998).

4.5.3 Tectonic implications

The age constraints discussed above document two ages of lithospheric mantle beneath the central North China Craton: at ~1.8 Ga in the north, and at ~2.5 Ga in the south, with a boundary between these two age provinces running through the Fansi locality (Figs. 4-1 and 4-9). These ages provide information about the tectonic history of this section of the North China Craton and, combined with equilibrium temperatures, the timing of lithospheric thinning beneath this portion of the craton.

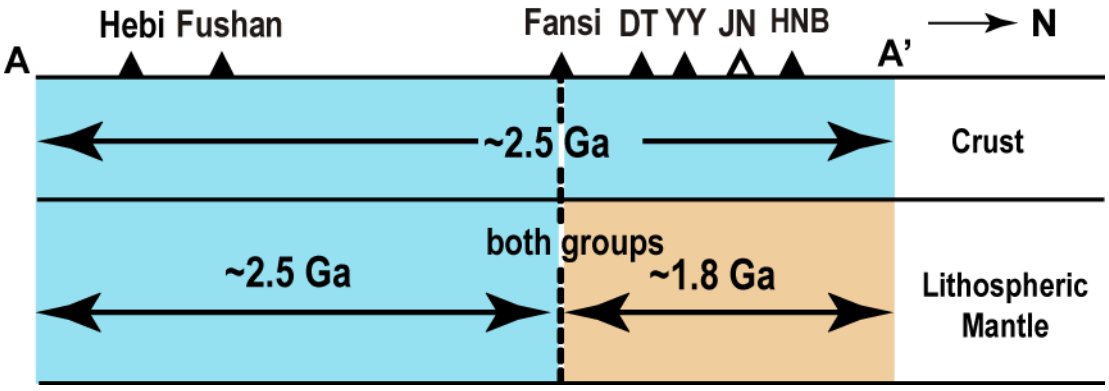

Fig. 4-9. The age dichotomy of crust and lithospheric mantle beneath the central North China Craton along the profile A-A' (see Fig. 4-1). HNB: Hannuoba; JN: Jining; YY: Yangyuan; and DT: Datong.

4.5.3.1 Precambrian tectonics in central North China Craton

The similarity between the age of the crust and lithospheric mantle in the southern region (Neoarchean to Early Paleoproterozoic) suggests that ~2.5 Ga represents the time of cratonization of this portion of the North China Craton (Wu et al., 2005b; Liu et al., 2009). By contrast, the decidedly younger lithospheric mantle underlying Archean crust in the northern region points to replacement of the original Archean

lithospheric mantle at ~1.8 Ga. Several mechanisms have been advanced to explain younger lithospheric mantle underlying older continental crust, including thermal/chemical erosion (e.g., Griffin et al., 1998; Zheng et al., 2001), density foundering (often referred to as "delamination", (Kay and Kay, 1993; Lee et al., 2000; Gao et al., 2002; Wu et al., 2006), lateral escape during collision (Menzies et al., 1993; Wu et al., 2006), and transformation through refertilization (e.g., Zhang et al., 2002, 2009). Of these, only density foundering can explain removal of the entire Archean lithospheric mantle and its replacement by juvenile mantle in the Paleoproterozoic; the other mechanisms would presumably predict preservation of relict Archean lithospheric mantle at shallow depths beneath the region, which is not observed in the xenolith suites.

Previous studies of metamorphic crustal rocks have documented widespread regional granulite facies metamorphism at ~1.8-1.9 Ga in the northern region as well as the Khondalite Belt (e.g., Zhao et al., 2005, and references therein). These metamorphic rocks record clockwise P-T paths that are interpreted to have resulted from continent-continent collisional event(s). Thus, the ~1.8 Ga lithospheric mantle replacement could be the result of the ~1.8-1.9 Ga continent-continent collision(s). However, it is currently debated how the collisional processes proceeded in the tectonic framework of the North China Craton (e.g., Kusky and Li, 2003; Zhai and Liu, 2003; Zhao et al., 2005; Kusky, 2011).

Zhao and co-workers suggest that there were two separate collisional events in this region: one at ~1.95 Ga resulting in the formation of the Khondalite Belt, which marks the amalgamation of the Western Block, and a second at ~1.85 Ga, when the Western and Eastern blocks collided to form the Trans-North China Orogen,

representing the final assembly of the North China Craton (Zhao et al., 2005, and references therein; Fig. 4-1a). However, this tectonic scenario does not explain the north-south age dichotomy of the lithospheric mantle documented here (Fig. 4-9). For example, why would the lithospheric mantle replacement occur only in the northern region, not throughout the entire Trans-North China Orogen? One possible explanation is that lithospheric replacement was caused by greater shortening in the north than in the south of the Trans-North China Orogen. This appears to be broadly consistent with the current geometry of the Trans-North China Orogen, with the northern section narrower than the southern (Fig. 4-1a). Another possibility is that the Late Paleoproterozoic age of lithospheric mantle in the north was the result of extrusion of ~1.9 Ga lithosphere from the Khondalite Belt beneath the northern Trans-North China Orogen during the ~1.85 Ga collision of the Western and Eastern blocks (Fig. 4-1a), assuming that the Khondalite belt formed earlier than the Trans-North China Orogen (e.g., Yin et al., 2009; Zhao et al., 2010).

Alternatively, Kusky et al. (2001, 2007b) suggest that the central North China Craton marks the site of collision of the Eastern and Western blocks at ~2.5 Ga. The craton later experienced a major ~1.8-1.9 Ga continent-continent collision event along the northern margin during amalgamation of the Columbia supercontinent (Kusky, 2011, and references therein). In the Kusky model, the Khondalite Belt constitutes part of the Paleoproterozoic continent-continent collision in the northern North China Craton (Fig. 4-1b). In this scenario, the observed north-south age dichotomy of lithospheric mantle would reflect removal of the original Neoarchean lithospheric mantle and replacement of juvenile mantle along the northern margin of the craton due to the 1.8-1.9 Ga continent-continent collision, while the lithospheric mantle in

the southern region reflects its preservation since it formed during the ~2.5 Ga collision between the Eastern and Western blocks of the craton.

In summary, any model that seeks to explain the assembly history of the North China Craton should be able to predict the age dichotomy of lithospheric mantle documented here. While these data cannot currently be used to eliminate either tectonic model for the central North China Craton, aspects of the Kusky model would seem to fit the observations with little special pleading. In this scenario, Fansi would mark the northern boundary of lithospheric replacement that occurred due to collision along the northern margin of the North China Craton during the Paleoproterozoic assembly of the Columbia supercontinent. Alternatively, if the Zhao model is correct, the age dichotomy of lithospheric mantle in the central region would require either significant differences in the degree of lithospheric shortening from north to south in the Trans-North China Orogen, resulting in lithospheric removal in the north, but not the south, or extrusion of ~1.9 Ga lithosphere from the Khondalite Belt beneath the northern Trans-North China Orogen during the ~1.85 Ga continental collision between Eastern and Western blocks, with Fansi marking the southern boundary.

4.5.3.2 Timing of Phanerozoic lithospheric thinning

Lithospheric thinning beneath the eastern North China Craton occurred largely in the Mesozoic, as reflected by the timing of the magmatic flare-up that occurred throughout the Eastern Block (e.g., Xu, 2001; Wu et al., 2005a) and the change in lithospheric mantle composition reflected by xenolithic peridotites carried by Ordovician kimberlites and those in Tertiary alkali basalts (e.g., Menzies et al., 1993; Griffin et al., 1998; Chu et al., 2009). However, the exact timing, geometry and

vertical and lateral extent of thinning/replacement is still emerging, largely from studies of mantle xenoliths.

Mantle xenoliths found in a few Mesozoic localities provide important insights into the spatial and temporal signature of the thinning. For example, peridotites from the eastern edge of the North China Craton hosted by Triassic Korean kimberlites (Fig. 4-1) are characterized by elemental and Os isotopic compositions similar to modern convective mantle (Yang et al., 2010), suggesting that the lithospheric removal and replacement occurred no later than the Triassic beneath this region. Xenoliths in the Early Cretaceous Fuxin (~100 Ma) and Laiwu (124-133 Ma) localities, both of which occur in the center of the Eastern Block (Fig. 4-1), sample fragments of refractory, Archean lithospheric mantle but also appear to contain a proportion of fertile peridotites (Zheng et al., 2007; Gao et al., 2008), which can be interpreted to suggest that the mantle replacement was on-going during that time. In addition, unusual compositions of Mesozoic magmas in this region suggest that density foundering was occurring beneath the Eastern Block during the Late Jurassic to Early Cretaceous (Gao et al., 2004; 2008).

The data presented here shed additional light on the timing of lithospheric thinning beneath the North China Craton. Xenolithic samples from Fushan, which erupted at 125 Ma on the western boundary of the Eastern Block, are predominantly composed of highly refractory peridotites with Neoarchean to Early Paleoproterozoic Os model ages. This, together with very low estimated equilibrium temperatures (620-720^{o}C), suggests the presence of thick, cold, refractory Archean lithospheric mantle, which, in turn, indicates that lithospheric thinning probably commenced after 125 Ma in this region.

By contrast, peridotites from the nearby 4 Ma Hebi locality are also fragments of refractory Archean lithospheric mantle (Zheng et al., 2001, 2007; this study), but they have significantly higher equilibrium temperatures (1020-1090ºC). The lack of garnet in these peridotites limits their equilibrium depths to <100 km (O'Neill, 1981). Thus, the contrast in equilibrium temperatures between Fushan and Hebi presumably reflects an increase in the geotherm associated with lithospheric thinning, implying that complete lithospheric removal did not occur in this region, but the lithosphere was significantly thinned after the Early Cretaceous. Combining all observations, a picture begins to emerge of lithospheric thinning/removal commencing from east (Triassic, Yang et al., 2010) to west (<125 Ma, this study) in the North China Craton during the Mesozoic, with complete removal of the ancient lithospheric mantle in the east, and partial removal in the west.

4.6 Conclusions

The data reported here for nearly 100 peridotitic xenoliths from seven suites within the central North China Craton allow us to map lithospheric boundaries in this region. These data, in turn, shed light on the Precambrian accretion history of the craton, as well as Mesozoic to Tertiary thinning.

1) Peridotites from the northern region are generally more fertile than those from the south, and have maximum T_{RD} model ages suggesting their coeval formation at ~1.8 Ga. By contrast, peridotites from the southern region have older (2.1 to 2.5 Ga) maximum T_{RD} model ages. Peridotites with model ages of both groups are found at Fansi. Thus, there was diachronous formation of lithospheric mantle from north to south, with the boundary at or near Fansi.

2) Crust and lithospheric mantle have the same age in the southern region, whereas the lithospheric mantle is significantly younger than the overlying crust in the northern region. The coupled Neoarchean crust and mantle in the southern region marks the time of cratonization in this region. The crust-mantle decoupling in the north documents lithospheric mantle replacement at ~1.8 Ga, likely resulting either from a ~1.8-1.9 Ga continent-continent collision associated with amalgamation of the Columbia supercontinent, or from a large difference in the degree of tectonic shortening from north (more) to south (less), or extrusion of ~1.9 Ga lithosphere from the Khondalite Belt beneath the northern Trans-North China Orogen, during the ~1.85 Ga continental collision between Eastern and Western blocks.

3) The age structure of lithospheric mantle beneath the North China Craton recorded in mantle xenoliths erupted from the Paleozoic, through Mesozoic to Cenozoic, suggests that lithospheric thinning and replacement may have evolved from east to west with time, starting with mantle lithosphere removal before the Triassic on the eastern edge of the craton in the Korean peninsula, occurring during the Jurassic-Cretaceous within the interior of the Eastern Block, to thinning that post-dates 125 Ma on the westernmost boundary of the Eastern Block.

Supplemental Material for Chapter 4

Table S4-1. Modal mineralogy of the xenolithic peridotites from the North China Craton

Locality	Lithology	maximum length*	ol	opx	cpx	sp
Hannuoba						
DMP 04	lherzolite	N/A	67.6	21.9	8.9	1.6
DMP 19	lherzolite	N/A	61.6	29.8	7.8	0.8
DMP 25	harzburgite	N/A	70.5	24.2	3.8	1.5
DMP 41	lherzolite	N/A	57.6	30.9	9.6	1.9
DMP 51	lherzolite	N/A	64.5	27.0	7.6	0.9
DMP 56	lherzolite	N/A	54.9	27.7	15.3	2.1
DMP 58	lherzolite	N/A	56.6	28.4	13.0	2.0
DMP 60	lherzolite	N/A	44.7	37.4	16.1	1.8
DMP 67c	lherzolite	N/A	56.1	27.8	12.9	3.2
Yangyuan						
YY-04	harzburgite	4	69.6	25.5	4.3	0.6
YY-08	lherzolite	10	58.8	32.6	5.5	3.1
YY-09	lherzolite	8	72.6	21.1	5.4	0.9
YY-11	harzburgite	4	76.9	20.1	1.7	1.3
YY-13	lherzolite	35	69.2	21.4	7.9	1.4
YY-22	lherzolite	9	67.5	23.8	7.3	1.5
YY-23	lherzolite	5	67.2	26.9	5.5	0.5
YY-26	lherzolite	15	65.1	24.0	8.7	2.2
YY-27	lherzolite	10	67.1	22.0	8.0	3.0
YY-36	lherzolite	7	69.6	18.6	10.5	1.3
YY-40B	lherzolite	11	65.6	23.6	8.8	1.9
YY-42	harzburgite	8	74.6	19.5	4.0	1.8
YY-45	lherzolite	5	69.0	23.2	6.8	1.0
YY-50	lherzolite	5	52.0	30.3	16.1	1.6
YY-51	harzburgite	4	78.3	17.1	2.1	2.6
YY-52	lherzolite	5	67.7	22.7	8.7	0.9
YY-58	harzburgite	10	75.8	19.7	3.4	1.0
YY-60	harzburgite	4	78.3	16.8	3.9	0.9
Datong						
DAT-05	lherzolite	3.5	64.9	30.7	3.7	0.7
DAT-09	harzburgite	2.5	89.3	8.4	1.1	1.2
DAT-15	lherzolite	2	77.9	9.3	12.2	0.6
DAT-30	harzburgite	2	82.7	16.2	1.0	0.1
DAT-31	lherzolite	3	66.7	23.9	7.4	1.9
Jining						
JN-01	harzburgite	9	82.0	13.0	3.6	2.1
JN-02	harzburgite	7	77.0	17.0	4.7	1.2
JN-06	harzburgite	6	62.2	33.4	3.5	0.8
JN-16	lherzolite	4.5	87.4	4.8	6.3	1.6
JN-17	lherzolite	4	79.0	12.6	6.9	1.5

Note: ol: olivine, opx: orthopyroxene, cpx: clinopyroxene, and sp: spinel.

Table S4-1. *continued*

Locality	Lithology	maximum length*	ol	opx	cpx	sp
JN-19	harzburgite	7	71.8	23.5	4.4	0.3
JN-26	harzburgite	8	80.4	13.4	4.4	1.8
JN-27	lherzolite	7	75.3	11.1	10.9	2.7
JN-29	lherzolite	6	78.7	13.7	6.2	1.4
JN-31	lherzolite	7	79.7	12.2	6.9	1.2
JN-35	lherzolite	7	80.1	10.3	7.6	2.0
JN-52	lherzolite	6	80.1	13.5	5.4	0.9
Fansi						
FS-01	lherzolite	8	73.7	16.9	7.9	1.4
FS-04(2)		4				
FS-18	harzburgite	6	63.1	36.9	0.0	0.0
FS-36	lherzolite	3	66.3	22.8	9.8	1.0
FS-42	harzburgite	3	60.3	38.4	0.9	0.5
FS-43	harzburgite	4	78.7	19.7	1.5	0.1
FS-44	lherzolite	3	67.8	20.2	10.6	1.5
FS-45	lherzolite	3	75.0	15.0	8.3	1.7
FS-50	lherzolite	5	69.8	20.4	7.0	2.8
FS-62	harzburgite	6	73.8	24.5	0.9	0.8
FS-68	lherzolite	5	89.1	7.5	3.1	0.3
FS2-04	harzburgite	7	84.9	12.7	1.9	0.4
FS2-05	lherzolite	5	70.8	18.8	7.7	2.7
FS2-09	lherzolite	4	68.4	19.5	10.6	1.5
FS2-10	lherzolite	3	69.6	13.8	15.3	1.3
Hebi						
HB-09	dunite	drill	96.5	3.4	0.0	0.1
HB-10	harzburgite	drill	73.4	26.6	0.0	0.0
HB-12	harzburgite	drill	78.5	21.0	0.3	0.2
HB-13	lherzolite	drill	86.2	11.3	2.2	0.2
HB-15	lherzolite	drill	68.0	29.6	1.8	0.7
HB-21-2	dunite	drill	93.2	6.7	0.0	0.1
HB-22	harzburgite	drill	84.7	11.0	4.0	0.3
HB-24	dunite	drill	93.7	4.5	0.4	1.5
Fushan						
FS7-13	dunite	N/A	97.5	0.0	0.0	2.5
FS6-19	dunite	N/A	91.2	8.8	0.0	0.0
FS7-10	harzburgite	N/A	87.6	9.5	1.1	1.6
FS6-56	harzburgite	N/A	87.5	8.0	1.7	2.0
FS6-18	harzburgite	N/A	85.6	8.0	3.3	2.6
FS6-29	harzburgite	N/A	81.9	12.3	3.4	2.4
FS6-55	lherzolite	N/A	79.4	11.1	6.7	2.0
FS7-1	lherzolite	N/A	80.8	10.6	5.6	3.0
FS7-9	lherzolite	N/A	83.3	11.2	5.0	0.6

Note: Modal mineral contents were calculated by point counting (4000 to 9000 counts).

Data sources in addition to this study: Hannuoba (Rudnick et al., 2004) and Fushan (Xu et al., 2010)

* The maximum length of the sample indicates its size, as most of samples are nearly round-shaped. However, the Jining samples are generally very thin, yielding a few grams of powder, although their maximum length is not very small. Hebi samples were all drilled. They are small, around ~2 to 4 cm in length. Fushan samples range from 3 to 7 cm in the maximum dimension, while Hannuoba samples vary from a few centimeters up to 60 cm.

Table S4-2a. Olivine compositions of peridotites from Hannuoba

Sample	Points	SiO2	FeO	MgO	CaO	NiO	MnO	Total	Mg#
HNB2	2	40.6	10.63	48.37				99.6	89.0
HNB3	2	40.7	10.10	48.76				99.5	89.6
HNB4	2	40.8	9.01	49.36				99.2	90.7
HNB5A	2	40.8	8.23	50.11				99.1	91.6
HNB5B	2	40.9	8.55	49.93				99.4	91.2
HNB5C	2	40.8	9.21	49.19				99.2	90.5
HNB5D	2	41.1	7.68	50.31				99.1	92.1
HNB5E	2	41.2	8.37	50.14				99.7	91.4
HNB6	2	40.9	8.82	49.72				99.4	90.9
HNB7	2	41.0	8.71	50.05				99.8	91.1
HNB8	2	40.9	10.39	48.82				100.1	89.3
HNB9	2	41.2	8.56	50.37				100.1	91.3
HNB10	2	40.8	9.57	49.38				99.8	90.2
HNB11	2	41.1	9.06	49.88				100.1	90.8
HNB12	2	41.0	10.28	49.06				100.3	89.5
HNB13	2	41.0	8.66	50.19				99.9	91.2
HNB14	2	40.9	9.01	49.95				99.9	90.8
HNB15	2	41.4	7.99	50.65				100.0	91.9
HNB16	2	40.8	9.16	49.44				99.4	90.6
HNB17	2	40.8	8.61	49.72				99.1	91.1
HNB18	2	40.8	8.95	49.37				99.1	90.8
HNB19	2	41.0	8.03	50.10				99.2	91.7
HNB20	2	40.4	10.16	48.37				98.9	89.5
HNB21	2	40.8	8.03	50.00				98.9	91.7
HNB22	2	40.7	8.69	49.41				98.8	91.0
HNB23	2	40.5	8.94	49.09				98.5	90.7
HNB24	2	40.5	10.50	47.94				98.9	89.1
HNB25	2	41.5	8.74	50.75				101.0	91.2
HNB 26	2	41.3	10.25	49.20				100.7	89.5
HNB27	2	41.4	8.91	50.17				100.4	90.9
HNB29	2	41.5	9.60	49.60				100.7	90.2
HNB30	2	41.5	8.96	50.02				100.5	90.9
HNB31	2	41.5	9.15	50.01				100.6	90.7
HNB32	2	41.3	8.39	50.43				100.2	91.5
HNB33	2	41.3	9.24	49.81				100.3	90.6
HNB34	2	41.3	8.88	49.96				100.1	90.9
HNB35	2	41.0	8.51	49.68				99.2	91.2
HNB36	2	41.1	8.92	49.59				99.6	90.8
HNB38	2	41.4	7.80	50.29				99.5	92.0
HNB39	2	40.9	8.77	49.65				99.4	91.0
HNB40	2	41.3	8.34	50.22				99.8	91.5
HNB41	2	41.1	9.13	49.59				99.8	90.6
HNB42	2	41.1	9.51	49.16				99.7	90.2
HNB43	2	41.1	8.59	49.78				99.5	91.2
HNB44	2	41.2	9.46	49.53				100.2	90.3
HNB45	2	41.2	8.02	50.47				99.7	91.8
HNB46	2	41.4	8.69	50.20				100.3	91.1
HNB48	2	41.4	8.55	50.48				100.5	91.3
HNB49	2	41.4	8.22	50.62				100.3	91.6
HNB50	2	41.4	9.07	49.81				100.2	90.7
HNB51	2	41.4	9.64	49.46				100.5	90.1
HNB52	2	40.9	11.15	48.59				100.7	88.6
HNB54	2	41.1	10.30	48.86				100.3	89.4
HNB55	2	40.7	10.16	48.60				99.5	89.5
HNB56	2	41.1	7.83	50.45				99.4	92.0

HNB57	2	40.9	9.71	49.10			99.8	90.0
HNB58	2	40.7	9.32	49.26			99.3	90.4

Table S4-2b. Olivine compositions of peridotites from Yangyuan

Sample	Points	SiO2	FeO	MgO	CaO	NiO	MnO	Total	Fo
YY-01	2	41.0	9.89	49.5	0.04		0.12	100.5	89.9
YY-02	2	40.9	8.97	50.1	0.06		0.09	100.1	90.9
YY-03	2	40.7	9.38	50.0	0.05		0.15	100.3	90.5
YY-04	2	41.2	7.96	51.1	0.04		0.14	100.4	92.0
YY-06	2	40.6	8.99	50.1	0.02		0.11	99.9	90.9
YY-07	2	40.8	9.01	50.3	0.02		0.12	100.2	90.9
YY-08	2	40.6	9.38	49.9	0.02		0.13	100.1	90.5
YY-09	2	40.7	8.98	50.2	0.05		0.15	100.1	90.9
YY-10	2	40.9	9.07	50.2	0.03		0.11	100.3	90.8
YY-11	2	40.8	9.03	50.0	0.05		0.16	100.1	90.8
YY-12	2	40.8	8.74	50.3	0.02		0.11	100.0	91.1
YY-13	2	40.8	8.91	50.1	0.05		0.12	100.0	90.9
YY-14	2	41.1	8.65	50.4	0.06		0.08	100.3	91.2
YY-15	2	40.7	8.93	49.7	0.03		0.15	99.4	90.8
YY-16	2	40.6	8.54	50.1	0.05		0.11	99.4	91.3
YY-17	2	40.2	8.99	49.7	0.04		0.15	99.1	90.8
YY-18	2	40.5	8.88	49.8	0.08		0.13	99.4	90.9
YY-18B	2	40.4	8.83	49.8	0.03		0.13	99.2	91.0
YY-18C	2	40.8	9.06	49.7	0.06		0.13	99.7	90.7
YY-19A	2	40.5	8.86	49.7	0.05		0.11	99.2	90.9
YY-19B	4	40.8	8.40	50.1	0.04		0.11	99.5	91.4
YY-20A	2	40.6	8.82	49.7	0.06		0.12	99.3	90.9
YY-20B	2	40.6	8.69	50.2	0.07		0.10	99.6	91.2
YY-20C	2	40.4	9.35	49.4	0.03		0.14	99.4	90.4
YY-21	2	40.7	9.20	50.0	0.05		0.14	100.0	90.6
YY-22	2	40.5	8.62	50.0	0.02		0.13	99.2	91.2
YY-23	2	40.5	9.03	50.3	0.10		0.13	100.1	90.8
YY-24	2	40.8	8.54	50.4	0.02		0.12	99.9	91.3
YY-25	2	40.9	8.74	50.4	0.03		0.15	100.2	91.1
YY-25A	2	41.0	8.23	50.7	0.02		0.12	100.1	91.6
YY-25B	2	40.8	8.61	50.3	0.04		0.13	99.9	91.2
YY-26	2	40.7	9.18	50.2	0.03		0.14	100.2	90.7
YY-27	2	40.4	9.67	49.7	0.01		0.15	99.9	90.2
YY-28A	2	40.6	8.73	50.0	0.06		0.09	99.4	91.1
YY-28B	2	40.8	8.92	50.4	0.04		0.12	100.3	91.0
YY-28C	2	40.9	8.17	51.1	0.04		0.11	100.3	91.8
YY-29	2	40.7	8.98	50.1	0.06		0.09	99.9	90.9
YY-30	2	40.9	8.58	50.7	0.04		0.15	100.3	91.3
YY-31	2	40.9	8.62	50.7	0.08		0.12	100.4	91.3
YY-32	2	40.5	8.69	49.7	0.11		0.10	99.1	91.1
YY-33	2	40.5	8.86	50.0	0.06		0.13	99.6	91.0
YY-34	2	40.5	9.06	49.7	0.03		0.13	99.5	90.7
YY-35A	2	40.4	9.25	49.7	0.03		0.17	99.6	90.5
YY-35B	2	40.6	8.67	49.8	0.04		0.12	99.2	91.1
YY-36	2	40.7	8.72	50.0	0.02		0.12	99.6	91.1
YY-37A	2	40.5	8.56	50.2	0.08		0.14	99.5	91.3
YY-37B	2	40.7	8.98	50.0	0.02		0.16	99.8	90.8
YY-38	2	40.5	8.59	50.2	0.05		0.12	99.5	91.2
YY-39	2	40.3	9.20	49.6	0.02		0.13	99.3	90.6
YY-40A	2	40.6	8.97	49.8	0.07		0.12	99.6	90.8
YY-40B	2	40.6	8.64	50.2	0.01		0.13	99.6	91.2

YY-41	2	40.4	9.02	49.9	0.07		0.16	99.6	90.8
YY-42	2	40.3	8.71	49.6	0.05		0.13	98.7	91.0
YY-43	2	40.5	9.17	49.4	0.01		0.14	99.2	90.6
YY-44	2	40.3	8.86	49.5	0.07		0.13	98.9	90.9
YY-45	2	40.5	8.90	49.3	0.09		0.12	99.0	90.8
YY-46	2	40.3	8.62	49.7	0.04		0.14	98.8	91.1
YY-47	2	40.4	8.68	49.7	0.09		0.13	99.0	91.1
YY-48	2	39.7	12.15	47.1	0.01		0.19	99.2	87.4
YY-50	2	40.3	9.07	49.3	0.03		0.10	98.8	90.6
YY-51	2	40.4	8.18	50.3	0.04		0.12	99.0	91.6
YY-52	2	40.3	8.94	49.3	0.07		0.13	98.8	90.8
YY-53	2	40.6	8.97	49.7	0.05		0.09	99.4	90.8
YY-54	2	40.4	8.87	48.9	0.08		0.13	98.4	90.8
YY-55	2	40.3	8.92	49.5	0.05		0.13	98.9	90.8
YY-56A	2	40.5	8.91	49.3	0.07		0.13	98.9	90.8
YY-56B	2	40.7	8.47	49.7	0.03		0.13	99.0	91.3
YY-57	2	40.7	8.33	49.4	0.01		0.15	98.6	91.4
YY-58	2	40.9	8.04	49.5	0.08		0.13	98.7	91.7
YY-59	2	40.7	8.73	49.4	0.05		0.16	99.0	91.0
YY-60	2	40.8	8.30	49.5	0.05		0.13	98.7	91.4
YY-61	2	40.7	8.74	49.4	0.02		0.13	99.0	91.0
YY-62a	3	40.8	7.94	49.9	0.06		0.13	98.9	91.8
YY-62b	2	40.3	9.94	48.3	0.01		0.13	98.7	89.7
YY-63	2	40.6	8.89	49.0	0.02		0.17	98.8	90.8
YY-64	2	40.5	9.32	49.3	0.05		0.14	99.3	90.4
YY-65	2	40.3	9.02	49.9	0.07		0.13	99.4	90.8
YY-66	2	40.3	9.35	49.3	0.05		0.14	99.2	90.4
YY-70	2	40.5	8.82	49.9	0.04		0.10	99.3	91.0
YY-71	2	40.5	8.35	50.0	0.06		0.13	99.0	91.4

Table S4-2c. Olivine compositions of peridotites from Datong

Sample	Points	SiO2	FeO	MgO	CaO	NiO	MnO	Total	Fo
DAT-01	2	40.6	8.47	49.6	0.06		0.13	98.9	91.3
DAT-02	2	40.5	8.91	49.4	0.04		0.13	99.0	90.8
DAT-03	1	40.8	7.94	50.4	0.03		0.09	99.3	91.9
DAT-04	2	40.5	9.37	49.3	0.05		0.15	99.4	90.4
DAT-05	2	40.5	8.27	49.8	0.06		0.15	98.8	91.5
DAT-06	2	40.5	8.66	49.9	0.04		0.14	99.3	91.1
DAT-07	2	40.6	8.42	50.0	0.05		0.12	99.2	91.4
DAT-08	2	40.5	8.91	49.5	0.07		0.14	99.1	90.8
DAT-09	2	40.3	8.15	50.1	0.06		0.13	98.7	91.6
DAT-10	2	40.9	7.80	50.4	0.03		0.13	99.2	92.0
DAT-11	2	40.5	8.50	49.8	0.08		0.13	99.0	91.3
DAT-12	2	40.6	8.53	49.6	0.04		0.14	98.9	91.2
DAT-13	2	40.4	8.44	49.7	0.06		0.13	98.7	91.3
DAT-14	2	40.6	8.77	49.3	0.04		0.12	98.9	90.9
DAT-15	5	40.7	8.96	49.4		0.41	0.12	99.6	90.8
DAT-16	2	40.5	9.52	48.7	0.06		0.15	99.0	90.1
DAT-17	2	40.5	8.66	48.9	0.05		0.13	98.3	91.0
DAT-18	2	40.3	9.00	48.9	0.04		0.14	98.3	90.6
DAT-19	2	40.3	9.71	48.3	0.05		0.16	98.5	89.9
DAT-20	2	40.4	8.92	49.1	0.05		0.09	98.5	90.7
DAT-21	2	40.2	8.68	49.1	0.03		0.12	98.1	91.0
DAT-22	2	40.3	8.53	49.0	0.07		0.11	98.1	91.1

DAT-23	2	40.5	8.71	48.6	0.07		0.14	98.0	90.9
DAT-24	2	40.4	8.69	49.1	0.05		0.12	98.4	91.0
DAT-26	2	40.4	8.84	49.0	0.05		0.17	98.4	90.8
DAT-27	2	40.3	8.27	49.1	0.05		0.13	97.8	91.4
DAT-28	2	40.5	8.85	49.1	0.05		0.11	98.6	90.8
DAT-29	2	40.3	9.37	49.0	0.06		0.13	98.8	90.3
DAT-30	5	40.9	8.11	50.4		0.41	0.12	99.9	91.7
DAT-31	5	40.7	8.73	50.0		0.38	0.12	99.9	91.1
DAT2-01	2	40.6	8.46	50.6	0.05		0.13	99.8	91.4
DAT2-02	2	41.0	7.99	51.1	0.05		0.11	100.2	91.9
DAT2-03	2	40.9	8.46	50.7	0.08		0.12	100.3	91.4
DAT2-04	2	40.9	8.57	50.6	0.07		0.11	100.3	91.3
DAT3-01	2	40.4	8.36	50.6	0.04		0.14	99.5	91.5
DAT3-02	2	40.7	9.06	50.0	0.04		0.16	100.0	90.8
DAT3-03	2	40.7	8.93	50.3	0.05		0.16	100.2	90.9
DAT3-04	2	40.6	9.44	49.8	0.05		0.08	100.0	90.4
DAT3-05	2	40.5	8.85	49.9	0.04		0.14	99.4	90.9
DAT3-06	2	40.5	8.90	50.3	0.05		0.11	99.9	91.0
DAT3-07	2	40.5	8.52	49.8	0.05		0.10	98.9	91.2
DAT3-08	2	40.7	8.38	50.4	0.04		0.14	99.7	91.5
DAT3-09	2	40.8	9.12	50.2	0.07		0.11	100.3	90.8
DAT3-10	2	40.4	9.39	49.8	0.04		0.15	99.7	90.4
DAT3-11A	2	40.8	8.55	50.6	0.05		0.11	100.0	91.3
DAT3-11B	2	41.0	7.66	51.1	0.05		0.12	99.9	92.2
DAT3-12	2	40.4	9.68	49.5	0.08		0.17	99.9	90.1
DAT3-13	2	40.7	9.21	50.0	0.06		0.11	100.1	90.6
DAT3-14	2	40.6	9.17	49.9	0.05		0.13	99.8	90.7
DAT3-15	2	40.6	9.07	49.9	0.02		0.13	99.7	90.7
DAT3-16	2	40.6	9.06	49.9	0.04		0.11	99.7	90.8
DAT3-17	2	40.7	8.98	50.1	0.06		0.14	100.0	90.9
DAT3-18	2	40.2	8.86	49.4	0.07		0.13	98.6	90.9
DAT3-19	2	40.3	8.78	49.9	0.05		0.15	99.2	91.0
DAT3-20	2	40.1	8.80	49.8	0.05		0.14	98.9	91.0
DAT3-21	2	40.2	9.47	49.3	0.05		0.08	99.2	90.3
DAT3-22	2	40.3	9.21	49.3	0.06		0.11	98.9	90.5
DAT3-23	2	40.4	8.74	49.9	0.06		0.11	99.2	91.1
DAT3-24	2	40.3	8.22	50.2	0.04		0.14	98.9	91.6
DAT3-25	2	40.5	8.33	50.1	0.03		0.12	99.1	91.5
DAT3-26	2	40.2	9.45	49.5	0.07		0.15	99.4	90.3
DAT3-27	2	40.6	7.95	50.9	0.05		0.13	99.7	92.0
DAT3-28A	1	41.1	8.47	51.4	0.04		0.09	101.0	91.5
DAT3-28B	2	40.6	10.67	49.5	0.15		0.15	101.1	89.2
DAT3-29	2	40.6	9.21	50.5	0.05		0.17	100.5	90.7
DAT3-30	2	40.7	8.69	50.9	0.02		0.12	100.4	91.3
DAT3-31	2	40.6	9.36	50.5	0.05		0.13	100.6	90.6
DAT3-32	2	41.1	8.38	51.2	0.06		0.14	100.8	91.6

Table S4-2d. Olivine compositions of peridotites from Jining

Sample	Points	SiO2	FeO	MgO	CaO	NiO	MnO	Total	Fo
JN-01	4	40.4	8.97	49.1	0.04		0.13	98.6	90.7
JN-02	3	40.9	8.93	49.9	0.03		0.17	99.9	90.9
JN-03	3	41.0	8.81	49.2	0.04		0.12	99.2	90.9
JN-04	3	40.6	8.90	49.4	0.03		0.14	99.1	90.8
JN-05	3	41.0	9.28	49.3	0.02		0.14	99.7	90.5

JN-06	2	41.1	9.00	49.4	0.05	0.15	99.7	90.7
JN-07	3	40.7	9.24	49.3	0.04	0.12	99.4	90.5
JN-08	3	41.1	9.18	48.9	0.04	0.12	99.4	90.5
JN-09	4	41.0	9.34	49.6	0.05	0.14	100.1	90.4
JN-10	3	41.1	9.44	49.8	0.02	0.15	100.5	90.4
JN-11	3	41.1	9.13	49.6	0.03	0.15	100.0	90.6
JN-12	3	41.1	8.63	49.9	0.01	0.13	99.8	91.2
JN-13A	3	41.0	8.96	50.0	0.03	0.11	100.2	90.9
JN-13B	2	40.8	8.90	49.9	0.03	0.12	99.7	90.9
JN-13C	3	41.0	8.85	49.7	0.02	0.13	99.7	90.9
JN-14A	4	40.8	9.49	49.5	0.03	0.12	100.0	90.3
JN-14B	3	40.9	9.75	49.0	0.02	0.11	99.8	90.0
JN-15	3	41.0	9.47	49.3	0.03	0.16	99.9	90.3
JN-16	2	40.9	9.28	49.4	0.02	0.13	99.8	90.5
JN-17	2	40.3	11.63	47.5	0.04	0.18	99.7	87.9
JN-18	2	41.2	8.97	49.9	0.03	0.12	100.2	90.8
JN-19	2	40.9	9.64	49.1	0.04	0.14	99.8	90.1
JN-20	3	40.9	9.30	49.3	0.03	0.14	99.6	90.4
JN-21	3	41.1	8.17	50.2	0.04	0.13	99.6	91.6
JN-23	3	40.9	9.44	49.3	0.04	0.12	99.7	90.3
JN-24	3	41.1	8.93	50.0	0.02	0.14	100.2	90.9
JN-25	4	40.6	8.29	48.6	0.03	0.13	97.6	91.3
JN-26	4	40.7	8.11	49.7	0.04	0.13	98.7	91.6
JN-27	2	40.7	9.16	49.1	0.03	0.12	99.1	90.5
JN-28	3	40.6	9.20	49.0	0.03	0.15	99.0	90.5
JN-29	3	40.7	9.12	49.3	0.02	0.14	99.3	90.6
JN-30	2	40.6	8.91	49.0	0.04	0.13	98.7	90.7
JN-31	3	40.3	11.90	46.9	0.04	0.17	99.4	87.5
JN-32	3	40.9	8.39	49.9	0.01	0.13	99.4	91.4
JN-33	3	40.1	12.01	46.9	0.02	0.23	99.3	87.5
JN-34	2	40.7	9.17	49.2	0.04	0.13	99.3	90.5
JN-35	3	40.9	8.85	49.2	0.03	0.14	99.1	90.8
JN-36	3	40.5	10.35	48.1	0.02	0.15	99.1	89.2
JN-37	3	40.7	8.66	49.7	0.03	0.14	99.3	91.1
JN-38	4	40.5	8.99	49.1	0.02	0.14	98.8	90.7
JN-39A	3	40.5	9.05	48.9	0.03	0.13	98.6	90.6
JN-39B	4	40.1	10.72	47.9	0.04	0.19	99.0	88.9
JN-40	2	40.4	10.20	47.8	0.03	0.14	98.5	89.3
JN-41	3	40.5	8.97	48.9	0.03	0.11	98.5	90.7
JN-42	3	40.6	9.07	49.0	0.03	0.14	98.9	90.6
JN-43	2	40.6	8.61	49.4	0.02	0.11	98.7	91.1
JN-44	2	40.2	9.98	48.2	0.04	0.12	98.5	89.6
JN-45	4	40.5	10.02	48.2	0.03	0.15	98.8	89.5
JN-46	3	40.7	8.91	49.1	0.04	0.14	98.9	90.8
JN-47	3	40.4	9.22	49.1	0.04	0.13	98.9	90.5
JN-48	3	40.5	9.71	48.6	0.03	0.12	98.9	89.9
JN-49	2	40.2	10.25	48.1	0.04	0.18	98.7	89.3
JN-50	2	40.8	9.12	49.4	0.03	0.11	99.4	90.6
JN-51	2	40.6	9.35	49.3	0.04	0.14	99.4	90.4
JN-52	2	40.9	9.02	49.3	0.02	0.14	99.4	90.7
JN-53	3	41.0	9.27	49.3	0.04	0.14	99.7	90.5
JN-54	3	40.8	9.51	49.0	0.04	0.16	99.5	90.2
JN-56	3	40.6	9.93	48.8	0.01	0.17	99.5	89.7

Table S4-2e. Olivine compositions of peridotites from Fansi

Sample	Points	SiO2	FeO	MgO	CaO	NiO	MnO	Total	Fo
FS-01	3	40.7	9.40	49.1	0.04		0.12	99.37	90.3
FS-02A	3	40.6	9.87	48.9	0.03		0.15	99.54	89.8
FS-02B	2	40.8	9.36	49.3	0.04		0.15	99.71	90.4
FS-02C	3	40.8	9.69	49.0	0.05		0.14	99.65	90.0
FS-03	3	41.0	8.83	49.6	0.04		0.15	99.63	90.9
FS-03B	3	41.2	7.42	50.9	0.04		0.13	99.64	92.4
FS-04	3	41.2	7.38	50.7	0.04		0.11	99.47	92.5
FS-10	3	40.9	8.25	50.1	0.05		0.12	99.36	91.5
FS-13	3	40.6	9.54	49.3	0.04		0.14	99.69	90.2
FS-14	3	40.8	10.11	48.6	0.02		0.16	99.64	89.5
FS-17	3	41.2	7.74	50.6	0.03		0.11	99.69	92.1
FS-18	3	41.1	7.38	50.5	0.04		0.12	99.14	92.4
FS-19	3	40.7	9.44	49.1	0.05		0.13	99.46	90.3
FS-20	3	40.9	8.26	49.8	0.07		0.15	99.17	91.5
FS2-01B	3	40.9	8.81	49.4	0.05		0.13	99.23	90.9
FS2-01B2	3	40.6	8.84	48.9	0.04		0.12	98.48	90.8
FS2-01C	3	40.6	9.89	48.5	0.05		0.15	99.12	89.7
FS2-01D	4	41.0	7.67	50.4	0.04		0.11	99.22	92.1
FS2-02	3	40.7	9.38	49.1	0.05		0.14	99.30	90.3
FS2-03	2	40.5	10.54	48.4	0.05		0.15	99.70	89.1
FS2-04	3	40.9	8.88	49.7	0.05		0.13	99.67	90.9
FS2-05	3	40.7	9.13	49.5	0.05		0.14	99.58	90.6
FS2-06	2	40.8	9.07	49.1	0.03		0.13	99.12	90.6
FS2-07	3	40.6	9.10	49.2	0.07		0.16	99.18	90.6
FS2-08	3	40.7	9.41	49.0	0.03		0.15	99.36	90.3
FS2-09	2	40.6	9.74	48.6	0.05		0.13	99.13	89.9
FS-21	3	40.7	10.17	48.4	0.03		0.13	99.38	89.5
FS2-10	3	40.3	11.41	47.7	0.04		0.16	99.65	88.2
FS2-11	2	40.5	9.82	48.9	0.03		0.15	99.35	89.9
FS2-12	3	40.6	10.13	48.5	0.05		0.16	99.39	89.5
FS2-13	3	40.4	9.79	48.8	0.05		0.14	99.10	89.9
FS2-14	3	40.4	10.22	48.3	0.04		0.15	99.10	89.4
FS2-15	3	40.4	9.15	49.3	0.04		0.15	99.03	90.6
FS2-16	3	40.5	9.16	48.8	0.05		0.13	98.67	90.5
FS2-17	3	40.4	10.05	48.5	0.05		0.14	99.16	89.6
FS2-18	3	40.4	9.48	48.7	0.05		0.15	98.75	90.1
FS2-19	3	40.7	8.81	49.2	0.06		0.13	98.91	90.9
FS-22A	3	40.9	9.84	48.7	0.04		0.15	99.65	89.8
FS-23	2	40.5	10.04	48.6	0.02		0.16	99.30	89.6
FS-24	3	40.8	9.83	48.8	0.04		0.13	99.52	89.8
FS-26	3	40.4	11.55	47.5	0.04		0.16	99.66	88.0
FS-27	3	40.7	9.52	48.8	0.04		0.13	99.24	90.1
FS-28	4	41.1	8.10	50.2	0.05		0.11	99.59	91.7
FS-29	3	40.6	9.84	48.9	0.03		0.15	99.54	89.9
FS-31	2	40.7	9.73	49.1	0.04		0.14	99.74	90.0
FS-32	2	40.9	8.78	49.4	0.04		0.14	99.30	90.9
FS-33	5	40.7	8.67	49.7	0.04		0.13	99.28	91.1
FS-34	3	40.4	9.92	48.5	0.05		0.14	98.97	89.7
FS-36	3	40.5	9.80	48.5	0.05		0.14	98.94	89.8
FS-37	3	40.6	8.45	49.5	0.05		0.12	98.69	91.3
FS-38	3	40.4	9.17	48.9	0.04		0.15	98.63	90.5
FS-39	3	39.3	15.68	43.4	0.03		0.20	98.62	83.2
FS-41	3	40.1	11.28	47.2	0.07		0.18	98.80	88.2
FS-42	3	40.7	7.51	50.0	0.03		0.11	98.26	92.2

FS-43	3	40.6	7.81	49.6	0.06	0.14	98.21	91.9
FS-44	3	40.4	9.25	48.9	0.04	0.15	98.70	90.4
FS-45	3	40.3	9.38	48.6	0.05	0.13	98.44	90.2
FS-46	3	40.6	9.11	48.9	0.02	0.12	98.74	90.5
FS-47	3	39.8	14.12	45.2	0.04	0.29	99.37	85.1
FS-48	3	40.7	9.73	49.2	0.04	0.17	99.79	90.0
FS-50	4	40.4	10.48	48.3	0.06	0.16	99.44	89.2
FS-51	3	40.7	8.82	49.5	0.05	0.11	99.20	90.9
FS-51-2	3	40.3	10.55	48.2	0.06	0.15	99.33	89.1
FS-52	3	40.5	10.54	48.5	0.05	0.15	99.76	89.1
FS-53	3	40.9	8.04	50.4	0.04	0.12	99.50	91.8
FS-55	4	40.8	7.87	50.3	0.03	0.11	99.20	91.9
FS-56	3	40.7	8.65	49.3	0.04	0.15	98.90	91.0
FS-57	2	40.2	10.55	48.0	0.04	0.20	98.96	89.0
FS-58	3	40.6	9.69	48.9	0.05	0.14	99.40	90.0
FS-62	3	41.2	7.44	50.8	0.05	0.09	99.52	92.4
FS-63	3	41.0	8.25	50.0	0.05	0.12	99.47	91.5
FS-64	3	40.3	9.86	48.5	0.03	0.16	98.88	89.8
FS-65	4	40.7	8.29	50.0	0.04	0.14	99.11	91.5
FS-66	2	40.5	9.01	50.0	0.03	0.16	99.76	90.8
FS-68	4	40.9	8.13	50.2	0.04	0.12	99.44	91.7
FS-69	4	40.7	9.01	49.4	0.03	0.13	99.23	90.7
FS-69-2	3	40.7	9.52	49.0	0.03	0.14	99.45	90.2

Table S4-2f. Olivine compositions of peridotites from Hebi

Sample	Points	SiO2	FeO	MgO	CaO	NiO	MnO	Total	Fo
HB-01	2	41.1	7.28	50.8	0.05		0.13	99.3	92.6
HB-02	2	40.8	7.57	50.5	0.10		0.13	99.1	92.2
HB-03	2	41.2	7.63	50.5	0.10		0.12	99.5	92.2
HB-04	3	41.1	7.03	50.9	0.02		0.12	99.2	92.8
HB-05	3	40.8	7.94	50.1	0.01		0.13	99.0	91.8
HB-06	3	41.0	7.98	50.7	0.07		0.13	99.9	91.9
HB-07	3	40.8	7.51	50.6	0.09		0.08	99.0	92.3
HB-08	4	40.7	8.60	49.8	0.08		0.14	99.3	91.2
HB-09	3	41.0	7.33	50.6	0.03		0.09	99.1	92.5
HB-10	3	40.9	8.29	49.8	0.05		0.12	99.2	91.5
HB-11	3	41.1	7.31	50.8	0.03		0.11	99.3	92.5
HB-12	2	41.1	7.66	50.6	0.08		0.11	99.6	92.2
HB-13	3	41.0	7.56	50.4	0.08		0.12	99.2	92.2
HB-14	3	41.1	7.61	50.2	0.09		0.12	99.1	92.2
HB-15	3	40.9	8.05	50.1	0.05		0.14	99.3	91.7
HB-16	3	40.8	7.74	50.5	0.07		0.09	99.1	92.1
HB-17	3	40.7	8.63	49.6	0.05		0.12	99.0	91.1
HB-18	3	40.7	7.67	50.2	0.07		0.12	98.8	92.1
HB-19	3	40.7	7.62	50.2	0.03		0.10	98.7	92.2
HB-20	3	40.9	7.50	50.2	0.06		0.15	98.8	92.3
HB-21-1	2	41.1	7.20	50.7	0.06		0.09	99.2	92.6
HB-21-2	4	41.0	7.55	50.6	0.07		0.09	99.3	92.3
HB-22	2	41.1	7.73	50.4	0.05		0.12	99.5	92.1
HB-24	6	40.4	10.0	48.3		0.30	0.13	99.2	89.6

Table S4-3a. Average EPMA analyses of olivines from spinel peridotites

Sample	n	SiO_2	FeO	MnO	NiO	MgO	Total	Fo
Datong								
DAT-05	5	41.1	8.35	0.11	0.38	50.3	100.2	91.5
DAT-09	5	40.7	8.21	0.12	0.36	50.1	99.5	91.6
DAT-15	5	40.7	8.96	0.12	0.41	49.4	99.6	90.8
DAT-30	5	40.9	8.11	0.12	0.41	50.4	99.9	91.7
DAT-31	5	40.7	8.73	0.12	0.38	50.0	99.9	91.1
Jining								
JN-01	5	41.0	9.06	0.12	0.33	50.3	100.8	90.8
JN-02	5	40.9	9.47	0.14	0.35	50.4	101.2	90.5
JN-06	6	40.8	10.4	0.15	0.39	49.5	101.2	89.5
JN-16	6	41.1	9.45	0.12	0.39	50.1	101.1	90.4
JN-17	5	40.6	12.2	0.15	0.37	48.0	101.3	87.5
JN-19	5	41.3	8.96	0.13	0.38	50.9	101.7	91.0
JN-26	6	41.3	8.31	0.12	0.37	51.1	101.1	91.6
JN-27	5	41.0	9.13	0.14	0.39	50.3	101.0	90.8
JN-29	6	41.0	9.20	0.12	0.37	50.4	101.1	90.7
JN-31	6	40.3	14.1	0.21	0.34	46.7	101.7	85.5
JN-35	6	41.1	9.03	0.12	0.37	50.6	101.2	90.9
JN-52	6	41.2	9.08	0.15	0.37	50.2	101.0	90.8
Fansi								
FS-01	5	41.0	9.81	0.12	0.37	49.9	101.2	90.1
FS-18	5	41.3	9.07	0.10	0.38	50.6	101.5	90.9
FS-36	5	41.0	9.99	0.14	0.39	49.7	101.1	89.9
FS-42	5	41.3	7.64	0.11	0.39	51.2	100.6	92.3
FS-43	5	41.6	7.97	0.11	0.39	51.4	101.4	92.0
FS-44	5	40.9	9.44	0.13	0.37	50.2	101.0	90.5
FS-50	5	40.8	10.9	0.13	0.36	48.8	101.0	88.9
FS-62	5	41.5	7.55	0.10	0.41	52.2	101.7	92.5
FS-64	5	40.7	10.1	0.14	0.39	49.3	100.7	89.7
FS-68	6	41.6	8.15	0.12	0.37	51.9	102.1	91.9
FS-69	5	41.0	9.15	0.12	0.38	50.5	101.2	90.8
FS2-04	5	41.1	9.11	0.11	0.37	50.7	101.4	90.8
FS2-05	5	41.2	9.43	0.15	0.38	50.5	101.6	90.5
FS2-09	5	40.8	10.1	0.17	0.35	49.6	101.0	89.7
FS2-10	5	40.6	11.6	0.17	0.35	48.4	101.1	88.2
Hebi								
HB-09	7	41.1	7.36	0.09	0.39	51.3	100.2	92.6
HB-10	5	41.2	8.42	0.13	0.39	50.6	100.8	91.5
HB-12	5	41.2	7.65	0.10	0.38	51.6	100.9	92.3
HB-13	5	41.1	7.68	0.12	0.39	51.1	100.3	92.2
HB-15	6	41.1	8.11	0.10	0.42	51.1	100.9	91.8
HB-21-2	5	41.3	7.61	0.12	0.35	51.2	100.5	92.3
HB-22	6	41.5	7.92	0.10	0.39	51.6	101.5	92.1
HB-24	6	40.4	10.0	0.13	0.30	48.3	99.2	89.6
Fushan								
FS7-13	4	40.9	8.77	0.12	0.29	49.2	99.3	90.9
FS7-10	2	41.1	7.11	0.14	0.38	50.7	99.4	92.7
FS6-56	4	40.7	7.10	0.12	0.36	51.2	99.5	92.8
FS6-29	2	41.2	7.11	0.13	0.45	51.6	100.5	92.8
FS6-18	2	40.9	7.97	0.16	0.36	50.5	99.9	91.9
FS6-55	2	40.1	8.32	0.14	0.38	50.3	99.2	91.5
FS7-1	2	40.4	8.33	0.14	0.36	49.7	99.0	91.4
FS7-9	2	40.8	7.40	0.07	0.42	51.1	99.8	92.5

Data sources in addition to this study: Fushan (Xu et al., 2010), n: number of analyses

Table S4-3b. Average EPMA analyses of orthopyroxenes from spinel peridotites

Sample	n	SiO_2	TiO_2	Al_2O_3	Cr_2O_3	FeO	MnO	MgO	CaO	Na_2O	Total
Datong											
DAT-05	5	54.9	0.05	6.02	0.51	5.59	0.01	32.8	0.99	0.07	100.9
DAT-09	4	55.2	0.03	3.53	0.63	5.37	0.04	33.2	1.08	0.04	99.1
DAT-15	5	54.8	0.10	5.86	0.36	5.91	0.01	32.2	0.82	0.07	100.1
DAT-30	4	55.6	0.06	4.17	0.57	5.28	0.01	33.1	0.94	0.07	99.8
DAT-31	5	55.0	0.08	5.60	0.40	5.82	0.01	32.9	0.78	0.06	100.7
Jining											
JN-01	5	54.8	0.09	5.00	0.38	5.84	0.14	32.8	0.71	0.04	99.8
JN-02	5	54.8	0.06	4.91	0.38	5.92	0.13	33.2	0.71	0.04	100.2
JN-06	4	55.0	0.08	4.44	0.58	5.93	0.13	32.9	0.84	0.06	99.9
JN-16	2	54.9	0.06	5.21	0.36	6.13	0.13	32.6	0.77	0.16	100.3
JN-17	5	54.5	0.09	5.47	0.41	6.62	0.13	32.3	0.71	0.16	100.4
JN-19	5	55.5	0.03	3.64	0.50	5.73	0.12	33.3	0.80	0.08	99.7
JN-26	5	55.2	0.05	4.12	0.50	5.37	0.11	33.3	0.73	0.10	99.6
JN-27	5	54.2	0.08	5.68	0.37	6.01	0.14	32.3	0.68	0.07	99.5
JN-29	5	54.8	0.01	4.79	0.42	5.95	0.14	32.9	0.79	0.03	99.9
JN-31	5	54.6	0.02	4.63	0.38	6.87	0.14	32.2	0.73	0.10	99.7
JN-35	5	54.9	0.05	4.89	0.34	5.81	0.15	33.1	0.70	0.04	100.1
JN-52	1	55.2	0.03	4.55	0.31	5.77	0.13	32.7	0.77	0.08	99.4
Fansi											
FS-01	5	55.0	0.12	4.70	0.31	6.32	0.14	32.6	0.71	0.06	100.0
FS-18	5	54.9	0.06	5.36	0.29	6.00	0.12	32.8	0.84	0.11	100.5
FS-36	5	54.3	0.07	5.71	0.30	6.68	0.15	32.4	0.86	0.06	100.6
FS-42	5	55.8	0.00	3.43	0.50	5.01	0.11	33.8	0.79	0.10	99.6
FS-43	5	55.4	0.07	4.31	0.67	5.23	0.12	33.1	1.09	0.10	100.1
FS-44	5	54.9	0.02	4.29	0.39	6.04	0.13	32.7	0.75	0.03	99.2
FS-50	5	53.7	0.16	6.63	0.35	6.71	0.13	30.8	1.40	0.25	100.2
FS-62	5	55.2	0.02	3.11	0.48	4.74	0.11	33.6	0.77	0.08	98.1
FS-64	1	56.1	0.02	2.68	0.53	5.26	0.12	33.9	0.89	0.05	99.6
FS-68	5	56.3	0.01	2.68	0.53	5.33	0.11	34.0	0.90	0.06	99.9
FS-69	2	55.2	0.09	4.14	0.38	6.15	0.13	34.0	0.73	0.04	100.8
FS2-04	5	55.9	0.05	3.58	0.45	5.97	0.12	33.3	0.92	0.07	100.4
FS2-05	5	55.6	0.02	4.81	0.50	6.07	0.13	33.0	1.05	0.08	101.3
FS2-09	5	54.9	0.05	5.57	0.37	6.44	0.14	32.3	1.00	0.13	100.9
FS2-10	3	55.5	0.04	3.34	0.38	7.41	0.16	31.9	0.92	0.13	99.8
Hebi											
HB-09	5	54.9	0.00	4.18	0.59	4.87	0.11	33.4	0.97	0.06	99.1
HB-10	5	55.5	0.09	3.48	0.78	5.53	0.13	33.0	1.21	0.15	99.9
HB-12	5	55.3	0.00	3.71	0.84	5.00	0.10	33.4	1.38	0.03	99.8
HB-13	5	55.3	0.00	3.77	0.78	5.04	0.12	33.3	1.33	0.06	99.8
HB-15	5	54.8	0.01	3.91	0.82	5.33	0.12	33.0	1.40	0.04	99.4
HB-21-2	5	55.3	0.03	2.70	0.76	4.91	0.11	33.5	1.38	0.03	98.8
HB-22	5	55.7	0.02	3.59	0.75	5.18	0.12	33.6	1.25	0.08	100.3
HB-24	4	55.0	0.02	4.11	0.84	6.82	0.14	31.8	1.24	0.21	100.2
Fushan											
FS7-10	3	56.82	0	1.76	0.43	5	0.15	34.94	0.38	0.02	99.5
FS6-56	1	56.34	0.04	2.85	0.43	4.91	0.13	34.47	0.49	0.05	99.7
FS6-29	2	56.81	0.01	2.31	0.47	4.84	0.1	34.91	0.36	0.07	100.0
FS6-18	2	57.14	0	1.65	0.54	5.05	0.13	35.2	0.32	0.09	100.2
FS6-55	2	55.78	0.09	3.28	0.46	5.78	0.12	33.76	0.33	0.04	99.7
FS7-1	3	56.11	0.07	2.71	0.36	5.77	0.13	34.11	0.32	0.04	99.7
FS7-9	1	56.32	0.01	2.29	0.51	4.75	0.11	34.63	0.35	0.1	99.1

Table S4-3c. Average EPMA analyses of clinopyroxenes from spinel peridotites

Sample	n	SiO_2	TiO_2	Al_2O_3	Cr_2O_3	FeO	MnO	MgO	CaO	Na_2O	Total
Datong											
DAT-05	5	52.7	0.25	5.47	1.00	2.41	0.02	16.6	20.0	1.21	99.7
DAT-09	4	53.5	0.05	2.85	1.19	2.28	0.07	17.8	20.7	0.66	99.0
DAT-15	5	52.2	0.42	6.25	0.87	2.38	0.02	15.5	19.8	1.42	98.9
DAT-30	5	53.7	0.15	4.50	1.29	2.15	0.02	16.4	19.4	1.62	99.3
DAT-31	5	52.4	0.36	6.17	1.04	2.35	0.02	15.8	20.1	1.38	99.6
Jining											
JN-01	5	51.7	0.36	5.27	0.93	2.19	0.08	16.0	21.9	1.05	99.5
JN-02	5	52.2	0.29	5.14	0.97	2.28	0.06	16.2	22.0	1.04	100.2
JN-06	5	52.0	0.34	4.71	1.41	2.45	0.10	16.0	21.4	1.21	99.7
JN-16	5	51.9	0.39	3.81	1.47	2.47	0.09	16.9	22.0	0.75	99.8
JN-17	5	52.1	0.48	3.52	1.16	3.04	0.07	16.4	21.8	0.81	99.4
JN-19	4	53.9	0.19	3.31	1.19	2.45	0.08	17.0	20.7	1.47	100.2
JN-26	2	52.9	0.31	5.79	1.58	2.49	0.07	16.7	18.1	2.03	99.9
JN-27	5	51.6	0.44	6.63	0.90	2.26	0.06	15.0	20.9	1.64	99.4
JN-29	5	52.5	0.09	4.15	0.83	2.25	0.06	16.7	22.8	0.69	100.1
JN-31	5	52.9	0.09	4.05	0.95	3.05	0.08	15.9	21.0	1.31	99.3
JN-35	5	52.2	0.22	5.46	0.93	2.27	0.07	16.1	21.9	1.18	100.4
JN-52	5	52.8	0.15	4.71	0.89	2.34	0.09	16.2	21.3	1.29	99.7
Fansi											
FS-01	5	52.1	0.49	5.19	0.80	2.51	0.08	15.9	21.7	1.23	100.0
FS-36	5	51.8	0.35	5.78	0.68	3.13	0.07	16.0	21.2	1.23	100.2
FS-42	4	52.9	0.10	5.09	1.56	2.47	0.06	15.8	20.3	1.81	100.1
FS-43	5	52.5	0.38	5.23	1.62	2.37	0.07	16.5	20.1	1.58	100.4
FS-44	5	52.7	0.08	3.78	0.80	2.43	0.07	16.7	22.3	0.74	99.7
FS-50	5	51.3	0.58	7.00	0.75	3.38	0.10	16.2	19.2	1.48	99.9
FS-62	5	52.8	0.08	3.75	1.31	2.04	0.07	16.6	20.7	1.41	98.8
FS-64	4	51.8	0.29	4.52	0.67	2.75	0.08	16.5	22.5	0.72	99.8
FS-68	5	53.8	0.08	3.02	1.38	2.29	0.07	17.2	21.3	1.18	100.2
FS-69	3	52.6	0.36	4.12	0.96	2.57	0.07	16.3	22.4	0.89	100.3
FS2-04	5	53.6	0.13	3.65	1.00	2.69	0.07	17.3	20.6	1.17	100.1
FS2-05	5	53.1	0.09	4.60	0.99	2.70	0.08	17.1	21.2	1.10	100.9
FS2-09	5	53.3	0.16	8.73	0.64	2.58	0.09	13.9	18.8	1.97	100.2
FS2-10	5	52.9	0.22	4.56	1.39	3.14	0.11	16.5	19.7	1.42	100.0
Hebi											
HB-10	4	53.1	0.32	4.35	2.06	2.78	0.06	16.4	19.0	1.92	100.0
HB-12	3	53.1	0.00	2.96	1.26	2.20	0.08	18.3	21.7	0.43	100.0
HB-13	3	53.3	0.00	3.14	1.24	2.27	0.08	18.1	21.5	0.72	100.3
HB-15	5	52.8	0.00	3.03	1.18	2.45	0.07	18.1	21.4	0.57	99.6
HB-22	3	53.6	0.05	3.34	1.36	2.29	0.05	17.8	21.4	0.94	100.9
Fushan											
FS7-10	2	54.4	0.02	2.07	0.85	1.63	0.11	17.9	23.4	0.69	101.1
FS6-18	1	53.7	0.00	1.32	1.59	1.91	0.06	17.0	22.9	0.92	99.5
FS6-55	2	52.1	0.39	5.50	1.30	1.83	0.05	15.2	22.4	1.61	100.4
FS7-1	2	52.0	0.35	5.40	1.20	1.89	0.15	15.0	22.4	1.46	99.9
FS7-9	1	53.0	0.03	2.34	2.02	1.72	0.07	16.4	23.2	0.89	99.7

Table S4-3d. Average EPMA analyses of spinels from spinel peridotites

Sample	n	SiO_2	TiO_2	Al_2O_3	Cr_2O_3	FeO	MnO	NiO	MgO	Total	Cr#
Datong											
DAT-05	5	0.02	0.12	52.6	16.9	9.83	0.12	0.34	21.7	101.6	17.7
DAT-09	5	0.04	0.12	30.6	38.0	13.2	0.21	0.19	17.7	100.1	45.4
DAT-15	5	0.02	0.10	56.6	12.5	9.72	0.13	0.35	21.8	101.2	12.9
DAT-30	3	0.03	0.12	39.7	29.7	11.2	0.17	0.22	19.7	100.8	33.5
DAT-31	5	0.02	0.09	55.0	14.2	10.1	0.10	0.35	21.7	101.6	14.8
Jining											
JN-01	5	0.03	0.09	54.7	14.0	9.73	0.12	0.28	21.4	100.3	14.6
JN-02	5	0.03	0.10	54.3	14.7	10.1	0.13	0.29	21.3	101.0	15.4
JN-06	4	0.03	0.18	43.9	24.8	12.2	0.16	0.25	19.4	100.9	27.5
JN-16	5	0.03	0.08	49.6	19.5	10.7	0.14	0.29	21.0	101.2	20.8
JN-17	5	0.03	0.05	52.2	15.3	12.9	0.14	0.33	19.8	100.7	16.4
JN-19	5	0.04	0.22	38.2	31.5	12.7	0.18	0.21	18.6	101.7	35.6
JN-26	5	0.02	0.30	40.9	28.5	11.8	0.16	0.23	19.3	101.3	31.8
JN-29	5	0.07	0.03	51.4	17.7	10.6	0.13	0.30	20.7	101.1	18.8
JN-31	5	0.03	0.01	49.0	16.9	18.4	0.19	0.26	16.1	100.9	18.8
JN-35	5	0.02	0.04	55.5	13.6	9.62	0.11	0.32	21.6	100.9	14.2
JN-52	6	0.03	0.06	51.8	16.6	10.6	0.12	0.31	20.8	100.3	17.7
Fansi											
FS-01	5	0.03	0.14	55.2	13.5	10.6	0.11	0.34	21.0	100.9	14.1
FS-18	3	0.04	0.14	49.2	18.9	11.9	0.14	0.31	20.6	101.2	20.5
FS-36	5	0.04	0.11	56.0	10.6	11.8	0.11	0.38	21.2	100.2	11.2
FS-42	5	0.04	0.01	36.3	32.9	12.5	0.16	0.23	19.0	101.1	37.8
FS-43	4	0.05	0.35	37.8	31.5	12.1	0.16	0.25	19.5	101.8	35.8
FS-44	6	0.04	0.06	48.7	20.1	11.5	0.13	0.28	20.3	101.1	21.6
FS-50	6	0.06	0.21	56.9	10.6	11.8	0.11	0.37	21.4	101.5	11.1
FS-62	5	0.04	0.09	34.0	36.0	11.9	0.17	0.19	18.8	101.2	41.5
FS-64	4	0.03	0.11	51.9	16.2	11.6	0.13	0.33	20.3	100.6	17.4
FS-68	5	0.03	0.17	26.7	42.9	14.4	0.21	0.16	16.8	101.3	51.9
FS-69	4	0.06	0.24	44.7	23.4	13.2	0.15	0.30	19.6	101.6	26.0
FS2-04	5	0.03	0.19	35.9	32.4	14.3	0.17	0.22	18.1	101.3	37.7
FS2-05	5	0.05	0.05	47.2	22.0	11.8	0.13	0.29	20.1	101.6	23.9
FS2-09	5	0.04	0.05	54.2	14.1	11.1	0.12	0.32	21.3	101.2	14.8
FS2-10	4	0.12	0.23	31.1	35.9	17.9	0.24	0.17	15.2	100.8	43.7
Hebi											
HB-09	4	0.18	0.01	37.9	30.7	11.2	0.15	0.24	19.6	99.9	35.2
HB-10	5	0.05	0.60	25.3	41.7	15.7	0.21	0.20	16.7	100.5	52.4
HB-12	5	0.21	0.06	27.8	40.2	12.7	0.18	0.16	17.3	98.7	49.3
HB-13	5	0.06	0.01	28.9	40.1	13.5	0.19	0.18	17.8	100.8	48.2
HB-15	5	0.05	0.01	29.2	39.2	13.9	0.20	0.22	17.6	100.4	47.4
HB-21-2	5	0.61	0.12	20.7	47.4	14.2	0.23	0.13	16.1	99.5	60.6
HB-22	5	0.05	0.08	28.3	41.0	13.7	0.20	0.18	17.6	101.2	49.3
HB-24	5	0.13	0.44	28.2	37.3	18.3	0.21	0.20	15.9	100.6	47.0
Fushan											
FS7-13	10	0.08	0.44	7.7	52.6	30.2	1.11	0.08	6.6	98.8	82.2
FS7-10	2	0.07	0.03	32.8	36.6	14.7	0.32	0.05	15.6	100.2	42.8
FS6-56	2	0.10	0.02	32.3	33.3	20.1	0.55	0.10	13.5	100.0	40.9
FS6-29	2	0.06	0.01	40.2	30.2	12.6	0.36	0.12	17.8	101.3	33.5
FS6-18	1	0.03	0.00	25.1	45.6	15.0	0.48	0.05	14.5	100.7	54.9
FS7-1	2	0.08	0.05	46.7	21.5	13.2	0.36	0.18	18.1	100.1	23.6
FS7-9	1	0.03	0.02	38.9	29.7	14.4	0.33	0.19	17.5	101.0	33.9

Cr# = molar (Cr/(Cr+Al)x100

Table S4-4. Whole rock analyses for peridotites from the North China Craton determined using XRF

Sample	SiO_2	TiO_2	Al_2O_3	Al_2O_3 (*)	Fe_2O_{3T} [a]	MnO	MgO	CaO	CaO (*)	Na_2O	LOI	Total	WR Mg#[b]	T_{BKN} (^0C)[c]
Hannuoba														
DMP-04	44.4	0.06	2.29	2.3	8.14	0.13	42.1	1.94	1.9	0.28		98.8	91.1	1050
DMP-05	44.2	0.13	2.83		8.37	0.13	41.6	2.18		0.26		99.5	90.8	
DMP-19	44.8	0.03	1.91	1.9	7.85	0.12	40.7	1.80	1.8	0.19		97.4	91.1	1020
DMP-23a	44.2	0.10	2.32		8.63	0.13	41.3	1.64		0.24		98.5	90.4	1040
DMP-25	44.4	0.08	1.61	1.4	7.90	0.12	43.9	1.00	1.0	0.3		99.3	91.7	1030
DMP-41	44.8	0.06	2.76	2.8	8.60	0.13	40.2	2.12	2.1	0.27		98.7	90.2	940
DMP-51	44.8	0.05	1.96	1.8	8.23	0.12	42.0	1.89	1.7	0.24		99.1	91.0	1030
DMP-56	44.8	0.13	3.49	3.5	8.85	0.14	38.2	3.21	3.2	0.36		98.9	89.5	1040
DMP-57	44.3	0.06	1.96		8.23	0.12	42.5	1.56		0.16		98.8	91.1	
DMP-58	44.9	0.08	3.16	3.2	8.80	0.13	38.8	2.76	2.8	0.34		98.7	89.7	1030
DMP-59	44.0	0.06	2.58		8.88	0.13	40.4	2.43		0.27		98.5	90.0	1000
DMP-60	46.3	0.11	3.67	3.7	8.31	0.13	36.7	3.47	3.4	0.38		98.9	89.7	990
DMP-67c	44.0	0.20	3.78	3.9	9.32	0.14	37.8	2.88	2.9	0.30		98.5	88.9	1060
DA20-02	44.8	0.10	3.12		8.69	0.11	40.0	2.70		0.08	0.39	100.0	90.1	
DA20-05	45.3	0.05	2.71		7.86	0.10	40.8	2.48		0.07	0.55	99.8	91.1	
DA20-16	43.1	0.08	1.20		9.94	0.10	43.6	1.55		0.04	0.65	100.2	89.6	
DA20-17	44.7	0.05	2.40		8.07	0.18	39.1	2.38		0.12	2.79	99.7	90.5	
DA20-19	44.9	0.14	3.74		8.69	0.11	38.2	3.07		0.19	0.91	99.9	89.6	
Yangyuan														
YY-04	43.9	0.04	1.63	1.5	8.00	0.13	44.4	1.03	1.1	0.02	0.22	99.1	91.7	860
YY-08	44.4	0.08	2.97	3.7	8.79	0.14	39.9	2.89	1.4	0.11	0.22	99.3	90.0	840
YY-09	44.4	0.09	3.04	2.1	8.39	0.14	40.8	2.12	1.3	0.13	0.06	99.1	90.6	1020
YY-11	42.5	0.05	1.77	2.0	9.22	0.14	44.8	1.08	0.5	0.03	0.72	99.6	90.6	980
YY-13	43.8	0.11	2.44	2.4	8.70	0.13	41.9	1.90	1.8	0.11	-0.06	99.1	90.5	1020
YY-22	44.0	0.05	2.45	2.3	8.25	0.13	42.3	1.81	1.7	0.08	0.06	99.0	91.0	940
YY-23	*43.5*	*0.11*	*3.06*	*2.4*	*8.33*	*0.13*	*39.7*	*3.68*	*1.3*	*0.23*	*0.57*	*103.0*	*90.4*	*1150*
YY-26	43.4	0.08	3.08	2.9	8.76	0.14	41.7	2.15	2.0	0.10	0.26	99.4	90.4	880
YY-27	42.8	0.12	2.87	3.4	9.49	0.15	41.2	2.48	1.9	0.13	-0.07	99.2	89.6	880
YY-36	*44.0*	*0.06*	*2.30*	*2.0*	*8.43*	*0.13*	*41.7*	*2.46*	*2.3*	*0.17*	*0.13*	*103.7*	*90.8*	*975*
YY-40B	*44.6*	*0.06*	*2.80*	2.8	*8.09*	*0.13*	*40.0*	*2.93*	2.0	*0.16*	*-0.05*	*103.5*	*90.7*	*990*
YY-42	*43.3*	*0.04*	*2.35*	2.1	*8.66*	*0.13*	*42.4*	*2.40*	1.0	*0.10*	*-0.02*	*102.5*	*90.7*	*1020*
YY-45	*43.5*	*0.10*	*2.44*	*2.4*	*8.55*	*0.13*	*41.1*	*2.84*	*1.5*	*0.19*	*0.34*	*103.2*	*90.5*	*1140*
YY-50	*44.5*	*0.15*	*4.02*	*4.0*	*8.29*	*0.13*	*38.2*	*3.63*	*3.4*	*0.26*	*0.23*	*106.8*	*90.1*	*1070*
YY-51	41.3	0.03	1.12	1.3	8.54	0.13	46.0	1.40	0.6	0.02	0.66	98.6	91.4	1010
YY-52	43.7	0.08	2.70	2.4	8.52	0.14	41.5	2.26	2.0	0.12	0.18	99.0	90.6	1100
YY-58	43.8	0.07	2.40	1.9	8.07	0.13	42.4	2.00	0.9	0.12	0.15	98.9	91.2	1100
YY-60	42.5	0.05	1.26	1.1	8.86	0.13	44.9	1.23	1.0	0.03	0.65	99.0	90.9	950
YYB-2	46.1	0.02	1.45		9.03	0.12	42.8	0.90		0.07	− 0.49	99.9	90.4	
YYB-4	46.7	0.06	2.15		8.85	0.12	40.6	1.85		0.17	− 0.48	100.0	90.1	1080
YYB-7	44.9	0.01	0.89		9.75	0.12	44.7	0.44		0.04	− 0.88	100.0	90.1	1100

YG-18	42.7	0.02	1.20		9.43	0.13	46.1	0.73		0.11	0.13	100.6	90.6	940
Datong														
DAT-05	44.1	0.14	3.21	2.4	8.28	0.13	40.5	2.85	1.0	0.26	0.17	99.5	90.6	1090
DAT-09	42.6	0.20	1.62	0.7	9.29	0.13	44.1	1.15	0.3	0.29	-0.20	99.5	90.4	1090
DAT-15	43.5	0.29	3.66	1.7	9.30	0.14	38.6	3.60	2.5	0.43	0.62	99.7	89.2	1060
DAT-30	43.3	0.20	2.27	0.8	8.90	0.14	43.1	0.97	0.3	0.18	-0.05	99.2	90.6	1090
DAT-31	44.3	0.15	2.60	2.8	8.73	0.14	41.3	2.15	1.7	0.22	-0.19	99.6	90.3	1060
Jining														
JN-01	41.8	0.04	4.91	2.0	9.00	0.14	42.4	1.04	0.9	0.10	0.17	99.6	90.3	880
JN-02	42.2	0.04	4.33	1.7	8.63	0.14	42.4	1.37	1.2	0.12	0.29	99.4	90.7	890
JN-06	42.5	0.06	3.65	2.0	9.07	0.14	42.8	0.99	1.0	0.13	0.23	99.6	90.3	920
JN-16	42.1	0.03	0.86	1.3	9.91	0.15	45.7	0.62	1.4	0.10	0.44	99.9	90.1	930
JN-17	42.4	0.09	1.65	1.7	12.6	0.18	40.4	1.48	1.6	0.19	0.58	99.6	86.4	920
JN-19	40.5	0.03	4.03	1.1	9.62	0.14	44.4	0.39	1.1	0.08	0.02	99.2	90.1	990
JN-26	42.4	0.07	4.94	1.5	8.07	0.13	41.9	1.46	0.9	0.17	0.65	99.8	91.1	1150
JN-27[d]	42.5			2.7	8.7		43.6		2.3					
JN-29	41.1	0.03	5.69	1.6	8.88	0.14	42.0	1.46	1.5	0.08	0.34	99.7	90.4	900
JN-31	42.2	0.03	1.48	1.4	12.2	0.18	41.0	1.95	1.5	0.18	0.81	100.0	87.0	850
JN-35	41.6	0.07	6.5	2.0	8.64	0.14	39.6	2.4	1.7	0.21	1.3	100.4	90.1	940
JN-41	40.6	0.02	3.73		9.20	0.14	43.8	1.51		0.08	0.28	99.3	90.4	880
JN-52	42.1	0.05	4.54	1.4	8.90	0.14	41.1	1.72	1.3	0.31	2.8	101.7	90.2	930
Fansi														
FS-01	43.0	0.06	1.94	2.0	9.74	0.12	42.4	1.57	1.8	0.02	0.08	99.0	89.6	880
FS-04(2)	42.2	0.03	0.88		8.56	0.09	46.7	0.42		<0.01	0.32	99.3	91.5	
FS-18	45.7	0.11	2.00	2.0	8.06	0.11	40.9	1.44	0.3	0.03	0.61	99.2	91.0	960
FS-36	44.4	0.08	3.46	2.4	9.20	0.13	38.3	2.84	2.3	0.05	0.67	99.2	89.2	950
FS-42	45.0	0.01	1.31	1.5	7.64	0.10	43.8	0.94	0.5	<0.01	0.35	99.1	91.9	970
FS-43	44.1	0.04	1.23	1.0	8.02	0.10	44.7	0.85	0.5	<0.01	0.18	99.2	91.7	1040
FS-44	43.9	0.03	2.16	2.0	9.05	0.12	41.2	2.28	2.5	0.02	0.41	99.2	90.0	900
FS-45	43.9	0.07	2.54	2.5	8.99	0.13	38.5	3.43	1.8	0.05	1.8	99.5	89.5	
FS-50	42.9	0.12	2.59	1.8	9.98	0.13	39.7	3.12	1.6	0.04	0.55	99.2	88.7	1100
FS-62	44.4	0.02	1.26	1.1	7.66	0.10	44.0	0.62	0.4	<0.01	1.1	99.2	91.9	970
FS-64	42.8	0.03	2.01		10.2	0.13	43.0	1.06		0.01	-0.09	99.2	89.3	890
FS-68	42.4	0.08	1.12	0.4	9.21	0.11	45.0	0.87	0.7	<0.01	0.2	99.1	90.6	980
FS2-04	43.9	0.02	1.53	0.7	9.17	0.11	43.5	0.81	0.5	<0.01	0.12	99.2	90.4	1050
FS2-05	43.6	0.03	1.89	2.5	9.11	0.12	42.3	2.16	1.8	0.02	-0.23	99.0	90.2	1010
FS2-09	44.5	0.08	3.93	2.8	8.83	0.12	37.4	3.07	2.2	0.10	0.69	99.1	89.3	1100
FS2-10	42.9	0.13	2.67	1.6	11.2	0.14	39.7	1.51	3.1	0.09	0.08	99.0	87.6	1060
Hebi														
HB-01	42.3	0.03	1.18		7.84	0.10	46.8	0.41		<0.01	0.31	99.0	92.2	
HB-02	43.4	0.02	1.79		7.95	0.11	44.4	0.80		<0.01	0.31	98.8	91.7	
HB-07	43.2	0.01	1.36		7.79	0.10	45.9	0.45		<0.01	0.19	99.2	92.1	
HB-09	43.1	0.02	1.95	0.2	7.57	0.10	45.4	0.39	0.1	<0.01	0.17	99.0	92.2	
HB-10	43.3	0.04	1.16	0.9	8.63	0.10	45.3	0.53	0.3	<0.01	0.14	99.3	91.2	1090
HB-12	42.6	0.01	1.68	0.8	7.99	0.10	46.1	0.41	0.4	<0.01	0.19	99.2	92.0	1060
HB-13	41.9	0.02	1.10	0.6	8.19	0.10	47.1	0.51	0.6	<0.01	0.14	99.1	91.9	1040

HB-15	46.7	0.03	2.21	1.4	7.39	0.10	41.1	1.02	0.4	0.03	0.51	99.3	91.7	1050
HB-15R	46.7	0.03	2.20		7.38	0.10	41.1	1.02		0.03	0.51	99.2	91.7	
HB-19	42.8	0.01	1.56		7.84	0.10	44.1	2.24		<0.01	0.07	98.8	91.8	
HB-21-2	42.8	0.02	1.16	0.2	7.65	0.10	46.6	0.26	0.1	<0.01	0.34	99.0	92.3	
HB-22	42.7	0.02	1.17	0.6	8.27	0.10	46.6	0.34	1.0	<0.01	0	99.3	91.8	1020
HB-24	42.6	0.02	0.96	0.6	10.6	0.12	44.5	0.44	0.1	0.01	0	99.3	89.3	
Fushan														
FS7-13	40.2	0.02	0.15		10.4	0.14	47.5	0.31		0.07	0.57	99.3	90.1	
FS6-19	40.6	0.02	0.7		8.66	0.13	46.7	0.93		0.08	0.51	99.2	91.5	
FS7-10	43.2	0.02	0.65		7.68	0.10	46.2	0.30		0.07	0.88	99.2	92.3	610-630
FS6-56	42.6	0.01	0.97		7.63	0.10	46.5	0.25		0.09	0.84	99.2	92.4	
FS6-18	43.2	0.01	0.59		8.12	0.11	45.3	0.41		0.10	1.35	99.3	91.7	
FS6-29	46.0	0.01	1.20		6.85	0.10	43.8	0.48		0.09	0.71	99.3	92.7	
FS6-55	43.3	0.05	1.47		8.72	0.12	43.7	1.06		0.13	0.51	99.3	90.9	720
FS7-1	42.2	0.01	0.73		8.43	0.11	47.0	0.31		0.08	0.44	99.3	91.7	620
FS7-9	43.8	0.03	0.8		7.6	0.1	44.7	0.39		1.47	0.43	99.3	92.1	720

Note: Major elements are reported as oxides with units of wt. %. R: replicate analysis.

Data sources in addition to this study: Hannuoba (Rudnick eta l., 2004; Zhang et al., 2009), Yangyuan (Y.G. Xu et al., 2008; this study), and Fushan (Xu et al., 2010). *Oxides wt. % are calculated based on mineral composition and modal mineralogy.

a. Fe_2O_{3T}: total Fe.

b. WR Mg#: whole rock molar $Mg/(Mg+Fe^{2+})x100$, assuming that all Fe is Fe^{2+}.

c. Two pyroxene equilibrium temperatures calculated using the method of Brey and Köhler (1990) at P = 1.5 Gpa

d. Major elements of sample JN-27 were not measured due to limited powder; report calculated oxide concentration based on modal mineralogy

Table S4-5a. Trace element analyses of blanks and reference materials analyzed by ICP-MS

Sample	Blank	AGV-2	AGV-2	RE	BHVO-2	BHVO-2	RE	BCR-2	BCR-2	RE	RGM-1	RGM-1
n	2	2	Ref		2	Ref		2	Ref		1	Ref
Li	0.022	10.9	11	-1.0%	4.4	4.8	-9.2%	9	9	-0.2%	56	57
Be	0.004	2.1	2.3	-8.6%	0.99	1	-1.2%	1.99	1.6	24%	2.33	2.37
Sc	0.045	13.1	13	0.8%	30.8	32	-3.6%	32.3	33	-2.2%	5.11	4.4
V	0.18	123	120	2.2%	321	317	1.2%	411	416	-1.1%	12.1	13
Cr	0.264	15.4	17	-9.7%	274.7	280	-1.9%	16.3	18	-9.2%	5.59	5.74
Co	0.052	16.2	16	1.2%	44.9	45	-0.1%	37.1	37	0.3%	2.04	2
Ni	0.054	18.9	19	-0.4%	120.2	119	1.0%	12.4	13	-4.6%	3.35	4.4
Cu	0.125	52.7	53	-0.5%	130.5	127	2.8%	18.7	21	-11%	10.8	11.6
Zn	1.507	90.3	86	5.0%	100.8	103	-2.1%	126.3	127	-0.5%	34.7	32
Ga	0.016	21.3	20	6.7%	21.3	21.7	-1.7%	21.8	23	-5.1%	16.2	15
Rb	0.055	70.1	68.6	2.1%	9.3	9.11	2.0%	46.3	46.9	-1.3%	148	150
Sr	0.199	668	658	1.5%	390	396	-1.5%	334	340	-1.9%	107	110
Y	0.015	20.5	20	2.6%	26.3	26	1.0%	35.9	37	-3.0%	23.7	25
Zr	0.124	235.6	230	2.4%	170	172	-1.0%	182	184	-1.1%	226	220
Nb	0.009	14	14.5	-3.7%	17.8	18.1	-1.8%	11.6	12.6	-7.9%	9.28	8.9
Mo	0.15	2.14	2.17	-1.6%	4.02	4	0.5%	248	248	-0.1%	2.75	2.3
Sn	0.051	2.05	2.06	-0.6%	1.85	1.7	8.6%	2.19	2.7	-19%	4.14	4.1
Cs	0.003	1.17	1.16	0.6%	0.1	0.1	-2.5%	1.11	1.1	0.7%	9.93	9.6
Ba	0.532	1152	1140	1.1%	130	131	-1.1%	671	677	-0.9%	816	810
La	0.014	39.4	38	3.6%	15.3	15.2	0.7%	24.7	24.9	-0.9%	23	24
Ce	0.033	70.5	68	3.7%	38	37.5	1.3%	52.3	52.9	-1.2%	45.9	47
Pr	0.004	8.44	8.3	1.6%	5.43	5.35	1.6%	6.81	6.7	1.7%	5.28	5.36
Nd	0.018	32	30	6.6%	24.6	24.5	0.2%	28.7	28.7	0.1%	19.3	19
Sm	0.003	5.71	5.7	0.1%	6.11	6.07	0.7%	6.59	6.58	0.2%	4.06	4.3
Eu	0.002	1.66	1.54	7.9%	2.05	2.07	-0.9%	1.97	1.96	0.4%	0.7	0.66
Gd	0.003	4.9	4.69	4.4%	6.19	6.24	-0.8%	6.65	6.75	-1.5%	3.82	3.7
Tb	0.001	0.68	0.64	6.0%	0.95	0.92	3.7%	1.08	1.07	1.2%	0.62	0.66
Dy	0.004	3.72	3.6	3.3%	5.47	5.31	3.0%	6.49	6.41	1.3%	3.79	4.1
Ho	0.001	0.69	0.71	-3.5%	1	0.98	1.6%	1.31	1.28	2.0%	0.77	0.82
Er	0.002	1.88	1.79	5.1%	2.52	2.54	-0.9%	3.65	3.66	-0.2%	2.36	2.35
Tm	0.001	0.26	0.26	1.3%	0.33	0.33	-0.1%	0.52	0.51	1.4%	0.36	0.36
Yb	0.004	1.71	1.6	7.1%	1.99	2	-0.6%	3.39	3.38	0.3%	2.55	2.6
Lu	0	0.26	0.25	2.2%	0.28	0.27	2.3%	0.51	0.5	2.3%	0.41	0.4
Hf	0.006	5.34	5.08	5.2%	4.39	4.36	0.8%	4.86	4.9	-0.9%	6.08	6.2
Ta	0.003	0.87	0.89	-2.4%	1.15	1.14	1.0%	0.77	0.78	-1.3%	0.98	0.95
Pb	0.117	13	13.2	-1.3%	1.9	1.6	16%	10.1	11	-7.9%	23.6	23.6
Th	0.01	6.37	6.1	4.5%	1.26	1.22	3.4%	6	5.7	5.2%	14.6	15.1
U	0.005	1.93	1.88	2.5%	0.43	0.4	7.2%	1.66	1.69	-1.8%	5.61	5.8

Note: Concentration unit is ppm. Ref: reference values; AGV-2, BHVO-2 and BCR-2 from GEOREM; RGM-1 from USGS. RE: relative error between measured and recommended values. 'n' presents the number of analyses

Table S4-5b. Whole rock trace element analyses for the Fansi and Hebi peridotites

Element	FS-01	FS-04(2)	FS-18	FS-36	FS-42	FS-43	FS-44	FS-45	FS-50	FS-62	FS-64	FS-68	FS2-04	FS2-05
Li	4.49	2.85	4.77	4.1	3.44	3.37	2.8	3.98	4.84	5.55	3.83	2.34	2.82	3.42
Be	0.11	0.18	0.22	0.034	0.062	0.065	0.05	0.07	0.079	0.068	0.035	0.17	0.1	0.074
Sc	10.3	5.19	7.91	15.7	6.87	7.18	13.4	13	12.5	7.14	8.66	6.33	8.35	11.8
V	50.2	22.1	40.4	83.1	31.8	30.7	66.3	65.3	60.3	35.5	46	30.9	38.9	52.2
Cr	2281	1971	2587	2796	2207	1995	3092	2436	1712	2748	2588	3049	2582	2506
Co	125	127	102	118	107	115	118	111	112	113	133	123	113	113
Ni	2366	2636	2071	2176	2275	2366	2127	1957	1926	2283	2394	2321	2085	2044
Cu	25.1	4.4	10.5	43.9	22.3	7.97	14.6	46.7	25.8	31.2	45.1	11.9	14.9	9.83
Zn	58.8	48.7	47.3	65.7	50	50.5	55.4	64.2	59.2	53.4	72	48.9	52.9	49.3
Ga	3.07	1.4	2.91	4.68	1.27	1.51	2.64	2.74	2.85	1.46	2.98	1.83	2.39	2.41
Rb	0.92	1.04	2.13	0.88	0.59	0.41	0.77	2.54	0.88	0.65	0.46	0.98	3.29	0.2
Sr	39.8	30.4	116	20.2	33.4	29.9	84.3	56.9	91	21.2	47.7	58.9	34.3	16.8
Y	1.72	0.56	1.87	3.44	0.4	0.68	1.03	2.08	2.92	0.76	0.94	1.19	0.56	0.91
Zr	4.9	10.1	19.9	4.44	4.46	5.27	3.48	5.63	12	3.89	2.44	17.1	3.22	8.47
Nb	0.72	1.37	2.98	0.097	0.49	0.47	0.31	0.55	0.73	0.57	0.18	3.33	0.41	0.5
Mo	0.68	0.13	0.29	0.53	0.11	0.15	0.13	0.073	0.12	0.12	0.18	0.17	0.92	0.094
Sn	0.18	0.34	0.33	0.17	0.12	0.11	0.15	0.13	0.2	0.92	0.25	0.46	0.14	0.15
Cs	0.04	0.017	0.03	0.039	0.082	0.064	0.039	0.027	0.023	0.85	0.038	0.02	0.044	0.0055
Ba	20	14.6	30.7	29.2	7.28	7.41	4.25	9.2	8.69	6.26	6.99	22.4	21.7	15.4
La	3.13	0.66	3.57	3.06	0.76	0.43	1.04	0.7	0.91	1.2	1.73	2.29	0.69	0.55
Ce	4.3	1.49	7.28	1.93	1.3	1.05	2.04	1.41	2.21	2.75	3.3	4.57	1.8	1.32
Pr	0.46	0.19	0.88	0.17	0.15	0.16	0.23	0.18	0.32	0.35	0.27	0.52	0.27	0.17
Nd	1.87	0.86	3.61	0.75	0.68	0.66	0.81	0.82	1.61	1.63	0.91	1.97	1.2	0.71
Sm	0.4	0.19	0.74	0.22	0.11	0.15	0.17	0.25	0.4	0.4	0.13	0.38	0.21	0.17
Eu	0.12	0.053	0.22	0.092	0.037	0.05	0.049	0.084	0.13	0.1	0.042	0.12	0.056	0.05
Gd	0.4	0.17	0.68	0.41	0.1	0.14	0.14	0.3	0.49	0.32	0.17	0.34	0.14	0.15
Tb	0.06	0.026	0.084	0.077	0.015	0.021	0.023	0.053	0.082	0.035	0.024	0.05	0.023	0.025
Dy	0.33	0.12	0.4	0.57	0.069	0.15	0.16	0.36	0.46	0.16	0.17	0.24	0.1	0.14
Ho	0.066	0.019	0.064	0.13	0.012	0.023	0.035	0.073	0.11	0.027	0.034	0.049	0.017	0.03
Er	0.15	0.047	0.16	0.37	0.044	0.051	0.13	0.23	0.3	0.086	0.12	0.11	0.055	0.099
Tm	0.024	0.0066	0.0194	0.055	0.0068	0.009	0.019	0.033	0.043	0.011	0.019	0.015	0.0088	0.016
Yb	0.18	0.044	0.11	0.38	0.049	0.076	0.13	0.23	0.29	0.065	0.15	0.097	0.067	0.13
Lu	0.028	0.0069	0.013	0.053	0.0082	0.012	0.022	0.039	0.051	0.01	0.021	0.013	0.01	0.017
Hf	0.14	0.21	0.42	0.16	0.09	0.11	0.062	0.15	0.3	0.077	0.055	0.29	0.059	0.2
Ta	0.049	0.11	0.2	0.024	0.046	0.055	0.031	0.038	0.073	0.046	0.024	0.15	0.044	0.044
Pb	0.8	0.53	0.42	0.9	0.34	0.15	0.48	0.4	0.32	0.61	0.87	0.38	0.57	0.82
Th	0.2	0.074	0.31	0.72	0.067	0.045	0.087	0.059	0.071	0.063	0.17	0.2	0.064	0.047
U	0.056	0.047	0.11	0.18	0.036	0.031	0.046	0.039	0.054	0.026	0.067	0.089	0.024	0.024
$(La/Yb)_N$	11.5	10.2	21.3	5.4	10.4	3.9	5.4	2.1	2.1	12.6	7.7	16	7	2.9

Note: Concentration unit: ppm. 'R' means replicate sample. $(La/Yb)_N$: chondrite-normalized to Sun and McDonough, 1989.

Table S4-5b. continued…

Element	FS2-09	FS2-10	HB-01	HB-02	HB-07	HB-09	HB-10	HB-12	HB-13	HB-15	HB-19	HB-21-1	HB-22	HB-24	YY-04	YY-26
Li	6.69	11.2													1.89	1.72
Be	0.29	0.35	0.12	0.13	0.24	0.4	0.11	0.29	0.19	0.52	0.3	0.39	0.12	0.35	0.079	0.041
Sc	13.8	7.82	5.95	8.7	7.25	8.19	6.74	7.09	5.58	9.42	9.86	5.87	6.35	5.68	8.59	14.3
V	71.1	43.6	14.8	25	20.3	20.1	25.8	28.3	17.3	47.3	41	18.4	21.4	14.8	36.6	66.8
Cr	2224	2084	1727	4411	1289	2827	2009	3666	1706	2414	4278	2552	2832	1314	2238	2946
Co	101	112	117	110	112	111	119	117	119	103	110	114	119	114	107	116
Ni	1691	1968	2403	2013	2153	2104	2162	2040	2191	1789	1857	2079	2368	1954	2090	2100
Cu	41.5	21.6	3.29	34.8	47	39.6	29.9	41.3	13.8	1.68	2.58	2.89	45.1	9.1	7.37	22
Zn	57.4	87	52.5	66.1	64.3	71.5	65.1	70.7	49.9	42	425	52.3	66	67.7	40.8	57.5
Ga	3.56	3.64	3.29	2.59	2.35	3.22	3.49	2.93	2.66	4.71	3.55	5.83	2.75	2.19	1.43	3.32
Rb	9.58	5.14	1.54	0.41	1.6	2.69	1.14	1.55	1.82	1.83	1.55	0.95	1.06	1.37	1.13	0.53
Sr	167	168	41.6	15.8	68.8	48.7	25.6	41.2	78.4	26.3	80	14.9	11.8	145	11.8	12.7
Y	3.84	4.26	0.29	0.11	0.13	0.35	0.34	0.093	0.21	0.24	0.27	0.19	0.12	1.77	0.44	2.64
Zr	7.27	25.9	3.52	1.2	3.02	9.29	4.15	2.71	4.12	3.63	2.27	2.81	2.36	3.73	1.69	3.17
Nb	0.64	5.3	1.97	0.68	1.44	4.03	2.08	1.49	2.08	2.75	1.42	2.08	1.46	1.62	0.38	0.12
Mo	0.35	0.34	0.14	0.1	0.33	0.24	0.22	0.17	0.17	0.22	0.14	0.16	0.17	5.49	0.058	0.22
Sn	0.13	0.37													0.15	0.12
Cs	0.024	0.034	0.09	0.041	0.026	0.021	0.013	0.029	0.052	0.17	0.08	0.081	0.033	0.032	0.056	0.04
Ba	349	563	23.3	3.32	27.2	75.2	18.2	39.9	32.8	33	20.2	6.59	26.2	124	2.43	0.73
La	4.21	15.1	0.59	0.24	0.23	2.56	0.77	0.31	0.68	0.55	0.28	0.56	0.52	2.05	0.19	0.13
Ce	12.4	26.6	1.17	0.42	0.45	6.06	1.6	0.48	1.29	1	0.5	1.02	0.89	0.84	0.4	0.42
Pr	1.86	2.96	0.15	0.048	0.054	0.64	0.21	0.05	0.16	0.12	0.068	0.12	0.1	0.27	0.06	0.072
Nd	8.08	10.8	0.54	0.2	0.2	1.99	0.81	0.17	0.56	0.46	0.34	0.46	0.34	1.15	0.23	0.43
Sm	1.19	1.85	0.11	0.04	0.042	0.22	0.15	0.034	0.11	0.073	0.068	0.091	0.078	0.19	0.068	0.16
Eu	0.37	0.59	0.028	0.016	0.017	0.067	0.036	0.013	0.033	0.037	0.025	0.022	0.024	0.075	0.024	0.061
Gd	0.91	1.43	0.095	0.045	0.033	0.15	0.13	0.031	0.078	0.064	0.065	0.073	0.05	0.28	0.083	0.24
Tb	0.11	0.19	0.015	0.0045	0.005	0.016	0.016	0.0044	0.013	0.013	0.012	0.012	0.007	0.037	0.012	0.052
Dy	0.64	0.87	0.063	0.019	0.029	0.079	0.073	0.023	0.054	0.054	0.057	0.038	0.032	0.19	0.079	0.4
Ho	0.13	0.14	0.013	0.0053	0.0069	0.014	0.013	0.006	0.01	0.0072	0.01	0.0094	0.0074	0.037	0.018	0.097
Er	0.36	0.37	0.031	0.012	0.013	0.031	0.04	0.012	0.027	0.017	0.027	0.014	0.022	0.11	0.048	0.33
Tm	0.055	0.05	0.0045	0.0024	0.0021	0.0055	0.0045	0.0019	0.0034	0.0036	0.0038	0.0022	0.0029	0.011	0.0073	0.05
Yb	0.4	0.32	0.031	0.023	0.016	0.046	0.024	0.014	0.021	0.035	0.025	0.015	0.018	0.054	0.054	0.37
Lu	0.07	0.043	0.0052	0.0043	0.0052	0.0092	0.0065	0.0049	0.0042	0.006	0.0053	0.0041	0.0027	0.0088	0.01	0.059
Hf	0.22	0.55	0.097	0.043	0.063	0.13	0.1	0.069	0.091	0.072	0.028	0.071	0.04	0.053	0.05	0.091
Ta	0.045	0.27	0.15	0.069	0.072	0.21	0.098	0.074	0.12	0.11	0.061	0.11	0.1	0.053	0.05	0.024
Pb	0.57	0.61	0.25	0.16	0.51	0.48	0.18	0.32	0.16	0.17	0.44	0.18	0.093	0.63	0.49	1.86
Th	0.26	1.2	0.11	0.043	0.099	0.18	0.13	0.12	0.13	0.11	0.16	0.11	0.066	0.032	0.028	0.015
U	0.071	0.35	0.048	0.022	0.14	0.18	0.06	0.099	0.091	0.14	0.12	0.086	0.078	0.17	0.012	0.0087
$(La/Yb)_N$	7.1	32.2	13.1	7.2	9.7	38.1	21.9	14.6	21.7	10.7	7.5	24.4	19.7	25.2	2.4	0.23

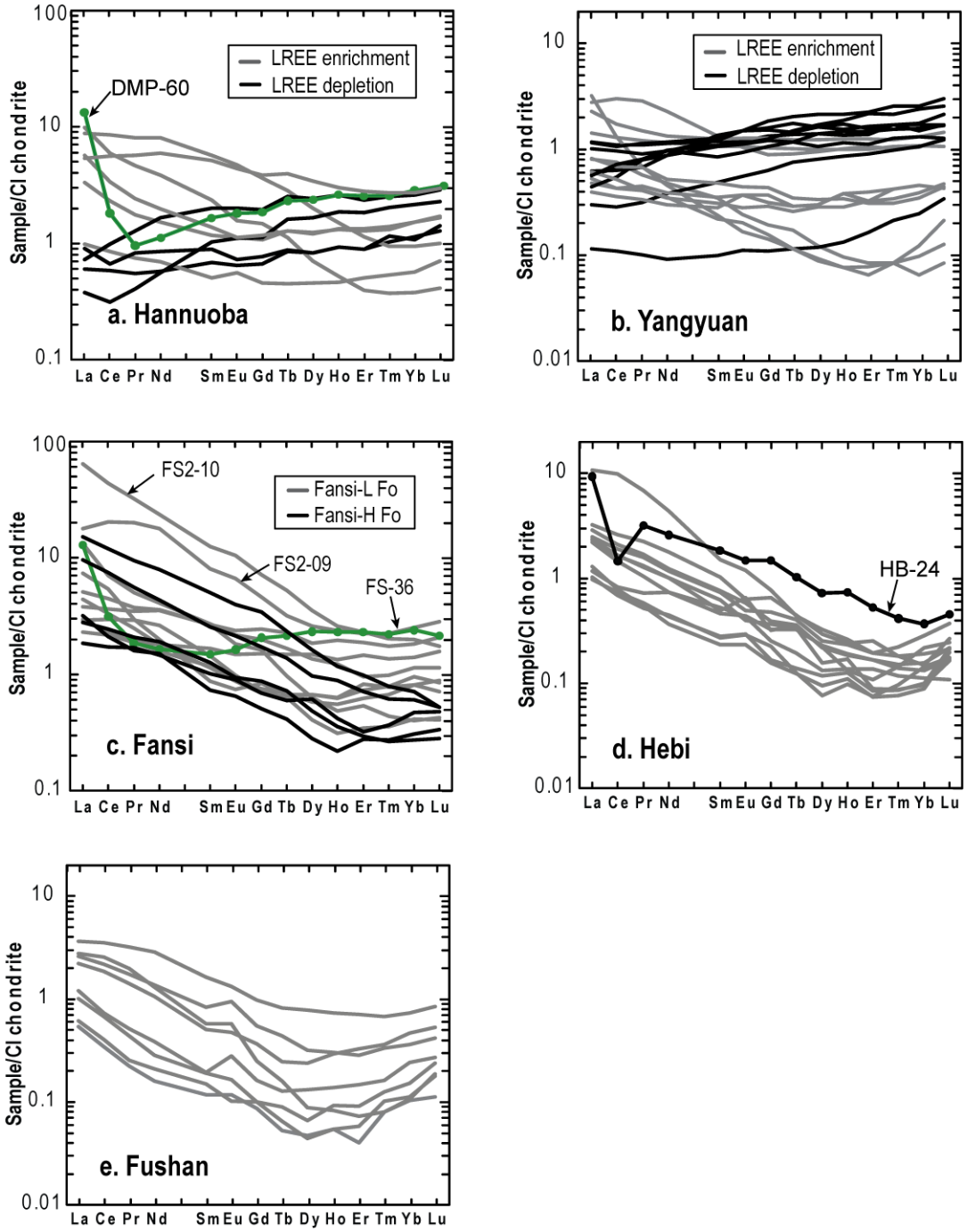

Fig. S4-1. Chondrite-normalized REE patterns of whole rock Hannuoba (a; data from Rudnick et al., 2004), Yangyuan (b; data from Y.G. Xu et al., 2008 and this study), Fansi (c), Hebi (d) and Fushan (e; data from Xu et al., 2010) peridotites. Chondrite values are from McDonough and Sun (1995).

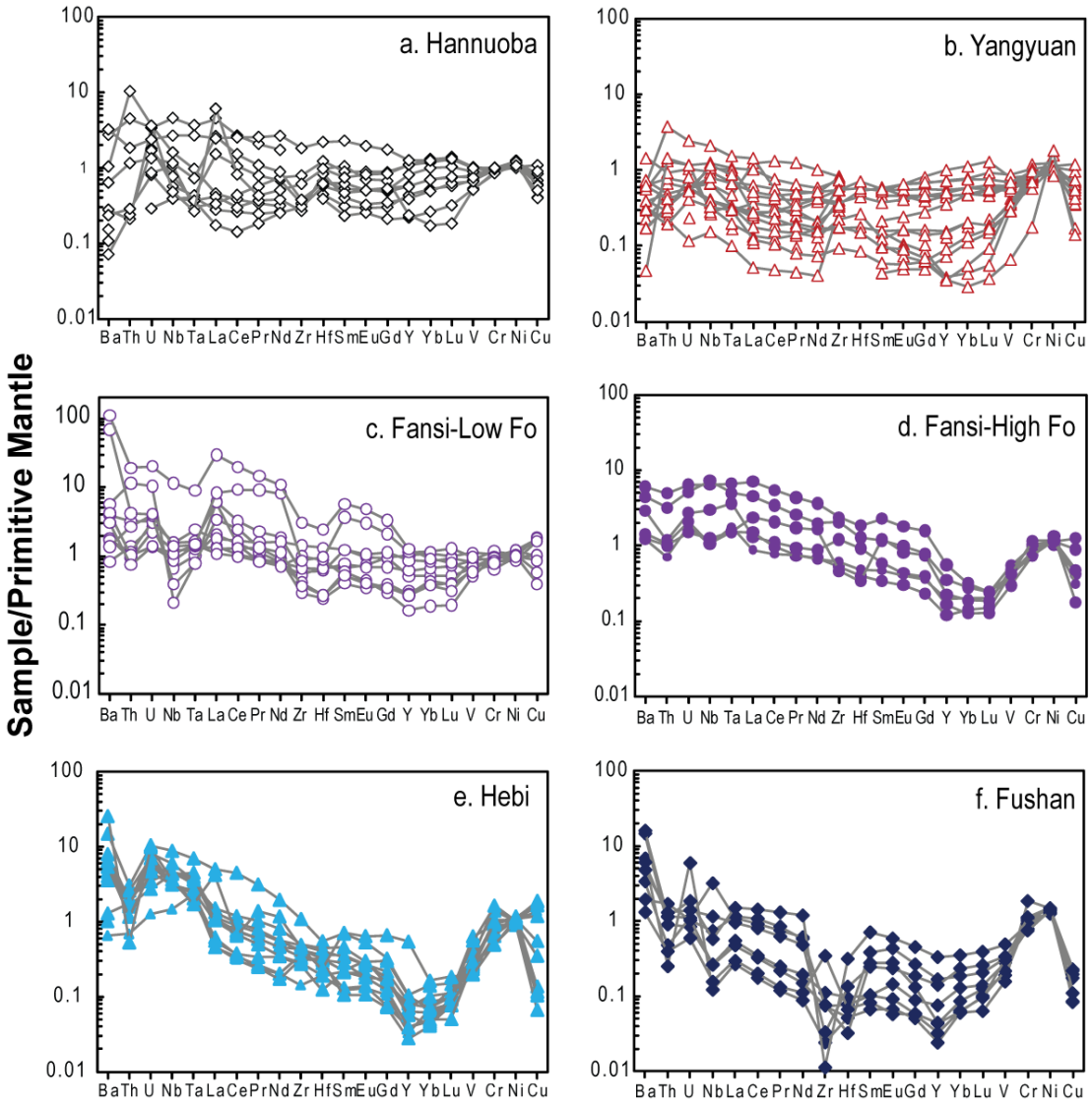

Fig. S4-2. Primitive mantle-normalized trace element diagrams of whole rock peridotites. Data sources are the same as Fig. S4-1. Primitive mantle values are from Lyubetskaya and Korenaga, 2007.

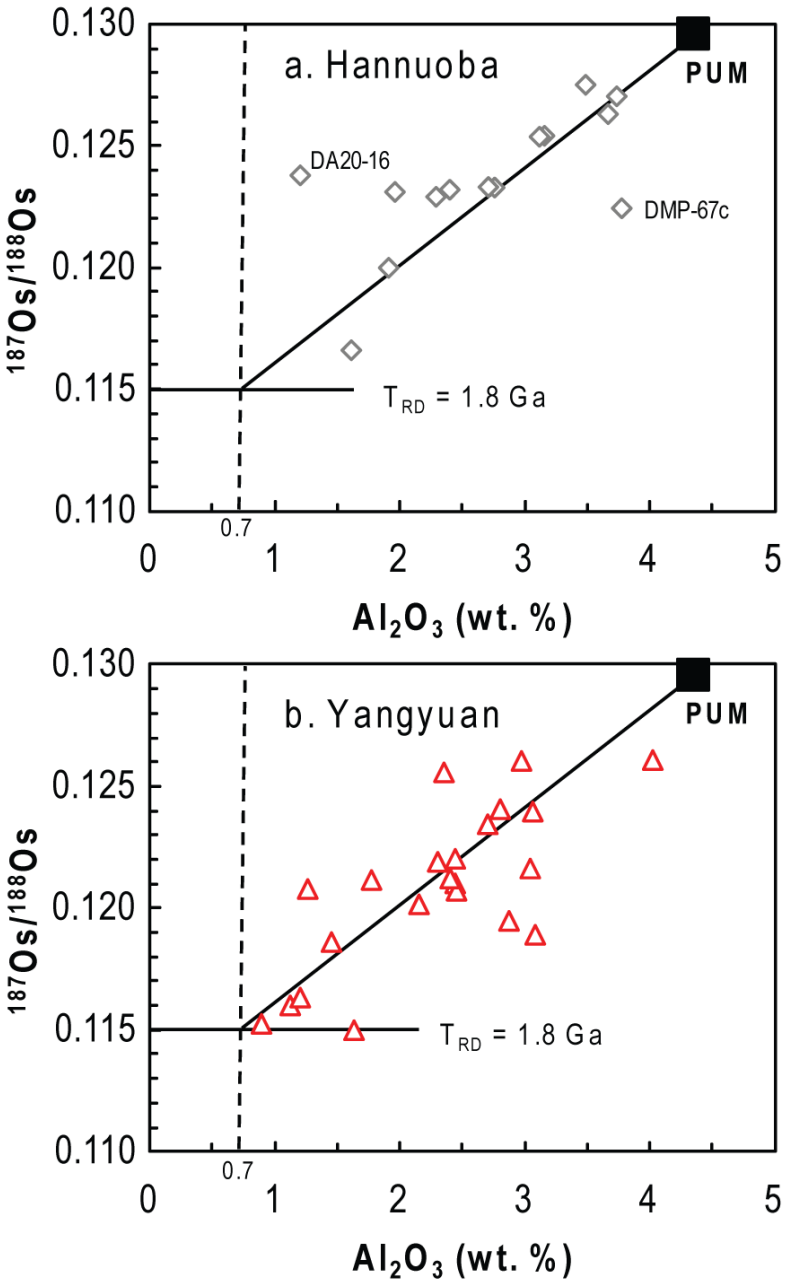

Fig. S4-3. Correlations between Al_2O_3 and $^{187}Os/^{188}Os$ for Hannuoba (a) and Yangyuan (b) peridotites. Data sources as in Fig. 4-8. PUM: primitive upper mantle. Sample DMP-67c from Hannuoba is a rare example of a Hannuoba peridotite in which sulfides have broken down (as described in Gao et al., 2002). Hannuoba sample DA20-16 is from Zhang et al. (2009) and the degree of sulfide preservation is not known.

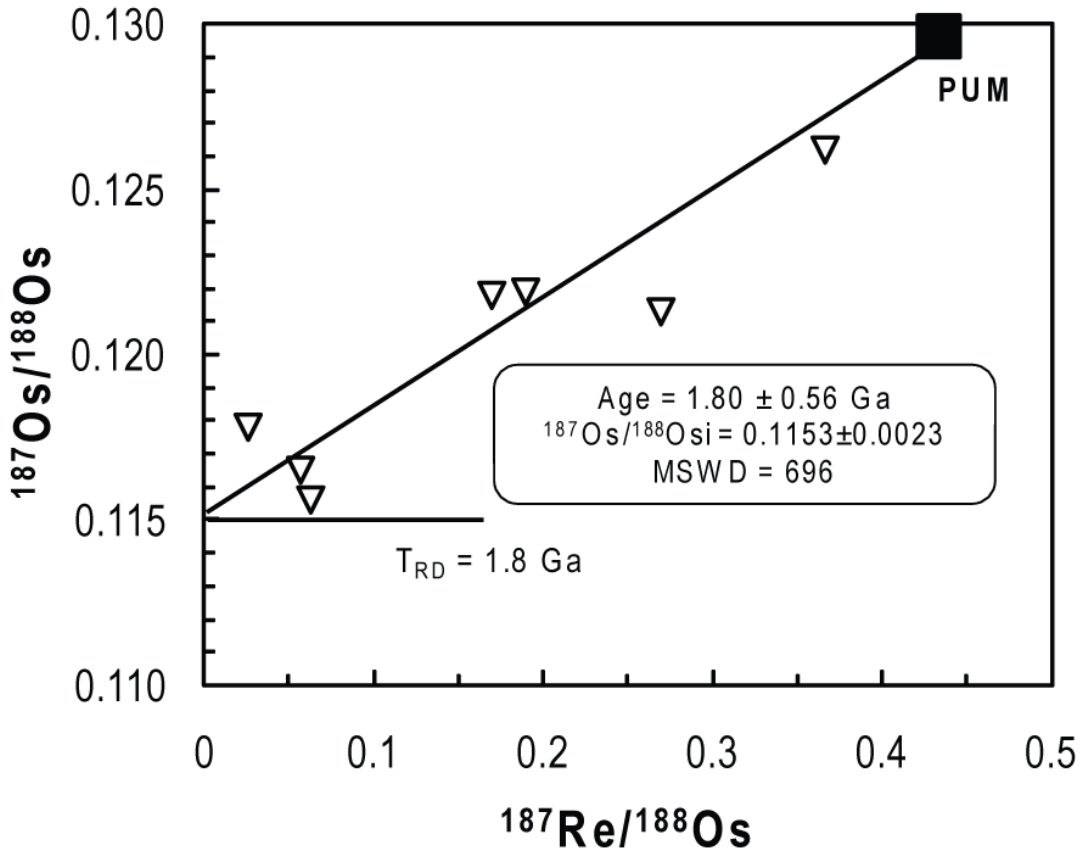

Fig. S4-4. Re-Os isochron plot for the Datong peridotites.

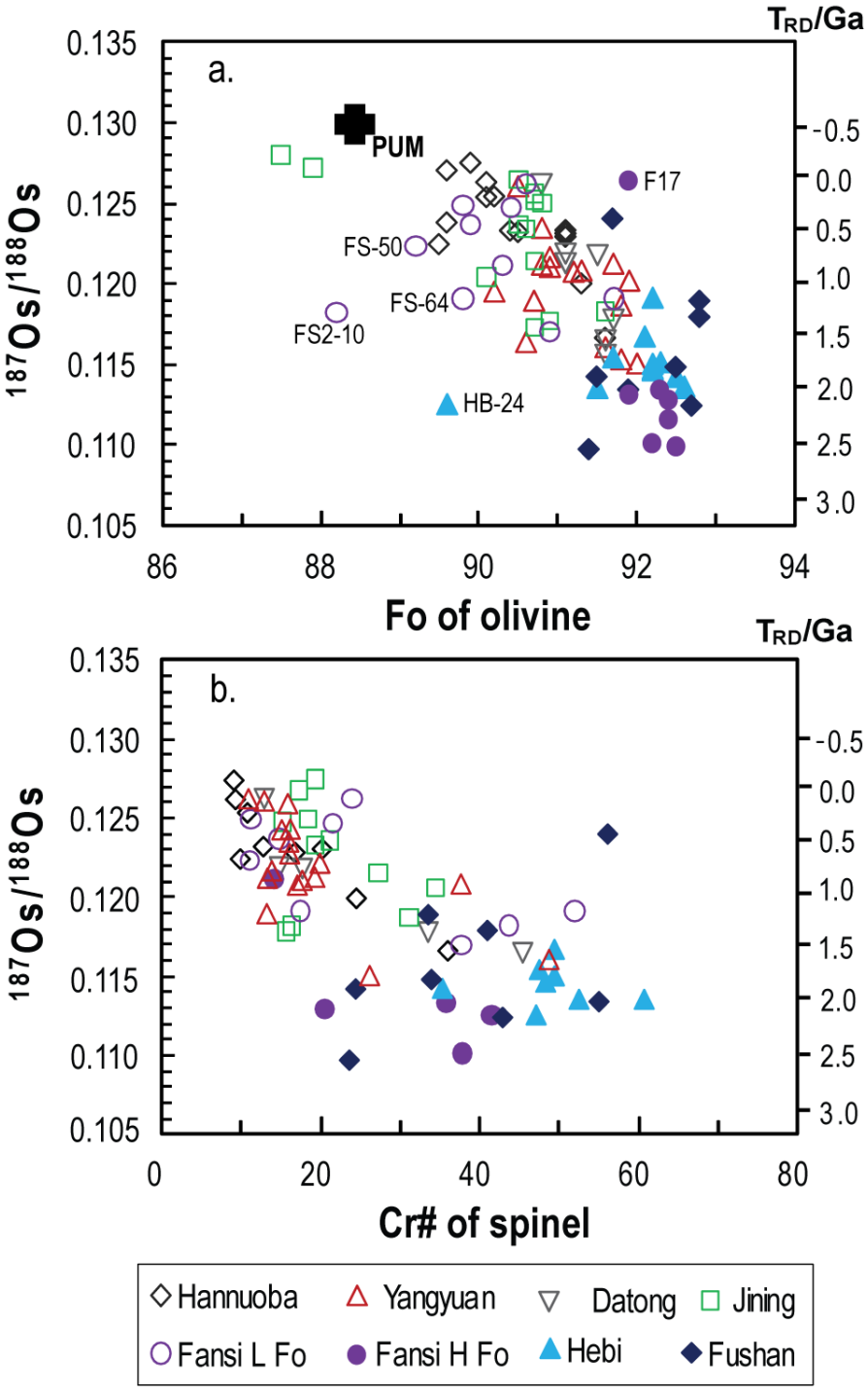

Fig. S4-5. $^{187}Os/^{188}Os$ versus Fo of olivine (a) and Cr# of spinel (b). Data sources in addition to this study are: Hannuoba (Gao et al., 2002; Rudnick et al., 2004) and Yangyuan (Liu et al., 2010)

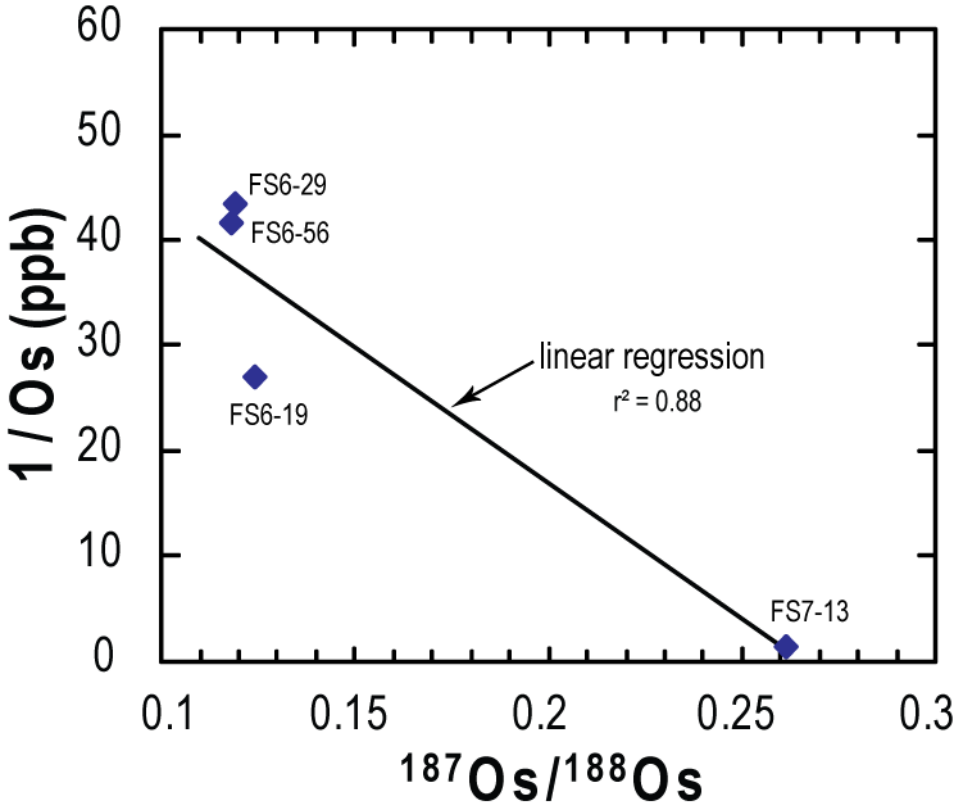

Fig. S4-6. $^{187}Os/^{188}Os$ versue 1/Os of low-HSE Fushan peridotites

Student t-test of $^{187}Os/^{188}Os$ populations between post-Archean peridotites and abyssal peridotites

Archean-Early Paleoproterozoic peridotites have obviously non-radiogenic Os isotopic compositions when compared to abyssal peridotites that represent modern convective upper mantle (Fig. 4-7b). The Os model ages for these ancient samples are relatively more robust than post-Archean peridotites that formed from a more evolved heterogeneous mantle. Post-Archean peridotites largely overlap in $^{187}Os/^{188}Os$ with abyssal peridotites (Fig. 4-7a), which produces large uncertainties of the model ages for post-Archean peridotites when utilized to interpret the formation ages of their associated lithospheric mantle. In literature, peridotitic $^{187}Os/^{188}Os$ data were generally shown in diagrams with the range of abyssal peridotites plotted for a comparison to qualitatively tell the difference or similarity between measured peridotites and abyssal peridotites. However, abyssal peridotites in literature have T_{RD} model ages ranging from future up to 2 Ga (e.g., Liu et al., 2008), which makes it nearly impossible to distinguish Proterozoic peridotites from abyssal peridotites based those diagrams. Since those few abyssal peridotites with low $^{187}Os/^{188}Os$ (Fig. 4-7b) likely reflect mantle heterogeneity, in order to tell post-Archean peridotites apart from abyssal peridotites, a feasible statistical method needs to be established.

Establishment of methods

The peridotites that experienced ancient melt depletion, over time, yield lower $^{187}Os/^{188}Os$ compared to convective upper mantle (abyssal peridotites) due to Re depletion. What I am trying to do is distinguish the $^{187}Os/^{188}Os$ populations of measured peridotites from that of abyssal peridotites. First, the normality test (*Shapiro–Wilk*) shows that abyssal peridotites exhibit a normal distribution $N(\mu_o,\sigma_o^2)$ in $^{187}Os/^{188}Os$ at the confidence level of 95% with a mean value μ_o of 0.1244 and a variance σ_o^2 of 0.0041^2. This distribution $N(\mu_o,\sigma_o^2)$ is taken as the base distribution for modern convective upper mantle. For peridotitic samples, the normality test (*Shapiro–Wilk*) is applied to see if they follow a normal distribution. If they do not show a normal distribution, we can only qualitatively judge their correlation in age based on either the histograms as shown in Fig. 4-7, or their mean value compared to that of abyssal peridotites, although the significant level cannot be well assessed. If the sample size n is large, the samples usually show a normal distribution $N(\mu,\sigma^2)$.

The observed values are usually expressed by ($\overline{X}$, s^2)- $\overline{X}$,the sample mean and s, the sample standard deviation. The test is to examine if ($\overline{X}$, s^2) belongs to a sample of the normal distribution $N(\mu_o,\sigma_o^2)$. The statistic method utilized is: *Hypothesis and Testing*. It is to test the null hypothesis H_o: $\overline{X} = \mu_o$ and $s^2=\sigma_o^2$ against the alternative hypothesis H_1: H_o is not true.

Consider the second part of H_o: $s^2=\sigma_o^2$. Under H_o: $(n-1)s^2/\sigma_o^2 \square \chi^2(n-1)$, the rejection region for H_o is $(n-1)s^2/\sigma_o^2 > \chi^2_{\frac{\alpha}{2}}(n-1)$ or $(n-1)s^2/\sigma_o^2 < \chi^2_{1-\frac{\alpha}{2}}(n-1)$, where α is the significant level 0.05 and n is the sample size.

Then consider the first part of Ho: $\overline{X}$ = μ_o. Under H_o: $T=\frac{\overline{X}-\overline{Y}}{s_{\overline{X}-\overline{Y}}} \sim t(n+m-2), s_{\overline{X}-\overline{Y}}=\sqrt{\frac{s_X^2}{n}+\frac{s_Y^2}{m}}$, where $\overline{X}$ is the sample mean, $\overline{Y}$ is the observed population mean of μ_o, s_X is the sample standard deviation, n is the sample size, s_Y is the observed population standard deviation, m is the observed population size. The rejection region for H_o is $|T| > t_{\frac{\alpha}{2}}(n+m-2)$, where α is the significant level 0.05 and n+m-2 is the degrees of freedom for a t distribution. If H_o is not rejected, the sample has the same distribution as abyssal peridotites. If Ho is rejected, the alternative H_1 is true. In general, the sample mean is greater than the population mean, implying that the samples represent older lithospheric mantle than do abyssal peridotites. In this case, the derived Os model ages are robust, e.g., based on the Al-Os pseudo-isochron.

Results of tests

1. Cenozoic-erupted peridotites in the eastern portion of the North China Craton

Normality Test (Shapiro-Wilk)

Dataset	N	W	Decision
1. AP	97	0.981	Normal at 0.95 level
2. EB	52	0.950	Normal at 0.95 level

AP: abyssal peridotites (data sources are outlined in Fig. 4-7).
EB: peridotites erupted in the Cenozoic from the eastern protion of the North China Craton.
N: the sample size
W: the statitic test. The user may reject the null hypothesis if W is too small.

Two Sample Independent t-Test

Sample	N	Mean	SD
1. AP	97	0.12442	0.0041
2. EB	52	0.12405	0.0035

Difference of Means: 0.00037
Null Hypothesis: Mean 1 - Mean 2 = 0

t	DoF
0.55	147

At the 0.95 level, the difference of the population means is not significantly different than the test difference (0).

t: the statisitic test.
DoF: degree of freedom

The conclusion is that the $^{187}Os/^{188}Os$ population of Cenozoic-erupted peridotites from the eastern poriton of the North China Craton has no difference from that of abyssal peridotites at the confident level of 95%. Such resultant test suggests that lithopsheric mantle beneath the eastern portion of the North China Craton was newly formed from the asthenosphere.

2. Cenozoic-erupted peridotites from the northern portion of the central region of the North China Craton

Normality Test (Shapiro-Wilk)

Dataset	N	W	Decision
1. AP	97	0.981	Normal at 0.95 level
2. CB	78	0.961	Normal at 0.95 level

CB: peridotites erupted in the Cenozoic from the northern portion of the central region of the North China Craton (i.e., the northern group; data sources as in Fig. 4-7a).

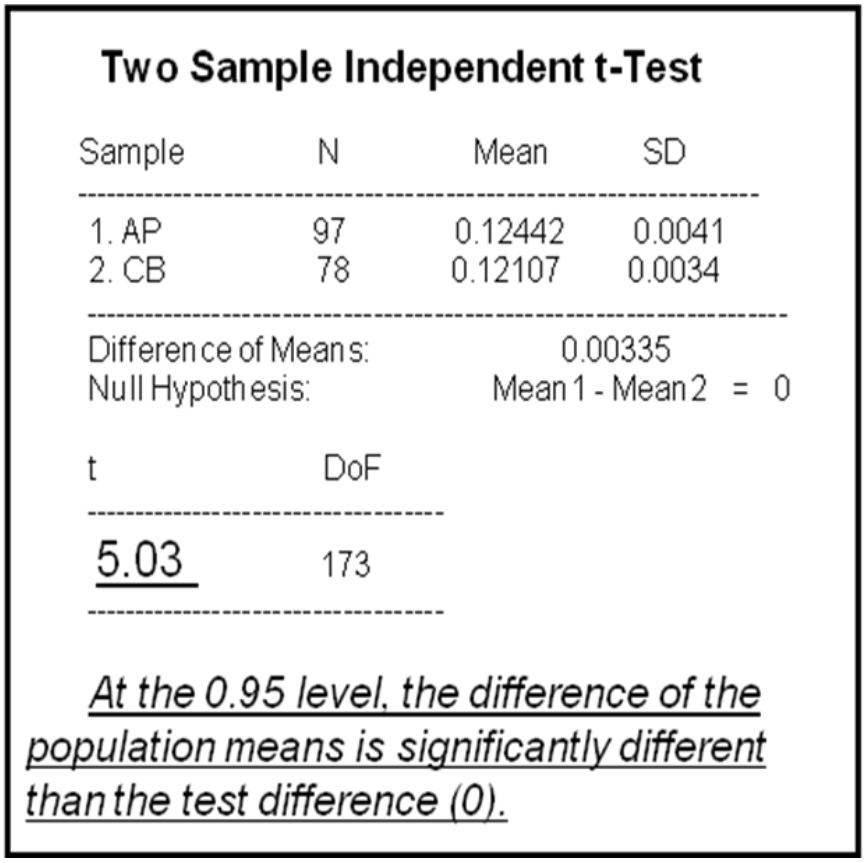

Two Sample Independent t-Test

Sample	N	Mean	SD
1. AP	97	0.12442	0.0041
2. CB	78	0.12107	0.0034

Difference of Means: 0.00335
Null Hypothesis: Mean 1 - Mean 2 = 0

t	DoF
5.03	173

At the 0.95 level, the difference of the population means is significantly different than the test difference (0).

The conclusion is that the $^{187}Os/^{188}Os$ population of Cenozoic-erupted peridotites from the northern portion of the central region of the North China Craton is characterized by significantly lower $^{187}Os/^{188}Os$ than that of abyssal peridotites at the confidence level of 95%. Such resultant test suggests that lithopsheric mantle sampled by these peridotites was formed earlier, which supports the Os model age derived from the Al-Os pseduo-isochron (Fig. 4-8).

Chapter 5: The history of melt depletion and later overprinting in peridotites using Sr-Nd-Hf-Pb isotopic tracers: an example from Yangyuan, North China Craton[1, 2, 3]

[1] The original version of this chapter was created/written by J.G. Liu. J.G. Liu, R.W. Carlson, R.L. Rudnick, and R.J. Walker contributed to the interpretation of the data.

[2] Trace element concentrations of pyroxenes were measured by J.G. Liu with assistance of Richard Ash. Clinopyroxene separation was done by J.G. Liu. Sr-Nd-Hf-Pb isotopic compositions of clinopyroxene separates were measured by J.G. Liu with assistance of Rick Carlson, Mary Horan and Tim Mock.

[3] In preparation for *Chemical Geology*.

Abstract

Trace element concentrations of orthopyroxenes and clinopyroxenes and Sr, Nd, Pb and Hf isotopic compositions for clinopyroxenes from 11 well-characterized spinel peridotite xenoliths carried in the ~30 Ma Yangyuan alkali basalts, North China Craton, reveal a history of chemical modification (i.e., initial melt depletion and later overprinting by melts/fluids) of the lithospheric mantle. The clinopyroxenes were separated from a suite of samples for which whole-rock Re-Os isotopic systematics have previously suggested a melt depletion event at ~1.8 Ga. The clinopyroxenes were chosen to span a range of rare earth element (REE) patterns (chondrite-normalized $(La/Yb)_N$ = 0.13 to 13.5). Present-day isotopic compositions are highly variable: $^{87}Sr/^{86}Sr$ = 0.70229 to 0.70443, ε_{Nd} = -0.6 to +24, $^{206}Pb/^{204}Pb$ = 15.74 to 19.08, and ε_{Hf} = +13.5 to +167). Two main types of chemical signatures are identified in these clinopyroxenes: 1) preservation of original ancient melt depletion, characterized by prominent depletions of light REE (LREE) relative to heavy REE (HREE), highly radiogenic Nd and Hf isotopic compositions, and comparatively

non-radiogenic Pb isotopic compositions; and 2) recent incompatible element overprinting, likely related to the Cenozoic magmatism. The latter form of overprinting is reflected in flat to LREE-enriched patterns and Sr-Nd-Pb isotope compositions that are similar to or plot towards the composition of the host basalt. Despite these overprinting events, the Yangyuan clinopyroxenes yield a Lu-Hf "errorchron" age (1.66 ± 0.10 Ga) that is within uncertainty of the oldest whole-rock Os model ages (1.8 ± 0.2 Ga), consistent with Paleoproterozoic primary melt depletion in these samples. The high initial ε_{Hf} value of +19 in these clinopyroxenes implies that the Lu-Hf isotopic system may record the cooling age at which the peridotites cooled below the closure temperature of the Lu-Hf isotope system. Nd-Hf decoupling in peridotitic clinopyroxenes, which causes them to plot to the high $^{176}Hf/^{177}Hf$ side of the mantle array defined by oceanic basalts, results from ancient Lu/Hf and Sm/Nd decoupling soon after or during mantle partial melting. The fact that oceanic basalts do not record such compositions suggests that ancient residual peridotites do not generally participate in later melting events, perhaps because they are sequestered within the lithosphere. High $^{176}Hf/^{177}Hf$ relative to $^{143}Nd/^{144}Nd$ may be a way to distinguish ancient lithospheric mantle inputs into continental, mantle-derived magmas.

5.1 Introduction

Dating melt depletion events recorded in peridotites from the lithospheric mantle and, hence, formation of the lithospheric mantle, is important for understanding the relationship between the lithospheric mantle and overlying crust, as well as continental tectonics (e.g., Lee et al., 2000; Gao et al., 2002). The Re-Os isotope system is resistant to overprinting and has been extensively used to date melt

depletion events in mantle peridotites (e.g., Walker et al., 1989; Pearson et al., 1995a; Reisberg and Lorand, 1995; Handler et al., 1997). The value of the Re-Os system in this application stems from the fact that Os is typically compatible, while Re behaves moderately incompatibly during melt extraction from the mantle. Thus, further growth of ^{187}Os in residues of mantle melting is retarded, and the typically high Os concentrations of residual peridotites make them resistant to later overprinting by melts/fluids that generally have low Os contents. Meaningful Re-Os isochrons reported for lithospheric mantle peridotites are, however, rare. This primarily reflects the narrow range of Re/Os ratios present in a suite of peridotites, the likelihood of isotopic heterogeneity in a mantle domain at the time of melt depletion, and, especially, recent Re (and sometimes Os) mobility in peridotites. By contrast, Re-Os model ages of individual whole-rock samples or sulfides are often utilized to date melt depletion events (e.g., Walker et al., 1989; Shirey and Walker, 1998; Pearson et al., 2002).

The Re-depletion model age (Walker et al., 1989) was defined in order to circumvent recent Re addition from the host magma to highly depleted peridotites, but this model age can be inaccurate if the Os isotopic composition of the sample was overprinted or modified by events that occurred after the initial melt depletion (e.g., Chesley et al., 1999; Büchl et al., 2002). As in any model age, Re-Os model ages also are sensitive to the accuracy with which the assumed mantle Re-Os evolutionary parameters reflect those of the Earth's mantle (Rudnick and Walker, 2009). The significant range in $^{187}Os/^{188}Os$ in modern mantle samples results in a potential model age imprecision that gets larger as the sample gets younger. For example, if the bulk modern mantle has $^{187}Os/^{188}Os$ of 0.1251, the average measured in abyssal peridotites

(e.g., Brandon et al., 2000), instead of the commonly used chondritic mantle value of 0.1270 (e.g., Shirey and Walker, 1998), this would change the Re-Os model age of a modern sample by 280 Ma, but would change the model age of a 1.8 Ga sample by 110 Ma. The development of corroborating chronologic information is, therefore, important (e.g., Schmidberger et al., 2002; Pearson and Nowell, 2003).

In comparison to the siderophile and chalcophile Re-Os isotope system, most other long-lived radiogenic isotope chronometers, such as Rb-Sr, Sm-Nd, U-Pb and Lu-Hf, are based on incompatible lithophile (or chalcophile, in the case of Pb) trace elements. Previous studies of incompatible element-based isotope systems in xenolithic peridotites have mostly focused on Rb-Sr, U-Pb and, especially, the Sm-Nd system. However, such results often prove difficult to interpret in terms of constraining the timing of original melt depletion due to: 1) contamination during transit in the host lavas, which are normally enriched in these highly incompatible elements compared to peridotite xenoliths (Carlson and Irving, 1994; Bedini and Bodinier, 1999; Schmidberger and Francis, 2001); 2) significant diffusion at mantle temperatures (Van Orman et al., 2001) that can partially to completely reset the isotopic ratios of minerals in peridotites (McDonough and McCulloch, 1987; Pearson et al., 1995b); and 3) overprinting of incompatible elements at some point after melt depletion, which may obscure the effects of primary melt depletion in peridotites (e.g., Frey and Green, 1974; Stosch and Seck, 1980; Nixon et al., 1981; McDonough, 1990; Carlson and Irving, 1994). As a consequence, these incompatible element-based isotope systems have proven more useful for understanding secondary overprinting processes subsequent to melt depletion (e.g., Menzies and Hawkesworth, 1987; Menzies and Chazot, 1995), rather than dating melt depletion events.

In contrast to the U-Pb, Rb-Sr and Sm-Nd systems, the Lu-Hf isotope system has been shown by several studies to remain relatively immune to overprinting events and, thus, may provide a valuable complement to the Re-Os isotope system for constraining the timing of melt depletion in peridotites (Schmidberger et al., 2002; Pearson and Nowell, 2003; Carlson et al., 2004; Wittig et al., 2006; Bizimis et al., 2007; Choi et al., 2008, 2010). The utility of the Lu-Hf system in this type of application derives from the fact that: 1) Hf diffuses considerably more slowly in silicate minerals than do Pb, Sr and Nd (Scherer et al., 2000; Ionov et al., 2005a), and 2) clinopyroxene has relatively high Lu and Hf concentrations compared to other minerals in spinel peridotites and compared to possible infiltrating melts/fluids.

In this study, I determined the trace element concentrations of clinopyroxenes and orthopyroxenes and Sr, Nd, Pb and Hf isotopic compositions of clinopyroxene separates from a suite of spinel peridotites contained within the ~30 Ma Yangyuan alkali basalts, North China Craton (Fig. 2-1). These peridotites have been previously studied for bulk petrologic and geochemical characteristics, including Re-Os isotope systematics and highly siderophile element (HSE) abundances. The Os data suggest a Paleoproterozic age (1.8 ± 0.2 Ga) for melt depletion (Liu et al., 2010, 2011a). The main objectives here are to 1) compare Sr-Nd-Hf-Pb isotope systematics in clinopyroxene separates to whole-rock Re-Os systematics of the same rocks, 2) use these isotopic tracers, in combination with trace element data, to determine the history of initial melt depletion and later overprinting of incompatible elements in these rocks, and 3) evaluate the utility of the Lu-Hf isotope system to date melt depletion in xenolithic peridotites.

Table 5-1. Summary of basic petrologic and geochemical characteristics of Yangyuan peridotites

Samples	Lithology	Mode[a]				MgO[b]	Al_2O_3[b]	Fo[c]	$^{187}Re/^{188}Os$	$^{187}Os/^{188}Os$	T_{RD}[d]	T_{MA}[e]	T[f]
		Ol	Opx	Cpx	Sp	%	%				Ga	Ga	°C
YY-04	Harzburgite	69.6	25.5	4.3	0.6	44.4	1.63	92.0	0.08	0.1152	1.8	2.1	860
YY-08	Lherzolite	58.8	32.6	5.5	3.1	39.9	2.97	90.5	0.13	0.1261	0.2	0.2	820
YY-13	Lherzolite	69.2	21.4	7.9	1.4	41.9	2.44	90.9	0.17	0.1210	0.9	1.5	1020
YY-23	Lherzolite	67.2	26.9	5.5	0.5	39.7	3.06	90.8	0.15	0.1240	0.5	0.7	1150
YY-26	Lherzolite	65.1	24.0	8.7	2.2	41.7	3.08	90.7	0.46	0.1189	1.2	-8.6	880
YY-36	Lherzolite	69.6	18.6	10.5	1.3	41.7	2.30	91.1	0.48	0.1219	0.8	-3.8	975
YY-40B	Lherzolite	65.6	23.6	8.8	1.9	40.0	2.80	91.2	0.31	0.1241	0.4	2.0	990
YY-42	Harzburgite	74.6	19.5	4.0	1.8	42.4	2.35	91.0	0.33	0.1256	0.2	1.1	1020
YY-45	Lherzolite	69.0	23.2	6.8	1.0	41.1	2.44	90.8	0.10	0.1220	0.7	1.0	1140
YY-50	Lherzolite	52.0	30.3	16.1	1.6	38.2	4.02	90.6	0.31	0.1261	0.1	0.6	1070
YY-58	Harzburgite	75.8	19.7	3.4	1.0	42.4	2.40	91.7	0.23	0.1212	0.9	2.0	1100

Note: all samples are fresh, coarse-grained, and protogranular in texture.

a. Modal mineralogy (Ol: olivine, Opx: orthopyroxene, Cpx: clinopyroxene, and Sp: spinel)

b. Whole rock MgO and Al_2O_3 content (wt. %)

c. Forsterite content of olivine (molar $Mg/(Mg+Fe^{2+})x100$)

d. T_{RD}: rhenium depletion model age (see Shirey and Walker, 1998)

e. T_{MA}: Os model age (see Shirey and Walker, 1998)

f. Two-pyroxene equilibration temperature at P = 1.5 GPa

All data from Liu et al. (2010, 2011a).

5.2 Samples

Xenoliths from Yangyuan, the focus of this study, are spinel peridotites contained within ~30 Ma alkali basalts (Fig. 2-1) and have been previously investigated for petrology, mineral compositions and whole-rock major and trace element compositions, including HSE abundances and Re-Os isotopic systematics (Liu et al., 2010, 201l), as well as Sr-Nd isotope systematics on clinopyroxene separates (Y.G. Xu et al., 2008). Petrologic and geochemical results for samples analyzed in this study are summarized in Table 5-1. In addition, the host basalt was sampled from a lava rind on one of the Yangyuan mantle xenoliths for comparison with the peridotites.

5.3 Analytical methods

Trace element concentrations of clinopyroxenes and orthopyroxenes extracted from the Yangyuan peridotites studied by Liu et al. (2010, 2011) were determined on polished mineral mounts using a New Wave Research UP213 (213 nm) laser-ablation system coupled to a Thermo-Finnigan inductively coupled plasma-mass spectrometer (ICP-MS/Element 2) at the University of Maryland (UMd) following the protocol of Arevalo and McDonough (2008). The analyses were performed by scanning the laser, with a spot size of 54-150 μm, along lines of ~1 mm length. Data were collected in a time-resolved mode so that inclusions and mineral zoning could be detected. ^{43}Ca was used as an internal standard to monitor ablation yield. Detection limits, calculated as the concentration equivalent to three times the standard deviation of the background counts, are provided in Table S5-1. The NIST 610 glass standard reference material was used for external calibration in order to calculate the element concentrations in the samples. Replicate analyses of the BHVO glass standard, analyzed periodically

during analytical sessions, yielded an external precision of typically better than 8% (1σ relative standard deviation) (Table S5-1). No trace element zoning or inclusions were observed in the clinopyroxene and orthopyroxene grains for any of the elements analyzed here. Four to six separate analyses of each mineral were made and the average results are reported. Based on the trace element compositions of clinopyroxene and the amount of available material, eleven large xenolithic samples (as shown in Table 5-1) whose clinopyroxenes span a large range in parent-daughter ratios (e.g., Lu/Hf and Sm/Nd) were selected as representative samples for Sr-Nd-Hf-Pb isotopic analyses; isotopic analyses of the same elements were conducted for the host basalt.

Ultrapure clinopyroxene separates were carefully prepared from gently disaggregated rocks, sieved to 250 - 500 μm, handpicked under a binocular microscope, and finally crushed to less than 100 μm in an agate mortar and pestle. About 0.1-0.2 grams of pulverized clinopyroxene grains were weighed into a 15 ml Teflon beaker and leached in ~5 ml 2.5 N HCl for 15 minutes followed by addition of a few drops of concentrated HF for 5 minutes (during these leaching steps, the beaker was capped and placed in an ultrasonic water bath), and then rinsed repeatedly in 10^{18} ohm deionized water. One bulk host basalt (pulverized to < 100 μm) was weighed (~35 mg) into a beaker, but was not leached by acids. Prior to decomposition, all samples were appropriately spiked with ^{87}Rb, ^{84}Sr, ^{150}Nd, ^{149}Sm, ^{176}Lu, ^{180}Hf, ^{205}Pb and ^{235}U to determine elemental concentrations by isotope dilution. All samples were completely dissolved in a mixture of ~1 ml concentrated Teflon distilled HNO_3 and ~2 ml concentrated Teflon distilled HF in capped beakers on a hotplate (~90^0C) for three days.

The elements of interest were separated and purified by column chromatography at the Department of Terrestrial Magnetism (DTM), Carnegie Institution of Washington using the procedures described in Carlson et al. (2004). Strontium and Nd isotopic compositions were determined in static mode on a Triton thermal ionization mass spectrometry (TIMS) at DTM. The Sr and Nd isotopic ratios were corrected for instrumental mass fractionation using a $^{86}Sr/^{88}Sr$ value of 0.1194 and a $^{146}Nd/^{144}Nd$ value of 0.7219, respectively. In the analysis of Nd, ^{140}Ce and ^{147}Sm were measured to monitor and correct the potential isobaric interferences. Replicate analyses of standards were performed during the analytical sessions and yielded: NBS 987 $^{87}Sr/^{86}Sr = 0.710247 \pm 10$ (2σ; n=4), identical to the accepted value of 0.710250, and JNdi-1 $^{143}Nd/^{144}Nd = 0.512103 \pm 11$ (2σ; n=4), equivalent to the value of 0.512115 ± 7 (2σ) obtained by Tanaka et al. (2000).

Uranium, Rb, Sm and Lu concentrations and Hf and Pb isotopic compositions were determined using a Nu Plasma MC-ICP-MS: U, Sm, Lu and Hf at UMd, and Pb and Rb at DTM. In the U, Rb and Pb measurements, isotopic mass fractionation was corrected for by periodic measurements of standards: U was corrected to $^{238}U/^{235}U$ = 349.1 (UMD-1); Rb to $^{87}Rb/^{85}Rb = 0.3857$ and the ^{87}Sr isobaric interference on ^{87}Rb was monitored and corrected using ^{88}Sr with measured $^{87}Sr/^{86}Sr$. Pb was corrected using the isotopic composition obtained by Todt et al. (1996) for the NBS 981 standard. ^{140}Ce, ^{146}Nd and ^{156}Gd were monitored and corrected for isobaric interferences on Sm, and instrumental mass fractionation was corrected using $^{147}Sm/^{152}Sm = 0.56081$. In the Lu analysis, instrumental mass fractionation was corrected using $^{173}Yb/^{172}Yb = 0.73889$; the accuracy of the Yb isobaric correction to Lu was monitored by measuring a Lu standard to which various amounts of Yb had

been added. For the Hf analysis, ^{173}Yb, ^{175}Lu, ^{181}Ta and ^{182}W were measured for isobaric corrections; instrumental mass fractionation was corrected using ^{179}Hf/^{177}Hf = 0.7325. Isobaric correction for ^{180}Hf is small, given ^{180}Ta/^{177}Hf < 2 x 10^{-6} and ^{180}W/^{177}Hf < 3 x 10^{-5}, while correction for Yb and Lu interference on ^{176}Hf is significant (~0.1 to 0.8 %), given ^{176}Yb/^{177}Hf = 2.0 x 10^{-4} to 2.2 x10^{-3} and ^{176}Lu/^{177}Hf = 1.0 x 10^{-5} to 1.2 x 10^{-4}. During the analytical session, the JMC-475 standard was run repeatedly and yielded a mean ^{176}Hf/^{177}Hf ratio of 0.282158 ± 14 (2σ; n=35), identical to the recommended value of 0.282160 (Nowell et al., 1998). The Yb-doped JMC-475 solutions with ^{176}Yb/^{177}Hf ratios (~ 10^{-4}) comparable to those of samples yielded Yb-corrected ^{176}Hf/^{177}Hf ratios consistent with non-doped JMC-475 solutions, indicating that the method of Yb correction in this study was accurate within stated errors. Recent blanks at DTM for samples of this size are: Pb - 100 pg; Rb - 7 pg; Sr - 300 pg; Sm - 3 pg; Nd - 12 pg; Lu - 7 pg; and Hf - 70 pg, which are negligible (typically less than 0.2 %) for correction of isotopic compositions and concentrations of the samples, except for the Pb blank, which constitutes 0.1 to 2.9 % of the total Pb.

5.4 Results

Petrography, whole-rock major and trace element concentrations, major element compositions for minerals, as well as whole-rock Re-Os isotope data and HSE abundances, were reported previously in Liu et al. (2010, 2011a). The correlations between whole-rock Al_2O_3 vs. MgO and ^{187}Os/^{188}Os are plotted in Fig. 5-1.

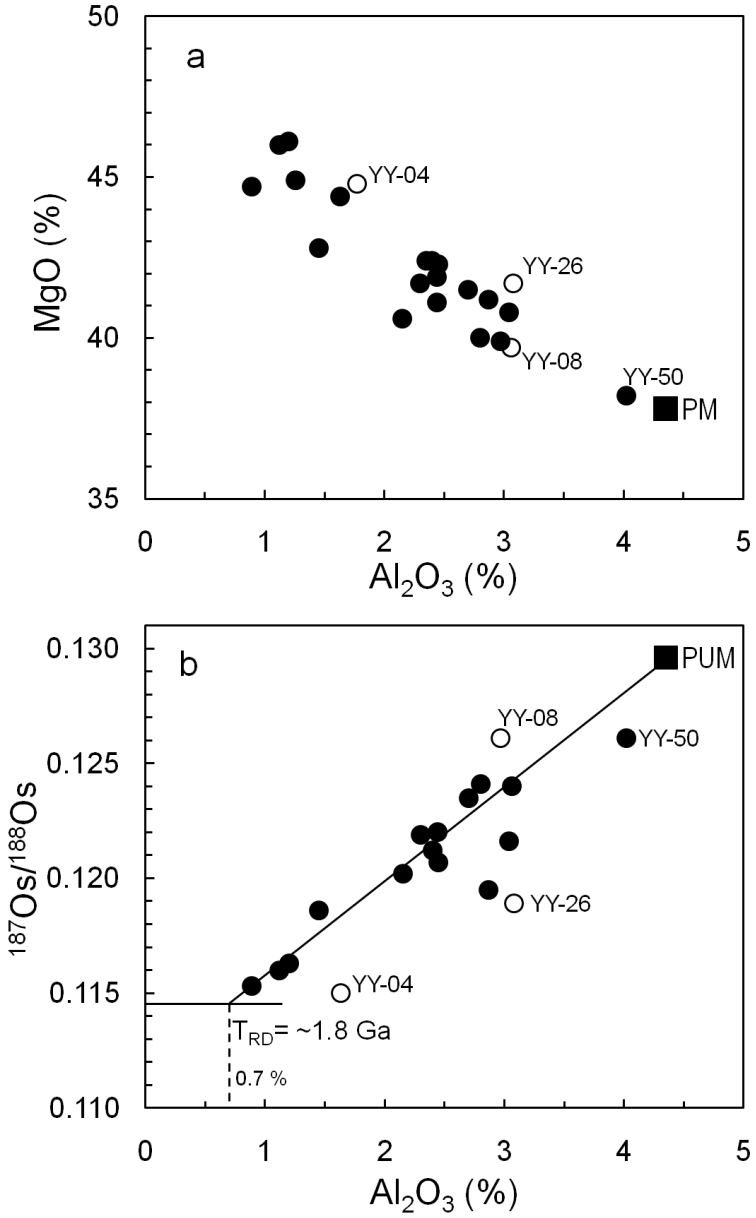

Fig. 5-1. Plots of whole-rock MgO (in wt. %; a) and $^{187}Os/^{188}Os$ (b) versus Al_2O_3 (in wt. %) of Yangyuan peridotites. PM: primitive mantle (McDonough and Sun, 1995). PUM: primitive upper mantle ($^{187}Os/^{188}Os$ = 0.1296 from Meisel et al., 2001 and Al_2O_3 = 4.35 wt. % from McDonough and Sun, 1995). T_{RD} – Re-depletion age (Walker et al., 1989). Minimum Al_2O_3 is assumed to occur at 0.7 wt. % (Handler et al., 1997). Samples having Os concentration less than 0.5 ppb (n= 4) were excluded in panel b. Open circles: YY-04, having experienced melt addition; and, YY-08 and YY-26, not cogenetic with the other samples (solid circles).

Table 5-2. Trace element concentrations for Yangyuan clinopyroxenes determined by laser ablation ICP-MS

sample	YY-04	YY-08	YY-13	YY-23	YY-26	YY-36	YY-40B	YY-42	YY-45	YY-50	YY-58
TiO_2	0.15	0.31	0.52	0.40	0.38	0.22	0.19	0.13	0.39	0.53	0.29
V	248	274	264	259	268	240	231	248	259	265	243
Cr	8820	5230	7330	6790	5340	7490	6660	6650	7090	5070	8360
Rb	BD	BD	BD	BD	BD	BD	BD	BD	BD	BD	BD
Sr	33.9	41.1	57.4	81.9	67.1	110	15.3	9.19	82.5	65.8	138
Y	5.78	12.2	13.6	17.5	16.8	8.19	8.52	9.61	14.3	17.5	11.7
Zr	8.95	6.15	28.9	28.0	19.9	10.7	3.26	3.25	23.6	30.2	20.5
Nb	0.43	0.10	0.85	1.11	0.052	0.36	0.25	0.22	1.04	0.089	0.21
La	1.46	0.90	0.83	2.43	1.02	11.6	0.41	0.22	2.49	0.69	1.12
Ce	3.24	2.10	2.62	6.26	3.70	9.09	1.06	0.64	6.49	2.88	4.56
Pr	0.44	0.36	0.53	0.94	0.67	0.79	0.18	0.11	1.00	0.59	0.84
Nd	2.16	2.19	3.55	5.46	4.01	3.39	1.09	0.77	5.22	4.23	5.07
Sm	0.67	1.00	1.65	1.74	1.43	1.10	0.52	0.45	1.56	1.76	1.62
Eu	0.27	0.44	0.75	0.67	0.65	0.42	0.28	0.18	0.71	0.73	0.67
Gd	0.76	1.43	2.19	2.22	2.06	1.18	0.89	0.82	1.99	2.46	1.80
Tb	0.14	0.29	0.40	0.48	0.39	0.23	0.20	0.20	0.42	0.45	0.34
Dy	1.03	2.12	2.67	2.96	2.83	1.62	1.53	1.57	2.72	3.06	2.24
Ho	0.22	0.49	0.55	0.65	0.69	0.34	0.32	0.36	0.61	0.66	0.48
Er	0.65	1.36	1.45	1.86	2.07	0.96	0.94	1.22	1.59	1.91	1.30
Tm	0.092	0.21	0.20	0.26	0.30	0.14	0.14	0.18	0.24	0.26	0.18
Yb	0.68	1.49	1.34	1.94	2.18	0.96	1.06	1.23	1.51	1.96	1.19
Lu	0.088	0.20	0.17	0.23	0.30	0.14	0.14	0.18	0.20	0.25	0.16
Hf	0.28	0.32	0.90	0.87	0.65	0.36	0.15	0.11	0.75	0.95	0.57
Sm/Nd	0.31	0.45	0.47	0.32	0.36	0.32	0.48	0.58	0.30	0.42	0.32
Lu/Hf	0.32	0.64	0.19	0.26	0.46	0.40	0.92	1.66	0.27	0.27	0.28
wr Sm/Nd	0.32	0.49	0.48	0.34	0.37	0.33	0.48	0.61	0.32	0.43	0.34
wr Lu/Hf	0.55	1.10	0.257	0.470	0.610	0.480	1.36	2.62	0.41	0.35	0.44
$(La/Yb)_N$	1.44	0.41	0.42	0.84	0.32	8.18	0.26	0.12	1.11	0.24	0.64

Note: TIO_2 in wt. %, all other elements are in ppm. BD: below detection limit.

$(La/Yb)_N$ is normalized to chondritic values of Sun and McDonough (1989).

wr: calculated whole rock Sm/Nd and Lu/Hf assuming none of these elements in olivine and spinel.

Table 5-3. Trace element concentrations for Yangyuan orthopyroxenes determined by laser ablation ICP-MS

sample	YY-04	YY-08	YY-13	YY-23	YY-26	YY-36	YY-40B	YY-42	YY-45	YY-50	YY-58
TiO_2	0.069	0.10	0.19	0.16	0.11	0.074	0.062	0.047	0.16	0.16	0.12
V	127	134	130	147	120	105	107	128	139	127	128
Cr	4880	2810	4400	4740	3230	3640	3570	3510	4740	2940	5620
Rb	BD	BD	BD	BD	BD	BD	BD	BD	BD	BD	BD
Sr	BD	0.15	0.28	0.49	0.11	0.22	0.12	0.05	0.40	0.20	0.76
Y	0.403	0.718	1.10	1.57	0.840	0.478	0.579	0.674	1.74	1.22	1.19
Zr	0.546	0.357	2.13	2.37	1.10	0.558	0.242	0.212	2.54	1.87	1.91
Nb	0.024	0.007	0.046	0.066	0.004	0.009	0.014	0.009	0.036	0.005	0.020
La	0.0059	0.0054	0.0046	0.013	0.0029	0.027	0.0030	BD	0.010	0.0019	0.0065
Ce	0.013	0.0077	0.015	0.050	0.0081	0.024	0.0048	0.0010	0.042	0.013	0.031
Pr	0.0023	0.0019	0.0034	0.011	0.0019	0.0031	0.0017	BD	0.0097	0.0043	0.0096
Nd	0.010	0.0078	0.027	0.068	0.014	0.019	0.0081	0.0043	0.066	0.015	0.055
Sm	0.0058	0.017	0.031	0.049	0.017	0.011	0.0039	0.0067	0.047	0.027	0.036
Eu	0.0042	0.0062	0.020	0.020	0.0076	0.0044	0.0055	0.0043	0.019	0.016	0.016
Gd	0.017	0.026	0.083	0.068	0.026	0.017	0.020	0.020	0.073	0.051	0.057
Tb	0.0058	0.0090	0.016	0.018	0.0059	0.0027	0.0083	0.0062	0.024	0.015	0.017
Dy	0.050	0.081	0.16	0.22	0.091	0.065	0.066	0.064	0.22	0.17	0.15
Ho	0.014	0.028	0.039	0.057	0.029	0.019	0.022	0.023	0.066	0.046	0.044
Er	0.060	0.11	0.14	0.22	0.13	0.080	0.086	0.10	0.24	0.18	0.16
Tm	0.013	0.024	0.024	0.041	0.031	0.015	0.020	0.021	0.047	0.034	0.028
Yb	0.13	0.24	0.26	0.38	0.29	0.16	0.18	0.21	0.39	0.34	0.24
Lu	0.023	0.048	0.038	0.065	0.058	0.030	0.039	0.041	0.069	0.060	0.040
Hf	0.021	0.021	0.066	0.060	0.036	0.028	0.011	0.0075	0.094	0.060	0.058
Sm/Nd	0.56	2.19	1.14	0.71	1.23	0.56	0.48	1.55	0.71	1.80	0.65
Lu/Hf	1.09	2.29	0.58	1.08	1.60	1.06	3.67	5.53	0.73	0.99	0.69
$(La/Yb)_N$	0.031	0.015	0.012	0.023	0.0066	0.12	0.011	<0.001	0.017	0.0039	0.018

Note: TIO_2 in wt. %, all other elements are in ppm. BD: below detection limit.
$(La/Yb)_N$ is normalized to chondritic values of Sun and McDonough (1989).

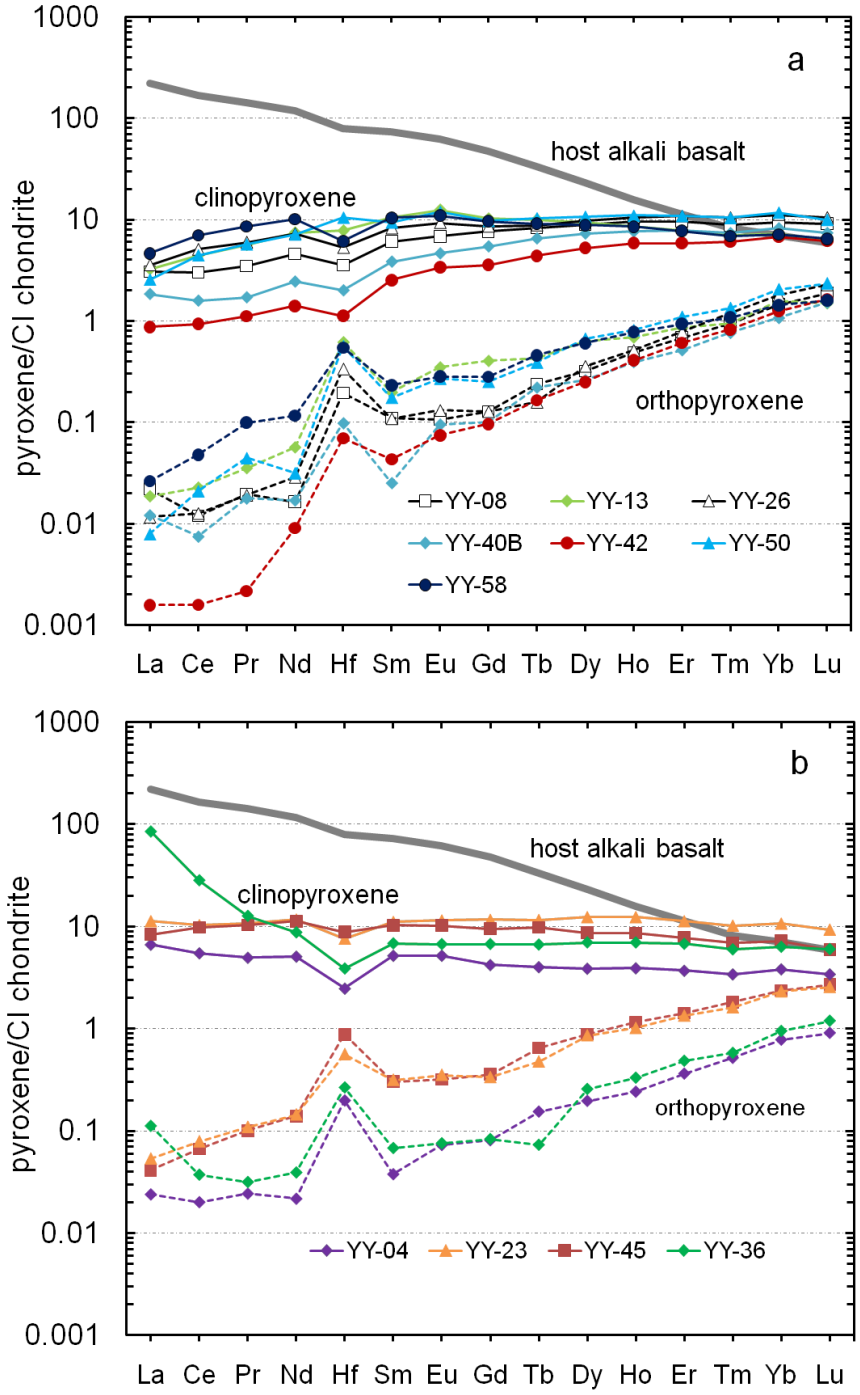

Fig. 5-2. Chondrite-normalized rare earth element (REE) and Hf patterns for clinopyroxenes (solid lines) and orthopyroxenes (dashed lines) from the Yangyuan peridotites determined by LA-ICP-MS (Tables 5-2 and 5-3). The pattern of the host basalt is shown for comparison (data from Ma and Xu, 2004). Chondrite normalizing values are from Sun and McDonough (1989).

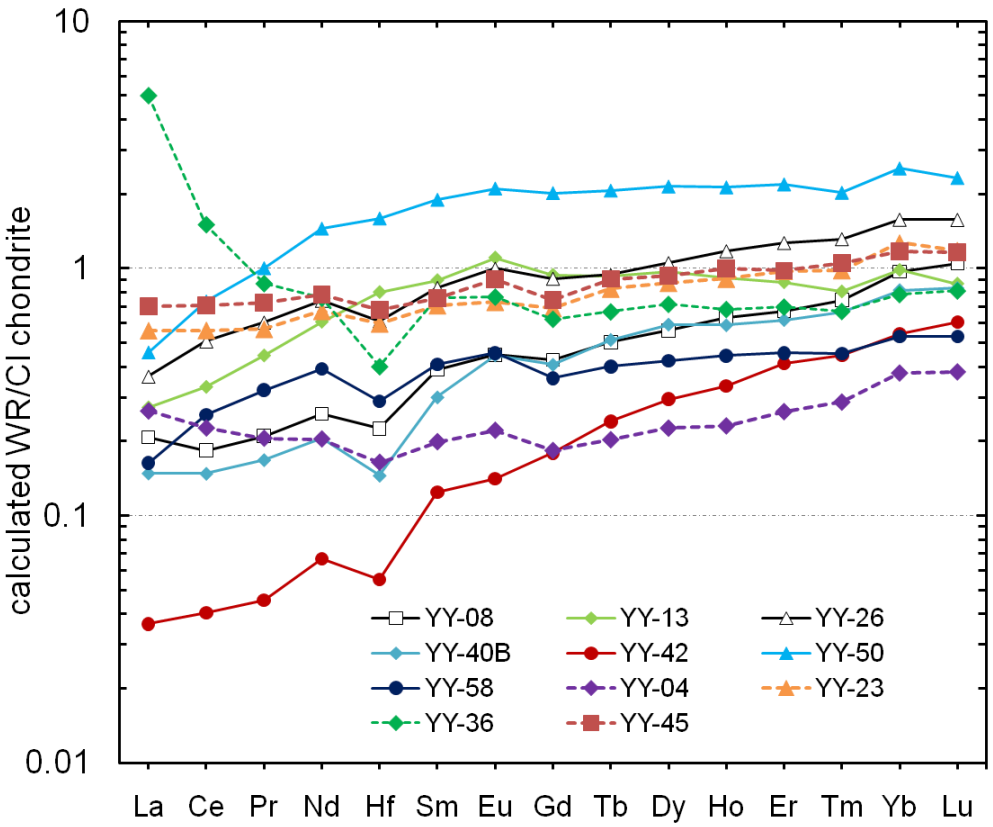

Fig. 5-3. Calculated chondrite-normalized REE and Hf patterns for whole-rock peridotites, constructed using modal mineralogy and pyroxene trace element compositions and assuming no REE or Hf in olivine and spinel.

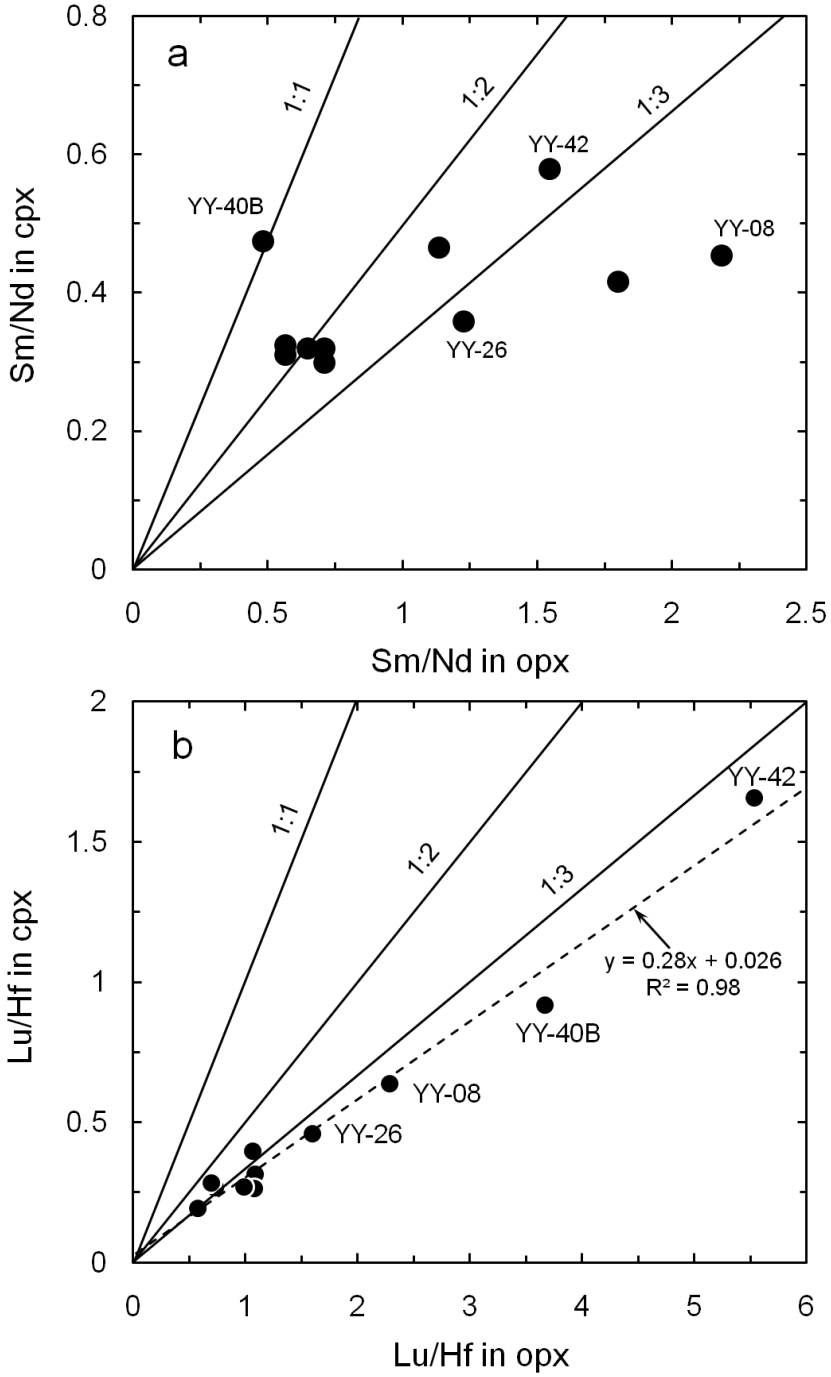

Fig. 5-4. Plots of Sm/Nd (a) and Lu/Hf (b) ratios in clinopyroxene (cpx) vs. the same ratios in coexisting orthopyroxene (opx) of the Yangyuan peridotites. Orthopyroxenes generally have higher Sm/Nd and Lu/Hf ratios than clinopyroxenes. Lines represent constant Lu/Hf ratios of clinopyroxene to orthopyroxene of 1:1, 1:2, and 1:3.

5.4.1 Pyroxene trace element concentrations

The trace element concentrations in clinopyroxene and orthopyroxene from the Yangyuan peridotites are presented in Table 5-2 and Table 5-3, respectively. Chondrite-normalized rare earth element (REE) and Hf patterns of clinopyroxene and orthopyroxene are shown in Fig. 5-2. The clinopyroxene patterns range from light REE (LREE)-depleted (Fig. 5-2a) to flat or LREE-enriched (Fig. 5-2b), with chondrite-normalized $(La/Yb)_N$ ranging from 0.13 to 13.5; most clinopyroxenes have flat HREE patterns with negative Hf anomalies compared to Nd and Sm. By contrast, orthopyroxenes are characterized by LREE depletion and positive Hf anomalies, with two samples (YY-04 and YY-36) having flat lightest REE (Fig. 5-2). Whole rock trace element compositions, calculated from the pyroxene data, are shown in Fig. 5-3. Some peridotites show a positive slope in HREE (e.g., YY-08, YY-26 and YY-42) and others show flat HREE (e.g., YY-50 and YY-58). A comparison of Sm/Nd and Lu/Hf fractionation between clinopyroxene and orthopyroxene are shown in Fig. 5-4a and b, respectively, where it can be seen that orthopyroxenes have systematically higher Sm/Nd and, especially, Lu/Hf ratios than coexisting clinopyroxenes. Moreover, the correlation is much better for Lu/Hf than Sm/Nd, which may suggest that the Sm-Nd isotopic system is farther from the equilibrium partitioning between the two pyroxenes than is the Lu-Hf isotopic system.

5.4.2 Sr, Nd, Pb and Hf isotopic compositions

The Sr, Nd, Pb and Hf isotopic compositions of the host basalt and clinopyroxenes from the Yangyuan spinel peridotites are given in Table 5-4. The Sm, Nd, Lu and Hf concentrations in clinopyroxenes determined by isotope dilution are generally within

Table 5-4. Sr, Nd, Pb and Hf isotopic compositions of clinopyroxene separates from the Yangyuan peridotites and the host basalt (YY-35A)

Samples	YY-04	YY-08	YY-13	YY-23	YY-26	YY-36	YY-40B	YY-42	YY-45	YY-50	YY-58	YY-35A
Rb (ppm)	0.029	0.106	0.015	0.094	0.029	0.092	0.0050	0.031	0.090	0.023	0.044	54.77
Sr (ppm)	32.54	32.11	53.88	57.32	47.51	191.5	14.69	10.36	71.06	61.50	128.1	1107
$^{87}Rb/^{86}Sr$	0.0025	0.00957	0.0008	0.0047	0.0018	0.0014	0.0010	0.0085	0.0036	0.0011	0.0010	0.1431
$^{87}Sr/^{86}Sr\pm2\sigma$	0.703553±8	0.704434±6	0.703100±13	0.702945±5	0.704041±5	0.703860±9	0.703228±11	0.703647±9	0.702916±5	0.702294±10	0.704385±6	0.704139±7
$^{87}Sr/^{86}Sr(t)$	0.703552	0.704430	0.703099	0.702943	0.704040	0.703860	0.703228	0.703644	0.702915	0.702294	0.704384	0.704078
Sm (ppm)	0.7083	0.7951	1.624	1.668	1.389	1.015	0.5656	0.3373	1.486	1.568	1.546	9.704
Nd (ppm)	2.278	1.867	3.550	5.332	3.759	4.672	1.085	0.6678	4.634	3.743	4.817	47.48
$^{147}Sm/^{144}Nd$	0.1880	0.2575	0.2766	0.1891	0.2234	0.1313	0.3152	0.3054	0.1938	0.2533	0.1941	0.1236
$^{143}Nd/^{144}Nd\pm2\sigma$	0.512929±9	0.512798±4	0.513162±5	0.513039±4	0.512828±5	0.512829±8	0.513727±6	0.513892±4	0.513043±4	0.513300±6	0.512609±4	0.512890±5
$^{143}Nd/^{144}Nd(t)$	0.512893	0.512748	0.513108	0.513038	0.512784	0.512803	0.513665	0.513832	0.513005	0.513251	0.512571	0.512937
$\varepsilon_{Nd}(t)$	5.87	3.05	10.07	8.71	3.76	4.13	20.9	24.2	8.06	12.9	-0.41	5.36
$\varepsilon_{Nd}(i)$	10.1	-7.32	-4.27	12.7	0.57	20.3	-1.46	3.88	11.1	3.42	2.54	
T_{DM}/Ga	1.29	-1.17	0.05	0.42	-4.59	0.58	0.87	1.24	0.78	0.60	4.27	0.43
Lu (ppm)	0.1068	0.1869	0.1984	0.2389	0.3332	0.1467	0.1728	0.1409	0.2187	0.2647	0.1780	0.1685
Hf (ppm)	0.3483	0.3517	1.076	0.8350	0.7215	0.4546	0.2184	0.1203	0.7589	1.008	0.6845	7.258
$^{176}Lu/^{177}Hf$	0.04353	0.07543	0.02618	0.04062	0.06555	0.04583	0.1124	0.1664	0.04091	0.03730	0.03691	0.003296
$^{176}Hf/^{177}Hf$	0.284283±8	0.283389±17	0.283153±5	0.283491±12	0.283391±9	0.283661±8	0.285793±11	0.287499±59	0.283469±7	0.283340±5	0.283577±12	0.282989±6
$^{176}Hf/^{177}Hf(t)$	0.284259	0.283347	0.283138	0.283469	0.283354	0.283635	0.285730	0.287406	0.283446	0.283319	0.283556	0.282987
$\varepsilon_{Hf}(t)$	52.8	20.5	13.2	24.8	20.8	30.7	105	164	24.0	19.5	27.9	7.81
$\varepsilon_{Hf}(i)$	42.1	-25.2	21.3	17.2	-14.2	17.5	18.8	19.1	16.1	15.6	24.4	
T_{DM}/Ga	10.6	0.20	0.41	6.68	0.28	3.65	1.82	1.76	5.29	-3.30	-10.2	0.39
U (ppm)	n.d.	n.d.	0.0273	n.d.	n.d.	2.942	n.d.	n.d.	n.d.	0.0082	n.d.	1.688
Pb (ppm)	0.0537	0.4155	0.1605	0.0498	0.1523	0.5519	0.0308	0.0180	0.0459	0.0704	0.0852	3.740
$^{208}Pb/^{204}Pb\pm2\sigma$	38.409±66	37.881±4	37.427±41	37.689±21	37.287±7	38.728±3	38.41±18	37.233±38	37.812±35	36.517±36	35.645±21	38.017±5
$^{207}Pb/^{204}Pb\pm2\sigma$	15.546±26	15.473±1	15.334±17	15.420±9	15.410±3	15.540±1	15.661±75	15.433±16	15.480±14	15.323±14	15.191±8	15.496±2
$^{206}Pb/^{204}Pb\pm2\sigma$	18.325±29	17.911±2	17.508±18	17.778±10	17.352±3	19.079±1	18.390±86	17.397±18	17.834±16	16.801±17	15.745±9	17.996±2
$^{206}Pb/^{204}Pb(t)$			17.459			17.474				16.768		17.863
$^{238}U/^{204}Pb$			10.4			344				6.9		28.4

Note to Table 5-4: All elemental concentrations were determined using isotope dilution. n.d.: not determined. t: basalt eruption date (30Ma). i: 1.66 Ga. Blank means data not available or meaningless.
CHUR values: $^{147}Sm/^{144}Nd$ = 0.1960 and $^{143}Nd/^{144}Nd$ =0.512630, and $^{176}Lu/^{177}Hf$ = 0.0336 and $^{176}Hf/^{177}Hf$ = 0.282785 (Bouvier et al., 2008).
T_{DM}(Nd) was calculated based on the single-stage depleted mantle values ($^{147}Sm/^{144}Nd$ = 0.2129 and $^{143}Nd/^{144}Nd$ = 0.51313; Nowell et al., 1998 and Bouvier et al., 2008)
T_{DM}(Hf) was calculated based on the depleted mantle values ($^{176}Hf/^{177}Hf$ = 0.28325 (Nowell et al., 1998), which would require $^{176}Lu/^{177}Hf$ = 0.0388 using the average chondrite Lu-Hf parameters of Bouvier et al., (2008))

uncertainty of data obtained by laser ablation (see Fig. S5-1 in the Supplemental Material).

The Nd isotopic result for the host basalt ($^{143}Nd/^{144}Nd$ = 0.512890 ± 5, 2σ) is slightly lower than previously reported results for Yangyuan alkali basalts ($^{143}Nd/^{144}Nd$ = 0.51292 ± 2; n = 5), and the $^{87}Sr/^{86}Sr$ (0.704139 ± 7, 2σ) is somewhat higher than the narrow range of 0.70379 ± 2 (n = 5) that was previously reported (Ma and Xu, 2004).

Clinopyroxenes from the Yangyuan peridotites display highly variable isotopic compositions: $^{87}Sr/^{86}Sr$ = 0.70229-0.70443, $^{143}Nd/^{144}Nd$ = 0.51261-0.51389 (ε_{Nd} = -0.6 to +24.5), $^{206}Pb/^{204}Pb$ = 15.74-19.08, $^{207}Pb/^{204}Pb$ = 15.19-15.66, $^{208}Pb/^{204}Pb$ = 35.64-38.73, and $^{176}Hf/^{177}Hf$ = 0.28315-0.28750 (ε_{Hf} = +13.5 to +167). Sm-Nd, Sr-Nd, and Pb-Pb isotopic correlation diagrams are shown in Figs. 5-5 to 5-7. The Sr and Nd isotopic compositions of clinopyroxenes analyzed here largely overlap with the ranges of Sr-Nd data ($^{87}Sr/^{86}Sr$ = 0.70309 to 0.70471 and $^{143}Nd/^{144}Nd$ = 0.51208 to 0.51366) obtained by Xu et al. (2008) for a different set of Yangyuan clinopyroxenes (Fig. 5-6). In the Rb-Sr isochron diagram (not shown), the Yangyuan clinopyroxenes define a nearly vertical array due to their extremely low Rb/Sr ratios ($^{87}Rb/^{86}Sr$ = 0.001 to 0.01, much lower than that (0.143) of the host basalt). They show a rough positive, but scattered, trend on a Sm-Nd isochron plot (Fig. 5-5), with a large range of Sm/Nd

($^{147}Sm/^{144}Nd$ = 0.131-0.315). There is a negative correlation between $^{87}Sr/^{86}Sr$ and ε_{Nd} (Fig. 5-6), with most of the data plotting within the isotopic compositions of depleted MORB mantle. Two samples from this study (YY-40B and YY-42) are distinguished by very high ε_{Nd} and plot above the Sr-Nd trend defined by the majority of samples.

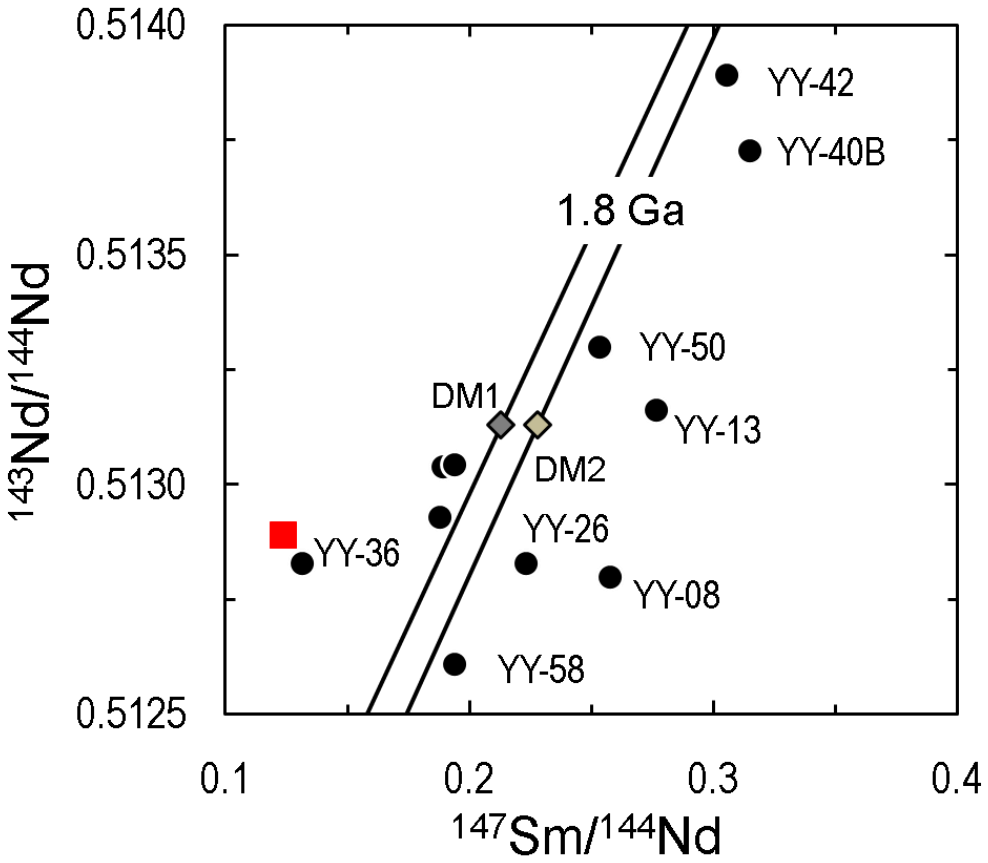

Fig. 5-5. Sm-Nd isochron diagram for clinopyroxenes from the Yangyuan peridotites. The 1.8 Ga reference line reflects the maximum Re depletion model age of bulk peridotites (Liu et al., 2011a). DM1 represents a single-stage depleted mantle ($^{143}Nd/^{144}Nd$ = 0.51313 (Nowell et al., 1998) and $^{147}Sm/^{144}Nd$ = 0.2129 calculated using the average Sm-Nd parameters of Bouvier et al. (2008); and DM2 represents a progressively depleted mantle ($^{143}Nd/^{144}Nd$ = 0.51313 (Nowell et al., 1998) requiring $^{147}Sm/^{144}Nd$ = 0.2278 at 1.8 Ga calculated using the modern $^{147}Sm/^{144}Nd$ = 0.2485 (Workman and Hart, 2005 and references therein).

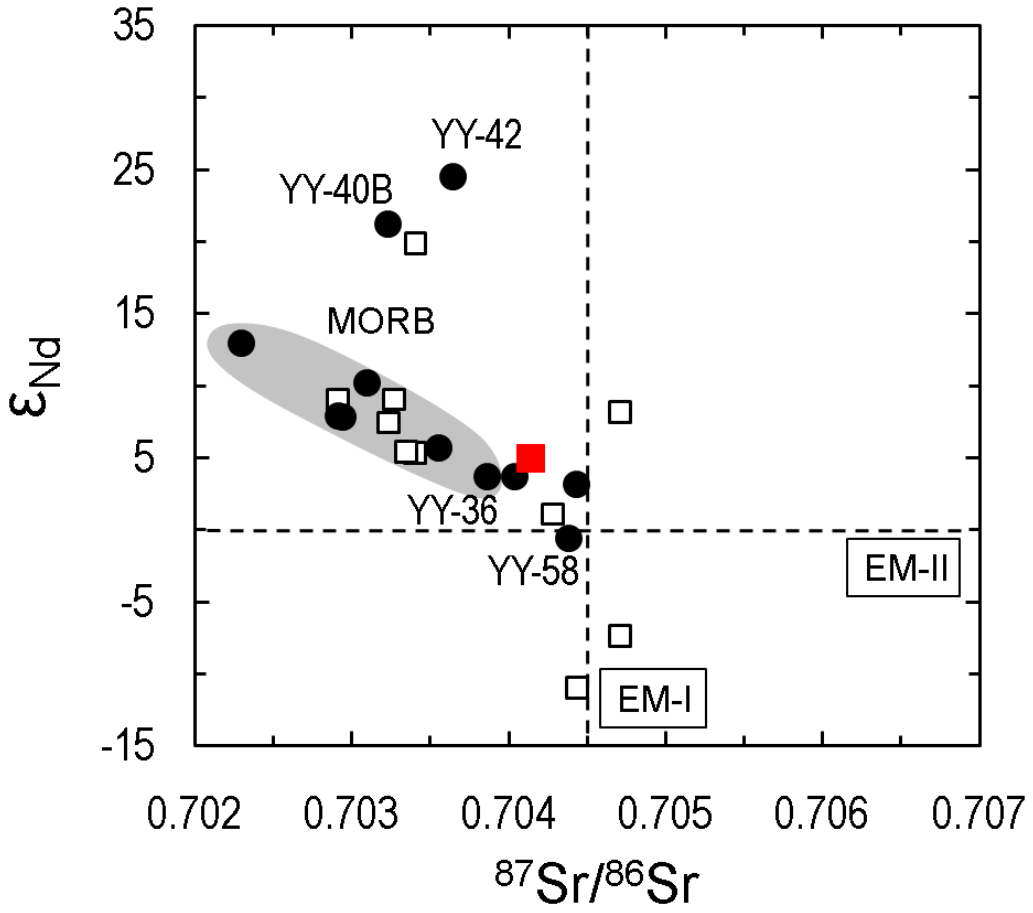

Fig. 5-6. $^{87}Sr/^{86}Sr$ vs. ε_{Nd} for clinopyroxenes from the Yangyuan peridotites. Also shown in is the previously reported Sr-Nd isotopic compositions for the Yangyuan clinopyroxenes (open squares; Y.G., Xu et al., 2008). MORB field represents Atlantic and Pacific MORB as compiled by Hofmann, 2003. Mantle components are from Zindler and Hart (1986): EM-I and EM-II, enriched mantle of type 1 and 2, respectively.

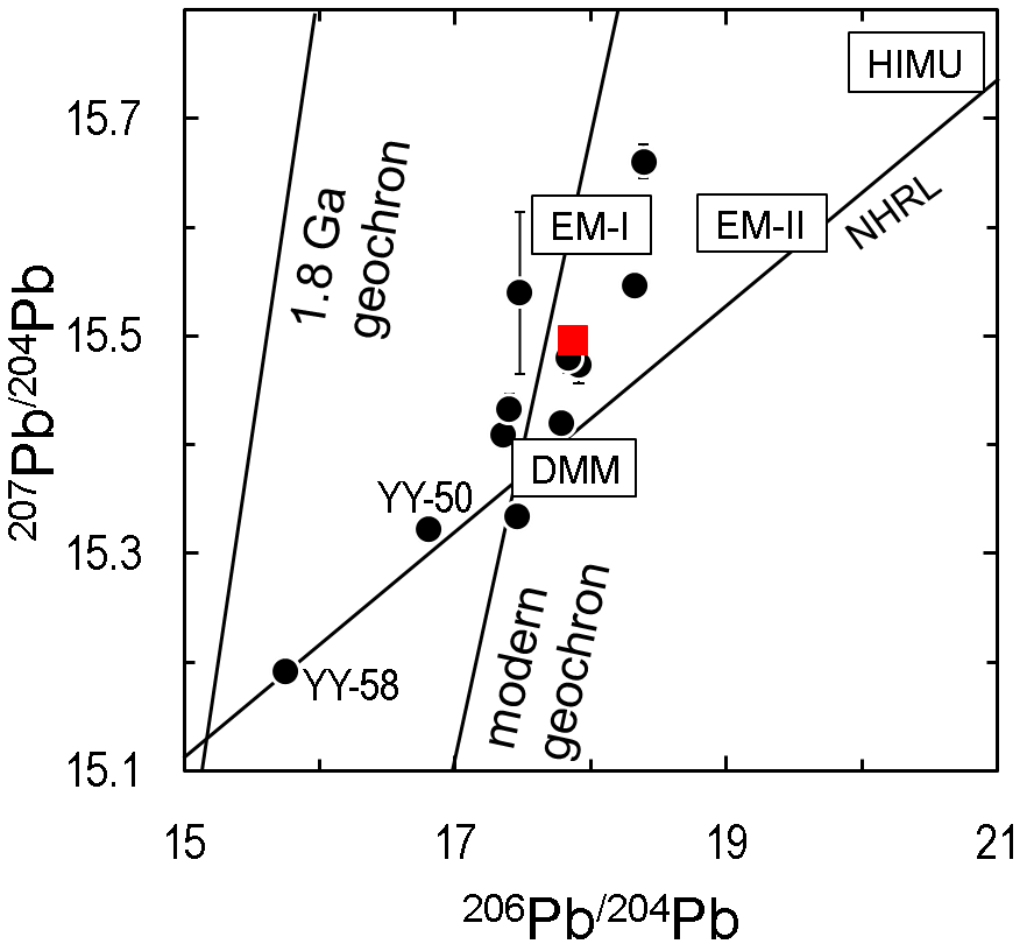

Fig. 5-7. $^{206}Pb/^{204}Pb$ vs. $^{207}Pb/^{204}Pb$ for clinopyroxenes from the Yangyuan peridotites. Error bars represent 2σ uncertainties, and are shown only when they are larger than the symbol size. NHRL: the Northern Hemisphere Reference Line (after Hart, 1984). Mantle components are from Zindler and Hart (1986): DMM, depleted mantle; EM-I and EM-II, enriched mantle of type 1 and 2, respectively; and HIMU, mantle with high time-integrated U/Pb ratios.

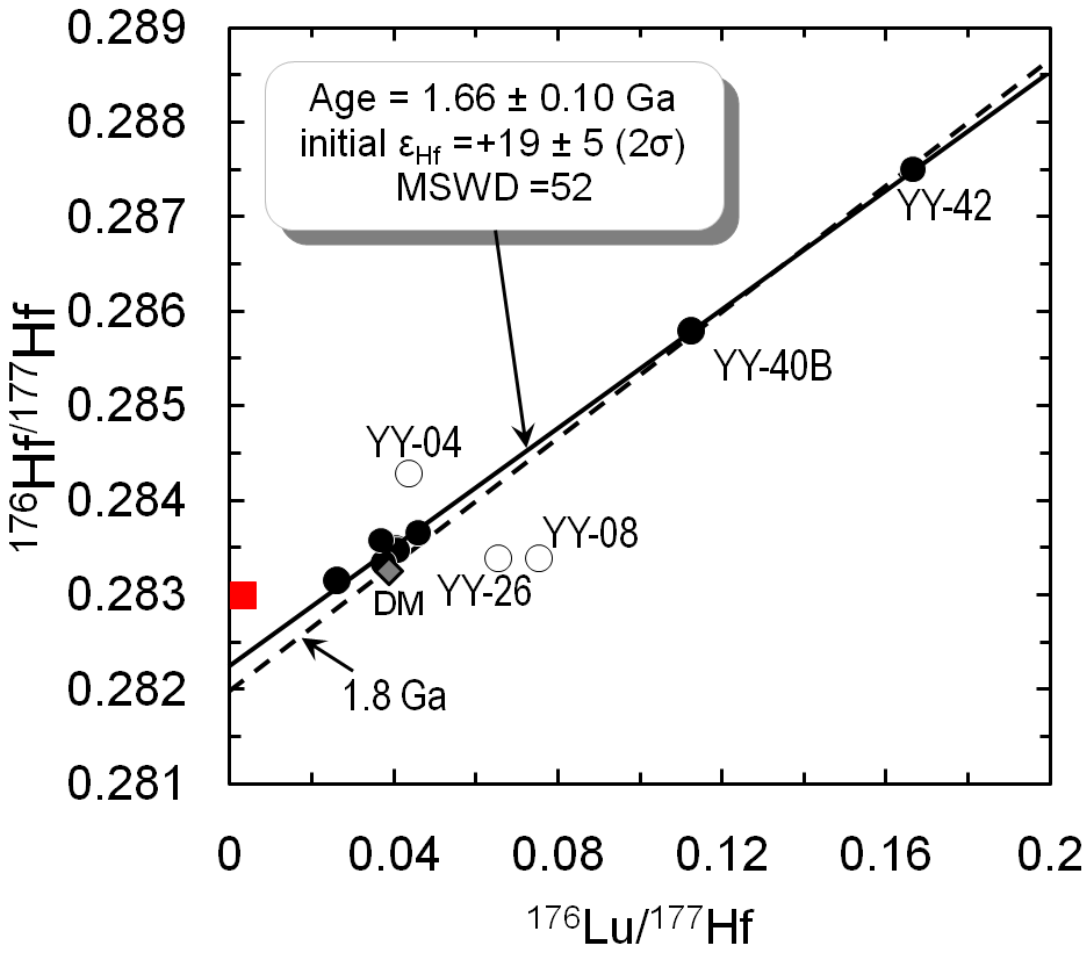

Fig. 5-8. Lu-Hf isochron diagram for clinopyroxenes from the Yangyuan peridotites. Error bars represent 2σ uncertainties, and are given only when they are larger than the symbol size. The solid line is a regression "errorchron" for the Yangyuan clinopyroxenes, excluding the outlier samples (YY-04, YY-08 and YY-26). The dashed line is the 1.8 Ga reference line passing through the depleted mantle. The Lu-Hf "errorchron" age is calculated using the decay constant $\lambda^{176}Lu=1.865x10^{-11}$ $year^{-1}$ (Scherer et al., 2001). DM: depleted mantle ($^{176}Hf/^{177}Hf$ = 0.28325, Nowell et al., 1998), which would require $^{176}Lu/^{177}Hf$ = 0.0388 using the average chondrite Lu-Hf parameters of Bouvier et al. (2008).

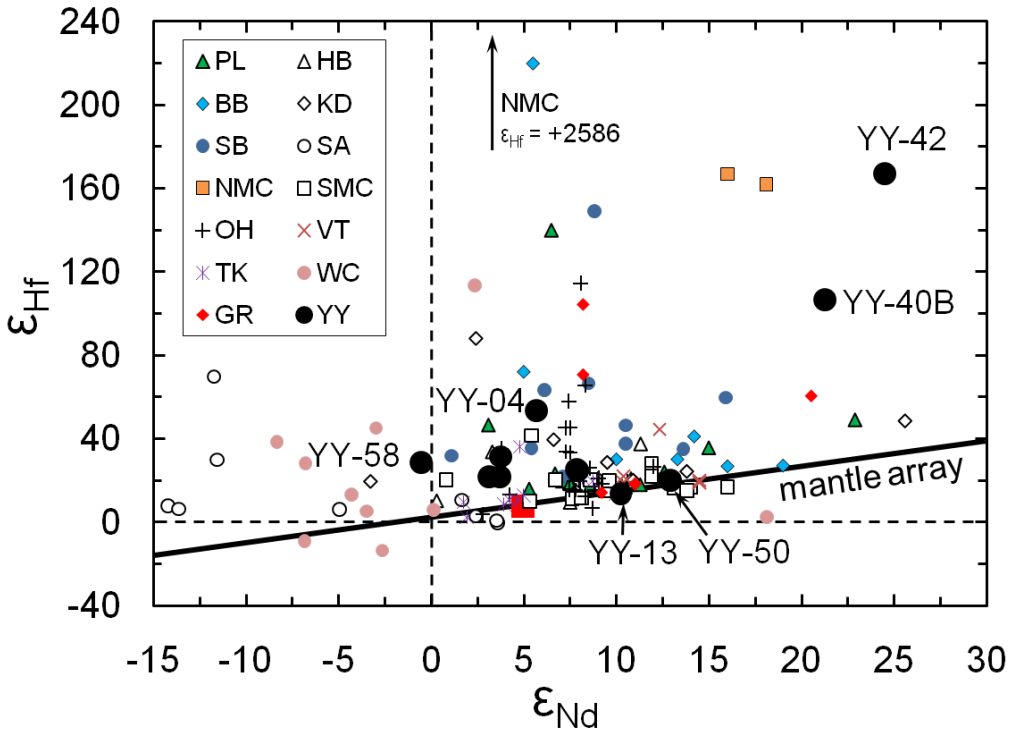

Fig. 5-9. ε_{Hf} vs. ε_{Nd} for clinopyroxenes from mantle peridotites (YY: Yangyuan). Data sources: Penglai (PL), China (Chu et al., 2009); Hannuoba (HB), China (Choi et al., 2008); Kuandian (KD), China (Wu et al., 2006); Beni Bousera (BB), Morocco (Pearson and Nowell, 2003); Spitsbergen (SB), Svalbard (Choi et al., 2010); South Africa (SA; Bedini et al., 2004); Northern French Massif Central (NMC; Wittig et al., 2006); Southern FMC (SMC; Wittig et al., 2007); Oahu (OH), Hawaii (Bizimis et al., 2004, 2007), Vitim (VT), Siberia (Ionov et al., 2005a, 2005b), Tok (TK), Siberia (Ionov et al., 2006), Wyoming Craton (WC) and adjacent regions, north America (Carlson et al., 2004), and Gakkel Ridge, Arctic (Stracke et al., 2011). The solid line marks the mantle array from Nowell et al. (1998).

The Yangyuan clinopyroxenes exhibit a very wide range of Pb isotopic compositions (e.g., $^{206}Pb/^{204}Pb$ = 15.74-19.08), with two samples (YY-50 and YY-58) plotting well to the left of the modern geochron on the $^{206}Pb/^{204}Pb$ vs. $^{207}Pb/^{204}Pb$ diagram (Fig. 5-7).

The Hf isotopic compositions of all Yangyuan clinopyroxenes are similar to, or more radiogenic than, a depleted mantle reservoir, consistent with long-term elevated Lu/Hf. With the exception of three samples, the data form a good positive correlation between $^{176}Lu/^{177}Hf$ and $^{176}Hf/^{177}Hf$ (Fig. 5-6), yielding a regression age of 1.66 ± 0.10 Ga (2σ) with an initial ε_{Hf} = +19 ± 5. Like other peridotite clinopyroxenes (e.g., Pearson and Nowell, 2003; Carlson et al., 2004; Bizimis et al., 2004, 2007; Bedini et al., 2004; Ionov et al., 2005a, 2005b, 2006; Choi et al., 2008, 2010; Chu et al., 2009), most Yangyuan clinopyroxenes plot well above the Nd-Hf mantle array defined by oceanic basalts (Fig. 5-9).

5.5 Discussion

Major and trace element compositions of mantle peridotites can reflect multiple processes of chemical modification (i.e., melt depletion and later overprinting) in the mantle. The isotope data obtained for these rocks provide chronologic information regarding these mantle processes. In this study, trace element compositions and Sr-Nd-Hf-Pb isotope systematics are utilized to determine the history of these mantle processes in the Yangyuan peridotites.

5.5.1 Melt depletion

Melt extraction leads to depletion of incompatible elements in residual peridotite, and the relative extent of depletion generally follows elemental incompatibility, with

LREE being more depleted compared to HREE. Bulk Al_2O_3 content is often used as a convenient indicator of melt depletion, since aluminum is progressively lost during melt depletion, and generally immobile during secondary processes, such as serpentinization, surface weathering and metamorphism. The Al_2O_3 content of Yangyuan peridotites correlates well with other indices of melt depletion, such as MgO content, olivine forsterite content (Fo = molar $Mg/(Mg+Fe^{2+})x100$) and Cr# (molar $Cr/(Cr+Al)x100$) of spinel, as well as $^{187}Os/^{188}Os$, a proxy of long-term Re/Os ratio (Liu et al., 2010, 2011; Fig. 5-1). Such correlations suggest that the Yangyuan peridotites have not been significantly affected by refertilization, and the large range of Al_2O_3 (i.e., 0.9 to 4.0 wt. %) reflects varying degrees of melt depletion.

5.5.1.1 Timing of melt depletion: Re-Os and Lu-Hf

The positive correlation between $^{176}Lu/^{177}Hf$ and $^{176}Hf/^{177}Hf$ in the Yangyuan clinopyroxenes (Fig. 5-6) yields a regression age of 1.66 ± 0.10 Ga (2σ), which overlaps the oldest Re-Os model ages (1.8 ± 0.2 Ga) obtained for the whole rocks (Liu et al., 2010, 2011a), suggesting insignificant overprinting of the Lu-Hf isotope system for clinopyroxenes of most peridotites. Thus, the primary melt depletion of Yangyuan peridotites occurred at ~1.7 to 1.8 Ga, and the clinopyroxene Lu-Hf isotope and whole rock Re-Os isotope systems both provide coincident chronological information regarding melt depletion of mantle peridotites. This is a similar outcome to prior studies of peridotites (e.g., Schmidberger et al., 2002; Pearson and Nowell, 2003; Wittig et al., 2006; Choi et al., 2010).

5.5.1.2 The cause of high initial ε_{Hf} and implication

In spite of the exhibition of a Lu-Hf errorchron yielding an age similar to the whole rock Re-Os model age, these Yangyuan clinopyroxenes have comparatively

high initial ε_{Hf} values of +19 at 1.66 Ga (Table 5-4; Fig. 5-8) relative to that (+10) of the depleted mantle source at that time. Such high initial ε_{Hf} would suggest that the mantle source already had lower Re/Os and $^{187}Os/^{188}Os$ ratios compared to chondritic or primitive mantle at that time, but there is no evidence within the Re-Os results to support this. In the Yangyuan peridotites, orthopyroxene has roughly three times higher Lu/Hf than coexisting clinopyroxene (Fig. 5-4b) and contains 10 to 40 % (with an average of ~23 %) of the Hf and 30 to 60 % (with an average of ~47 %) of the Lu in the analyzed Yangyuan peridotites (Fig. S5-2; Table S5-2). The calculated Lu/Hf of the bulk rock is 1.3 to 2.2 (with an average of ~1.6) times that of clinopyroxene. This causes the orthopyroxene and bulk rock to develop more radiogenic Hf than that in 'pristine' clinopyroxene, of which the Lu-Hf isotope system is assumed to be closed immediately after melt depletion. Calculation shows that the bulk rock will grow in higher ε_{Hf} (average ~4.6 epsilon units, ranging from 1.0 up to 19) than pristine clinopyroxene over 150 Ma. If the peridotite resides above the closure temperature for Lu-Hf exchange between minerals (e.g., Bedini et al., 2004), the high initial ε_{Hf} value in present-day clinopyroxene could reflect incorporation of a radiogenic Hf component from coexisting orthopyroxene. Thus, if the melting event responsible for lithospheric mantle formation can be dated by the Re-Os isotopic system (e.g., Walker et al., 1989), the Lu-Hf isotopic system in pyroxene may be used to date the cooling age at which the mantle cooled below the Lu-Hf closure temperature (~900ºC).

5.5.1.3 Characteristics of ancient melt depletion

Clinopyroxenes and orthopyroxenes from samples YY-42 and YY-40B are the most LREE depleted relative to HREE (Fig. 5-2a), and their clinopyroxenes have the most radiogenic Nd and Hf isotopic signatures, which must reflect time-integrated

responses to elevated Sm/Nd and Lu/Hf ratios produced by melt depletion. Their LREE-depleted patterns may be typical of pristine residues reflecting melt depletion in the mantle. In addition to YY-42 and YY-40B, sample YY-50 is also LREE depleted ($(La/Yb)_N = 0.22$ for clinopyroxene; Fig. 5-2a), and has the lowest $^{87}Sr/^{86}Sr$ (0.70229) of the samples analyzed, as well as relatively non-radiogenic Pb ($^{206}Pb/^{204}Pb = 16.801$; Table 5-4) that plots to the left of the modern geochron (Fig. 5-7). These features require long-term low Rb/Sr and U/Pb ($^{238}U/^{204}Pb = 6.9$), consistent with the expectation of ancient melt depletion. Samples that have clinopyroxenes characterized by LREE-depletion and slight MREE enrichment relative to HREE (i.e., YY-13 and YY-58) may also preserve the characteristic of melt depletion, as shown in their LREE-depleted whole rock patterns having no MREE enrichment (Fig. 5-3).

In the absence of overprinting, the REE patterns in clinopyroxene and bulk rocks are controlled by the degrees of melt depletion, and the style of melting (e.g., fractional melting causes greater depletion of LREE compared to MREE and HREE than batch melting for a given melt fraction; Johnson et al., 1990). For example, clinopyroxene from YY-50, the least refractory sample investigated ($Al_2O_3 = 4.02$ wt. %; Table 5-1), has higher incompatible trace element concentrations, compared to YY-40B and YY-42 (Fig. 5-2a; Table 5-2), as well as a $^{176}Lu/^{177}Hf$ that is slightly lower than that of the depleted mantle. A lower degree of melt depletion experienced by YY-50 compared to YY-40B and YY-42 is also consistent with its Re-Os systematics, which suggests that it experienced only very slight Re depletion relative to PUM (Fig. 5-1).

Sample YY-58 has the least radiogenic Pb ($^{206}Pb/^{204}Pb$ = 15.745; Table 5-4), plotting just to the right of the 1.8 Ga geochron on the $^{206}Pb/^{204}Pb$ vs. $^{207}Pb/^{204}Pb$ diagram (Fig. 5-7). This suggests its long-term evolution with a low U/Pb ratio in a closed system. Based on melt depletion indices (Al_2O_3 = 2.40 wt. % and Fo = 91.7; Table 5-1), sample YY-58 experienced a degree of melt depletion similar to that of the relatively refractory Yangyuan sample YY-42 (Al_2O_3 = 2.35 wt. % and Fo = 91.0). However, subtle LREE depletion relative to HREE in its clinopyroxene (Fig. 5-2a) and higher incompatible trace element concentrations in the bulk rock (Fig. 5-3) indicate less depletion of incompatible trace elements. This discrepancy may suggest that YY-58 experienced batch melting, while YY-42 likely experienced fractional melting (see melting models in Fig. 5-10 and Supplemental Material).

By contrast, the other Yangyuan clinopyroxenes (i.e., YY-04, YY-23, YY-36 and YY-45) are characterized by flat- to LREE-enriched patterns (Fig. 5-2b) and likely experienced variable degrees of overprinting superimposed onto pristine residual peridotites that had trace element characteristics similar to these ancient, least overprinted residual peridotites (Fig. 5-2a). This process is discussed next.

5.5.2 The processes and timing of overprinting

Residual peridotites with low LREE concentrations are especially vulnerable to overprinting by interaction with LREE-enriched melts/fluids (Frey and Green, 1974). As clinopyroxene is the major repository of many incompatible trace elements in spinel peridotites (e.g., Zindler and Jagoutz, 1988; McDonough et al., 1992; Eggins et al., 1998; Bedini and Bodinier, 1999; Fig. S5-2; Table S5-2), clinopyroxene trace

element concentrations and isotopic compositions (except for Lu-Hf) can be used as a proxy for the bulk rock composition for these elements.

In comparison to those samples that retain evidence for ancient melt depletion in their incompatible element signatures, overprinted samples are characterized by flat to LREE-enriched patterns in clinopyroxene and bulk rock (YY-04, YY-23, YY-36 and YY-45; Fig. 5-2b and Fig. 5-3), and sample YY-36 plots to the left of the 1.8 Ga Sm-Nd reference isochron, towards the composition of the host basalt (Fig. 5-5). This suggests that they likely experienced recent enrichment of incompatible trace elements from the host basalt or related precursor melts. Based on clinopyroxene patterns, samples YY-04 and YY-36, with a LREE-enriched signature, possibly experienced a larger extent of overprinting than YY-23 and YY-45, which have a flat LREE signature. This is consistent with the fact that orthopyroxenes in YY-04 and YY-36 show similar enrichment to their coexisting clinopyroxenes, while no evident enrichment appears in orthopyroxenes of YY-23 and YY-45 (Fig. 5-2b).

Harzburgite YY-04, the most refractory sample analyzed (Al_2O_3 = 1.63 wt.%, Table 5-1), is characterized by a radiogenic Hf isotopic composition (ε_{Hf} = 53.4; Table 5-4), but relatively low Lu/Hf ratio ($^{176}Lu/^{177}Hf$ = 0.0425; Table 5-4); modification of its Lu-Hf isotope system may have resulted from recent Hf addition (along with Sr and Nd enrichment) due to its much lower original Hf concentration, compared to the other samples that do not show significant overprinting of the Lu-Hf isotope system.

Sample YY-36 has the highest Pb concentration and $^{206}Pb/^{204}Pb$, as well as high U/Pb ($^{238}U/^{204}Pb$ = 344; Table 5-4), Sr/Nd (41) and the highest $(La/Yb)_N$ ratio (13.5) in the analyzed clinopyroxene suite, inconsistent with its low whole-rock Al_2O_3 (2.30 wt. %). Such extreme compositions are indicative of significant recent overprinting of

this sample. The initial $^{206}Pb/^{204}Pb$ (17.474) of YY-36 at 30 Ma is just slightly lower (2.2 %) than that of the host basalt (17.863), and the Pb isotopic composition of YY-36 also plots along a mixing line between the host basalt and non-radiogenic samples. This relationship, together with its similar Sr and Nd isotopic compositions (but different Sr/Nd) to the host basalt (Fig. 5-6), suggests that the clinopyroxene (and orthopyroxene) in YY-36 experienced substantial exchange with a silicate melt that had an isotopic composition similar to the host basalt shortly preceding eruption.

In summary, the above observations suggest that some Yangyuan peridotites experienced recent overprinting, likely via infiltration of basaltic melts prior to eruption. This scenario is consistent with the whole-rock HSE patterns of Yangyuan peridotites, which are characterized by Os depletion relative Ir. These patterns were interpreted to be caused by recent infiltration of an oxidizing melt (Liu et al., 2010).

5.5.3 The origin of samples YY-08 and YY-26

Clinopyroxenes in two samples (YY-08 and YY-26) plot significantly to the right of the Lu-Hf errorchron (Fig. 5-6). These samples have relatively high Lu/Hf ratios that are inconsistent with their relatively non-radiogenic Hf isotopic compositions (Fig. 5-6). These observations may indicate a recent increase in their Lu/Hf ratios, or the samples may not be cogenetic with the rest of the suite.

Given elevated Lu/Hf ratios in their orthopyroxenes (Fig. 5-4), the bulk rocks of YY-08 and YY-26 should have high Lu/Hf. This, together with their prominent LREE-depleted REE-Hf patterns (Fig. 5-2a and Fig. 5-3), could result from a recent melt depletion event. However, YY-08 and YY-26 have the lowest two-pyroxene equilibration temperatures in the sample suite (820 and 880^{o}C at P = 1.5 GPa,

respectively; Table 5-1; Liu et al., 2011a), which is inconsistent with them having experienced recent melting.

Clinopyroxene in YY-26 has a relatively high Lu concentration (0.333 ppm), which may indicate that it experienced enrichment of Lu, instead of depletion of Hf to give rise to its high Lu/Hf. As garnet is a high Lu and Lu/Hf ratio phase in mantle peridotites, the garnet-spinel transition may be implicated in the re-distribution of HREE in peridotitic phases (Ionov et al., 2005a, and references therein). The elevation of Lu/Hf in clinopyroxenes and bulk rocks of YY-08 and YY-26 may have been caused by recent breakdown of garnet emplaced into the spinel stability field. This is consistent with fractionated HREE in their bulk rocks characteristic of garnet in residue (Fig. 5-3). However, precursor garnet peridotites should also have high Lu/Hf ratios, given high Lu/Hf ratios in bulk rocks of the two samples. If the residual garnet peridotites formed at ~1.8 Ga, the high Lu/Hf ratios, over ~1.8 Ga, would lead to radiogenic Hf isotopic compositions, which are not inherited in these two samples.

Alternatively, these two samples may not be cogenetic with the rest of the suite, but rather derived from a different source, and perhaps experienced melt depletion at a different time. Several lines of evidence are consistent with this interpretation. First, their trace element patterns (Fig. 5-2a and Fig. 5-3) appear to record the characteristics of melt depletion, but their isotopic compositions are inconsistent with this depletion being ancient. Second, these two samples lie furthest from the Al_2O_3-$^{187}Os/^{188}Os$ correlation (Fig. 5-1; Liu et al., 2011a), which may indicate a different origin from the rest of the suite. However, if they are residues of relatively recent melting of convecting upper mantle (in garnet stability field) and accreted recently to the base of the 1.8 Ga lithosphere, one would expect them to record high

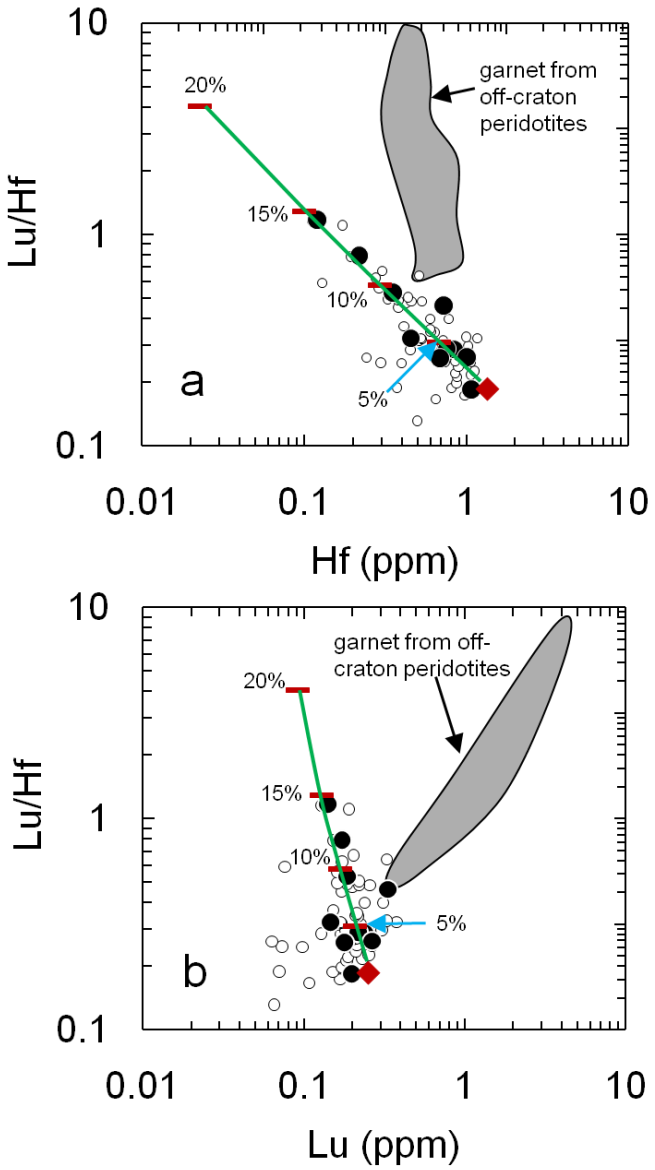

Fig. 5-10. Lu/Hf vs. Hf (a) and Lu (b) concentrations for clinopyroxenes from Yangyuan peridotites. The green line shows 0 to 20 % degrees of fractional melting using equations of Johnson et al. (1990) (details of the model are provided in the Supplemental Material). Red diamond represents the starting composition of clinopyroxene in primitive mantle, calculated from the whole-rock Lu and Hf concentrations from McDonough and Sun (1995) using the mineralogy and partition coefficients provided in the Supplemental Material. Garnet field is from Ionov et al. (2005a) and references therein. Small open circles are laser ablation data for clinopyroxenes from other Yangyuan peridotites that have not been analyzed for Sr-Nd-Hf-Pb isotopic compositions.

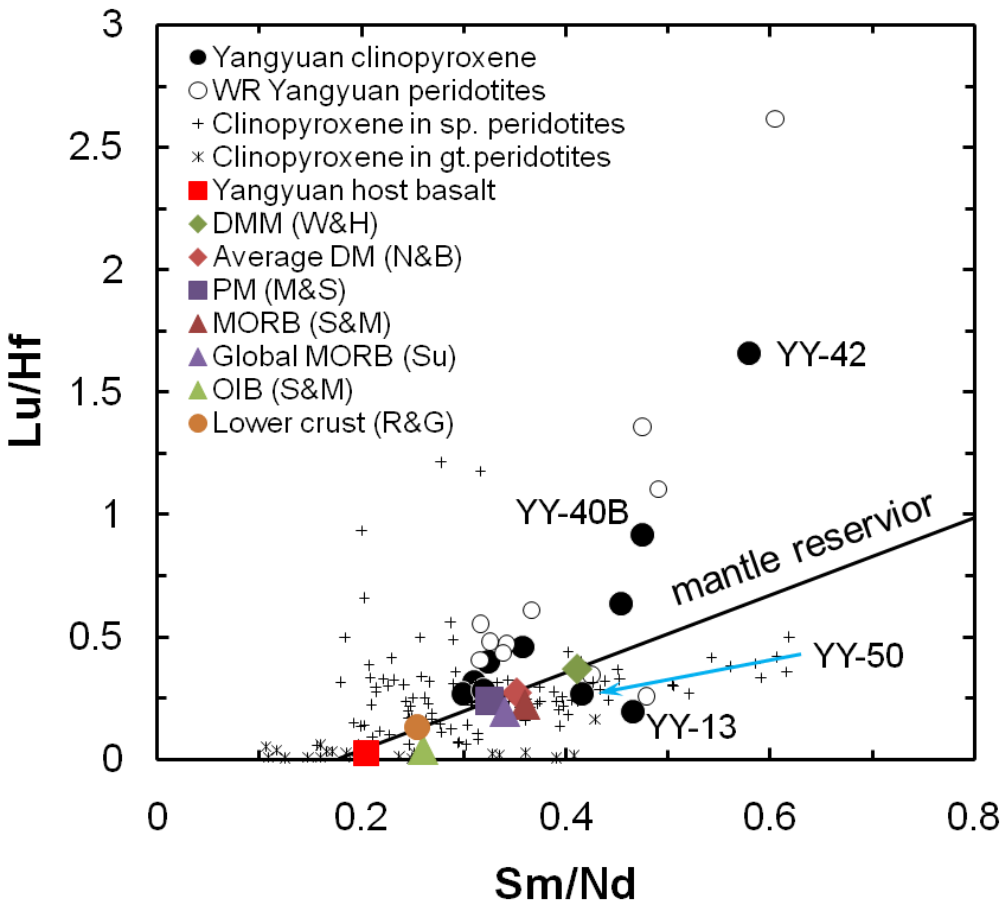

Fig. 5-11. Correlation between Sm/Nd and Lu/Hf in clinopyroxenes of peridotites. Also shown are reconstructed Yangyuan whole rock peridotites, clinopyroxene in spinel peridotites (data sources as in Fig. 5-9), clinopyroxene in garnet peridotites (data sources as in Fig. 5-9), Yangyuan host basalt (this study), modern depleted MORB mantle (DMM; Workman and Hart, 2005), single-stage or average depleted mantle (Average DM calculated using the parameters in Nowell et al. (1998) and Bouvier et al. (2008)), primitive mantle (PM; McDonough and Sun, 1995), MORB (Sun and McDonough, 1989), Global MORB (Su, 2002), Ocean island basalt (OIB; Sun and McDonough, 1989), and average lower crust (Rudnick and Gao, 2003). The mantle reservoir line is defined by PM, DMM and DM.

equilibration temperatures. Yet, as noted above, they record the lowest equilibration temperatures of the suite, unless they were tectonically emplaced to shallow levels prior to eruption.

In summary, none of the scenarios mentioned above can fully explain all the petrological, elemental and isotopic data for these two samples, perhaps reflecting a complex history.

5.5.4 The cause of decoupling of the Nd-Hf isotope systems

Like clinopyroxene from many other suites of peridotites (e.g., Blichert-Toft et al., 2000; Pearson and Nowell, 2003; Bedini et al., 2004; Carlson et al., 2004; Bizimis et al., 2004, 2007; Ionov et al., 2005a, 2005b, 2006; Choi et al., 2008, 2010; Chu et al., 2009), all but two Yangyuan clinopyroxenes plot above the mantle Nd-Hf array defined by oceanic basalts (Nowell et al., 1998; Fig. 5-9). The potential processes that have been suggested to cause Nd-Hf decoupling in clinopyroxenes include: 1) spinel-garnet phase transition in the mantle (Ionov et al., 2005a, and references therein), and 2) recent incompatible element overprinting of ancient depleted peridotite through interaction with melts/fluids (e.g., Salters and Zindler, 1995; Bizimis et al., 2004). Each of these processes is examined below.

Melting in the garnet stability field followed by subsolidus garnet breakdown has been previously proposed to explain Nd-Hf decoupling in spinel peridotites (Ionov et al., 2005a, and references therein). Garnet takes in HREE relative to LREE and Hf, and is characterized by high Lu/Hf ratio compared to that of primitive mantle. The high Lu/Hf ratios in garnet-bearing peridotites are not accompanied by correspondingly high Sm/Nd ratios. Over time, the radiogenic Hf isotopic compositions derived from high Lu/Hf ratios will not be matched by equally

radiogenic Nd isotopic compositions, due to relatively low Sm/Nd ratios, which may lead to samples plotting well above the Nd-Hf mantle array (Fig. 5-9). However, the Yangyuan clinopyroxenes show a negative correlation between Hf concentrations and Lu/Hf ratios (Fig. 5-10a), yet lack the high Lu concentrations (except YY-26, mentioned above), and Lu/Hf ratios that are diagnostic of the original presence of garnet (Fig. 5-10b). This indicates that the melting event experienced by the Yangyuan peridotites likely occurred in the spinel stability field, or that the influence of garnet breakdown in raising Lu/Hf of clinopyroxene was largely diluted by orthopyroxene that contains 30 to 60 % of the Lu in the bulk peridotites (Fig. S5-2; Table S5-2). Thus, subsolidus garnet breakdown can be ruled out as the main cause of high Lu/Hf ratios observed in the Yangyuan clinopyroxene relative to Sm/Nd.

Overprinting by a normally high Nd/Hf and low Sm/Nd ratios melt (e.g., Salters and Zindler, 1995; Bizimis et al., 2004) can lower Sm/Nd ratio and add relatively non-radiogenic Nd to peridotites, but does not significantly modify the Lu-Hf isotopic system. This process may explain the Nd-Hf decoupling of those Yangyuan samples that show evidence for overprinting, such as YY-04 and YY-36. However, it cannot account for the samples that primarily maintain the characteristics of melt depletion and plot to the right of the 1.8 Ga Sm/Nd reference isochron (Fig. 5-5), especially the most depleted samples that plot furthest above the Nd-Hf array (Fig. 5-9).

Considering that orthopyroxene has higher Lu/Hf ratio than coexisting clinopyroxene, the bulk rock must have even higher Lu/Hf ratio relative to Sm/Nd than those seen in clinopyroxene (Fig. 5-11). Over time, the bulk rock develops more radiogenic Hf than Nd, and plots well above the Nd-Hf array defined by oceanic basalts. Thus, the observed Nd-Hf isotopic decoupling is a result of ancient

decoupling of Sm/Nd and Lu/Hf ratios soon after or during initial partial melting. This is supported by the fact that all but two samples (YY-13 and YY-50) in the Yangyuan suite plot to the higher Lu/Hf side of the mantle reservoir line defined by primitive and depleted mantle reservoirs (Fig. 5-11). The two samples that plot on or under the mantle reservoir line (Fig. 5-11) also plot on or under the Nd-Hf mantle array (Fig. 5-9).

Oceanic basalts do not record Nd-Hf isotopic decoupling (Vervoort et al., 1999; Vervoort and Blichert-Toft, 1999, and references therein). This fact suggests that ancient residual peridotites characterized by Nd-Hf isotopic decoupling (Figs. 5-7 and 5-9), do not generally participate in later melting events, perhaps because they are sequestered within the lithosphere. Melting ancient residual peridotites would lead to Nd-Hf decoupling inherited in the melts. Thus, high $^{176}Hf/^{177}Hf$ relative to $^{143}Nd/^{144}Nd$ may be a way to distinguish ancient lithospheric mantle inputs into continental, mantle-derived magmas (e.g., Beard and Johnson, 1993).

5.6 Conclusions

Trace element concentrations of orthopyroxene and clinopyroxene and Sr-Nd-Hf-Pb isotopic compositions of clinopyroxenes in the Yangyuan peridotites and the host basalt, as well as the previously measured whole-rock Re-Os isotopic compositions for these samples, allow us to determine the characteristics of melt depletion and later overprinting and constrain the timing of original melt depletion of these peridotites. The main conclusions are as follows:

1) Some peridotites largely retain original ancient melt depletion signatures characterized by prominent depletions of LREE relative to HREE, highly radiogenic Nd and Hf isotopic compositions and comparatively non-radiogenic

Pb isotope compositions. Other peridotites experienced recent overprinting, likely related to the Cenozoic magmatism, as reflected by flat to LREE-enriched patterns and Sr-Nd-Pb isotope compositions that plot towards that of the host basalt.

2) Nd-Hf decoupling in peridotitic clinopyroxenes can be caused by ancient Lu/Hf and Sm/Nd decoupling soon after or during mantle partial melting. High $^{176}Hf/^{177}Hf$ relative to $^{143}Nd/^{144}Nd$ may be a way to distinguish ancient lithospheric mantle inputs into continental, mantle-derived magmas.

3) The similarity of both clinopyroxene Lu-Hf errorchron age (1.66 ± 0.10 Ga) and whole rock Re-Os model ages (1.8 ± 0.2 Ga) suggests that primary melt depletion of the Yangyuan peridotites occurred at ~1.7 to 1.8 Ga. The high initial ε_{Hf} value of +19 in these clinopyroxenes, likely resulting from diffusion of a more radiogenic Hf component from coexisting orthopyroxene, implies that the Lu-Hf isotopic system may be used to potentially date the cooling age when the peridotites cooled below the closure temperature of the Lu-Hf isotope system.

Supplemental Material for Chapter 5

Table S5-1. Trace element concentration results of BHVO glass standard (n=20) determined using laser ablation ICP-MS in this study

BHVO	Average	1σ	RSD[a]	RV[b]	RE[c]	DL[d]
TiO_2	2.51	0.04	1.5%	2.77	-9.6%	4E-05
V	314	7	2.4%	320	-1.8%	0.010
Cr	277	7	2.6%	289	-4.3%	0.21
Rb	8.55	0.68	8.0%	9.5	-10.0%	0.12
Sr	382	12	3.1%	390	-2.0%	0.012
Y	23.5	1.1	4.9%	27	-13.0%	0.002
Zr	160	5	3.2%	180	-10.9%	0.003
Nb	15.4	0.6	3.6%	19.5	-21.3%	0.0009
La	16.0	0.5	3.2%	15.5	3.3%	0.0005
Ce	36.7	1.2	3.4%	38	-3.5%	0.0005
Pr	4.99	0.17	3.5%	5.45	-8.4%	0.0003
Nd	24.3	0.8	3.3%	24.7	-1.5%	0.001
Sm	6.06	0.27	4.4%	6.17	-1.7%	0.001
Eu	2.18	0.14	6.6%	2.06	5.7%	0.002
Gd	5.88	0.38	6.4%	6.22	-5.5%	0.009
Tb	0.907	0.064	7.1%	0.95	-4.5%	0.0003
Dy	5.11	0.24	4.7%	5.25	-2.6%	0.0007
Ho	0.960	0.050	5.2%	1.00	-4.0%	0.0004
Er	2.36	0.13	5.6%	2.56	-8.0%	0.0006
Tm	0.297	0.025	8.6%	0.335	-11.5%	0.0008
Yb	1.99	0.12	6.0%	1.98	0.3%	0.002
Lu	0.272	0.023	8.4%	0.278	-2.1%	0.0008
Hf	4.28	0.18	4.2%	4.3	-0.5%	0.0002

TiO_2 in wt. %, all other elements in ppm.

a. RSD, relative standard deviation

b. RV: reference value

c. RE, relative error between measured and the reference value

d. DL: detection limit.

Table S5-2. Clinopyroxene trace element proportions in the Yangyuan peridotites assuming no REE or Hf in olivine and spinel

Sample	YY-04	YY-08	YY-13	YY-23	YY-26	YY-36	YY-40B	YY-42	YY-45	YY-50	YY-58
La	97.7%	96.5%	98.5%	97.4%	99.2%	99.6%	98.1%	99.2%	98.6%	99.5%	96.8%
Ce	97.7%	97.9%	98.5%	96.2%	99.4%	99.5%	98.8%	99.2%	97.8%	99.1%	96.3%
Pr	97.0%	96.9%	98.3%	94.8%	99.2%	99.3%	97.5%	99.1%	96.8%	98.7%	93.9%
Nd	97.3%	97.9%	98.0%	94.2%	99.1%	99.0%	98.0%	97.3%	95.9%	99.3%	94.1%
Sm	95.2%	90.8%	95.3%	88.0%	96.9%	98.3%	98.0%	93.2%	90.7%	97.2%	88.7%
Eu	91.6%	92.2%	93.2%	87.0%	96.8%	98.2%	94.9%	89.7%	91.8%	96.1%	87.7%
Gd	88.7%	90.2%	90.8%	87.0%	96.6%	97.5%	94.2%	89.5%	88.9%	96.2%	84.5%
Tb	80.6%	84.5%	90.1%	84.6%	96.0%	98.0%	89.9%	86.6%	83.4%	94.3%	77.4%
Dy	77.8%	81.4%	86.2%	73.6%	91.8%	93.3%	89.6%	83.5%	78.1%	90.6%	71.9%
Ho	73.3%	74.8%	83.8%	70.0%	89.5%	91.0%	84.2%	76.2%	73.2%	88.5%	65.4%
Er	64.9%	66.7%	79.0%	63.1%	85.2%	87.1%	80.3%	71.3%	66.4%	84.8%	59.4%
Tm	54.3%	58.7%	75.0%	55.9%	78.3%	84.0%	72.8%	63.7%	59.8%	79.9%	52.7%
Yb	47.6%	51.1%	65.5%	51.0%	72.8%	77.6%	69.0%	54.8%	53.3%	75.6%	46.8%
Lu	39.6%	41.4%	62.7%	41.9%	65.3%	72.7%	56.9%	47.7%	45.8%	69.4%	40.9%
Hf	69.2%	71.7%	83.4%	74.7%	86.8%	87.7%	84.0%	75.2%	69.9%	89.3%	63.0%

Table S5-3. Parameters of partial melting modeling

Mineral	D values [a]		Source mineralogy (x) [b]	Melt proportion (p) [c]
	Lu	Hf		
Olivine	0.0001	0.0001	0.534	0.05
Orthopyroxene	0.2	0.03	0.255	0.25
Clinopyroxene	0.6	0.3	0.183	0.65
Spinel	0.0045	0.007	0.028	0.05
Starting compositions [d]	Lu (ppm)	Hf (ppm)		
	0.0675	0.283		

a. D-values of olivine and spinel are from Chauvel and Blichert-Toft (2001), and D-values of orthopyroxene and clinopyroxene are modified from Chauvel and Blichert-Toft (2001), with ratios of modified D-values between orthopyroxene and clinopyroxene close to the estimates of Witt-Eickschen and O'Neill (2005).

b. Source mineralogy (x) is from Wittig et al. (2006).

c. Melt proportion (p) is from Wittig et al. (2006).

d. Starting bulk compositions of Lu and Hf are from McDonough and Sun (1995).

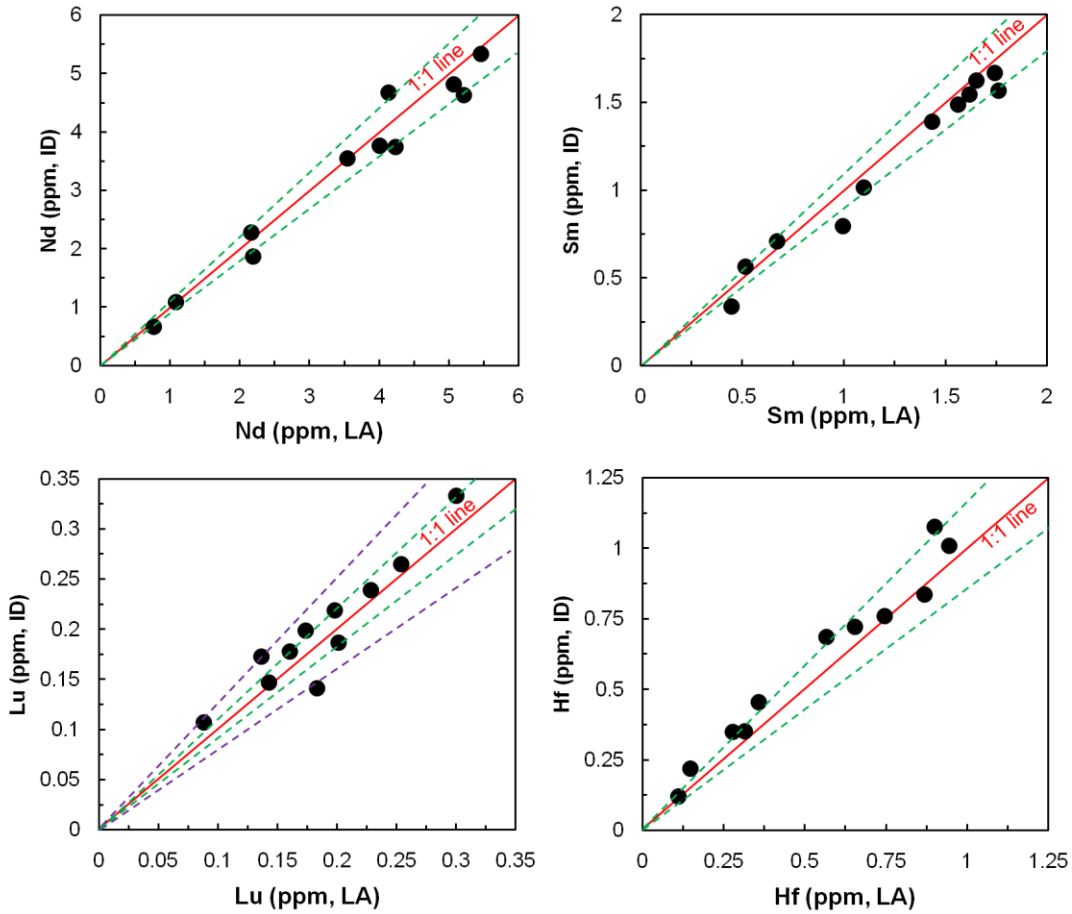

Fig. S5-1 Comparisons of concentrations in clinopyroxene of Yangyuan peridotites analyzed by laser ablation ICP-MS (LA) and isotope dilution (ID) methods. Red, green and purple lines represent the boundaries of 0 %, 10 % and 20 % uncertainties of 1:1 lines, respectively.

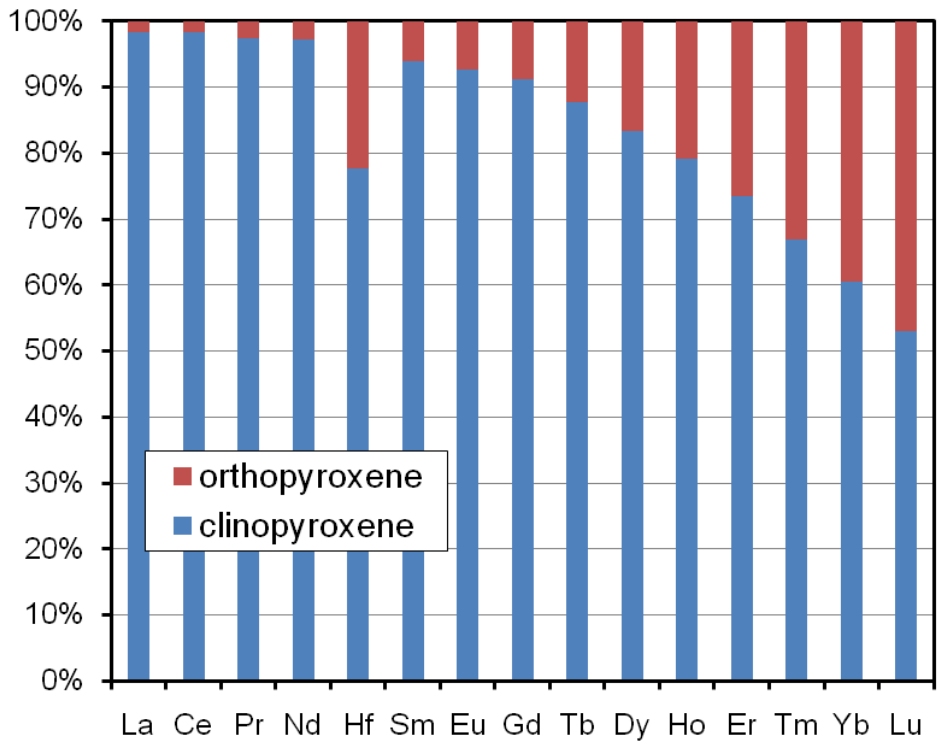

Fig. S5-2. Average trace element contribution (Table S5-2) of pyroxenes in Yangyuan peridotites calculated from modal mineralogy and trace element concentrations in pyroxenes determined by LA-ICP-MS, assuming no REE or Hf in olivine and spinel.

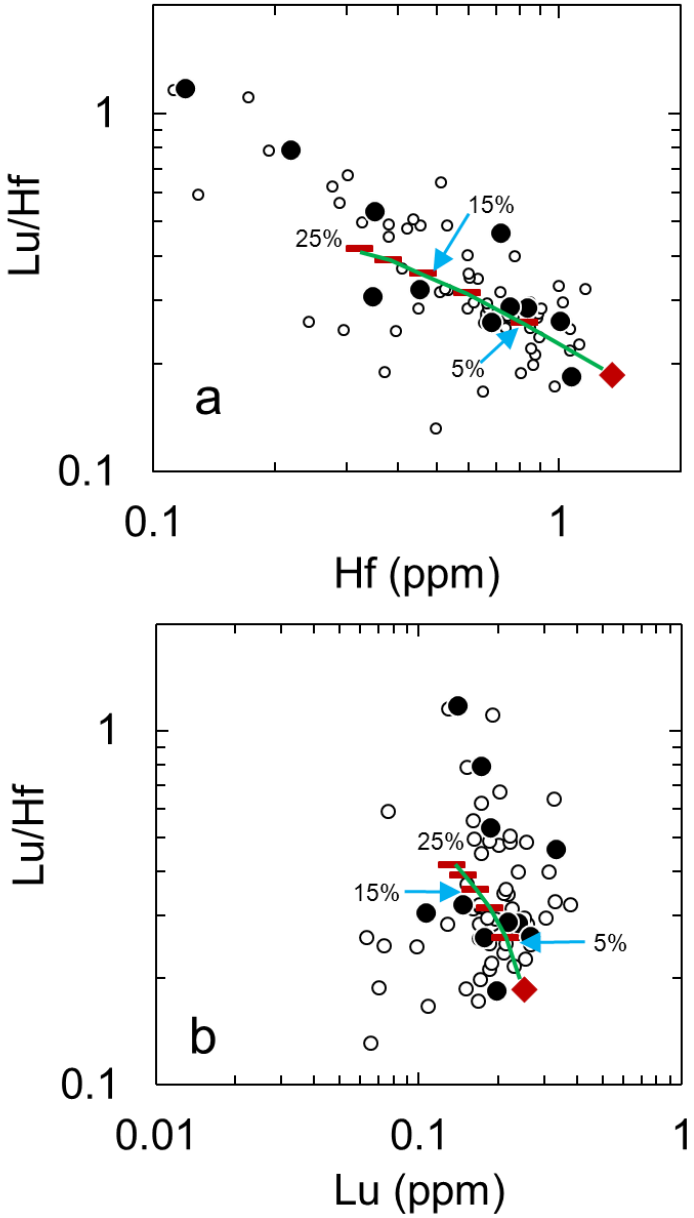

Fig. S5-3. Lu/Hf vs. Hf (a) and Lu (b) concentrations for clinopyroxenes from Yangyuan peridotites (large solid circles). Small open circles are laser ablation data for clinopyroxenes from other Yangyuan peridotites that have not been analyzed for Sr-Nd-Hf-Pb isotopic compositions. The green line shows 0 to 25 % degrees of batch melting with tick marks showing 5% increment (see details below). Red diamond represents the starting composition of clinopyroxene in primitive mantle.

Modeling I: ***Fractional melting of mantle melt depletion***

In this modeling, the influence of mantle partial melting on the concentrations of Lu and Hf in clinopyroxenes was modeled using the fractional melting equation of Johnson et al. (1990).

$$C_i^{cpx} = \frac{C_i^o D_i^{cpx/l}}{D_i^o - FP}\left[1 - \frac{FP}{D_i^o}\right]^{\frac{1}{P}}$$

where C_i^{cpx} is the concentration of element i in clinopyroxene of the residue, C_i^o is the initial concentration of element i in bulk source, $D_i^o = \sum_j X^j D_i^{j/l}$ (the initial bulk partition coefficients of element i), $D_i^{j/l}$ is the partition coefficient of element i in phase j), X^j is modal mineralogy of Phase j in the initial bulk source, $P = \sum_j p^j D_i^{j/l}$ (j represents mineral phase j in source, p^j is the melt proportion of phase j), and F is melt fraction.

The modeling parameters are given in Table S5-3 and results of 0-20% degrees of melting are shown in Fig. 5-10.

Modeling II: ***batch melting of mantle melt depletion***

In this modeling, the influence of mantle partial melting on the concentrations of Lu and Hf in clinopyroxenes was modeled using the batch melting equation of Johnson et al. (1990).

$$C_i^{cpx} = \frac{C_i^o D_i^{cpx/l}}{D_i^o + F(1-P)}$$

where C_i^{cpx} is the concentration of element i in clinopyroxene of the residue, C_i^o is the initial concentration of element i in bulk source, $D_i^o = \sum_j X^j D_i^{j/l}$ (the initial bulk partition coefficients of element i), $D_i^{j/l}$ is the partition coefficient of element i in phase j), X^j is modal mineralogy of Phase j in the initial bulk source, $P = \sum_j p^j D_i^{j/l}$ (j represents mineral phase j in source, p^j is the melt proportion of phase j), and F is melt fraction.

The modeling parameters are given in Table S5-3 and results of 0-25 % degrees of melting are shown in Fig. S5-3.

Chapter 6: Timing and processes of lithospheric thinning in the eastern North China Craton[1]

[1] The text, tables and figures in this chapter were created/written by J.G. Liu.

Abstract

The Mesozoic era was a significant period for lithospheric thinning beneath the eastern portion of the North China Craton, but the exact timing and mechanism(s) of this thinning are controversial. The study of peridotites hosted in the Early Cretaceous (~100 Ma) Fuxin basalts located at the northern edge of the eastern North China Craton provides new constraints on these issues. The Fuxin spinel peridotites consist of both fertile (forsterite content (Fo) < 91) and refractory (Fo > 91) compositions. The Re-Os data show that one harzburgite sample with Fo = 91.0 has an Archean-Paleoproterozoic Os model age, and the remaining five samples with Fo < 90.3 have Os isotopic compositions akin to modern convective upper mantle. The new Os data suggest the coexistence of ancient and young peridotites in lithospheric mantle beneath Fuxin. This observation suggests that lithospheric thinning occurred prior to ~100 Ma in this region. The coexistence of both ancient and young peridotites is more consistent with the prediction of the thermo-mechanical erosion model, rather than the other models such as delamination and transformation via melt-rock reaction.

6.1 Introduction

The eastern portion of the North China Craton lost its Archean lithospheric root sometime after the Ordovician (e.g., Menzies et al., 1993; Griffin et al., 1998). The timing and mechanism(s) of lithospheric thinning and replacement, as well as its

driving force, are debated. Prior studies of xenolithic peridotites and mantle-derived volcanic rocks have suggested that the Mesozoic was a critical period for lithospheric thinning (e.g., Wu et al., 2005a; Zheng et al., 2007; Gao et al., 2008; Xu et al., 2009). The processes advanced as potentially responsible for lithospheric thinning include: 1) delamination or density foundering that removes a portion of lower crust and the entire underlying lithospheric mantle (e.g., Wu et al., 2003; Gao et al., 2004, 2008); 2) transformation via melt-rock reaction that transforms refractory compositions to fertile compositions (e.g., Zhang et al., 2002, 2007, 2007); and 3) thermo-mechanical erosion that gradually removes the base of the lithosphere (e.g., Griffin et al., 1998; Xu et al., 2001; Zheng et al., 2001, 2007). Each of these models would produce a distinctive chemical and age structure in the remaining lithospheric mantle. Delamination would result in formation of completely new lithospheric mantle. Melt-rock reaction would result in lithospheric mantle with interfingered refractory through fertile compositions. Thermo-mechanical erosion would be characterized by relict ancient lithospheric mantle underlain by newly formed lithospheric mantle.

The investigation of xenolithic peridotites transported to the surface in the Mesozoic is important for constraining the timing and mechanism of lithospheric thinning. Previously, the lithospheric mantle that was present during the Mesozoic was not well constrained due to the scarcity of xenolithic peridotites in Mesozoic volcanic centers. Mantle xenoliths carried in Early Cretaceous high-Mg diorites from Laiwu in the central Eastern Block (Fig. 2-1) sampled Archean refractory lithospheric mantle but also contained a significant proportion of fertile peridotites (Gao et al., 2008), one interpretation of which could be that lithospheric replacement was ongoing at that time. Similar types of mantle rocks occurred in Early Cretaceous high-Mg

diorites from Fushan on the western boundary of the Eastern Block, but the Archean refractory peridotites in these rocks record a low geotherm, which can be interpreted to indicate that the lithospheric thinning had not yet begun in this region at that time (Xu et al., 2010; Liu et al., 2011a). Qian and Hermann (2010) argued that these high-Mg diorites were derived from felsic melts that had interacted with previously emplaced peridotites at crustal rather than mantle depths. If this argument is correct, it would lead to diverse interpretations for origin of these mantle xenoliths and difficulty in evaluating their role in constraining the lithospheric thinning process of the craton. In this chapter, Re-Os data for peridotites entrained in Early Cretaceous mantle-derived alkali basalts from Fuxin are reported. Possible implications regarding lithospheric thinning in the eastern North China Craton are discussed.

6.2 Samples

Xenoliths from Fuxin are hosted by ~100 Ma alkali basalts that occur at the northern margin of the eastern North China Craton (Fig. 2-1). The peridotite xenoliths are dominantly spinel lherzolites with minor harzburgites (Zheng et al., 2007; this study). They are relatively fresh, but small in size (<2 cm across). Mineral major element compositions and clinopyroxene trace element compositions for a different suite of the Fuxin peridotites have been previously investigated by Zheng et al. (2007).

6.3 Analytical methods

6.3.1 Olivine composition and sample selection

Mineral mounts of olivine were prepared for 15 peridotites and analyzed in order to assess the range in degrees of melt depletion exhibited by the peridotite suite.

Olivine compositions were measured using a JEOL 8900 EPMA at UMd. The operating parameters and calculation method are provided in the section 3.3.1 of Chapter Three. Three spots per sample were measured and average results are reported (Table 6-1). Six relatively large (1 to 2 cm across) samples that largely span the entire range of Fo were selected and processed for analyses of whole rock Re-Os isotopic compositions and HSE abundances. The basalt surrounding the xenolith was first carefully sawn off and then ground away to expose the xenolith using a polisher with a coarse-grained silicon carbide-coated paper. The basalt-free xenolith was crushed and pulverized to fine powders using agate mortar and pestle by hand. These samples yielded 0.38 to 1.4 g of material for whole-rock analyses.

6.3.2 Os isotopes and HSE abundances

Due to the sample size limitation, ~0.2 to 0.5 g of powder were processed per sample. The analytical procedures are detailed in section 3.3.4 of Chapter Three, but the samples were digested using a smaller volume of acids, i.e., a mixture of 2 ml concentrated HCl and 4 ml concentrated HNO_3. One blank was measured, yielding Os – 0.72 pg, Ir – 0.43 pg, Ru – 4.7 pg, Pt – 1.4 pg, Pd – 6.5 pg, and Re – 0.88 pg. Blank corrections for Os, Ir, Ru, Pt, and Pd are negligible (less than 0.4 %) for samples, while the Pd and Re blanks constitute 0.3 to 3.2 % and 0.5 to 13 % of the total Pd and Re in samples, respectively.

6.4 Results

6.4.1 Forsterite contents

The Fuxin peridotites analyzed in this study exhibit relatively low Fo contents (Fo = 86.8 to 91.0, with an average of 89.0; Table 6-1), and are plotted as a histogram

in Fig. 6-1. Their Fo contents are similar to the majority of the samples analyzed by Zheng et al. (2007), but none of the samples analyzed have as high Fo contents (> 92.0) as the two refractory harzburgites reported by Zheng et al. (2007). The samples selected for whole-rock analyses have Fo ranging from 87.4 to 91.0 (Table 6-2).

Table 6-1. Olivine compositions of the Fuxin peridotites determined by EPMA

Sample	SiO2	FeO	MgO	SiO2	NiO	MnO	Total	Fo
JG-13	40.6	10.6	48.5	40.6	0.35	0.14	100.2	89.1
JG-14	40.6	9.48	49.3	40.6	0.34	0.16	99.9	90.3
JG-15	40.6	8.85	49.8	40.6	0.38	0.12	99.8	91.0
JG-19	40.4	10.1	48.6	40.4	0.35	0.16	99.6	89.5
JG-21	40.6	10.8	48.1	40.6	0.33	0.18	100.1	88.9
JG-24	40.4	10.1	49.0	40.4	0.34	0.16	100.0	89.6
JG-25	40.3	11.5	47.6	40.3	0.23	0.17	99.8	88.1
JG-26	40.6	10.1	48.9	40.6	0.37	0.14	100.2	89.6
JG-30	39.9	12.7	46.8	39.9	0.35	0.20	99.9	86.8
JG-32	40.4	10.7	48.2	40.4	0.35	0.15	99.8	88.9
JG-33	40.3	12.2	47.5	40.3	0.30	0.17	100.5	87.4
JG-52	40.4	11.1	48.5	40.4	0.35	0.20	100.6	88.6
JG-55	40.4	10.3	48.8	40.4	0.36	0.15	100.0	89.4

Note: Oxides in wt. %. Forsterite content (Fo) = molar $Mg/(Mg+Fe^{2+})x100$

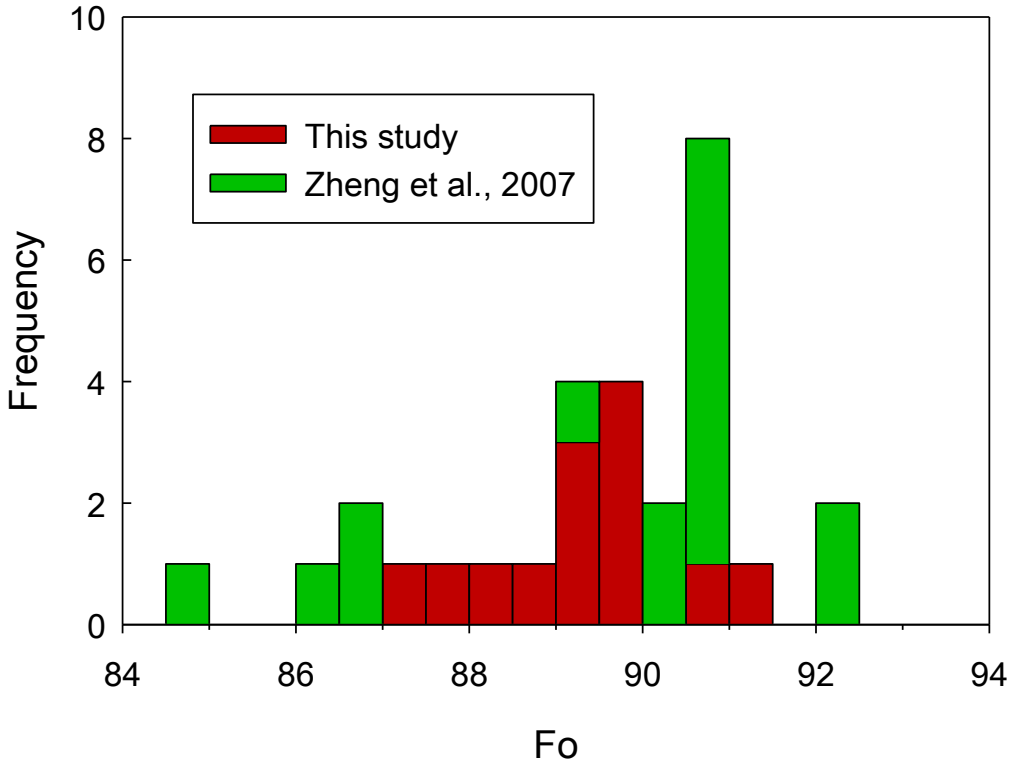

Fig. 6-1. Histograms of average forsterite contents of olivines from the Fuxin peridotites. The data for the green color are from Zheng et al. (2007).

6.4.2 HSE abundances and Os isotopes

The HSE abundances of the Fuxin peridotites are generally lower than those of PUM (Fig. 6-2; Table 6-2). Despite the fact that only six samples were analyzed, these samples show a large variation of HSE abundances and patterns (Fig. 6-2), e.g., Os ranging from 0.13 to 3.52 ppb. Samples JG-15 and JG-25 are characterized with PPGE and Re depletions relative to IPGE, with a slight Re enrichment relative to Pd. The patterns of JG-14 and JG-33 are similar to that of PUM, except that JG-33 has an apparent Re depletion relative to other HSEs. The remaining samples have atypical HSE patterns characterized by variable positive Pt (and Pd) anomalies. Five of the six samples have chondritic to suprachondritic Os isotopic compositions ($^{187}Os/^{188}Os$ = 0.1249 to 0.1357 and $^{187}Re/^{188}Os$ = 0.066 to 1.6), while the most refractory sample, JG-15, has very low $^{187}Os/^{188}Os$ of 0.1128, with T_{RD} and T_{MA} model ages of 2.13 and 3.80 Ga.

Table 6-2. HSE abundances and Os isotopic compositions of the Fuxin peridotites

Sample	Os	Ir	Ru	Pt	Pd	Re	$^{187}Re/^{188}Os$	$^{187}Os/^{188}Os$	$(^{187}Os/^{188}Os)_i$	T_{RD}	T_{MA}	Fo
	ppb	ppb	ppb	ppb	ppb	ppb				Ga	Ga	
JG-14	3.52	3.10	6.23	6.36	5.04	0.232	0.318	0.1249	0.1244	0.39	1.46	90.3
JG-15	1.54	2.31	3.12	2.66	1.01	0.059	0.18	0.1128	0.1125	2.13	3.80	91.0
JG-25	3.14	2.81	5.87	2.94	1.47	0.070	0.11	0.1283	0.1281	-0.16	-0.26	88.1
JG-33	2.32	1.83	3.76	4.02	3.92	0.032	0.066	0.1276	0.1275	-0.07	-0.11	87.4
JG-52	0.131	0.104	0.803	6.66	1.77	0.044	1.6	0.1285	0.1258	0.18	0.07	88.6
JG-55	1.81	2.64	2.01	22.9	21.9	0.431	1.30	0.1357	0.1335	-0.98	0.58	89.4

Note: The parameters used in model age calculation are: $\lambda_{Re} = 1.666 \times 10^{-11}$/year, $(^{187}Re/^{188}Os)_{CI} = 0.402$, $(^{187}Os/^{188}Os)_{CI,0} = 0.1270$ (Shirey and Walker, 1998). $(^{187}Os/^{188}Os)_i$ represents the initial value when xenolith was erupted (~100 Ma).

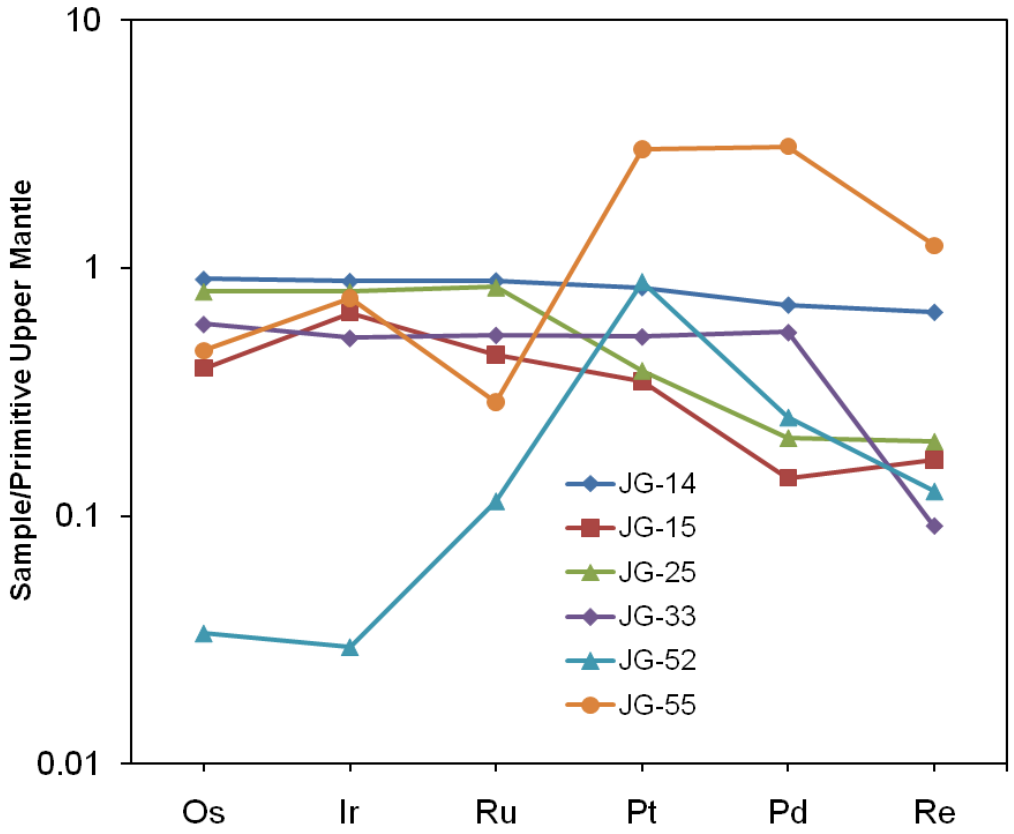

Fig. 6-2. HSE abundances of the Fuxin peridotites normalized to primitive upper mantle (primitive upper mantle values are from Becker et al., 2006).

6.5 Discussion

6.5.1 Coexistence of young, fertile and ancient, refractory mantle

6.5.1.1 Forsterite contents of olivine

Based on forsterite contents, Zheng et al. (2007) divided the Fuxin peridotites into three subgroups: 1) Type 1, the dominant lherzolites with Fo = 88.9 to 90.7; 2) Type 2, two harzburgites with Fo = 92.1 and 92.2, respectively; and 3) Type 3, four lherzolites with very low Fo = 84.4 to 86.5. The origins of these three types of peridotites were interpreted as follows. The Type 1 peridotites experienced relatively low degrees of melt extraction and represent the majority of lithospheric mantle at the time of eruption (~100 Ma). The Type 2 peridotites having major and relatively immobile trace element compositions similar to typical cratonic peridotites, e.g., Hebi (Zheng et al., 2001; Liu et al., 2011a), were interpreted as relics of Archean cratonic lithospheric mantle. The Type 3 peridotites were produced via interaction of Type 1 or Type 2 peridotites with melts similar to host basalts during or prior to eruption.

The samples from this study fill the gap in Fo between Type 1 and Type 3 seen in Zheng et al.'s samples (Fig. 6-1), with one sample, JG-15, having Fo = 91.0, which is slightly higher than the range of Fo in Zheng's Type 1 xenoliths, but lower than the Fo in Type 2 xenoliths. Sample JG-15 may be a transitional sample between Type 1 and Type2.

6.5.1.2 HSE abundances and Os isotopic compositions

The depletions of PPGE relative to IPGE in samples JG-15 and JG-25 typically reflect partial melting of the mantle (Pearson et al., 2004). Unlike JG-15 (Fo = 91.0), JG-25 has a much lower Fo of 88.1 that is inconsistent with its PPGE-depleted pattern.

This discrepancy may suggest that JG-25 experienced substantial melt removal that caused the depletion of PPGE, and later experienced melt addition or melt-rock reaction that led to the low Fo. This process evidently did not significantly impact the HSE, except for Re. Despite similar HSE patterns, these two samples exhibit distinctly different Os isotopic compositions, with $^{187}Os/^{188}Os$ = 0.1128 for JG-15 and $^{187}Os/^{188}Os$ = 0.1283 for JG-25. Sample JG-15 has a Paleoproterozoic T_{RD} age of 2.13 Ga and a substantially higher T_{MA} of 3.8 Ga. The old T_{MA} age may reflect recent Re addition, as suggested by its subtle Re enrichment relative to Pd (Fig. 6-2), or incomplete removal of Re during melt depletion, given its Fo value that is somewhat lower than typical cratonic peridotites. The Archean-Paleoproterozoic model ages of sample JG-15 can be interpreted as preserved peridotitic residue of ancient melt depletion. By contrast, sample JG-25 has near-zero model ages (T_{RD} = -0.16 Ga and T_{MA} = -0.26 Ga). These model ages suggest either that melt depletion was recent, or that Os has been completely overprinted by the melt-rock reaction. Given no significant alteration evident in the HSE pattern, this sample most likely experienced recent melt depletion that removed a portion of PPGE but had little or no effect on Os isotopic composition; the low Fo value reflects subsequent Fe-enrichment.

The PUM-like HSE patterns of JG-14 and JG-33 are likely the results of relatively low degrees of partial melting, consistent with their low Fo (90.3 and 87.4, respectively), while the prominent depletion of Re in sample JG-33 most likely reflects recent Re mobility in the mantle, or during transit to the surface. The Os isotopic compositions of these rocks lie within the range of modern convective upper mantle, and there is no obvious correlation between $^{187}Os/^{188}Os$ and melt depletion indicator (e.g., Fo), suggesting their recent addition to the lithospheric mantle. Like

the two samples in the Datong peridotites (DAT-05 and DAT-31; Liu et al., 2011a), the remaining samples JG-52 and JG-55 have variable positive Pt (and Pd) anomalies that can be explained by Pt and Pd mobility via melt percolation (Ackerman et al., 2009). The process causing Pt and Pd anomalies may also have modified their Re-Os isotopic compositions, given their highly suprachondritic $^{187}Re/^{188}Os$ (1.6 and 1.30, respectively) and $^{187}Os/^{188}Os$ (0.1285 and 0.1357, respectively) and near-zero or future T_{RD} ages (Table 6-2). Like other low-Fo samples, these two samples did not experience significant ancient melt removal, but experienced significant subsequent melt-rock reaction, as reflected in their PGE patterns.

In summary, the Type 1 and Type 3 peridotites are characterized by relatively low Fo values and represent newly accreted residual peridotites, like many other suites of peridotites in the Late Cretaceous-Cenozoic volcanic centers in the eastern North China Craton (Fig. 2-1). Sample JG-15, however, likely represents a piece of ancient lithospheric mantle coupling with the overlying crust, similar to Type 2 peridotites (Zheng et al., 2007). Considering the heterogeneous nature of Os isotopic composition in the mantle (e.g., Harvey et al., 2006; Liu et al., 2008), the Archean-Paleoproterozoic formation ages need to be confirmed by more Re-Os analyses of the high-Fo Type 2 peridotites. If the age is confirmed, the results would demonstrate the coexistence of young fertile peridotites and ancient refractory peridotites in the Early Cretaceous Fuxin locality. If no additional ancient ages are determined, the Paleoproterozoic T_{RD} age of sample JG-15 may represent a piece of a Paleoproterozoic lithospheric mantle, which is younger in age than expected Archean lithospheric mantle coupling with the overlying crust. Alternatively, such a single ancient age is a result of sampling mantle heterogeneity.

6.5.2 Implications for lithospheric tectonics

Multiple scenarios regarding the tectonic implications of the North China Craton based on the results of the Fuxin peridotites are considered below.

6.5.2.1 Coexistence of young, fertile peridotites and ancient, refractory peridotites?

If via analysis of additional samples, the Archean Os model ages of the refractory Fuxin peridotites are confirmed, such ancient peridotites would represent relict fragments of the Archean lithospheric mantle that was present beneath the eastern North China Craton in the Paleozoic (Gao et al., 2002; Wu et al., 2006; Zhang et al., 2008; Chu et al., 2009). The lack of garnet in the peridotites indicates a relatively thin (< 80km) lithosphere during the time of eruption. The observation of dominant young, fertile, spinel peridotites may suggest that most of the thick Archean lithospheric mantle beneath Fuxin was removed, or transformed, and replaced by fertile peridotites. The lithospheric thinning and replacement must have occurred prior to ~100 Ma, when the xenoliths were erupted. This is consistent with the thinning period provided by widespread Jurassic to Early Cretaceous (194-110 Ma, with a peak of 130 Ma) mantle-derived magmas in the eastern North China craton, which are characterized by negative $\varepsilon_{Nd}(t)$ values of < -5 (Lu et al., 2005, and references therein) and were interpreted to be derived from an enriched lithospheric mantle, instead of depleted asthenosphere.

Melt-rock reaction occurred in the Fuxin peridotites (Zheng et al., 2007; this study), but the HSE patterns of these samples are not consistent with overprinting of Archean $^{187}Os/^{188}Os$ that would transform non-radiogenic $^{187}Os/^{188}Os$ in ancient

peridotites to the observed chondritic to superchondritic $^{187}Os/^{188}Os$ comparable to peridotites in the modern convective upper mantle. The bimodal distribution of ancient and young peridotites is not consistent with lithospheric thinning via delamination, but rather with the predictions of thermo-mechanical erosion. However, the limited data currently available are insufficient to confirm a stratified structure with ancient peridotites overlying young peridotites (Zheng et al., 2007).

6.5.2.2 Paleoproterozoic lithospheric mantle?

If no Archean model ages are found in the most refractory Fuxin peridotites, it may ultimately be concluded that sample JG-15 represents a fragment of Paleoproterozoic lithospheric mantle. Given the overlying Archean crust, the younger Paleoproterozic age suggests an ancient lithospheric replacement event prior to the Mesozoic lithospheric thinning discussed above. Previous studies of mantle xenoliths have shown that Paleoproterozoic lithospheric replacement occurred in the northern portion of the central region of the North China Craton (Gao et al., 2002; Liu et al., 2011a). Considering that Fuxin is located in the east-west-trending Paleoproterozoic collisional belt (Fig. 2-1b; Kusky et al., 2001, 2007a), this would be evidence that the Paleoproterozoic lithospheric replacement may have continued to the east, at least as far as Fuxin. If so, it may provide additional support that the Paleoproterozoic lithospheric replacement along the northern margin of the craton was caused by a major Paleoproterozoic north-south continent-continent collision during amalgamation of the Columbia supercontinent (Liu et al., 2011a). Regardless of whether ancient lithospheric loss occurred during the Paleoproterozoic, current results indicate that Mesozoic lithospheric thinning occurred prior to ~100 Ma beneath Fuxin.

6.5.2.3 Paleoproterozoic model age in the convective mantle?

In addition to the two scenarios discussed above, sample JG-15 with ancient Os model ages may not necessarily indicate the antiquity of lithospheric mantle sampled but reflect the heterogeneity of the mantle. A large number of samples need to be analyzed to determine if such individual samples come from the modern convective upper mantle. If the results statistically demonstrate the heterogeneous characteristic of the modern convective upper mantle, this would suggest that Mesozoic lithospheric thinning occurred prior to ~100 Ma beneath Fuxin and the ancient lithospheric mantle was completely removed likely via delamination.

6.5.3 Spatial and temporal variations of lithospheric thinning

Comprehensive studies of xenolithic peridotites in volcanic centers provide a complex composition and age structure of lithospheric mantle beneath the eastern North China Craton through time. Early Mesozoic-erupted peridotites from the easternmost edge (Korean; 223 Ma) and southwestern corner (Xinyang; 178 Ma) of the Eastern Block (Fig. 2-1) are spinel-facies peridotites with elemental and/or Os isotopic compositions similar to modern convective upper mantle (Zheng et al., 2005; Yang et al., 2010). Both refractory (Archean-Paleoproterozic Os model ages) and fertile (Os isotopic compositions similar to modern convective upper mantle) peridotites are found in the Early Cretaceous localities within the interior of the craton, e.g., Laiwu (Gao et al., 2008), and at the northern edge of the craton, e.g., Fuxin (Zheng et al., 2007; this study). All the xenoliths in the Late Cretaceous-Cenozoic localities are predominantly fertile, spinel-facies peridotites with Os isotopic compositions overlapping with abyssal peridotites, except that refractory peridotites

are dominant in Hebi and Fushan localities on the western boundary of the Eastern Block (Fig. 2-1; Zheng et al., 2001; Liu et al., 2011a). The observed composition and age structure of lithospheric mantle beneath the eastern North China Craton suggests that lithospheric thinning initiated in the Early Mesozoic along margins and evolved to its interior in the Late Mesozoic. The lithosphere evidently experienced complete removal along margins and partial removal in its interior during the Mesozoic.

6.6 Conclusions

The Os data and olivine compositions likely reflect the coexistence of ancient, refractory (Fo > 91) and young (Os isotopic compositions overlapping with modern convective upper mantle), fertile (Fo < 91) peridotites in the Late Cretaceous Fuxin locality. This observation suggests that lithospheric thinning occurred prior to ~100 Ma in this region. The coexistence of both ancient and young peridotites is likely consistent with the predication of thermo-mechanical erosion model.

Chapter 7: Synthesis and future directions[1]

[1] The text and figure in this chapter were created/written by J.G. Liu.

Since the recognition nearly twenty years ago that the North China Craton became "decratonized" (Menzies et al., 1993), much attention has been paid to identifying temporal and spatial constraints on the thinning that occurred, as well as determining the mechanism(s) and driving force(s) responsible for its initiation. The main goal of this project was to investigate the compositional variation and age structure within the lithospheric mantle beneath the North China Craton using Re-Os isotope systematics and HSE abundances in mantle xenoliths. The new elemental and isotopic data for xenolithic peridotites from this study provide new insights into lithospheric thinning under the North China Craton.

The peridotites from the central region of the North China Craton record a north-south coupled composition and age dichotomy in the underlying lithospheric mantle. The age dichotomy is characterized by ~1.8 Ga lithospheric mantle in the northern portion and ~2.5 Ga lithospheric mantle in the southern portion. The younger lithospheric mantle, compared to overlying Archean crust in the northern portion, suggests a major lithospheric thinning event at ~1.8 Ga in the northern portion of the central region of the North China Craton. The similarity in age between crust and lithospheric mantle in the southern portion suggests ~2.5 Ga cratonization in this region. The diachronous formation of lithospheric mantle in the central region was associated with the amalgamation of the craton and, in turn, provides significant constraints on the long term construction of the craton.

In contrast to the Paleoproterozoic lithospheric thinning and replacement in the northern portion of the central region of the North China Craton, a number of previous studies have documented Phanerozoic lithospheric thinning and replacement beneath the eastern portion of the North China Craton (e.g., Menzies et al., 1993; Griffin et al., 1998; Gao et al., 2002; Wu et al, 2003, 2006; Chu et al., 2009; Yang et al., 2010). However, the exact timing and mechanisms, as well as spatial variation, of the lithospheric thinning and destruction remain poorly constrained.

Throughout the Phanerozoic era, the North China Craton was surrounded by several major collision/subduction zones (Fig. 7-1; Li et al., 1993; Xiao et al., 2003; Tomurtugoo et al. 2005). The lithospheric mantle beneath the North China Craton along its margins was hydrated and weakened by melts/fluids derived from the subducted slabs, and later shortened and thickened by subsequent continent-continent collisions. The collisional processes could also have caused high-pressure metamorphism of lower continental crust that resulted in the formation of garnet-bearing assemblages with higher densities than the underlying lithospheric mantle (Xu et al., 2006). This, in turn, may have resulted in density instability in the over-thickened lithosphere. However, calculations show that the transformation of 10 to 20 km mafic lower crust into denser garnet-bearing assemblages would not provide sufficient negative buoyancy to balance the positive buoyancy of >200 km refractory lithospheric mantle compared to ambient asthenosphere and initiate lithospheric removal until at least 55 Ma later (Morency et al., 2002), which is consistent with the observation that lithospheric delamination occurred ~100 Ma later than the continent-continent collisions (Gao et al., 2004; Huang et al., 2007).

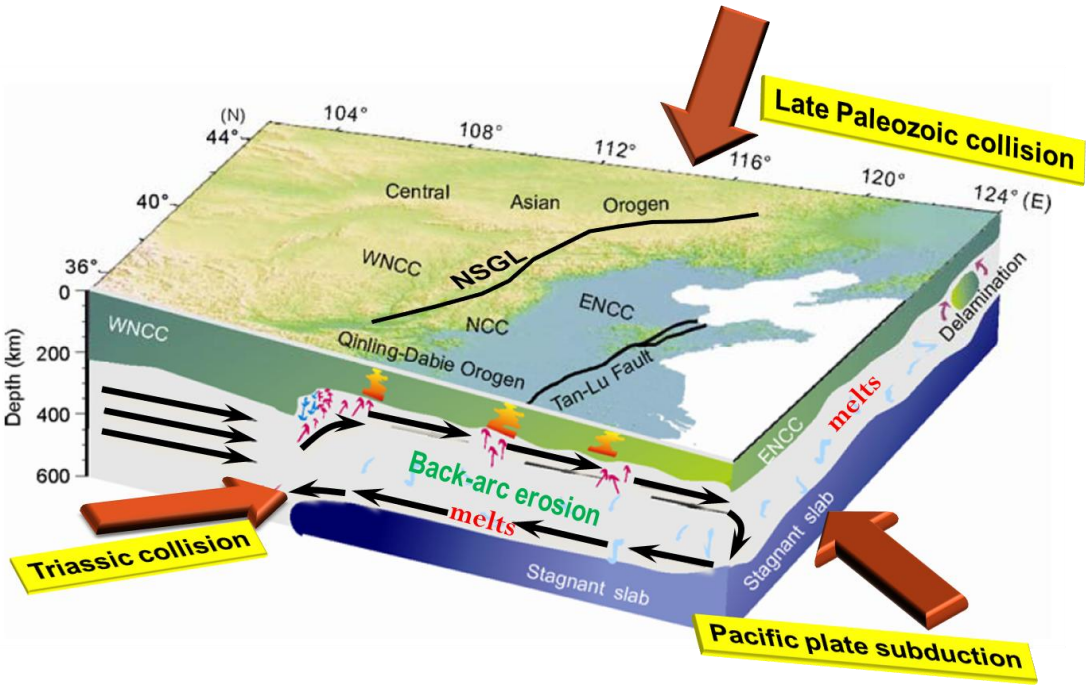

Fig. 7-1. Schematic 3-D diagram of a model of upper mantle flow beneath the North China Craton (modified from Zhu and Zheng, 2009). The top plane is a topographic map. The structure of the stagnant slab (dark blue), cratonic lithosphere (green) and the mantle convection pattern are shown in the profiles. Black arrows mark stable convection, and small red and blue arrows mark the directions of local disturbed flow. Large brown arrows mark subduction/collision along the margins of the North China Craton (NCC): Late Paleozoic collision along the Central Asian Orogen in the north; Triassic collision along the Qinling-Dabie Orogen in the south; and Pacific plate subduction in the east since the Jurassic.

The new data from this dissertation and previous data in the literature regarding xenolithic peridotites in the eastern portion of the North China Craton suggest that the removal and replacement of lithospheric mantle occurred prior to the Triassic on the eastern edge of the craton (Yang et al., 2010), in the Early Cretaceous in its interior (Gao et al., 2008; Zheng et al., 2007; this study), and after the Cretaceous on the westernmost boundary of the NSGL (this study). This temporal evolution matches the westward subduction of the Paleo-Pacific plate beneath eastern China, and tomographic studies (Huang and Zhao, 2006) show that the forward edge of the subducting slab reached the NSGL at depth of ~400 km (believed to be the westernmost demarkation of the Phanerozoic thinning; Griffin et al., 1998). Such comparative temporal and spatial correlations between lithospheric thinning and subduction of the Paleo-Pacific plate suggest that subduction of the Paleo-Pacific plate played a significant role in the lithospheric thinning and replacement.

Subduction of the Paleo-Pacific plate beneath eastern China since at least the Jurassic (Zhou and Li, 2000; Li and Li, 2007) generated massive amounts of melts/fluids from the mantle wedge, further weakened the subcontinental lithospheric mantle, and initiated back-arc convection (i.e., eastward mantle corner flow) that may have gradually removed the base of the lithospheric mantle upward and westward by lateral shear stress (Fig. 7-1). In the over-thickened lithosphere in the northern and southern margins of the eastern portion of the North China Craton, the removal of a lower portion of the lithospheric mantle via eastward shear stress would initiate the foundering of dense lower crust and underlying lithospheric mantle. The foundered lower crust experienced partial melting and produced silicic melts that reacted with upwelling asthenospheric mantle, which replaced the foundered lithospheric mantle.

The melting of the metasomatized asthenospheric mantle yielded voluminous Mesozoic mantle-derived mafic igneous rocks that are characterized by a "continental" geochemical signature (e.g., high $^{87}Sr/^{86}Sr_i$ = 0.705 to 0.711, low $\varepsilon_{Nd}(t)$ = -4 to -21, and non-radiogenic Pb isotopic compositions, relative to the Paleozoic kimberlites and peridotites; Huang et al., 2007 and references therein; Gao et al., 2008). Along the westernmost boundary of the eastern portion of the North China Craton, the lithosphere likely did not experience significant thickening in the continent-continent collisions along the margins. As a result, relict Archean lithospheric mantle was sampled at shallow depths in this region (e.g., Hebi peridotites; Fig. 2-1), where thermal-mechanical erosion was the main mechanism for lithospheric removal, and delamination did not occur. In the weak zones, such as the Tan-Lu fault that developed in the Early Cretaceous (Xu et al., 1987; Zhu et al., 2005), the upwelling of hot mantle material may have accelerated the removal and replacement of the lithospheric mantle by the observed young, fertile mantle present in this region (Gao et al., 2002; Chu et al., 2009).

Mesozoic mantle-derived mafic rocks with "continental" geochemical signatures indicate the contributions of lower crust that was delaminated, then melted and added to the mantle source. The eruption time of Mesozoic mantle-derived mafic rocks marks the timing of lithospheric delamination: mid-Jurassic in the northern margin of the eastern North China Craton (Gao et al., 2004) and Late Cretaceous in the central and southern margin (Zhang et al., 2003; Gao et al., 2008). This observation may be explained by the change in direction of the Pacific plate in the Late Jurassic-Early Cretaceous from roughly southward to northwestward (Sun et al., 2007).

In summary, the subduction/collision zones along the northern and southern margins of the eastern portion of the North China Craton weakened the lithospheric mantle via fluids/melts derived from the subducted slabs and shortened and thickened the lithosphere via subsequent collisions, while westward subduction of the Paleo-Pacific plate beneath eastern China triggered the extensive destabilization of the North China Craton and its lithospheric thinning that likely evolved from east to west. It is noted that the NSGL extends north and south of the North China Craton, and is roughly parallel to the margin of the subducting Pacific plate. Hence, subduction of the Pacific plate may have also led to the lithospheric thinning in the South China Block, but the lack of lithospheric thickening in this block may have precluded the operation of multiple mechanisms (such as delamination) of thinning other than thermal-mechanism erosion due to back-arc convection.

Despite the new insights provided from this study on mantle peridotites, a number of questions regarding the age of melt depletion of mantle peridotites, as well as the formation and evolution of the North China Craton remain. These main questions and possible future directions are outlined as follows in two categories:

1. General application of Re-Os isotope systematics to dating melt depletion of peridotites

Determining the age of melt depletion of a peridotite is necessary to investigate the origin of the lithospheric mantle sampled by peridotite. There are uncertainties to be addressed in order to better date these mantle rocks. Although the Re-Os isotopic compositions of peridotites can be accurately and precisely determined, Re-Os model

ages have large uncertainties, given the diverse Re-Os evolutionary parameters for the mantle (see section 5.1 of Chapter Five for more details). A better understanding of the Re-Os evolution for the Earth's mantle through time is needed. Given the significant heterogeneity in modern convective upper mantle, it is difficult to use Os isotopic compositions to distinguish post-Archean peridotites from modern convective upper mantle. A robust statistical method must be established to determine how many random samples are required to distinguish a suite of Proterozoic or early Phanerozoic samples from modern convective upper mantle.

2. Lithospheric thinning and destruction of the North China Craton

In order to gain a better understanding of processes that led to lithospheric thinning and destruction of the eastern North China Craton, several future directions may be pursued. First, the original lithospheric mantle beneath the eastern North China Craton prior to the Mesozoic thinning is not well characterized, other than visa samples from three Ordovician kimberlite localities. Whether lithospheric mantle in other regions was the same as that sampled by the three Ordovician kimberlitic localities remains an open question. Whether this question can be addressed depends on whether similar or older volcanic centers bearing xenoliths exist and can be found.

Second, almost all of the mantle xenoliths carried in the Mesozoic-Cenozoic host magmas are garnet-free spinel peridotites/pyroxenites, and represent an already relatively thin or thinning lithosphere. The eruption ages of the magmas provide only a lower limit for the timing of lithospheric thinning in these regions. By contrast, mafic magmas derived from the mantle can provide the formation depth and reflect

the nature of the mantle source (e.g., Xu et al., 2009). Investigations of mantle-derived magmas that may or may not carry mantle xenoliths could provide additional significant constraints on the timing of lithospheric thinning.

Third, there is a need for dating additional samples from Fuxin and other Mesozoic-Cenozoic localities using Re-Os isotope systematics in order to determine the ages of peridotites present at these times. Because of the lack of garnet peridotites, it is difficult to determine whether there was a vertical composition and age stratification of lithospheric mantle that contains both refractory and fertile peridotites (both types of peridotites often have overlapping equilibration temperatures at P = 1.5 Ga, as the pressure-dependence of the thermometers are probably not large). Investigation of the vertical distribution for the two types of peridotites should be done in order to constrain the thinning process, as an age-stratified lithosphere would not be consistent with removal of lithosphere via delamination. Sampling fragments of the thinned or thinning lithospheric mantle (e.g., Gao et al., 2008) or mantle peridotites previously emplaced at crustal levels (Qian and Hermann, 2010) would lead to diverse interpretations for the origin of the peridotites. Consideration and evaluation of such scenarios would benefit our understanding of the thinning process.

Fourth, lithospheric thinning may be accompanied by the generation of melts that react with peridotites. The study of such melts preserved in peridotites (as veins; e.g., Chen and Zhou, 2006) or carrying peridotites (e.g., high-Mg adakites, diorites or basalts; Gao et al., 2008; W.L. Xu et al., 2008) would provide information on the nature and source of the melts (e.g., delaminated lower crust, or subducting slab),

which may, in turn, provide new insights into the processes and/or driving forces by which the lithosphere was removed and replaced.

Finally, previous studies tend to consider different processes proposed for lithospheric thinning and destruction of the North China Craton in isolation (e.g., Zheng et al., 2001; Zhang et al., 2003; Gao et al., 2004). Each of these processes is partially supported by preserved in a variety of rocks, although no one process can account for all observations. The possible connection of these processes in the destruction of the craton, as briefly mentioned above, needs to be systematically considered in a broader-scale, under ambient Phanerozoic geological events.

References:

Ackerman, L., Walker, R. J., Puchtel, I. S., Pitcher, L., Jelinek, E., and Strnad, L., 2009. Effects of melt percolation on highly siderophile elements and Os isotopes in subcontinental lithospheric mantle: A study of the upper mantle profile beneath Central Europe. Geochimica et Cosmochimica Acta, v. 73, p. 2400-2414.

Alard, O., Griffin, W. L., Lorand, J. P., Jackson, S. E., and O'Reilly, S. Y., 2000. Non-chondritic distribution of the highly siderophile elements in mantle sulphides. Nature, v. 407, p. 891-894.

Allegre, C. J., and Luck, J. M., 1980. Osmium Isotopes as Petrogenetic and Geological Tracers. Earth and Planetary Science Letters, v. 48, p. 148-154.

Arai, S., 1994. Characterization of Spinel Peridotites by Olivine Spinel Compositional Relationships - Review and Interpretation. Chemical Geology, v. 113, p. 191-204.

Arevalo, R., and McDonough, W. F., 2008. Tungsten geochemistry and implications for understanding the Earth's interior. Earth and Planetary Science Letters, v. 272, p. 656-665.

Ballhaus, C., Berry, R. F., and Green, D. H., 1990. Oxygen Fugacity Controls in the Earths Upper Mantle. Nature, v. 348, p. 437-440.

Ballhaus, C., Bockrath, C., Wohlgemuth-Ueberwasser, C., Laurenz, V., and Berndt, J., 2006. Fractionation of the noble metals by physical processes. Contributions to Mineralogy and Petrology, v. 152, p. 667-684.

Barnes, S.-J., van Achterbergh, E., Makovicky, E., and Li, C., 2001. Proton microprobe results for the partitioning of platinum-group elements between monosulphide solid solution and sulphide liquid. South African Journal of Geology, v. 104, p. 274-286.

Beard, B. L., and Johnson, C. M., 1993. Hf Isotope Composition of Late Cenozoic Basaltic Rocks from Northwestern Colorado, USA - New Constraints on Mantle Enrichment Processes. Earth and Planetary Science Letters, v. 119, p. 494-509.

Becker, H., Horan, M. F., Walker, R. J., Gao, S., Lorand, J. P., and Rudnick, R. L., 2006. Highly siderophile element composition of the Earth's primitive upper mantle: Constraints from new data on peridotite massifs and xenoliths. Geochimica et Cosmochimica Acta, v. 70, p. 4528-4550.

Bedard, L. P., Savard, D., and Barnes, S. J., 2008. Total sulfur concentration in geological reference materials by elemental infrared analyser. Geostandards and Geoanalytical Research, v. 32, p. 203-208.

Bedini, R. M., Blichert-Toft, J., Boyet, M., and Albarede, F., 2004. Isotopic constraints on the cooling of the continental lithosphere. Earth and Planetary Science Letters, v. 223, p. 99-111.

Bedini, R. M., and Bodinier, J. L., 1999. Distribution of incompatible trace elements between the constituents of spinel peridotite xenoliths: ICP-MS data from the East African Rift. Geochimica et Cosmochimica Acta, v. 63, p. 3883-3900.

Birck, J. L., RoyBarman, M., and Capmas, F., 1997. Re-Os isotopic measurements at the femtomole level in natural samples. Geostandards Newsletter-the Journal of Geostandards and Geoanalysis, v. 21, p. 19-27.

Bizimis, M., Griselin, M., Lassiter, J. C., Salters, V. J. M., and Sen, G., 2007. Ancient recycled mantle lithosphere in the Hawaiian plume: Osmium-Hafnium isotopic evidence from peridotite mantle xenoliths. Earth and Planetary Science Letters, v. 257, p. 259-273.

Bizimis, M., Sen, G., and Salters, V. J. M., 2004. Hf-Nd isotope decoupling in the oceanic lithosphere: constraints from spinel peridotites from Oahu, Hawaii. Earth and Planetary Science Letters, v. 217, p. 43-58.

Blichert-Toft, J., Ionov, D. A., and Albarede, F., 2000. The nature of the sub-continental lithospheric mantle: Hf isotope evidence from garnet peridotite xenoliths from Siberia. J. Conf. Abstr. 5, 217., v.

Bockrath, C., Ballhaus, C., and Holzheid, A., 2004. Fractionation of the platinum-group elements during mantle melting. Science, v. 305, p. 1951-1953.

Bouvier, A., Vervoort, J. D., and Patchett, P. J., 2008. The Lu-Hf and Sm-Nd isotopic composition of CHUR: Constraints from unequilibrated chondrites and implications for the bulk composition of terrestrial planets. Earth and Planetary Science Letters, v. 273, p. 48-57.

Boyd, F. R., 1989. Compositional distinction between oceanic and cratonic lithosphere. Earth and Planetary Science Letters, v. 96, p. 14-26.

Boyd, F. R., and Mertzman, S. A., 1987. Composition of structure of the Kaapvaal lithosphere, southern Africa. In: Magmatic Processes - Physicochemical Principles, B.O. Mysen, Ed., The Geochemical Society, Special Publication, v. 1.

Boyd, F. R., Pearson, D. G., Nixon, P. H., and Mertzman, S. A., 1993. Low-Calcium Garnet Harzburgites from Southern Africa - Their Relations to Craton Structure and Diamond Crystallization. Contributions to Mineralogy and Petrology, v. 113, p. 352-366.

Brandon, A. D., Snow, J. E., Walker, R. J., Morgan, J. W., and Mock, T. D., 2000. Pt-190-Os-186 and Re-187-Os-187 systematics of abyssal peridotites. Earth and Planetary Science Letters, v. 177, p. 319-335.

Brenan, J. M., 2008. Re-Os fractionation by sulfide melt-silicate melt partitioning: A new spin. Chemical Geology, v. 248, p. 140-165.

Brey, G. P., and Kohler, T., 1990. Geothermobarometry in four-phase lherzolites II: new thermobarometers, and practical assessment of existing thermobarometers. Journal of Petrology, v. 31, p. 1353-1378.

Büchl, A., Brugmann, G., Batanova, V. G., Münker, C., and Hofmann, A. W., 2002. Melt percolation monitored by Os isotopes and HSE abundances: a case study from the mantle section of the Troodos Ophiolite. Earth and Planetary Science Letters, v. 204, p. 384-402.

Büchl, A., Brugmann, G. E., Batanova, V. G., and Hofmann, A. W., 2004. Os mobilization during melt percolation: The evolution of Os isotope heterogeneities in the mantle sequence of the Troodos ophiolite, Cyprus. Geochimica et Cosmochimica Acta, v. 68, p. 3397-3408.

Carlson, R. W., and Irving, A. J., 1994. Depletion and Enrichment History of Subcontinental Lithospheric Mantle - an Os, Sr, Nd and Pb Isotopic Study of Ultramafic Xenoliths from the Northwestern Wyoming Craton. Earth and Planetary Science Letters, v. 126, p. 457-472.

Carlson, R. W., Irving, A. J., Schulze, D. J., and Hearn, B. C., 2004. Timing of Precambrian melt depletion and Phanerozoic refertilization events in the lithospheric mantle of the Wyoming Craton and adjacent Central Plains Orogen. Lithos, v. 77, p. 453-472.

Chauvel, C., and Blichert-Toft, J., 2001. A hafnium isotope and trace element perspective on melting of the depleted mantle. Earth and Planetary Science Letters, v. 190, p. 137-151.

Chen, L., 2010. Concordant structural variations from the surface to the base of the upper mantle in the North China Craton and its tectonic implications. Lithos, v. 120, p. 96-115.

Chen, S. H., O'Reilly, S. Y., Zhou, X. H., Griffin, W. L., Zhang, G. H., Sun, M., Feng, J. L., and Zhang, M., 2001. Thermal and petrological structure of the lithosphere beneath Hannuoba, Sino-Korean Craton, China: evidence from xenoliths. Lithos, v. 56, p. 267-301.

Chesley, J. T., Rudnick, R. L., and Lee, C. T., 1999. Re-Os systematics of mantle xenoliths from the East African Rift: Age, structure, and history of the Tanzanian craton. Geochimica et Cosmochimica Acta, v. 63, p. 1203-1217.

Choi, S. H., Mukasa, S. B., Zhou, X. H., Xian, X. H., and Andronikо, A. V., 2008. Mantle dynamics beneath East Asia constrained by Sr, Nd, Pb and Hf isotopic systematics of

ultramafic xenoliths and their host basalts from Hannuoba, North China. Chemical Geology, v. 248, p. 40-61.

Choi, S. H., Suzuki, K., Mukasa, S. B., Lee, J. I., and Jung, H., 2010. Lu-Hf and Re-Os systematics of peridotite xenoliths from Spitsbergen, western Svalbard: Implications for mantle-crust coupling. Earth and Planetary Science Letters, v. 297, p. 121-132.

Chu, Z. Y., Wu, F. Y., Walker, R. J., Rudnick, R. L., Pitcher, L., Puchtel, I. S., Yang, Y. H., and Wilde, S. A., 2009. Temporal Evolution of the Lithospheric Mantle beneath the Eastern North China Craton. Journal of Petrology, v. 50, p. 1857-1898.

Cohen, A. S., and Waters, F. G., 1996. Separation of osmium from geological materials by solvent extraction for analysis by thermal ionisation mass spectrometry. Analytica Chimica Acta, v. 332, p. 269-275.

Day, J. M. D., Pearson, D. G., and Hulbert, L. J., 2008. Rhenium-osmium isotope and platinum-group element constraints on the origin and evolution of the 1.27 Ga Muskox layered intrusion. Journal of Petrology, v. 49, p. 1254-1295.

Dong, C. Y., Liu, D. Y., Li, J. J., Wan, Y. S., Zhou, H. Y., Li, C. D., Yang, Y. H., and Xie, L. W., 2007. Palaeoproterozoic Khondalite Belt in the western North China Craton: New evidence from SHRIMP dating and Hf isotope composition of zircons from metamorphic rocks in the Bayan Ul-Helan Mountains area. Chinese Science Bulletin, v. 52, p. 2984-2994.

Eggins, S. M., Rudnick, R. L., and McDonough, W. F., 1998. The composition of peridotites and their minerals: a laser-ablation ICP-MS study. Earth and Planetary Science Letters, v. 154, p. 53-71.

Eggler, D. H., and Lorand, J. P., 1993. Mantle Sulfide Geobarometry. Geochimica et Cosmochimica Acta, v. 57, p. 2213-2222.

Elthon, D., 1992. Chemical Trends in Abyssal Peridotites - Refertilization of Depleted Suboceanic Mantle. Journal of Geophysical Research-Solid Earth, v. 97, p. 9014-9025.

Finnerty, A. A., and Boyd, F. R., 1987. Thermobarometry for garnet peridotites: basis for the determination of thermal and compositional structure of the upper mantle. In: P.H. Nixon (Editor), Mantle Xenoliths. John Wiley & Sons, Chichester, pp. 381-402. v.

Fleet, M. E., Stone, W. E., and Crocket, J. H., 1991. Partitioning of Palladium, Iridium, and Platinum between Sulfide Liquid and Basalt Melt - Effects of Melt Composition, Concentration, and Oxygen Fugacity. Geochimica et Cosmochimica Acta, v. 55, p. 2544-2554.

Fonseca, R. O. C., Campbell, I. H., O'Neill, H. S. C., and Fitzgerald, J. D., 2008. Oxygen solubility and speciation in sulphide-rich mattes. Geochimica et Cosmochimica Acta, v. 72, p. 2619-2635.

Frey, F. A., and Green, D. H., 1974. Mineralogy, Geochemistry and Origin of Ilherzolite Inclusions in Victorian Basanites. Geochimica et Cosmochimica Acta, v. 38, p. 1023-1059.

Gao, S., Rudnick, R. L., Carlson, R. W., McDonough, W. F., and Liu, Y. S., 2002. Re-Os evidence for replacement of ancient mantle lithosphere beneath the North China craton. Earth and Planetary Science Letters, v. 198, p. 307-322.

Gao, S., Rudnick, R. L., Xu, W. L., Yuan, H. L., Liu, Y. S., Walker, R. J., Puchtel, I. S., Liu, X. M., Huang, H., Wang, X. R., and Yang, J., 2008. Recycling deep cratonic lithosphere and generation of intraplate magmatism in the North China Craton. Earth and Planetary Science Letters, v. 270, p. 41-53.

Gao, S., Rudnick, R. L., Yuan, H. L., Liu, X. M., Liu, Y. S., Xu, W. L., Ling, W. L., Ayers, J., Wang, X. C., and Wang, Q. H., 2004. Recycling lower continental crust in the North China craton. Nature, v. 432, p. 892-897.

Griffin, W. L., Zhang, A. D., O'Reilly, S. Y., and Ryan, C. G., 1998. Phanerozoic evolution of the lithosphere beneath the Sino-Korean Craton. In: M. Flower, S.-L. Chung, C.-H. Lo and T.-Y. Lee (Editors). Mantle Dynamics and Plate Interactions in East Asia.

American Geophysical Union, Washington, D.C. Geodynamics Series, v. 27, p. 107-126.

Handler, M. R., and Bennett, V. C., 1999. Behaviour of Platinum-group elements in the subcontinental mantle of eastern Australia during variable metasomatism and melt depletion. Geochimica et Cosmochimica Acta, v. 63, p. 3597-3618.

Handler, M. R., Bennett, V. C., and Dreibus, G., 1999. Evidence from correlated Ir/Os and Cu/S for late-stage Os mobility in peridotite xenoliths: Implications for Re-Os systematics. Geology, v. 27, p. 74-78.

Handler, M. R., Bennett, V. C., and Esat, T. M., 1997. The persistence of off-cratonic lithospheric mantle: Os isotopic systematics of variably metasomatised southeast Australian xenoliths. Earth and Planetary Science Letters, v. 151, p. 61-75.

Hart, S. R., 1984. A Large-Scale Isotope Anomaly in the Southern-Hemisphere Mantle. Nature, v. 309, p. 753-757.

Hart, S. R., and Ravizza, G., 1996. Os partitioning between phases in lherzolite and basalt. Isotopic Studies of Crust-mantle Evolution , AGU Monograph, v. 95, p. 123-134.

Harvey, J., Gannoun, A., Burton, K. W., Rogers, N. W., Alard, O., and Parkinson, I. J., 2006. Ancient melt extraction from the oceanic upper mantle revealed by Re-Os isotopes in abyssal peridotites from the Mid-Atlantic ridge. Earth and Planetary Science Letters, v. 244, p. 606-621.

Hofmann, A. W., 2003. Sampling mantle heterogeneity through oceanic basalts: isotopes and trace elements. . In: Carlson, R.W. (Editor). The mantle and core, volume 2 of Treatise on Geochemistry (Turekian, K.K. and Holland, H.D., eds.), Oxford, Elsevier-Pergamon, p. 61–101.

Horan, M. F., Walker, R. J., Morgan, J. W., Grossman, J. N., and Rubin, A. E., 2003. Highly siderophile elements in chondrites. Chemical Geology, v. 196, p. 4-20.

Hu, S. B., He, L. J., and Wang, J. Y., 2000. Heat flow in the continental area of China: a new data set. Earth and Planetary Science Letters, v. 179, p. 407-419.

Huang, F., S. G. Li, S. G., and Yang, W., 2007. Contributions of the lower crust to Mesozoic mantle-derived mafic rocks from the North China Craton; implications for lithospheric thinning (in Mesozoic sub-continental lithospheric thinning under eastern Asia). Geological Society Special Publications, v. 280, p. 55-75.

Huang, J. L., and Zhao, D. P., 2006. High-resolution mantle tomography of China and surrounding regions. Journal of Geophysical Research-Solid Earth, v. 111.

Huang, J. Q., 1977. The basic outline of China tectonics. Acta Geol. Sin., v. 52, 117–135.

Ionov, D. A., Ashchepkov, I., and Jagoutz, E., 2005a. The provenance of fertile off-craton lithospheric mantle: Sr-Nd isotope and chemical composition of garnet and spinel peridotite xenoliths from Vitim, Siberia. Chemical Geology, v. 217, p. 41-75.

Ionov, D. A., Blichert-Toft, J., and Weis, D., 2005b. Hf isotope compositions and HREE variations in off-craton garnet and spinel peridotite xenoliths from central Asia. Geochimica et Cosmochimica Acta, v. 69, p. 2399-2418.

Ionov, D. A., Prikhodko, V. S., and Oreilly, S. Y., 1995. Peridotite Xenoliths in Alkali Basalts from the Sikhote-Alin, Southeastern Siberia, Russia - Trace-Element Signatures of Mantle beneath a Convergent Continental-Margin. Chemical Geology, v. 120, p. 274-294.

Ionov, D. A., Shirey, S. B., Weis, D., and Brugmann, G., 2006. Os-Hf-Sr-Nd isotope and PGE systematics of spinel peridotite xenoliths from Tok, SE Siberian craton: Effects of pervasive metasomatism in shallow refractory mantle. Earth and Planetary Science Letters, v. 241, p. 47-64.

Ireland, T. J., Walker, R. J., and Garcia, M. O., 2009. Highly siderophile element and Os-187 isotope systematics of Hawaiian picrites: Implications for parental melt composition and source heterogeneity. Chemical Geology, v. 260, p. 112-128.

Johnson, K. T. M., Dick, H. J. B., and Shimizu, N., 1990. Melting in the Oceanic Upper Mantle - an Ion Microprobe Study of Diopsides in Abyssal Peridotites. Journal of Geophysical Research-Solid Earth and Planets, v. 95, p. 2661-2678.

Jordan, T. H., 1988. Structure and formation of the continental lithosphere. In: M.A. Menzies and K. Cox (Editors), Oceanic and Continental Lithosphere; similarities and differences. J. Petrol., Special Lithosphere Issue, pp. 11-37.

Kay, R. W., and Kay, S. M., 1993. Delamination and Delamination Magmatism. Tectonophysics, v. 219, p. 177-189.

Klein, F., and Bach, W. G., 2009. FeNiCoOS Phase Relations in PeridotiteSeawater Interactions. Journal of Petrology, v. 50, p. 37-59.

Kroner, A., Wilde, S. A., Li, J. H., and Wang, K. Y., 2005. Age and evolution of a late Archean to Paleoproterozoic upper to lower crustal section in the Wutaishan/Hengshan/Fuping terrain of northern China. Journal of Asian Earth Sciences, v. 24, p. 577-595.

Kroner, A., Wilde, S. A., Zhao, G. C., O'Brien, P. J., Sun, M., Liu, D. Y., Wan, Y. S., Liu, S. W., and Guo, J. H., 2006. Zircon geochronology and metamorphic evolution of mafic dykes in the Hengshan Complex of northern China: Evidence for late Palaeoproterozoic extension and subsequent high-pressure metamorphism in the North China Craton. Precambrian Research, v. 146, p. 44-67.

Kullerud, G., Yund, R. A., and Moh, G. H., 1969. Phase relation in the Cu–Fe–Ni, Cu–Ni–S and Fe–Ni–S systems. Economic Geology, v. 4, p. 323–343.

Kusky, T., Li, J. G., and Santosh, M., 2007a. The Paleoproterozoic North Hebei orogen: North China craton's collisional suture with the Columbia supercontinent. Gondwana Research, v. 12, p. 4-28.

Kusky, T. M., and Li, J. H., 2003. Paleoproterozoic tectonic evolution of the North China Craton. Journal of Asian Earth Sciences, v. 22, p. 383-397.

Kusky, T. M., and Li, J. H., 2010. Origin and Emplacement of Archean Ophiolites of the Central Orogenic Belt, North China Craton. Journal of Earth Science, v. 21, p. 744-781.

Kusky, T. M., Zhi, X. C., Li, J. H., Xia, Q. X., Raharimahefa, T., and Huang, X. N., 2007b. Chondritic osmium isotopic composition of Archean ophiolitic mantle, North China craton. Gondwana Research, v. 12, p. 67-76.

Le Roux, V., Bodinier, J. L., Tommasi, A., Alard, O., Dautria, J. M., Vauchez, A., and Riches, A. J. V., 2007. The Lherz spinel lherzolite: Refertilized rather than pristine mantle. Earth and Planetary Science Letters, v. 259, p. 599-612.

Lee, C. T., Yin, Q. Z., Rudnick, R. L., Chesley, J. T., and Jacobsen, S. B., 2000. Osmium isotopic evidence for mesozoic removal of lithospheric mantle beneath the Sierra Nevada, California. Science, v. 289, p. 1912-1916.

Lee, C. T. A., 2002. Platinum-group element geochemistry of peridotite xenoliths from the Sierra Nevada and the Basin and Range, California. Geochimica et Cosmochimica Acta, v. 66, p. 3987-4005.

Li, C., Barnes, S. J., Makovicky, E., RoseHansen, J., and Makovicky, M., 1996. Partitioning of nickel, copper, iridium, rhenium, platinum, and palladium between monosulfide solid solution and sulfide liquid: Effects of composition and temperature. Geochimica et Cosmochimica Acta, v. 60, p. 1231-1238.

Li, C., van der Hilst, R. D., and Toksoz, A. N., 2006. Constraining P-wave velocity variations in the upper mantle beneath Southeast Asia. Physics of the Earth and Planetary Interiors, v. 154, p. 180-195.

Liu, C. Z., Snow, J. E., Brugmann, G., Hellebrand, E., and Hofmann, A. W., 2009. Non-chondritic HSE budget in Earth's upper mantle evidenced by abyssal peridotites from Gakkel ridge (Arctic Ocean). Earth and Planetary Science Letters, v. 283, p. 122-132.

Liu, C. Z., Snow, J. E., Hellebrand, E., Brugmann, G., von der Handt, A., Buchl, A., and Hofmann, A. W., 2008. Ancient, highly heterogeneous mantle beneath Gakkel ridge, Arctic Ocean. Nature, v. 452, p. 311-316.

Liu, J. G., Rudnick, R. L., Walker, R. J., Gao, S., Wu, F. Y., and Piccoli, P. M., 2010. Processes controlling highly siderophile element fractionations in xenolithic peridotites and their influence on Os isotopes. Earth and Planetary Science Letters, v. 297, p. 287-297.

Liu, J., Rudnick, R. L., Walker, R. J., Gao, S., Wu, F.-y., Piccoli, P. M., Yuan, H., Xu, W.-l., and Xu, Y.-G., 2011a. Mapping lithospheric boundaries using Os isotopes of mantle xenoliths: An example from the North China Craton. Geochimica et Cosmochimica Acta, v. 75, p. 3881-3902.

Liu, J., Carlson, R.W., Rudnick, R. L., Walker, R. W., Wu, F.-y., and Gao, S., 2011b. Comparative Sr-Nd-Hf-Os-Pb isotopic systematics of xenolithic peridotites from Yangyuan, North China Craton. Goldschmidt Conference. Prague, Czech Republic.

Liu, R., Chen, W., Sun, J., and Li, D., 1992. The K–Ar age and tectonic environment of Cenozoic volcanic rock in China. In: Liu, R., Editor, 1992. The Age and Geochemistry of Cenozoic Volcanic Rock in China, Seismology Published House, Beijing, v., p. 1-43.

Li, S., Xiao, Y., Liou, D., Chen, Y., Ge, N., Zhang, Z., Sun, S.-S., Cong, B., Zhang, R., Hart, S. R., and Wang, S., 1993, Collision of the North China and Yangtse Blocks and formation of coesite-bearing eclogites: Timing and processes: Chemical Geology, v. 109, p. 89-111.

Li, Z. X., and Li, X. H., 2007. Formation of the 1300-km-wide intracontinental orogen and postorogenic magmatic province in Mesozoic South China: A flat-slab subduction model. Geology, v. 35, p. 179-182.

Lorand, J. P., Alard, O., and Godard, M., 2009. Platinum-group element signature of the primitive mantle rejuvenated by melt-rock reactions: evidence from Sumail peridotites (Oman Ophiolite). Terra Nova, v. 21, p. 34-40.

Lorand, J. P., Alard, O., and Luguet, A., 2010. Platinum-group element micronuggets and refertilization process in Lherz orogenic peridotite (northeastern Pyrenees, France). Earth and Planetary Science Letters, v. 289, p. 298-310.

Lorand, J. P., Alard, O., Luguet, A., and Keays, R. R., 2003a. Sulfur and selenium systematics of the subcontinental lithospheric mantle: Inferences from the Massif Central xenolith suite (France). Geochimica et Cosmochimica Acta, v. 67, p. 4137-4151.

Lorand, J. P., Luguet, A., and Alard, O., 2008a. Platinum-group elements: A new set of key tracers for the earth's interior. Elements, v. 4, p. 247-252.

Lorand, J. P., Luguet, A., Alard, O., Bezos, A., and Meisel, T., 2008b. Abundance and distribution of platinum-group elements in orogenic lherzolites; a case study in a Fontete Rouge lherzolite (French Pyrenees). Chemical Geology, v. 248, p. 174-194.

Lorand, J. P., Reisberg, L., and Bedini, R. M., 2003b. Platinum-group elements and melt percolation processes in Sidamo spinel peridotite xenoliths, Ethiopia, East African Rift. Chemical Geology, v. 196, p. 57-75.

Lu, F.X., Zheng, J.P., Zhang, R.S., and Chen, M.H., 2005. Phanerozoic mantle secular evolution beneath the eastern North China Craton. Earth Science Frontiers, v. 12, p. 61-67.

Lu, L. Z., Xu, X. C., and Liu, F. L., 1996. Early Precambrian Khondalite Series of North China. Changchun Publishing House, v. Changchun, p. 1-272.

Luguet, A., Lorand, J. P., and Seyler, M., 2003. Sulfide petrology and highly siderophile element geochemistry of abyssal peridotites: A coupled study of samples from the Kane

Fracture Zone (45 degrees W 23 degrees 20N, MARK Area, Atlantic Ocean). Geochimica et Cosmochimica Acta, v. 67, p. 1553-1570.

Luguet, A., Shirey, S. B., Lorand, J. P., Horan, M. F., and Carlson, R. W., 2007. Residual platinum-group minerals from highly depleted harzburgites of the Lherz massif (France) and their role in HSE fractionation of the mantle. Geochimica et Cosmochimica Acta, v. 71, p. 3082-3097.

Lyubetskaya, T., and Korenaga, J., 2007. Chemical composition of Earth's primitive mantle and its variance: 1. Method and results. Journal of Geophysical Research-Solid Earth, v. 112.

Ma, J. L., and Xu, Y. G., 2004. Petrology and geochemistry of the Cenozoic Basalts from Yangyuan of Hebei Province and Datong of Shanxi Province: implications for the deep process in the Western North China Craton. Geochimica, v. 33, p. 74-88.

Ma, X. Y., and Wu, Z. W., 1981. Early tectonic evolution of China. Precambrian Res. 14, 185–202. v.

McDonough, W. F., 1990. Constraints on the Composition of the Continental Lithospheric Mantle. Earth and Planetary Science Letters, v. 101, p. 1-18.

Mcdonough, W. F., and Frey, F. A., 1989. Rare-Earth Elements in Upper Mantle Rocks. Reviews in Mineralogy, v. 21, p. 99-145.

McDonough, W. F., and Mcculloch, M. T., 1987. The Southeast Australian Lithospheric Mantle - Isotopic and Geochemical Constraints on Its Growth and Evolution. Earth and Planetary Science Letters, v. 86, p. 327-340.

McDonough, W. F., Stosch, H. G., and Ware, N. G., 1992. Distribution of Titanium and the Rare-Earth Elements between Peridotitic Minerals. Contributions to Mineralogy and Petrology, v. 110, p. 321-328.

McDonough, W. F., and Sun, S. S., 1995. The Composition of the Earth. Chemical Geology, v. 120, p. 223-253.

Meibom, A., Sleep, N. H., Chamberlain, C. P., Coleman, R. G., Frei, R., Hren, M. T., and Wooden, J. L., 2002. Re-Os isotopic evidence for long-lived heterogeneity and equilibration processes in the Earth's upper mantle. Nature, v. 419, p. 704-708.

Meisel, T., and Moser, J., 2004. Reference materials for geochemical PGE analysis: new analytical data for Ru, Rh, Pd, Os, Ir, Pt and Re by isotope dilution ICP-MS in 11 geological reference materials. Chemical Geology, v. 208, p. 319-338.

Meisel, T., Reisberg, L., Moser, J., Carignan, J., Melcher, F., and Brugmann, G., 2003. Re-Os systematics of UB-N, a serpentinized peridotite reference material. Chemical Geology, v. 201, p. 161-179.

Meisel, T., Walker, R. J., Irving, A. J., and Lorand, J. P., 2001. Osmium isotopic compositions of mantle xenoliths: A global perspective. Geochimica et Cosmochimica Acta, v. 65, p. 1311-1323.

Menzies, M., and Chazot, G., 1995. Fluid Processes in Diamond to Spinel Facies Shallow Mantle. Journal of Geodynamics, v. 20, p. 387-415.

Menzies, M., Xu, Y. G., Zhang, H. F., and Fan, W. M., 2007. Integration of geology, geophysics and geochemistry: A key to understanding the North China Craton. Lithos, v. 96, p. 1-21.

Menzies, M. A., Fan, W.-M., and Zhang, M., 1993. Paleozoic and Cenozoic lithoprobes and the loss of >120 km of Archean lithosphere, Sino-Korean craton, China. In: H.M. Prichard, H.M. Alabaster, T. Harris and C.R. Neary (Editors), Magmatic Processes and Plate Tectonics., Geological Soc., London, p. 71-81.

Menzies, M. A., and Hawkesworth, C. J., 1987. Mantle metasomatism. Academic Press, London, 472pp.

Morency, C., Doin, M. P., and Dumoulin, C., 2002. Convective destabilization of a thickened continental lithosphere. Earth and Planetary Science Letters, v. 202, p. 303-320.

Morgan, J. W., 1986. Ultramafic Xenoliths - Clues to Earths Late Accretionary History. Journal of Geophysical Research-Solid Earth and Planets, v. 91, p. 2374-2387.

Morgan, J. W., Walker, R. J., Brandon, A. D., and Horan, M. F., 2001. Siderophile elements in Earth's upper mantle and lunar breccias: Data synthesis suggests manifestations of the same late influx. Meteoritics & Planetary Science, v. 36, p. 1257-1275.

Mungall, J. E., Hanley, J. J., Arndt, N. T., and Debecdelievre, A., 2006. Evidence from meimechites and other low-degree mantle melts for redox controls on mantle-crust fractionation of platinum-group elements. Proceedings of the National Academy of Sciences of the United States of America, v. 103, p. 12694-12700.

Nixon, P. H., Rogers, N. W., Gibson, I. L., and Grey, A., 1981. Depleted and Fertile Mantle Xenoliths from Southern African Kimberlites. Annual Review of Earth and Planetary Sciences, v. 9, p. 284-309.

Norman, M. D., 1998. Melting and metasomatism in the continental lithosphere: laser ablation ICPMS analysis of minerals in spinel lherzolites from eastern Australia. Contributions to Mineralogy and Petrology, v. 130, p. 240-255.

Nowell, G. M., Kempton, P. D., Noble, S. R., Fitton, J. G., Saunders, A. D., Mahoney, J. J., and Taylor, R. N., 1998. High precision Hf isotope measurements of MORB and OIB by thermal ionisation mass spectrometry: insights into the depleted mantle. Chemical Geology, v. 149, p. 211-233.

Parkinson, I. J., Hawkesworth, C. J., and Cohen, A. S., 1998. Ancient mantle in a modern arc: Osmium isotopes in Izu-Bonin-Mariana forearc peridotites. Science, v. 281, p. 2011-2013.

Pearson, D. G., Carlson, R. W., Shirey, S. B., Boyd, F. R., and Nixon, P. H., 1995a. Stabilization of Archean Lithospheric Mantle - a Re-Os Isotope Study of Peridotite Xenoliths from the Kaapvaal Craton. Earth and Planetary Science Letters, v. 134, p. 341-357.

Pearson, D. G., Shirey, S. B., Carlson, R. W., Boyd, F. R., Pokhilenko, N. P., and Shimizu, N., 1995b. Re-Os, Sm-Nd, and Rb-Sr Isotope Evidence for Thick Archean Lithospheric Mantle beneath the Siberian Craton Modified by Multistage Metasomatism. Geochimica et Cosmochimica Acta, v. 59, p. 959-977.

Pearson, D. G., and Nowell, G. M., 2003. Dating mantle differentiation: a comparison of the Lu−Hf, Re−Os and Sm−Nd isotope systems in the Beni Bousera peridotite massif and constraints on the Nd−Hf composition of the lithospheric mantle. Geophys. Res. 05430 Abstracts 5.

Pearson, D. G., Irvine, G. J., Ionov, D. A., Boyd, F. R., and Dreibus, G. E., 2004. Re-Os isotope systematics and platinum group element fractionation during mantle melt extraction: a study of massif and xenolith peridotite suites. Chemical Geology, v. 208, p. 29-59.

Pearson, D. G., and Wittig, N., 2008. Formation of Archaean continental lithosphere and its diamonds: the root of the problem. Journal of the Geological Society, v. 165, p. 894-914.

Pearson, N. J., Alard, O., Griffin, W. L., Jackson, S. E., and O'Reilly, S. Y., 2002. In situ measurement of Re-Os isotopes in mantle sulfides by laser ablation multicollector-inductively coupled plasma mass spectrometry: Analytical methods and preliminary results. Geochimica et Cosmochimica Acta, v. 66, p. 1037-1050.

Peregoedova, A., Barnes, S. J., and Baker, D. R., 2004. The formation of Pt-Ir alloys and Cu-Pd-rich sulfide melts by partial desulfurization of Fe-Ni-Cu sulfides: results of experiments and implications for natural systems. Chemical Geology, v. 208, p. 247-264.

Peregoedova, A., Barnes, S. J., and Baker, D. R., 2006. An experimental study of mass transfer of platinum-group elements, gold, nickel and copper in sulfur-dominated vapor at magmatic temperatures. Chemical Geology, v. 235, p. 59-75.

Pollack, H. N., and Chapman, D. S., 1977. Regional variation of heat-flow, geotherms, and lithospheric thickness. Tectonophysics, v. 38, p. 279-296.

Puchtel, I., and Humayun, M., 2000. Platinum group elements in Kostomuksha komatiites and basalts: Implications for oceanic crust recycling and core-mantle interaction. Geochimica et Cosmochimica Acta, v. 64, p. 4227-4242.

Puchtel, I. S., and Humayun, M., 2005. Highly siderophile element geochemistry of Os-187-enriched 2.8 ga kostomuksha komatiites, Baltic shield. Geochimica et Cosmochimica Acta, v. 69, p. 1607-1618.

Puchtel, I. S., Walker, R. J., James, O. B., and Kring, D. A., 2008. Osmium isotope and highly siderophile element systematics of lunar impact melt breccias: Implications for the late accretion history of the Moon and Earth. Geochimica et Cosmochimica Acta, v. 72, p. 3022-3042.

Qian, Q., and Hermann, J., 2010. Formation of High-Mg Diorites through Assimilation of Peridotite by Monzodiorite Magma at Crustal Depths. Journal of Petrology, v. 51, p. 1381-1416.

Rehkämper, M., Halliday, A. N., Fitton, J. G., Lee, D. C., Wieneke, M., and Arndt, N. T., 1999. Ir, Ru, Pt, and Pd in basalts and komatiites: New constraints for the geochemical behavior of the platinum-group elements in the mantle. Geochimica et Cosmochimica Acta, v. 63, p. 3914-3934.

Reisberg, L., and Lorand, J. P., 1995. Longevity of Sub-Continental Mantle Lithosphere from Osmium Isotope Systematics in Orogenic Peridotite Massifs. Nature, v. 376, p. 159-162.

Reisberg, L., Zhi, X. C., Lorand, J. P., Wagner, C., Peng, Z. C., and Zimmermann, C., 2005. Re-Os and S systematics of spinel peridotite xenoliths from east central China: Evidence for contrasting effects of melt percolation. Earth and Planetary Science Letters, v. 239, p. 286-308.

Ritsema, J., Nyblade, A. A., Owens, T. J., Langston, C. A., and VanDecar, J. C., 1998. Upper mantle seismic velocity structure beneath Tanzania, east Africa: Implications for the stability of cratonic lithosphere. Journal of Geophysical Research-Solid Earth, v. 103, p. 21201-21213.

Rudnick, R. L., Gao, S., Yuan, H. L., Puchtel, I. S., and Walker, R. J., 2006. Persistence of Paleoproterozoic lithospheric mantle in the Central Zone of the North China Craton. Abstract for the International Conference on Continental Volcanism-IAVCEI, Guangzhou, China.

Rudnick, R. L., McDonough, W. F., and O'Connell, R. J., 1998. Thermal structure, thickness and composition of continental lithosphere. Chemical Geology, v. 145, p. 394-411.

Rudnick, R. L., Shan, G., Ling, W. L., Liu, Y. S., and McDonough, W. F., 2004. Petrology and geochemistry of spinel peridotite xenoliths from Hannuoba and Qixia, North China craton. Lithos, v. 77, p. 609-637.

Rudnick, R. L., and Walker, R. J., 2009. Interpreting ages from Re–Os isotopes in peridotites Lithos, v. 112S, p. 1083-1095.

Saal, A. E., Takazawa, E., Frey, F. A., Shimizu, N., and Hart, S. R., 2001. Re-Os isotopes in the Horoman peridotite: Evidence for refertilization? Journal of Petrology, v. 42, p. 24-37.

Salters, V. J. M., and Zindler, A., 1995. Extreme Hf-176 Hf-177 in the Sub-Oceanic Mantle. Earth and Planetary Science Letters, v. 129, p. 13-30.

Santosh, M., Sajeev, K., and Li, J. H., 2006. Extreme crustal metamorphism during Columbia supercontinent assembly: Evidence from North China Craton. Gondwana Research, v. 10, p. 256-266.

Santosh, M., Wilde, S. A., and Li, J. H., 2007. Timing of Paleoproterozoic ultrahigh-temperature metamorphism in the North China Craton: Evidence from SHRIMP U-Pb zircon geochronology. Precambrian Research, v. 159, p. 178-196.

Savard, D., Bedard, L. P., and Barnes, S. J., 2006. TCF selenium preconcentration in geological materials for determination at sub-mu gg(-1) with INAA (Se/TCF-INAA). Talanta, v. 70, p. 566-571.

Scherer, E., Munker, C., and Mezger, K., 2001. Calibration of the lutetium-hafnium clock. Science, v. 293, p. 683-687.

Scherer, E. E., Cameron, K. L., and Blichert-Toft, J., 2000. Lu-Hf garnet geochronology: Closure temperature relative to the Sm-Nd system and the effects of trace mineral inclusions. Geochimica et Cosmochimica Acta, v. 64, p. 3413-3432.

Schmidberger, S. S., and Francis, D., 2001. Constraints on the trace element composition of the Archean mantle root beneath Somerset Island, Arctic Canada. Journal of Petrology, v. 42, p. 1094-1117.

Schmidberger, S. S., Simonetti, A., Francis, D., and Gariepy, C., 2002. Probing Archean lithosphere using the Lu-Hf isotope systematics of peridotite xenoliths from Somerset Island kimberlites, Canada. Earth and Planetary Science Letters, v. 197, p. 244-259.

Shen, Q. H., and Qian, X. L., 1995. Archean rock assemblages, episodes and tectonic evolution of China. Acta Geol. Sin. 2, 113–120. v.

Shirey, S. B., and Walker, R. J., 1998. The Re-Os isotope system in cosmochemistry and high-temperature geochemistry. Annual Review of Earth and Planetary Sciences, v. 26, p. 423-500.

Snow, J. E., and Schmidt, G., 1998. Constraints on Earth accretion deduced from noble metals in the oceanic mantle. Nature, v. 391, p. 166-169.

Song, Y., and Frey, F. A., 1989. Geochemistry of Peridotite Xenoliths in Basalt from Hannuoba, Eastern China - Implications for Subcontinental Mantle Heterogeneity. Geochimica et Cosmochimica Acta, v. 53, p. 97-113.

Standish, J. J., Hart, S. R., Blusztajn, J., Dick, H. J. B., and Lee, K. L., 2002. Abyssal peridotite osmium isotopic compositions from Cr-spinel. Geochemistry Geophysics Geosystems, v. 3.

Stosch, H. G., and Seck, H. A., 1980. Geochemistry and Mineralogy of 2 Spinel Peridotite Suites from Dreiser-Weiher, West-Germany. Geochimica et Cosmochimica Acta, v. 44, p. 457-470.

Sun, S.-s., and McDonough, W. F., 1989. Chemical and isotopic systematics of oceanic basalts: implications for mantle composition and processes. Geological Society, London, Special Publications, v. 42, p. 313-345.

Sun, W. D., Ding, X., Hu, Y. H., and Li, X. H., 2007. The golden transformation of the Cretaceous plate subduction in the west Pacific. Earth and Planetary Science Letters, v. 262, p. 533-542.

Szabo, C., and Bodnar, R. J., 1995. Chemistry and Origin of Mantle Sulfides in Spinel Peridotite Xenoliths from Alkaline Basaltic Lavas, Nograd-Gomor Volcanic Field, Northern Hungary and Southern Slovakia. Geochimica et Cosmochimica Acta, v. 59, p. 3917-3927.

Tanaka, T., Togashi, S., Kamioka, H., Amakawa, H., Kagami, H., Hamamoto, T., Yuhara, M., Orihashi, Y., Yoneda, S., Shimizu, H., Kunimaru, T., Takahashi, K., Yanagi, T., Nakano, T., Fujimaki, H., Shinjo, R., Asahara, Y., Tanimizu, M., and Dragusanu, C., 2000. JNdi-1: a neodymium isotopic reference in consistency with LaJolla neodymium. Chemical Geology, v. 168, p. 279-281.

Tang, Y. H., Zhang, H. F., Ying, J. F., Zhang, J., and Liu, X. M., 2008. Refertilization of ancient lithospheric mantle beneath the central North China Craton: Evidence from petrology and geochemistry of peridotite xenoliths. Lithos, v. 101, p. 434-452.

Tang, Y. J., Zhang, H. F., Nakamura, E., Moriguti, T., Kobayashi, K., and Ying, J. F., 2007. Lithium isotopic systematics of peridotite xenoliths from Hannuoba, North China

Craton: Implications for melt-rock interaction in the considerably thinned lithospheric mantle. Geochimica et Cosmochimica Acta, v. 71, p. 4327-4341.

Tao, W., and Shen, Z. K., 2008. Heat flow distribution in Chinese continent and its adjacent areas. Progress in Natural Science, v. 18, p. 843-849.

Tian, Y., Zhao, D. P., Sun, R. M., and Teng, J. W., 2009. Seismic imaging of the crust and upper mantle beneath the North China Craton. Physics of the Earth and Planetary Interiors, v. 172, p. 169-182.

Todt, W., Cliff, R. A., Hanser, A., and Hofmann, A. W., 1996. Evaluation of a 202Pb-205Pb double spike for high precision lead isotope analysis. In: Hart, S.R., Basu, A. (Eds.), Earth Processes: Reading the Isotope Code. Amer. Geophys. Union, Washington, pp. 429-437.

Tomurtugoo., Windley, B. F., Kroner, A., Badarch, G. & Liu, D. Y. 2005. Zircon age and occurrence of the Adaatsag ophiolite and Muron shear zone, central Mongolia: constraints on the evolution of the Mongol–Okhatsk ocean, suture and orogen. Journal of the Geological Society, London, v. 162, p. 125–134.

Van Orman, J. A., Grove, T. L., and Shimizu, N., 2001. Rare earth element diffusion in diopside: influence of temperature, pressure, and ionic radius, and an elastic model for diffusion in silicates. Contributions to Mineralogy and Petrology, v. 141, p. 687-703.

Walker, R. J., Shirey, S. B., Hanson, G. N., Rajamani, V., and Horan, M. F., 1989. Re-Os, Rb-Sr, and O Isotopic Systematics of the Archean Kolar Schist Belt, Karnataka, India. Geochimica et Cosmochimica Acta, v. 53, p. 3004-3013.

Wan, Y. S., Song, B., Liu, D. Y., Wilde, S. A., Wu, J. S., Shi, Y. R., Yin, X. Y., and Zhou, H. Y., 2006. SHRIMP U-Pb zircon geochronology of Palaeoproterozoic metasedimentary rocks in the North China Craton: Evidence for a major Late Palaeoproterozoic tectonothermal event. Precambrian Research, v. 149, p. 249-271.

Wilde, S. A., Zhao, G. C., and Sun, M., 2002. Development of the North China Craton during the late Archaean and its final amalgamation at 1.8 Ga: Some speculations on its position within a global Palaeoproterozoic supercontinent. Gondwana Research, v. 5, p. 84-94.

Witt-Eickschen, G., and O'Neill, H. S. C., 2005. The effect of temperature on the equilibrium distribution of trace elements between clinopyroxene, orthopyroxene, olivine and spinel in upper mantle peridotite. Chemical Geology, v. 221, p. 64-101.

Wittig, N., Baker, J. A., and Downes, H., 2006. Dating the mantle roots of young continental crust. Geology, v. 34, p. 237-240.

Wittig, N., Baker, J. A., and Downes, H., 2007. U-Th-Pb and Lu-Hf isotopic constraints on the evolution of sub-continental lithospheric mantle, French Massif Central. Geochimica et Cosmochimica Acta, v. 71, p. 1290-1311.

Wood, S. A., 1987. Thermodynamic Calculations of the Volatility of the Platinum Group Elements (Pge) - the Pge Content of Fluids at Magmatic Temperatures. Geochimica et Cosmochimica Acta, v. 51, p. 3041-3050.

Wu, F. Y., Lin, J. Q., Wilde, S. A., Zhang, X. O., and Yang, J. H., 2005a. Nature and significance of the Early Cretaceous giant igneous event in eastern China. Earth and Planetary Science Letters, v. 233, p. 103-119.

Wu, F., Zhao, G., Wilde, S. A., and Sun, D., 2005b. Nd isotopic constraints on crustal formation in the North China Craton. Journal of Asian Earth Sciences, v. 24, p. 523-545.

Wu, F. Y., Walker, R. J., Ren, X. W., Sun, D. Y., and Zhou, X. H., 2003. Osmium isotopic constraints on the age of lithospheric mantle beneath northeastern China. Chemical Geology, v. 196, p. 107-129.

Wu, F. Y., Walker, R. J., Yang, Y. H., Yuan, H. L., and Yang, J. H., 2006. The chemical-temporal evolution of lithospheric mantle underlying the North China Craton. Geochimica et Cosmochimica Acta, v. 70, p. 5013-5034.

Xiao, W. J., Windley, B. F., Hao, J., and Zhai, M. G., 2003. Accretion leading to collision and the Permian Solonker suture, Inner Mongolia, China: Termination of the central Asian orogenic belt. Tectonics, v. 22(6), 1069.

Xu, J. W., Zhu, G., Tong, W. X., Cui, K. R., and Liu, Q., 1987. Formation and Evolution of the Tancheng-Lujiang Wrench Fault System - a Major Shear System to the Northwest of the Pacific-Ocean. Tectonophysics, v. 134, p. 273-310.

Xu, W. L., Gao, S., Wang, Q. H., Wang, D. Y., and Liu, Y. S., 2006. Mesozoic crustal thickening of the eastern North China craton: Evidence from eclogite xenoliths and petrologic implications. Geology, v. 34, p. 721-724.

Xu, W. L., Yang, D. B., Gao, S., Pei, F. P., and Yu, Y., 2010. Geochemistry of peridotite xenoliths in Early Cretaceous high-Mg# diorites from the Central Orogenic Block of the North China Craton: The nature of Mesozoic lithospheric mantle and constraints on lithospheric thinning. Chemical Geology, v. 270, p. 257-273.

Xu, X. S., Griffin, W. L., O'Reilly, S. Y., Pearson, N. J., Geng, H. Y., and Zheng, J. P., 2008. Re-Os isotopes of sulfides in mantle xenoliths from eastern China: Progressive modification of lithospheric mantle. Lithos, v. 102, p. 43-64.

Xu, Y. G., Blusztajn, J., Ma, J. L., Suzuki, K., Liu, J. F., and Hart, S. R., 2008. Late Archean to early proterozoic lithospheric mantle beneath the western North China craton: Sr-Nd-Os isotopes of peridotite xenoliths from Yangyuan and Fansi. Lithos, v. 102, p. 24-42.

Xu, Y.G., Li, H.Y., Pang, C.J, and He, B., 2009. On the timing and duration of the destruction of the North China Craton. Chinese Science Bulletin, v. 54, p. 1974-1989.

Yang, J. H., O'Reilly, S., Walker, R. J., Griffin, W., Wu, F. Y., Zhang, M., and Pearson, N., 2010. Diachronous decratonization of the Sino-Korean craton: Geochemistry of mantle xenoliths from North Korea. Geology, v. 38, p. 799-802.

Yin, C. Q., Zhao, G. C., Sun, M., Xia, X. P., Wei, C. J., Zhou, X. W., and Leung, W. H., 2009. LA-ICP-MS U-Pb zircon ages of the Qianlishan Complex: Constrains on the evolution of the Khondalite Belt in the Western Block of the North China Craton. Precambrian Research, v. 174, p. 78-94.

Yuan, X. H., 1996. Bouguer anomaly in Atlas of Geophysics in China, v. 29. Geological Publishing House, Beijing, pp. 22– 23.

Zhai, M. G., and Liu, W. J., 2003. Palaeoproterozoic tectonic history of the North China craton: a review. Precambrian Research, v. 122, p. 183-199.

Zhang, H. F., Sun, M., Zhou, X. H., Zhou, M. F., Fan, W. M., and Zheng, J. P., 2003. Secular evolution of the lithosphere beneath the eastern North China Craton: Evidence from Mesozoic basalts and high-Mg andesites. Geochimica et Cosmochimica Acta, v. 67, p. 4373-4387.

Zhang, H. F., Goldstein, S. L., Zhou, X. H., Sun, M., and Cai, Y., 2009. Comprehensive refertilization of lithospheric mantle beneath the North China Craton: further Os-Sr-Nd isotopic constraints. Journal of the Geological Society, v. 166, p. 249-259.

Zhang, H. F., Goldstein, S. L., Zhou, X. H., Sun, M., Zheng, J. P., and Cai, Y., 2008. Evolution of subcontinental lithospheric mantle beneath eastern China: Re-Os isotopic evidence from mantle xenoliths in Paleozoic kimberlites and Mesozoic basalts. Contributions to Mineralogy and Petrology, v. 155, p. 271-293.

Zhang, H. F., Sun, M., Zhou, X. H., Fan, W. M., Zhai, M. G., and Yin, J. F., 2002. Mesozoic lithosphere destruction beneath the North China Craton: evidence from major-, trace-element and Sr-Nd-Pb isotope studies of Fangcheng basalts. Contributions to Mineralogy and Petrology, v. 144, p. 241-253.

Zhang, W. H., and Han, B. F., 2006. K-Ar Chronology and Geochemistry of Jining Cenozoic basalts, Inner Mongolia, and geodynamic Implications. Acta Petrologica Sinica, v. 22, p. 1597–1607.

Zhao, D. P., Maruyama, S., and Omori, S., 2007. Mantle dynamics of Western Pacific and East Asia: Insight from seismic tomography and mineral physics. Gondwana Research, v. 11, p. 120-131.

Zhao, G. C., Sun, M., Wilde, S. A., and Li, S. Z., 2005. Late Archean to Paleoproterozoic evolution of the North China Craton: key issues revisited. Precambrian Research, v. 136, p. 177-202.

Zhao, G. C., Wilde, S. A., Cawood, P. A., and Lu, L. Z., 2000. Petrology and P-T path of the Fuping mafic granulites: implications for tectonic evolution of the central zone of the North China craton. Journal of Metamorphic Geology, v. 18, p. 374-391.

Zhao, G. C., Wilde, S. A., Cawood, P. A., and Sun, M., 2001. Archean blocks and their boundaries in the North China Craton: lithological, geochemical, structural and P-T path constraints and tectonic evolution. Precambrian Research, v. 107, p. 44-73.

Zhao, G. C., Wilde, S. A., Guo, J. H., Cawood, P. A., Sun, M., and Li, X. P., 2010. Single zircon grains record two Paleoproterozoic collisional events in the North China Craton. Precambrian Research, v. 177, p. 266-276.

Zhao, Z. P., 1993. Evolution of Precambrian crust of Sino-Korean Platform. Scientific Press, Beijing. pp. 3-79.

Zheng, J. P., Griffin, W. L., O'Reilly, S. Y., Yu, C. M., Zhang, H. F., Pearson, N., and Zhang, M., 2007. Mechanism and timing of lithospheric modification and replacement beneath the eastern North China Craton: Peridotitic xenoliths from the 100 Ma Fuxin basalts and a regional synthesis. Geochimica et Cosmochimica Acta, v. 71, p. 5203-5225.

Zheng, J. P., O'Reilly, S. Y., Griffin, W. L., Lu, F. X., Zhang, M., and Pearson, N. J., 2001. Relict refractory mantle beneath the eastern North China block: significance for lithosphere evolution. Lithos, v. 57, p. 43-66.

Zheng, J. P., Sun, M., Zhou, M. F., and Robinson, P., 2005. Trace elemental and PGE geochemical constraints of Mesozoic and Cenozoic peridotitic xenoliths on lithospheric evolution of the North China Craton. Geochimica et Cosmochimica Acta, v. 69, p. 3401-3418.

Zhi, X. C., Song, Y., Frey, F. A., Feng, J. L., and Zhai, M. Z., 1990. Geochemistry of Hannuoba Basalts, Eastern China - Constraints on the Origin of Continental Alkalic and Tholeiitic Basalt. Chemical Geology, v. 88, p. 1-33.

Zhou, X. M., and Li, W. X., 2000. Origin of Late Mesozoic igneous rocks in Southeastern China: implications for lithosphere subduction and underplating of mafic magmas. Tectonophysics, v. 326, p. 269-287.

Zhu, G., Wang, Y. S., Liu, G. S., Niu, M. L., Xie, C. L., and Li, C. C., 2005. Ar-40/Ar-39 dating of strike-slip motion on the Tan-Lu fault zone, East China. Journal of Structural Geology, v. 27, p. 1379-1398.

Zhu, R. X., and Zheng, T. Y., 2009. Destruction geodynamics of the North China craton and its Paleoproterozoic plate tectonics. Chinese Science Bulletin, v. 54, p. 3354-3366.

Zindler, A., and Hart, S., 1986. Chemical Geodynamics. Annual Review of Earth and Planetary Sciences, v. 14, p. 493-571.

Zindler, A., and Jagoutz, E., 1988. Mantle Cryptology. Geochimica et Cosmochimica Acta, v. 52, p. 319-333.